FAKULTÄT FÜR MASCHINENWESEN
LEHRSTUHL FÜR FLUGSYSTEMDYNAMIK

Frequency Response Estimation for Integrity Monitoring

Dipl.-Ing. (Univ.) Christian Merkl

Vollständiger Abdruck der von der Fakultät für Maschinenwesen
der Technischen Universität München
zur Erlangung des akademischen Grades eines
Doktor-Ingenieurs (Dr.-Ing.)
genehmigten Dissertation.

Vorsitzender:	Prof. Dr.-Ing. Manfred Hajek
Prüfer der Dissertation:	1. Prof. Dr.-Ing. Florian Holzapfel
	2. Prof. Dr. Carlo Bottasso

Die Dissertation wurde am 11.09.2018 bei der Technischen Universität München eingereicht und durch die Fakultät für Maschinenwesen am 26.02.2019 angenommen.

In Erinnerung an meine Eltern,
Mary und Günter.

VORWORT

Auf dem Weg zur Erstellung dieser Arbeit haben ich von vielen Seiten Unterstützung erfahren. Mein Dank gilt hier vor allem Prof. Florian Holzapfel, der mir die Promotion an seinem Lehrstuhl ermöglicht hat. My thanks also goes to Prof. Carlo L. Bottasso for his commitment as second examiner.

Ganz am Beginn meiner Forschungsarbeit stand die Idee einer geteilten Promotionsstelle mit einem Industriepartner: Herr Breitinger ließ sich stellvertretend für die IABG von der Idee überzeugen – Ihm gilt mein Dank für sein Vertrauen und die verbundene finanzielle Unterstützung durch die IABG. Dort konnte ich hautnah miterleben, wie sich die Arbeit in der Industrie und an der Universität gegenseitig ergänzen und habe dabei wertvolle Erfahrungen gewonnen. Ganz besonders möchte ich mich bei Roland Leitner für seine vielseitige fachliche und menschliche Unterstützung bedanken.

Am Lehrstuhl hatte ich die Gelegenheit, die neue Systemidentifikationsgruppe von Beginn an mitzugestalten. Beginnend mit einem zwei-Mann Team, hat sie sich erstaunlich entwickelt. Die heutige Vorlesung zur Systemidentifikation und die große Zahl der beitragenden Kollegen zeigt das sehr schön – vielen Dank an alle Kollegen, die mich in dieser Zeit begleitet haben. Ein ganz besonderes Dankeschön gilt Prof. Matze Heller, der bei Fragen zur robusten Regelung immer ein offenes Ohr für mich hatte. Bei verzwickten Statistikfragen war Lukas Höhndorf ein wertvoller Diskussionspartner – vielen Dank dafür!

Ein ganz besonderer Dank gilt meiner Frau Constanze, die mich durch unzählige Höhen und Tiefen begleitet und mich dabei stets unterstützt und ermutigt hat.

Garching, im Sommer 2018 Christian Merkl

ZUSAMMENFASSUNG

Die Arbeit untersucht die online-Schätzung von Frequenzgangmatrizen aus einem einzelnen Flugtest-Experiment. Während es bislang notwendig war, für jeden Systemeingang ein unabhängiges Experiment durchzuführen, ermöglicht die kürzlich entwickelte Local Polynomial Method (LPM) auch die Schätzung der Frequenzgangmatrix aus einem einzelnen Experiment. Anhand umfangreicher Simulationen wird die Genauigkeit des Algorithmus hinsichtlich luftfahrtrelevanter Größen bei unterschiedlichen Flugbedingungen untersucht. Daraus werden „Minimalbedingungen“ abgeleitet, die notwendig sind, um genaue Mehrgrößen-Frequenzgänge aus einem einzelnen Flugversuch erzielen zu können.

Ausgehend von den statistischen Eigenschaften der Schätzung wird ein Unsicherheitsmodell entwickelt, das mit Methoden der robusten Stabilitätsanalyse untersucht wird. Mit diesem Ansatz lässt sich ein Konfidenzniveau bestimmen, mit dem das geschätzte System robust stabil ist. Angewandt auf Flugregelungssysteme gibt dieser Ansatz eine unabhängige Möglichkeit, das dynamische Verhalten und die Stabilität des Flugreglers zu überwachen. Da der Algorithmus auf nicht-parametrischen Modellen aufbaut, kann der überwachte Frequenzbereich sehr einfach angepasst werden, um z.B. die Stabilität unbekannter aeroelastischer Moden zu überwachen. Aufgrund seiner einfachen Bedienung ist der entwickelte Ansatz sehr gut zur online Anwendung geeignet.

ABSTRACT

The thesis examines the online estimation of frequency response matrices from a single flight test experiment. While it was previously necessary to carry out independent experiments for each system input, the recently developed local polynomial method makes it possible to estimate frequency response matrices from a single experiment. Comprehensive simulations are used to investigate the achievable accuracy with respect to aviation related quantities under different flight conditions. Based on these, "minimum conditions" are derived which are required to achieve accurate multi-variable frequency responses from a single flight test.

An uncertainty model is developed based on the statistical properties of the estimates. It is analysed with robust stability methods, resulting in a confidence level for robust stability of the system. Applied to flight control systems, this approach provides an independent way to monitor the dynamic behaviour and stability of the flight control system. As the algorithm is based on non-parametric models, the analysed frequency range can be easily adjusted to monitor e.g. the stability of unknown aeroelastic modes. Due to its insensitivity to user choices, the algorithm is very well suited for online applications.

CONTENT

LIST OF FIGURES

LIST OF TABLES

LIST OF ACRONYMS

Acronym	Description
AC	Aircraft
AHRS	Attitude heading reference system
AIAA	The American Institute of Aeronautics and Astronautics
ARW	Angel random walk
BLA	Best linear approximation
CIFER	Comprehensive identification from frequency responses
CSL	Confident stability level
DFT	Discrete Fourier transform
DOI	Digital object identifier
DR	Dutch roll mode
EIV	Errors-in-variables
erf	Error response function
ETFE	Empirical transfer function estimate
ETFM	Extended transfer function model
FAA	Federal Aviation Administration
FCS	Flight control system
FFT	Fast Fourier transform
FOG	Fibre optical gyroscope
FRF	Frequency response function
FRM	Frequency response matrix
FRoI	Frequency range of interest
FSD	Lehrstuhl für Flugsystemdynamik der TU München
iid	Independent and identically distributed
IEEE	Institute of Electrical and Electronics Engineers
IFAC	International Federation of Automatic Control
IMU	Inertial measurement unit
LFT	Linear fractional transform
LPM	Local polynomial method
LPMC	Local polynomial method with constraints
LRM	Local rational method
LRMC	Local rational method with constraints
LLS	Lehrstuhl für Luftfahrtsystem der TU München
LS	Least squares
LTI	Linear time invariant
MIMO	Multiple-input, multiple-output

Acronym	Description
ML	Maximum likelihood
NSC	Nyquist stability criterion
ODE	Ordinary differential equation
OE	Output error (model structure)
pdf	Probability density function
PH	Phygoid mode
PSD	Power spectrum density
RMS	Root mean square
RS	Robust stability
SISO	Single input, single output
SP	Short period mode
ssv	Structured singular value
SNR	Signal-to-noise ratio
SVD	Singular value decomposition
TRIMM	Transient impulse response modelling method
VTOL	Vertical take-off and landing

NOMENCLATURE

LIST OF OPERATORS AND NOTATIONAL CONVENTIONS

Symbol	Definition	Description
$\otimes$		Kronecker matrix product
$a \cdot b$		Scalar product of a and b
$a(t) * b(t)$	$= \int_{-\infty}^{\infty} a(\tau) b(t-\tau) d\tau$	Convolution of a and b
$\hat{x}$		Estimate of x
x_0		True value of x
x_u		Quantity x with respect to the input u
x_y		Quantity x with respect to the output y
$\mathrm{Re}(x)$		Real part of x
$\mathrm{Im}(x)$		Imaginary part of x
$\bar{x}$		Conjugate complex of x
x^T		Matrix transpose
x^{-T}		Transpose of inverse matrix
x^H		Hermitian transpose of x, i.e. complex conjugate transpose of matrix x
x^{-H}		Hermitian transpose of inverse matrix of x
x^+		Moore-Penrose pseudoinverse
$\angle x$		Phase argument of complex number x
$\lvert x \rvert$	$= \sqrt{\left(\mathrm{Re}(x)\right)^2 + \left(\mathrm{Im}(x)\right)^2}$	Magnitude of complex number x
$\sphericalangle x$		Angle x
$\vec{x}$		Vector quantity
$\tilde{x}$		A tilde differentiates otherwise equally named variables
$x_{[i]}$		i-th entry of the vector x
$x_{[i,j]}$		Element in i-th row and j-th column of matrix x
$x_{[:,j]}$		j-th column of matrix x
$x_{[i,:]}$		i-th row of matrix x
$x_{[i:j,m:n]}$		Rows i to j and columns m to n of x
$x^{i \times j}$		Matrix with i rows and j columns, i.e. with dimension i-by-j, or $i \times j$ resp.
$\mathbb{X}^n$		Vector with n elements that are integer / real / complex numbers, where $\mathbb{X}$ is $\mathbb{Z}$, $\mathbb{R}$, $\mathbb{C}$, respectively

Symbol	Definition	Description
$\mathbb{X}^{n\times m}$		Matrix with n rows and m columns and elements that are integer / real / complex numbers, where $\mathbb{X}$ is $\mathbb{Z}, \mathbb{R}, \mathbb{C}$, respectively
$x^{[i]}$		i-th realization of a random process x
$\|x\|_2$		H_2-norm of x
$\|x\|_\infty$		Supremum- or H_∞-norm of x
$\mathcal{s}(x)$		Singular value of a matrix x
$\mathrm{ssv}(x)$		Structured singular value of matrix x
$x(t)$		Continuous time signal
$x[n]$		Discrete time signal
$X(j\omega)$		Fourier Transform of continuous time signal $x(t)$
$X(e^{j\omega})$		z-transform of discrete time signal $x[n]$ with $z = e^{j\omega}$
$X_{DFT}(j\omega)$		Discrete Fourier Transform coefficients at continuous frequency ω
$X(k)$		Discrete Fourier Transform coefficients of the samples $x(n\Delta t)$ or $x[n]$ at discrete frequency ω_k with $\omega_k = \frac{k}{T_{win}}, k \in \{0, 1, 2, \dots, F\}$
X_k		Fourier coefficients of the periodic signal $x(t)$
$\mathrm{ceil}(x)$		Ceiling function; returns next larger integer
$\mathrm{diag}(x_1, \dots, x_K)$		Block diagonal matrix with blocks x_1 to x_K
$\mathrm{herm}(x)$	$= \frac{X+X^H}{2}$	Hermitian symmetric part of an $n \times m$ matrix x
$\mathrm{rank}(x)$		Rank of the $n \times m$ matrix x, maximum number of linear independent rows (columns) of x
$\mathrm{std}(x)$	$= \sqrt{\mathbb{E}\{\|x - \mathbb{E}\{x\}\|^2\}}$	Standard deviation of x
$\mathrm{var}(x)$	$= \mathbb{E}\{\|x - \mathbb{E}\{x\}\|^2\})$	Variance of x
$\mathrm{rms}(x)$	$= \sqrt{\sum_{i=1}^{n} x_{[i]}^2}$, with $x \in \mathbb{R}^n$	Root mean square value of x
$\mathrm{vec}(x)$	$= \begin{bmatrix} x_{[:,1]} \\ \vdots \\ x_{[:,m]} \end{bmatrix}$	A column vector formed by stacking the columns of the $n \times m$ matrix x on top of each other
$\mathbb{E}\{x\}$		Expected value of x
$\mathrm{prob}(x)$		Probability of x
$\mathrm{prob}(x\|y)$		Conditional probability of x, given y

Symbol	Definition	Description
$\varepsilon(\lvert X\rvert)$	$= \frac{\lvert\hat{X}\rvert}{\lvert X_0\rvert}$	Magnitude ratio of estimate and true value
$\varepsilon(\angle X)$	$= \angle\hat{X} - \angle X_0$	Absolute error of phase of X
b_x	$= \mathbb{E}\{x\} - x_0$	Bias of x
$\mathrm{Cov}(X, Y)$	$= \mathbb{E}\{(X - \mathbb{E}\{X\})(Y - \mathbb{E}\{Y\})^H\}$	Cross-covariance matrix of X and Y
$\mathrm{covar}(x, y)$	$= \mathbb{E}\{(x - \mathbb{E}\{x\})\overline{(y - \mathbb{E}\{y\})}\}$	Covariance of x and y
$\mathrm{CV}(X)$	$= \frac{\mathrm{std}(X)}{\mathbb{E}\{X\}}$	Coefficient of Variation of X
$\mathrm{SCV}(X)$	$= \frac{var(X)}{(\mathbb{E}\{X\})^2} = CV(X)^2$	Squared Coefficient of Variation
$\mathrm{CR}(x)$	$= \frac{l_\infty(x)}{l_2(x)}$	Crest Factor of signal x
$\ln(x)$		Natural logarithm of x
$\log_y(x)$	$= \frac{\ln(x)}{\ln(y)}$	Logarithm of x to the base y
$\mathrm{dB}(X)$	$= 20 \cdot \log_{10}(\lvert X\rvert)$	Conversion to decibel (for field quantities)
$\mathrm{DFT}(x[n])$	$= \frac{1}{\sqrt{N}} \sum_{n=0}^{N-1} x[n] e^{\frac{-j2\pi kn}{N}}$	Discrete Fourier transform of the samples $x[n], n = 0, 1, \ldots N-1$
$\mathcal{F}\{x(t)\}$	$= \int_{-\infty}^{\infty} x(t) e^{-j2\pi ft}\, dt$	Continuous Fourier transform
I^m		$m \times m$ identity matrix
$\mathrm{lcm}(X_1, \ldots, X_k)$		Least common multiple of X_1 to X_k
$\mathrm{MSE}(X)$	$= \mathbb{E}\{(X - X_0)(X - X_0)^H\}$	Mean square error of the estimate X
$S_{xx}(j\omega)$	$= \lim_{T\to\infty} \frac{1}{T} E\left\{\left(X(j\omega)^{[k]}\right)\left(X(j\omega)^{[k]}\right)^H\right\}$	Auto power spectrum of $x(t)$
$S_{xy}(j\omega)$	$= \lim_{T\to\infty} \frac{1}{T} E\left\{\left(X(j\omega)^{[k]}\right)\left(Y(j\omega)^{[k]}\right)^H\right\}$	Cross power spectrum of $x(t)$ and $y(t)$ with finite Fourier transforms over k records of length T.
$\hat{S}_{XX}(k)$	$= \frac{1}{M}\sum_{m=1}^{M} X^{[m]}(k) X^{[m]H}(k)$	Sample auto power spectrum of $x(t)$
$\hat{S}_{XY}(k)$	$= \frac{1}{M}\sum_{m=1}^{M} X^{[m]}(k) Y^{[m]H}(k)$	Sample cross-power spectrum of $x(t)$
$\dot{x}(t)$	$= \frac{dx}{dt}$	First time derivative of $x(t)$
$\ddot{x}(t)$	$= \frac{d^2x}{dt^2}$	Second time derivative of $x(t)$
$x \in \mathcal{O}(y)$		x grows asymptotically not faster than y

LIST OF LATIN SYMBOLS

Symbol	Unit	Description
c_s	-	Safety factor for confidence regions
C_X	-	Covariance matrix of X, $C_X = \mathrm{Cov}(X, X)$
C_{XY}	-	Cross-covariance matrix of X and Y, $C_{XY} = \mathrm{Cov}(X, Y)$
$\hat{C}_X$	-	Sample covariance matrix of M realizations of X $\hat{C}_X = \frac{1}{M-1}\sum_{m=1}^{M}(X^{[m]} - \hat{X})(X^{[m]} - \hat{X})^H$
$\hat{C}_{XY}$	-	Sample cross covariance matrix of M realizations of X and Y, $\hat{C}_{XY} = \frac{1}{M-1}\sum_{m=1}^{M}\left(X^{[m]} - \hat{X}\right)\left(Y^{[m]} - \hat{Y}\right)^H$
$e(t)$	-	White noise at time t
$e(t)$	-	Control error signal
$E(k)$	-	Discrete Fourier transform of the samples $e(nT_s), n = 0,1, \dots, N-1$
f	Hz	Frequency
f_s	Hz	Sampling Frequency
Δf	Hz	Frequency spacing of DFT
F	-	Number of discrete frequencies
$G(j\omega)$	-	Frequency response function / matrix at frequency $\omega \in \mathbb{R}$
$G(j\omega_k)$	-	Frequency response function / matrix at discrete set of frequencies ω_k
$G_{yx}(j\omega)$	-	Frequency response function from signal x to signal y
$G_{BL}(j\omega_k)$	-	Frequency response function based on band limited signals.
$G_{BLA}(j\omega)$	-	Best linear approximation of a nonlinear plant
$G(j\omega, \theta)$	-	Frequency response function of parametric plant model with parameters θ
$G_p(j\omega)$	-	Particular realization of uncertain LTI system
j	-	Complex number ($j^2 = 1$)
L	Nm	Torque around the x-axis
M	-	Number of (repeated) experiments
M	Nm	Torque around the y-axis
N	-	Number of time domain data samples
N	Nm	Torque around the z-axis
n_ω	-	Number of frequencies
n_{in}, n_{out}	-	Number of input and output signals
p	-	Confidence level
$p_x(\cdot)$	-	General probability density function of random variable x

Symbol	Unit	Description
p_K	rad/sec[1]	Kinematic roll rate
p_S	rad/sec	Kinematic roll rate as measured by IMU
q	-	Degrees of freedom of covariance matrix estimate.
q_K	rad/sec	Kinematic pitch rate
q_S	rad/sec	Kinematic pitch rate as measured by IMU
$r(t)$	-	Reference excitation signal
r_K	rad/sec	Kinematic yaw rate
r_S	rad/sec	Kinematic yaw rate as measured by IMU
$r_p, r_{p,[i]}$	-	Confidence radius (of signal i) with confidence level p
R_p	-	Confidence radii matrix with confidence level p
R_X	-	Relation matrix of complex random vector X, $R_X = \mathbb{E}\{(X - \mathbb{E}\{X\})(X - \mathbb{E}\{X\})^T\}$
s	-	Laplace transform variable
SNR_X	-	Signal-to-noise ratio of signal X
t	sec	Continuous time variable
$\Delta t_s, \Delta t$	sec	Sampling period
T_k	sec	Oscillation period of sinusoid with frequency f_k
T_{win}	sec	Length of window function
$v_u(t), v_y(t)$	-	Disturbing time domain noise on the input $u(t)$ and output $y(t)$ respectively
$v_p(t)$	-	Process noise
$V_U(k), V_Y(k)$	-	Discrete Fourier transform coefficients for frequency k of the samples $v_u[n]$ and $v_y[n], n = 0,1, \dots N-1$ respectively
$V_P(k)$	-	DFT coefficients for frequency k of the process noise samples $v_p[n]$ with $n = 0,1, \dots N-1$ respectively
$u(t), y(t)$	-	Input and output signals (continuous time)
$u[n], y[n]$	-	Input and output signals (discrete time)
$U(k), Y(k)$	-	Discrete Fourier Transform coefficients for frequency k of the samples $u(n\Delta t)$ and $y(n\Delta t), n = 0, 1, \dots, N-1$
$U(j\omega), Y(j\omega)$	-	Fourier transform of $u(t)$ and $y(t)$
U_k, Y_k	-	Fourier coefficients of the periodic signals $u(t)$ and $y(t)$
$Z(k)$	-	Data vector containing the measured input and output (DFT) spectra at (DFT) frequency k (i.e. $Z(k) = \begin{bmatrix} Y(k) \\ U(k) \end{bmatrix}$)
X	Nm	Force component in x-direction
Y	Nm	Force component in y-direction
Z	Nm	Force component in z-direction

[1] To avoid confusion with the Laplace variable the unit second is denoted with sec instead of the SI-symbol s.

LIST OF GREEK AND OTHER SYMBOLS

Symbol	Unit	Description
$\gamma_{xy}^2(f)$	-	Coherence of $x(t)$ and $y(t)$ at frequency f
Γ_R	-	Real matrix of complex confidence region R
$\delta(k)$	-	Kronecker delta: $\delta(0) = 1$ and $\delta(k) = 0$ for $k \neq 0$
$\delta(t)$	-	Dirac function: $\delta(0) = \infty$, $\delta(t) = 0$ for $t \neq 0$ and $\int_{\infty}^{\infty} \delta(x)dx = 1$
$\mathfrak{d}_{\Delta t}(t)$	-	Dirac comb: $\mathfrak{d}_{\Delta t}(t) = \sum_{k=-\infty}^{\infty} \delta(t - k\Delta t)$
Δ	-	Norm bounded perturbation
ζ	-	Virtual rudder deflection (normalized)
ζ_0	-	Relative damping of complex conjugate pole pair
η	-	Virtual elevator deflection (normalized)
η_{yu}	-	Zero of transfer function from input u to output y
θ	-	Column vector of the model parameters
Θ	-	Matrix with unknown parameters in LS-estimate
Θ	rad	Pitch angle of aircraft
Ψ	rad	Heading angle of aircraft
Φ	rad	Roll angle of aircraft
κ	-	Maximum scaling of uncertainty weighting
$\lambda_i(A)$	-	i-th eigenvalue of matrix A
λ_{yu}	-	Pole of transfer function from input u to output y
μ_X	-	Mean value of X
ν	-	Ruddervator deflection (normalized)
ξ	-	Aileron deflection (normalized)
Π	-	Uncertainty set of LTI systems
ϕ	rad	Phase angle of multisine signal
φ		
ρ_{xy}	-	Correlation coefficient
$\mathfrak{r}(A)$	-	Spectral radius of matrix A
$\sigma_U^2(k)$	-	Variance of the measured input DFT spectrum
$\sigma_Y^2(k)$	-	Variance of the measured output DFT spectrum
$\sigma_{YU}^2(k)$	-	Covariance of the measured input and output DFT spectra
τ	sec	Time delay
ω	rad/sec	Angular frequency ($= 2\pi f$)
ω	rad/sec	Rotational rate
ω_0	rad/sec	Eigenfrequency of complex conjugate pole pair

List of Relevant Statistical Distributions

Symbol	Description
$\mathbb{N}(\mu, \sigma^2)$	Normal distribution with expected value μ and standard deviation σ
$\mathbb{N}^{-1}(p, \mu, \sigma^2)$	Inverse cumulative distribution function of a normally distributed random variable for probability p, expected value μ and standard deviation σ
$\mathbb{n}(x, \mu, \sigma^2)$	Probability density function of a normally distributed random variable at x, expected value μ and standard deviation σ
$\chi^2(a)$	χ^2-distribution with a degrees of freedom
$\mathbb{F}(a, b)$	F-distribution with parameters a and b
$\mathbb{F}(x, a, b)$	F-cumulative distribution function with parameters a and b at x
$\mathbb{F}^{-1}(p, a, b)$	Inverse cumulative distribution function of an F-distributed random variable for probability p and parameters a and b; the inverse cumulative distribution function equals the quantile function
$\mathbb{f}(x, \mu, \sigma^2)$	Probability density function of an f-distributed random variable at x, expected value μ and standard deviation σ
$\mathbb{U}(a, b)$	Uniform distribution with parameters a and b, i.e. with minimum value a and maximum value b
$\mathbb{W}(n, C_x)$	Wishart distribution with n degrees and associated parameter matrix C_x
$\mathbb{F}^c(\cdot), \chi^c(\cdot), \mathbb{W}^c(\cdot)$	Complex F- / chi- / Wishart distribution
$\mathbb{N}^c(\cdot)$	Circular complex normal distribution

List of Number Sets

Symbol	Description
$\mathbb{Z}^+, \mathbb{Z}_0^+$	Natural numbers[2] excluding / including 0
$\mathbb{Z}$	Integer numbers
$\mathbb{R}$	Real numbers
$\mathbb{C}$	Complex numbers
$\mathbb{Q}$	Rational numbers

[2] Note: To avoid ambiguities, natural numbers are denoted with $\mathbb{Z}^+$. The symbol $\mathbb{N}$ is used within this thesis to indicate a normally distributed random variable.

NOTES ON THE USE OF BRACKETS

Symbol	Usage
$(\cdot)$	Used for function arguments and in formulas
$[\cdot]$	Used for discrete time signals, vectors, matrices and intervals. Sporadically used in formulas for better readability. For use in super- and subscripts see *List of Operators and Notational Conventions*
$\{\cdot\}$	Used for expected value and Fourier transform

NOTES ON UNITS

Within this thesis generally SI units and accepted non-SI units are used (Bureau International des Poids et Mesures, 2006). Exceptions are made for aeronautical quantities, that are commonly denoted in non-SI units (ICAO, 2006). As an exception to these norms, the unit *second* is abbreviated with "sec" instead of "s", to avoid notational ambiguities with the Laplace operator s.

AIRCRAFT SIGNAL NAMING CONVENTION

Flight dynamics quantities are denoted with their respective reference points and reference frames. The figure shows the orientation and rotational sense for quantities given in body frame coordinates.

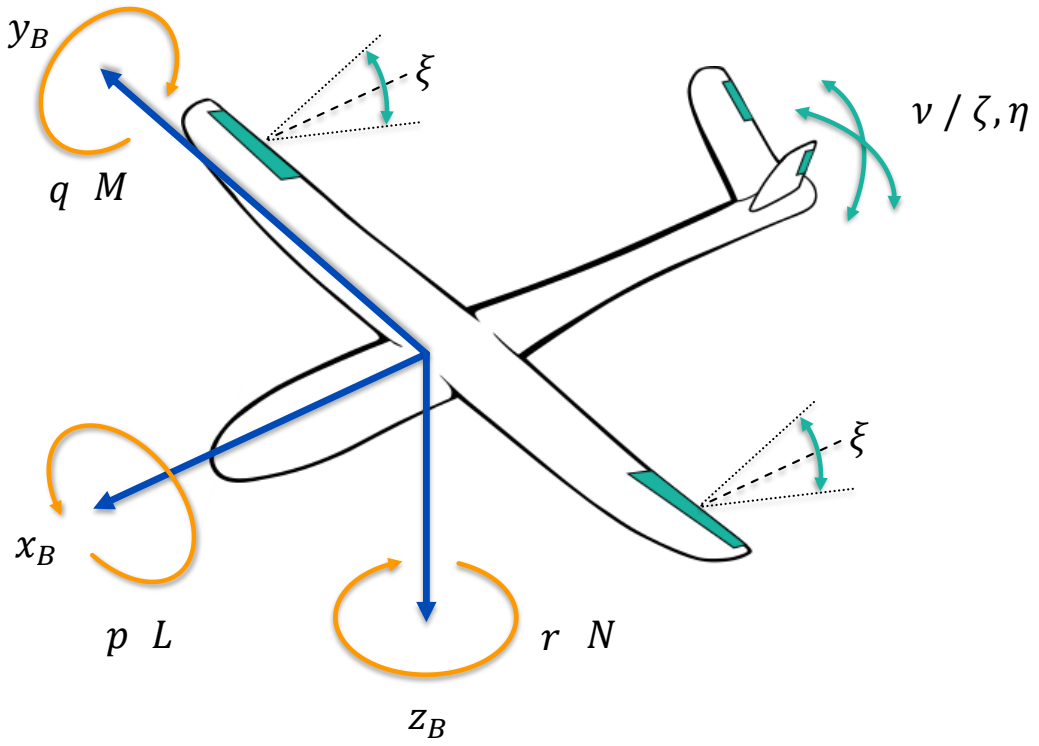

Body frame axis (x_B, y_B, z_B), components of rotational rates (p, q, r), angular moment components (L, M, N) and control surface deflections (ξ, ν)

Forces and moments are denoted as $\vec{F}$ and $\vec{M}$. The respective components are denoted with X, Y, Z (forces) and L, M, N (moments). The full notation includes the respective

- *reference point (rp):* The point where the force/moment act on.
- *origin:* The (physical) origin of the force/moment:
- *reference frame:* the reference frame in which the quantity is denoted

Full notation:

$$\left(\vec{F}^{\text{rp}}_{\text{origin}}\right)_{\text{frame}} = \begin{bmatrix} X \\ Y \\ Z \end{bmatrix}_{frame} \quad \text{and} \quad \left(M^{\text{rp}}_{\text{origin}}\right)_{\text{frame}} = \begin{bmatrix} L \\ M \\ N \end{bmatrix}_{frame}$$

Rotational rates are denoted as $\vec{\omega}$. The components are denoted with p, q, r. In this thesis, only kinematic rates of body frame w.r.t inertial frame are used. In full notation, rotational rates are denoted with indication of

- *type*: Type of angular rate (K: kinematic)
- *IB*: reference frames that are rotated (IB: body frame rotates w.r.t inertial frame)
- *frame*: reference frame in which the quantity is denoted

Full notation:

$$\left(\vec{\omega}^{IB}_{type}\right)_{frame} = \begin{bmatrix} p \\ q \\ r \end{bmatrix}_{frame}$$

The relevant reference frames, reference points and physical origins are listed in the following tables. Their definitions follow the common conventions as introduced in detail in many textbook on flight mechanics and flight control (Etkin & Reid, 1996; Klein & Morelli, 2006; Stevens & Lewis, 2003; Zipfel, 2007):

Symbol	Reference Frames
I	Inertial frame
B	Body fixed frame
S or IMU	Sensor frame

Symbol	Reference Points
A	Aerodynamic reference point
G	Centre of gravity of aircraft

Symbol	Physical origins
A	Aerodynamic forces and moments
$crtl$	Forces and moments of aircraft control surfaces

Symbol	Type (rotational rates)
K	Kinematic

1 INTRODUCTION

In recent years, numerous unmanned aircraft and new aircraft configurations like multicopters have been developed. Especially with regard to autonomous flight operations, they depend heavily on active flight control systems. The control approaches commonly used in aviation are based on highly accurate simulation models. For cost reasons, however, it is often not possible to create such simulation models. Instead, the focus is increasingly shifted to accepting uncertainties in the system and monitor if the overall behaviour of the system remains within safe limits.

In the context of flight control systems, this means that flight control laws are designed with rigid body models, knowing that they differ from reality. The associated risk lies in neglected dynamics, like elastic modes of the airframe or aeroelastic effects like flutter[3], that may be inadvertently destabilised by the controller feedback loop. Such instabilities can lead to possibly fatal structural failure and must be avoided. It is thus a well-established practice for the flight testing to carefully extend the flight envelope and monitor relevant measures like stability margins (Clarke, Burken, Bosworth, & Bauer, 1994). During the flight tests, it is continuously monitored whether the actual dynamics of the aircraft correspond to the desired ones or are within safe limits. It follows naturally, that such a monitoring system consists of two parts:

(a) A mathematical description of the system dynamics that are observed during operations, i.e. a model of the actual dynamics.
(b) A criterion to assess if the model is in a safe condition or not.

The mathematical modelling of system dynamics from observed data is the classical field of system identification. It combines estimation theory with signal- and systems theory and provides a probabilistic framework for statements about the dynamics of the real system. In the context of flight control systems, the criteria (b) is a stability criterion, that ensures that the closed loop dynamics of the system with its flight control system are stable. For the intended monitoring system, both parts need to be combined in an online algorithm to quantify and monitor the integrity of the flight control system.

The available approaches however have several shortcomings. On the model part, they are either based on parametric models, that are sensitive to the required model order selection – an improper choice of model order results in systematic modelling errors. Non-parametric models like frequency response functions avoid the model order decision and are thus better suited for monitoring tasks. The estimation of frequency response functions for multiple input systems is however not suited for monitoring applications.

The recently developed local polynomial method provides a different approach that bridges this gap: It allows to estimate frequency response functions in a different way that is suited for monitoring applications. It is here combined with robust stability criteria, that are valid for multiple input systems. Their combination provides a measure of the confidence that the closed loop aircraft dynamics are stable, solely based on measured data.

[3] In the course of this thesis, purely elastic modes and aeroelastic modes are not distinguished, as both can lead to closed loop instability in the same way. Transient aeroelastic effects like divergence are also not considered.

1.1 State of the Art

1.1.1 System Identification

The theoretic roots of system identification data back to the work of (Gauss, 1809) and (Fisher, 1912) who studied stochastic processes. In engineering, the practical importance of system identification grew with the advent of automatic control since the 1950s, that finally led to the "birth" of system identification as an own scientific field, with important publications by (Ho & Kalman, 1966) and (Åström & Bohlin, 1965). The name of the new field was coined by Lofti Zadeh, who defined it as

> *"[…] the determination, on the basis on input and output, of a system within in a specified class of systems, to which the system under test is equivalent." (Zadeh, 1962)*

This general principle can be applied to many scientific and engineering tasks and system identification methods are thus used in many science fields, albeit they are sometimes named differently (Ljung, 1996). What they all have in common is that that they are based on three entities (Ljung, 2009):

- A set of *data*.
- A *model structure* that contains a set of possible models.
- A *rule or criterion* that fits the model to the data.

The classification of today's system identification methods follows these entities:

Data is generally divided in *time-* and *frequency domain* data: General time domain system identification is covered in (Ljung, 2009), applications to flight dynamics are found in (Klein & Morelli, 2006) and (Jategaonkar, 2006).

Frequency domain methods are generally covered in (Pintelon & Schoukens, 2012); spectral methods are the focus in (Bendat & Piersol, 1971/2010) and (Stoica & Moses, 2005). Spectral methods are applied to flight dynamics identification, with special focus on rotorcrafts, in (Tischler & Remple, 2006). Many frequency domain methods implicitly assume linear dynamics; generalizations for nonlinear systems are studied e.g. in (Pintelon & Schoukens, 2012) and (Billings, 2013).

In engineering applications, models are typically distinguished in *parametric* and *non-parametric* ones. The first group contains all kinds of differential equations that describe e.g. linear time invariant (LTI) systems, or linear parameter varying (LPV) systems. Non-parametric models are e.g. frequency response functions (FRFs) (Ljung, 2009; Pintelon & Schoukens, 2012).

The *rules or criteria* are based on statistical principles like least squares (LS) estimation or maximum likelihood (ML) estimation that form the theoretic foundation for different estimation methods like the prediction error method (Åström & Bohlin, 1965; Ljung, 1976, 2009) or subspace methods (Ho & Kalman, 1966; Qin, 2006). The statistical framework is necessary to account for the effect of random noise in the data. As a consequence, any model contains uncertainties[4] and a full description of an identified model is not complete without measures of its uncertainty.

[4] Compare Ljung (2009, p. 7) on the fiction of a true system.

1.1.1.1 *Frequency Response Estimation*

In this thesis, frequency domain methods are used, with the focus on non-parametric models (frequency response functions). The FRF estimation algorithms are further distinct depending on the experimental conditions. Important criteria are

- Number of system inputs
- Periodicity of the excitation signal
- Operation in open or closed loop

Figure 1-1 gives an overview of the categorization of system identification methods; the entities used in this thesis are highlighted. The following subsections give a short overview of the respective effects on the FRF estimation.

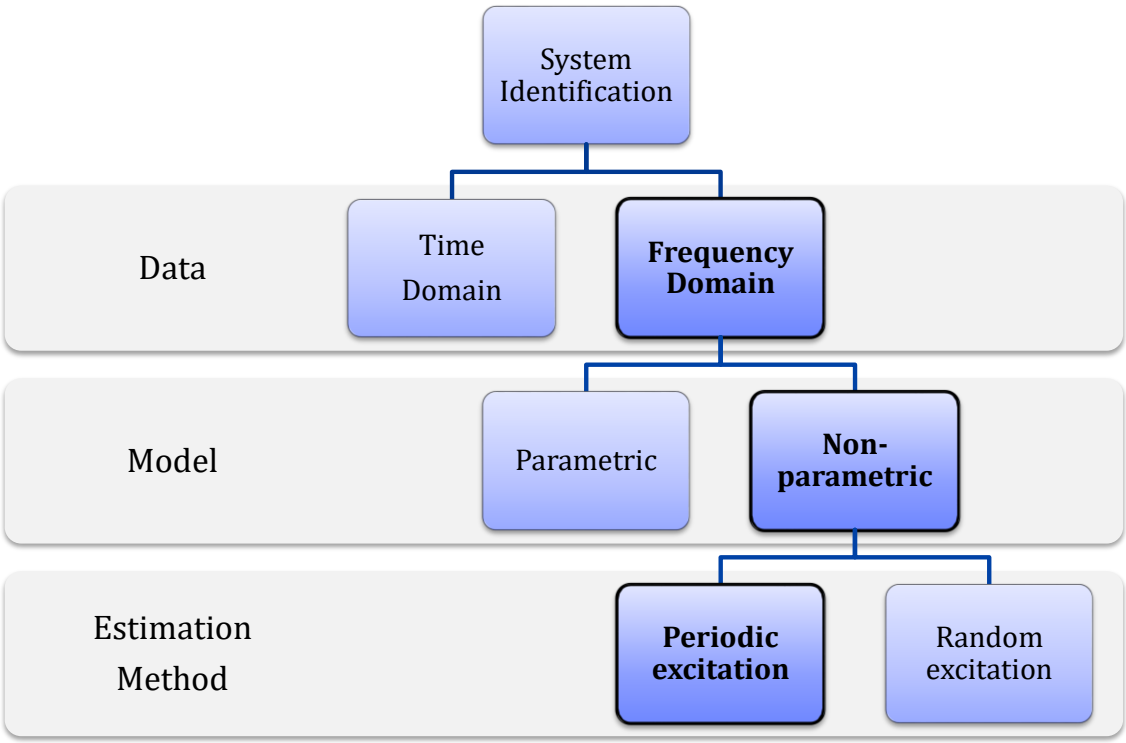

Figure 1-1: Overview and classification of system identification methods.

Single-Input Techniques

There are several ways to compute frequency response functions. The most direct way is to excite the linear time-invariant (LTI) system with a sinusoid. For LTI systems, the steady state system response is a sinusoid of the same frequency as the excitation and differs only in magnitude and phase. By changing the frequency and repeating the experiment, the FRF can be computed for any number of frequencies. Due to its simplicity, this approach can be implemented even with analogue devices only. As simple as it is, this approach is slow, as one frequency is excited after the other and for each frequency it must be waited until transients have died out.

A significant speed up can be achieved, when the signals are analysed in the frequency domain. Discrete Fourier transforms allow to convert the digitally measured signal in its frequency components. Thus multiple frequencies can be excited at the same time, substantially reducing the required test time. The development of fast Fourier transforms (FFT) (Cooley & Tukey, 1965) allowed to compute discrete Fourier transform very efficiently. The use of discrete Fourier transforms (DFTs) came at the cost of possible

leakage errors. Leakage is a major systematic error that can occur when non-periodic data is transformed with a DFT. Leakage is related to the finite data length used in DFTs; a more detailed introduction is found in section 2.2.

To reduce leakage effects, especially in the context of random signals, spectral methods have been developed (Welch, 1967). They are based on averaging and windowing techniques to reduce errors (Harris, 1978). The exact choice of window function and the details of averaging however can be tricky and is sometimes considered "*more art than science*" (Tischler & Remple, 2006, p. 145). A different approach that avoids leakage effects is the use of periodic input signals (Pintelon, Guillaume, Rolain, Schoukens, & van Hamme, 1994). The periodicity is necessary to ensure a leakage-free calculation of the input- and output DFT spectra (Brigham, 1974). In (Pintelon & Schoukens, 2001), the estimation bias and variance are studied for different estimators, based directly on Fourier coefficients of periodic signals. In (Pintelon, Rolain, & van Moer, 2003) analytical probability density functions for frequency response function estimates from periodic data are derived. Real-time estimation of single input frequency response functions is studied in (Holzel & Morelli, 2012).

Both, spectral methods and the methods based on periodic excitations, suffer from leakage errors, if the data contains transient signal components, e.g. from non steady-state initial conditions (see section 2.3 for details). As transients decay with time, it has become a standard procedure to discard the first two periods of any dataset, as in general transient components will be negligible after two full periods (Bailey & Markofski, 2001; The Mathworks, 2009).

Multiple Input Techniques

In case of multiple inputs, the frequency response *function* extends to a frequency response *matrix*. Due to the assumed linearity, the frequency response for each input can be identified separately; the frequency response matrix is then combined from the respective single input frequency response functions. This approach is however tedious as it requires many separate experiments. In addition, the experimental conditions may change from one experiment to the other, which makes the combination involved.

At least in principle, frequency response matrices can be estimated with spectral methods, based on uncorrelated excitation signals and conditioned spectral density functions (Bendat & Piersol, 1971/2010, pp. 232–245) from a single experiment. For practical considerations, however, one independent experiment for each individual input is highly recommended (Tischler & Remple, 2006, p. 237). Nevertheless, a slightly extended version of the spectral method is implemented in Cifer, a system identification software package that has been applied in numerous aircraft and helicopter projects (Tischler & Remple, 2006).

One common workaround to identify frequency response matrices for multiple input systems from a *single* experiment is the use of so-called zippered multisines, where each input is assigned an individual set of discrete frequencies. The zippered multisine approach results in a set of single input estimations, where each input is estimated at different frequencies (Morelli, 2003).

This approach has been applied to estimate e.g. stability margins and is also well suited for the estimation of parametric models (Klein & Morelli, 2006). However the zippered multisine approach does not provide a full frequency response matrix estimate, as it is required e.g. for the μ-analysis.

Open Loop Response Estimation From Closed Loop Experiments

Frequency response functions model only the input/output dynamics of the analysed system. Eventual inner dynamics are not explicitly modelled. Thus, when applied to data from open loop experiments, the open loop plant dynamics are estimated – when applied to closed loop data, the closed loop plant dynamics are estimated.

In many applications, however, the open loop dynamics are sought, but only closed loop experiments can be conducted, as e.g. in the case of unstable systems that must be operated in closed loop. It is shown in (Pintelon & Schoukens, 2001) that this setup can result in biased estimates; unbiased estimates are provided by indirect estimates (Girija & Raol, 1996; Pintelon & Schoukens, 2012, pp. 61–62; van den Hof & Schrama, 1993).

1.1.1.2 Aircraft System Identification

Offline Methods

Early publications of applications of system identification techniques to aircraft dynamics problems date back to the late 1940s, when methods for automatic control design required plant models (Milliken, 1947); these early methods were limited to linear systems (Greenberg, 1951). Thirty years later, the maximum likelihood framework provided a more rigorous framework for the identification of aircraft dynamics (Maine & Iliff, 1981, 1985), that was also applied to identify nonlinear models (Jategaonkar & Plaetschke, 1985).

The maximum likelihood framework is today widely used for the identification of, mostly parametric, aircraft flight dynamics models (Jategaonkar, 2006; Klein & Morelli, 2006). Rotorcraft are often (Mettler, 2003; Tischler & Remple, 2006), but not exclusively (Bottasso, Luraghi, & Maisano, 2009) identified in the frequency domain; comparisons of time and frequency domain approaches for rotorcraft are found in (Hamel & Kaletka, 1997) and (North Atlantic Treaty Organization, 1991). Due to their wide applicability, usually parametric models are identified; non-parametric models are mostly used as intermediate result in frequency domain approaches (Tischler & Remple, 2006).

Online Methods

In flight testing, it has many advantages to analyse data online, i.e. while the flight tests are conducted (Clarke et al., 1994). Online estimation is mostly performed in the frequency domain (Morelli, 1998, 2000), as the transformation is computationally cheap and reduces the computational effort of the estimation significantly.

Online or real-time estimation (Grauer & Morelli, 2013; Holzel & Morelli, 2012) offers further advantages, as it can be used to identify the degraded dynamics of damaged aircraft , e.g. for adjusting flight control laws.

Recent approaches in online estimation of FRFs include the real-time estimation of frequency response functions from recursive Fourier transforms (Grauer & Morelli, 2013; Holzel & Morelli, 2012). For multiple input systems, however, all online approaches rely on zippered multisines and do not provide frequency response matrix estimates with full frequency resolution from a single experiment.

1.1.2 Stability Measures & Robust Stability

With the development of automatic control systems, also the need for stability tests arose. Stability criteria based on transfer functions, like the Nyquist Stability Criterion (Nyquist, 1932), became popular. The related stability margins are a well-established stability criterion (Department of Defense, 1997) and have become a certification requirement for

flight control systems (SAE International, 2007), albeit stability margins can be unreliable for MIMO systems (Levine, 1999). The monitoring of stability margins has proven useful in several research programs (Balough, 1998; Clarke et al., 1994; Wise, 2003) to safely extend the flight envelope of newly developed flight control systems.

As alternative stability measures for MIMO-systems, criteria based on the robust control framework have been developed. The robust stability framework was developed to account for model uncertainties, cmp. (Skogestad & Postlethwaite, 2005). It turned out that some relevant model uncertainties can be easily formulated in the frequency domain, leading to frequency domain robust stability criteria, based on e.g. suitable matrix norms or structured singular values (Packard & Doyle, 1993). These criteria require the knowledge of the entire MIMO-dynamics, i.e. the full frequency response matrix for the entire frequency range of interest.

To simplify the analysis of MIMO stability during flight tests, it is desired to apply robust control algorithms directly on measured data, with as little user interaction as possible. Hence it is attractive to combine the robust stability criteria with system identification methods.

1.1.3 Combination of System Identification With Robust Control

1.1.3.1 Identification For Control and Least Costly Identification

The common roots of system identification and automatic control have been mention before. It is thus not surprising, that efforts have been undertaken to link system identification with robust control (Smith & Doyle, 1992; Vries & Hof, 1992).

From a practical point of view, this combination is appealing: In the design of automatic control systems, one major effort is the design (i.e. identification) of the plant model. On the other hand, the robust control framework can handle uncertain systems. Thus, the question arises, how accurate the plant model must be in order for the controller to stabilize it. The resulting trade-off – is it more advantageous to make to plant more accurate or the controller more robust – leads to the concept of *identification for control (Gevers, 1996)*: The combination of prediction error methods with robust control theory has been analysed for single input- (Bombois, Gevers, Scorletti, & Anderson, 2001) and multiple input systems (Bombois & Date, 2003). It is noted that all these efforts are based on parametric models. An approach to compute controller gains directly from non-parametric models is shown in (Holzel, Lacy, & Babuska, 2009).

With the advancing maturity of system identification methods, the focus in the practical application shifts more and more to the cost of identification (Gevers, 2014), where cost is multifaceted and also includes user friendly identification methods. In this context, non-parametric frequency domain methods based on local polynomial approximations have been developed (Gevers, Pintelon, & Schoukens, 2011; Pintelon, Schoukens, Vandersteen, & Barbé, 2010a, 2010b), that are easy to use and provide very accurate estimation results (Gevers, 2014). These algorithms are applied in this thesis in combination with robust control methods.

1.1.3.2 Aircraft Applications

Publications that explicitly combine system identification methods and robust/automatic control for aircraft applications are rather scarce. Although automatic control is a main reason for system identification, both topics rarely combined in publications. This may be owed to their complexity, but it also entails the risk that their close links may be overlooked.

A notable exception that utilizes the combination of system identification and (robust) control is (Scheid, Bayard, Chaing, & Mettler, 1995), where a structured uncertainty model is derived from estimated frequency responses. Scheid et al. estimate frequency responses and derive rational functions that are upper bounds of the frequency response estimates and their uncertainty regions of a specified confidence level. The robust control design framework is then applied to the resulting structured uncertainty model. The determination of the rational function results in a constrained optimization problem that accounts for the uncertainty structure. The uncertainty structure itself is computed in an elaborate way, that includes partitioning of the estimated frequency response matrix.

Noteworthy is the combination of hard uncertainty bounds, as used in robust control, and the soft bounds, as they are obtained from statistical estimation methods, by limiting the confidence level of the soft bounds (Scheid et al., 1995). This makes the approach very interesting for the application considered in this thesis; Scheid et al., however, focus on robust control design, not on stability analysis. Estimation uncertainty is considered in the approach, but is not studied in detail; for multiple input systems, multiple experiments are required. Furthermore, the approach requires the solution of an optimization problem that may not be suited for online applications.

Similarly to (Scheid et al., 1995), also (Feng, Lin, Yu, & Whorton, 1998) combine system identification methods with (robust) control design approaches. As before the focus is on control design; more specifically Feng et al. identify the closed loop dynamics and utilize the identification results to auto tune the controller gains.

In the context of aeroelastics, the combination of (online) system identification with robust control has been utilized by (Lind & Brenner, 1999) in the so called *flutterometer*; the approach is based on a nominal parametric model, estimates of full frequency response matrices and structured singular values that are related to flutter speed. The approach is extended in (Borglund & Nilsson, 2004) to control law design for flutter suppression.

1.1.4 Summary

From the preceding subsections it is seen that system identification is a wide field with many different applications. Its original roots to automatic control are still visible for example in combined approaches like identification for control, that is a current research topic. In the context of aircraft dynamics, today parametric time domain methods prevail for offline applications, while online approaches rely on frequency domain methods. Non-parametric methods are considered especially in the context of rotorcraft, where frequency response functions are an intermediate result for the parameter estimation. Due to their flexibility, that basically results from the absence of a fixed model order, frequency responses are in principle well suited for the intended monitoring task.

One relevant limitation of frequency responses is, however, their difficult estimation for multiple input systems: The estimation with full frequency resolution is either based on parametric models, or requires multiple experiments; no established method provides frequency response matrices with full frequency resolution from a single experiment. This reflects in the combined applications of system identification with robust control, where multiple input systems are handled either with parametric models (Lind & Brenner, 1999) or rely on multiple experiments (Scheid et al., 1995). As a consequence, non-parametric models are scarcely used in combined system identification / robust control approaches, albeit frequency responses and their estimation uncertainty are generally well suited for robust stability analysis, as they provide simple means for uncertainty modelling.

1.2 Objective and Contributions

Objective

As introduced before, a monitoring algorithm combines a modelling or system identification part with an analysis criterion. To provide accurate model estimates, even in case of dynamics changes, damages or system degradation, the dynamics model need to be based directly on measurements of the actual system behaviour, and should be based on as little a priori assumptions about the system as possible. This limits the usability of parametric models, as these always require some sort of model order decision, that may or may not be appropriate; the latter case can result in erroneous estimations. This makes non-parametric approaches, based e.g. on frequency response functions, very attractive for the monitoring task. Due to their lack of model order decision frequency responses naturally adapt to different configurations. For systems with multiple inputs, like aircraft, however, there is a lack of suitable estimation methods that provide frequency response matrices with full frequency resolution from a single experiment.

The decision for frequency response functions (instead of parametric models), has further consequences, that must be considered with respect to the stability criterion. Frequency response functions are naturally limited to a set of discrete frequencies and thus a limited frequency range. In the context of stability analysis, the system behaviour between these discrete frequencies must be considered explicitly.

Further important aspects of the identification part are:

- The model must account for the probabilistic nature of the measured signals. The signals are reliably provided by the common aircraft sensors.
- The intended online monitoring requires that the algorithm runs continuously; thus all required signals must be measured concurrently.
- The provided model should be easy to interpret.
- And it must provide measures to assess its quality and the accuracy of the estimation.

The stability criteria must work hand in hand with the estimation algorithm and need to be applied online. A simple handling and little user choices are obviously advantageous, as it allows for a fast adaption of the monitoring algorithm to different aircraft, with possibly very different configurations.

Contributions

This thesis aims at the application of non-parametric methods for online integrity monitoring. As shown above, the lack of an estimation method that provides frequency response matrix estimates with full frequency resolution from a single experiment is a significant limitation, that prevents the combination of non-parametric models with robust stability criteria. The main focus of this thesis is consequently the application of a novel estimation algorithm, that overcomes this limitation. The main contributions include:

- **Full frequency resolution frequency response from single experiment**: The recently developed *fast local polynomial method* (LPM) (Pintelon et al., 2010a, 2010b) overcomes the limitations of previous methods with respect to multiple input system. The LPM utilizes local polynomial fits over adjacent frequencies to estimate frequency response matrices for multiple input systems with full frequency resolution from a single experiment. It is applied for the first time to a flight dynamics application. The fast LPM can be applied to the first two periods of

data, that need to be discarded with current estimation methods. In addition, two periods of data are sufficient for the LPM algorithm, compared to at least five periods recommended for Welch's method.

- **In-depth analysis of estimation errors**: The LPM estimates are analysed for their systematic and stochastic estimation errors. The focus is specifically on the application in a monitoring system and includes the revision of bias estimates provided in the literature. The derived bias and covariance estimates are combined in simultaneous confidence regions that account for the total estimation uncertainty. Their reliability is tested with extensive Monte Carlo simulations.
- **Link of identification result to robust stability framework:** A structured uncertainty model is derived that links the multivariate confidence regions provided by the estimation to the robust stability framework. The stability criterion is further adjusted to account for the dynamics between analysed, discrete frequency grid (intergrid dynamics).
- **Derivation of integrity measure**: The proposed confident stability level is tested for its suitability and as integrity measure in flight dynamics applications and its responsiveness to dynamics changes. By combining the confidence levels for multiple frequencies, an integrity measure for the stability of the flight control system is provided for a user defined frequency range. The entire algorithm is implemented in an online framework, providing a continuous integrity measure of the stability of the multiple input system dynamics from a single experiment.

The estimation accuracy of the local polynomial methods is compared to current standard methods using Monte Carlo simulations.

1.3 Outline of the Thesis

This thesis consists of three major parts: The first part, consisting of chapter 2, focusses on theory and mathematical foundations. After the introduction of signal processing foundations and the empirical transfer function estimate (ETFE) as reference method for the estimation of SISO frequency response functions (section 2.2), the extended transfer function model (ETFM) is derived, starting from an ordinary difference equation, section 2.3. While the common transfer functions assume zero initial conditions, the extended transfer function model exactly accounts for non-zero initial and final conditions with an additional ("transient") term, that describes the effect of finite observation lengths of discrete Fourier transforms accurately. This additional transient term can be estimated in different ways: one approach, based on periodic excitation signals and local polynomial fits is introduced in section 2.4 and can be combined with the ETFE in a straight forward way, that results in the transient local polynomial method (section 2.5.1). The rest of section 2.5 is dedicated to a more elaborate estimation algorithm, the fast local polynomial method, that is based on local polynomial approximations of the frequency response to estimate frequency response matrices and the respective sample covariance matrices with full frequency resolution, thus a total of three different estimation algorithms are introduced. For all of them, the effect of noise on frequency response estimates is studied in section 2.6, where confidence regions for the estimates are derived. In section 2.7., uncertainty models and robust stability measures are introduced. The confidence regions derived previously are related to the uncertainty models in section 2.8, resulting in confident robust stability measures.

In the second part, consisting of chapters 3 and 4, the local polynomial methods are applied to estimate frequency responses of an aircraft. In chapter 3, the introduced estimation algorithms are compared with respect to their estimation accuracy. The effect of the non-zero initial and final conditions is demonstrated with Monte Carlo simulations of a single input / single output flight dynamics example. Section 3.2 describes the simulation model and the baseline configuration of the flight experiment, followed by the analysis criteria (section 3.3). In section 3.4 the estimation accuracy of the three estimators is compared. Finally, guidelines for the LPM user choices are summarized, see section 3.5.

In chapter 4, multiple input frequency response matrices are estimated with the fast local polynomial method. As for the SISO case in chapter 3, the numerical analysis is based on Monte Carlo simulations. The simulation setup is described in section 4.1, the estimation bias (section 4.2) and the estimation variance (section 4.3) are analysed in the subsequent sections.

The third and final part in chapter 5 covers the combination of system identification methods with robust stability and its application to integrity monitoring. The description of the simulation model and its setup (section 5.1) is followed by a detailed analysis of the signal-to-noise ratio of the input signal (section 5.2), a numerical validation of the confidence regions (section 5.3). The robust stability of the system, based solely on the frequency response estimate is analysed in three steps in the sections 5.4 to 5.6. The responsiveness of the integrity level to dynamics changes is finally discussed in section 5.7.

The thesis closes with the summary of the main results in chapter 6, with notes on pitfalls and shortcomings that provide opportunity for further improvement of the proposed integrity monitoring algorithm.

2 Theory on Local Polynomial Method and Robust Stability

2.1 Introduction to Frequency Response Function Estimation

Continuous-time, linear time-invariant (LTI) systems are described by ordinary differential equations (ODE)

$$\begin{aligned} a_p \frac{d^p y(t)}{dt^p} + a_{p-1} \frac{d^{p-1} y(t)}{dt^{p-1}} + \cdots + a_1 \frac{dy(t)}{dt} + a_0 y(t) = \\ = \mathscr{b}_q \frac{d^q u(t)}{dt^q} + \mathscr{b}_{q-1} \frac{d^{q-1} u(t)}{dt^{q-1}} + \cdots + \mathscr{b}_1 \frac{du(t)}{dt} + \mathscr{b}_0 u(t) \end{aligned} \tag{2.1}$$

where $t \in \mathbb{R}$ denotes time, $y(t)$ the system output, $u(t)$ the system input and $\frac{d^n}{dt^n}$ the n-th derivation with respect to time. The coefficients of the ODE are denoted with $a_p, \dots, a_0$ and $b_q, \dots, b_0$. For physical systems $q \leq p$ holds. In the frequency domain, equation (2.1) is conveniently described by a transfer function. Transfer functions of continuous time systems are defined in terms of the Laplace-transform of their input and output signals

$$G_{yu}(s) = \frac{Y(s)}{U(s)} \tag{2.2}$$

where $G_{yu}(s)$ can be written as

$$G_{yu}(s) = \frac{\mathscr{b}_q s^q + \mathscr{b}_{q-1} s^{q-1} + \cdots + \mathscr{b}_1 s + \mathscr{b}_0}{a_p s^p + a_{p-1} s^{p-1} + \cdots + a_1 s + a_0} \tag{2.3}$$

with s being the Laplace operator. Similarly, discrete time systems are described by difference equations with general form

$$\sum_{p=0}^{n_a} a_p y[n-p] = \sum_{q=0}^{n_b} b_q u[\mathrm{n}-q]. \tag{2.4}$$

Analogously to the discrete case[5], the transfer function is defined in terms of the z-transform (Ragazzini & Zadeh, 1952) as

$$\begin{aligned} G_{yu}(z) &= \frac{Y(z)}{U(z)} \\ &= \frac{b_q z^{-q} + b_{q-1} z^{-(q-1)} + \cdots + b_1 z^{-1} + b_0}{a_p z^{-p} + a_{p-1} z^{-(p-1)} + \cdots + a_1 z^{-1} + a_0} \\ &= \frac{\sum_{q=0}^{n_b} b_q z^{-q}}{\sum_{p=0}^{n_a} a_p z^{-p}} \\ &= \frac{B(z^{-1})}{A(z^{-1})} \end{aligned} \tag{2.5}$$

see (Oppenheim, Willsky, & Young, 1997, pp. 774–783); the numerator and denominator polynomials are conveniently written as $B(z^{-1}) = \sum_{q=0}^{n_b} b_q z^{-q}$ and $A(z^{-1}) = \sum_{p=0}^{n_a} a_p z^{-p}$. The z-transform is used in unilateral and bilateral form. The bilateral form is defined as

[5] Both transfer functions, continuous and discrete, are related to each other by the bilinear transform Sinha (1972). The Bilinear transformation closely approximates the continuous transfer function with a discrete one, but their coefficients $a, \mathscr{b}$ and a, b are generally different.

$$X(z) = \sum_{n=-\infty}^{\infty} x[n]z^{-n} \tag{2.6}$$

and requires the entire dataset from $n = -\infty$ to $n = \infty$. The unilateral transform is defined as

$$X(z) = \sum_{n=0}^{\infty} x[n]z^{-n}, \tag{2.7}$$

and assumes that the data is known from $n = 0$ till infinity, while data for $n < 0$ is ignored or can be assumed to be zero (Oppenheim et al., 1997, pp. 789–796).

2.1.1 Limitations in System Identification

In system identification neither can be provided: Experiments are started at some epoch (e.g. at $n = 0$) and the measurements are stopped after some finite time interval. So $x[n]$ is neither known till infinity, nor is it known before $n = 0$, where $x[0]$ is in general different from zero (cmp. Figure 2-1). The effect of initial and final values on frequency response function estimates is discussed in more detail in section 2.3.

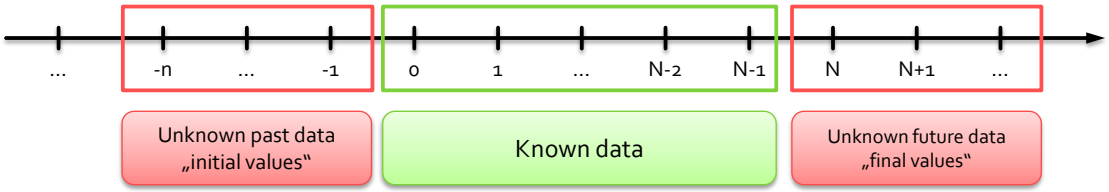

Figure 2-1: Schematic of known and unknown data.

For practical reasons, the z-transform is usually computed only for z on the complex unit circle, i.e. for $z = e^{j\omega}$ with angular frequency $\omega \in \mathbb{R}$ and for finite number of data samples, resulting in the *discrete Fourier transform* (DFT). Different scaling factors (all function of the sample number N) are common in the literature; in this thesis, the DFT is scaled with $\frac{1}{\sqrt{N}}$:

$$X_{DFT}(e^{j\omega}) = \frac{1}{\sqrt{N}} \sum_{n=0}^{N} x[n]e^{-j\omega n} \tag{2.8}$$

As the DFT is a special case of the z-transform, the DFT inherits its properties and computational rules. The DFT is usually computed for discrete frequencies ω_k only and is then denoted as $X(k)$; see sections 2.2.4 and 2.2.5 for further details. When the z-transform in the transfer function (2.5) is replaced by the DFT, the result is the so called empirical transfer function estimate (ETFE)[6]

$$\hat{G}_{yu}(j\omega) = \frac{Y_{DFT}(j\omega)}{U_{DFT}(j\omega)} \tag{2.9}$$

where the hat in $\hat{G}$ distinguishes the estimate from its true value, denoted with a subscript G_0 or $G_{0,yu}$. The ETFE $\hat{G}_{yu}(j\omega)$ from measured DFT spectra of the input and output signals U_{DFT}, Y_{DFT} is generally different from the true transfer function $G_{0,yu}$.

$$G_{0,yu}(j\omega) \neq \frac{Y_{DFT}(j\omega)}{U_{DFT}(j\omega)} \tag{2.10}$$

[6] The term *empirical* is used, as no assumptions on the system are made besides linearity Ljung (2009, p. 189)

This is due to several effects; the most important ones are:

- **Sampling**: The continuous signals are approximated by discrete samples. Inappropriate sampling can cause *aliasing*. It can be avoided by sufficiently high sampling rates with suitable anti-alias filters.
- **Windowing**: The DFT is computed from a finite number of samples. The restriction to a finite number of samples is called windowing and can result in spectral *leakage*. Leakage can be avoided when periodic signals are analysed and full periods are observed.
- **Frequency resolution:** The DFT can be computed only for a finite number of discrete frequencies. An unfavourable choice can result in leakage. Furthermore, the frequency resolution must be sufficiently fine to capture all relevant details of the true transfer function $G_{0,yu}$.
- **Noise:** Any measurement of a physical quantity will be disturbed by noise. In the context of aircraft dynamics, primary noise sources are turbulence, sensor noise and vibrations e.g. from engines. The effect of noise is non-systematic in nature and thus cannot be fully eliminated, but only reduced. In FRF estimates, noise introduces uncertainties; based on assumptions of the statistical noise properties, the uncertainties in the estimates can be determined.
- **Unknown initial and final conditions:** The effect of unknown initial and final conditions is similar to windowing as it is also a consequence of the finite observation length. While leakage is related to the transformation of *signals*, the effect of unknown initial and final conditions is specific to *systems*. It can be avoided, when the steady-states response to a periodic excitation signal is measured.
- **Multiple input systems:** The non-parametric estimation of frequency response functions for systems with multiple inputs requires in general one independent experiment for each input.

In the following section, these effects are analysed for their impact on the ETFE. As shown in sections 2.2.2 to 2.2.5, aliasing and windowing are related to digital signal processing and are well understood effects, see e.g. (Oppenheim et al., 1997) or (Kiencke & Jäkel, 2008). Likewise, leakage can be fully avoided with a proper choice of frequency resolution; this goes hand in hand with correct windowing. Thus all three effects can be avoided by proper signal processing

The noise contributions in the input and output measurements results in uncertainties in the FRF. The uncertainty can be described by the probability density function (pdf) of the estimate $\hat{G}_{yu}$. The pdf of the ETFE can be computed analytically, based on few assumptions on the noise characteristics. In practice, often confidence regions $\hat{r}_p$ around $\hat{G}_{yu}$ are computed that contain the true value $G_{0,yu}$ with certain probability p. As shown in section 2.2.6., the effect of noise on the ETFE can be reduced for periodic excitations by averaging over multiple periods.

The effect of initial and final conditions is specific to system identification from input- and output data (Pintelon, Schoukens, & Vandersteen, 1997). The ETFE is (only) accurate when the steady-state response is measured. In practice this requires to excite the system with a periodic signal and wait until the transient response due to the initial values has died out; otherwise the transient signal parts introduce systematic errors in the FRF estimate. As a general guideline, this is assumed after two full periods; thus it is a standard procedure to discard the data from the first two periods and use only later data for the estimation (Bailey & Markofski, 2001; Tischler & Remple, 2006, pp. 83–118). Due to the periodic excitation,

the final conditions are then very close to the initial conditions and have only negligible effect on the ETFE (Pintelon & Schoukens, 1997). For systems with large settling times this can take considerably long; in the context of aircraft system identification, e.g. the settling time of the Dutch roll mode can be in the order of minutes. Waiting for several minutes before the actual measurements even *start* is not only a waste of valuable time, but also bears practical issues as the aircraft must remain close to its trim state all the time.

The ETFE can be easily applied to systems with multiple *outputs* by simple stacking the individual single input-single output FRF estimates. However, it is more difficult to estimate frequency response matrices (FRM) for systems with multiple inputs. This is due to the underlying problem that the system response must be related to the correct input. With the classical non-parametric approaches, this issue makes it necessary to perform multiple, independent experiments (one independent experiment for each input) (Pintelon & Schoukens, 2012, p. 64); parametric approaches (Ljung, 2009) depend on the choice of a model structure and model order and bring further questions about optimal excitation (Gevers, Mišković, Bonvin, & Karimi, 2006; Hägg, Wahlberg, & Sandberg, 2011; Wahlberg, Hjalmarsson, & Martensson, 2008; Wahlberg, Hjalmarsson, & Mårtensson, 2008).

2.1.2 Outline of Theoretical Part

2.1.2.1 Novel Estimation Algorithms for Frequency Responses

In the first part of this chapter (sections 2.3 to 2.6) two novel estimation algorithms for frequency response functions are introduced. They are based on the *explicit estimation of the initial and final conditions* on spectral estimates and offer an alternative that avoids the discarding of data. Instead, the first two periods can be included in the estimation without introducing errors in $\hat{G}_{yu}$. The estimation of initial and final conditions is based on the extended transfer function model (ETFM) (Pintelon et al., 1997; Pintelon & Schoukens, 1997). The ETFM is derived in section 2.3 and is, by contrast to equation (2.10), an exact relation of the input/output DFT spectra U_{DFT}, Y_{DFT} and the true transfer function $G_{0,yu}$. The estimation of the initial and final conditions is based on at least two periods of periodic data and is introduced in section 2.4.

The estimation of initial and final conditions can be easily combined with the ETFE. The combination is called *transient local polynomial method* (tLPM) (Monteyne, Ugryumova, & Vandersteen, 2012) and is summarized in section 2.5.1. The tLPM gives not only unbiased estimates when the first two periods are included, but the first two periods are *sufficient* for the estimation. Hence the transient LPM can estimate frequency response functions solely from the data that previously had to be discarded; this clearly shows the potential of the transient LPM to reduce the duration of experiments. The ETFE, and thus the transient LPM, can be easily applied to systems with multiple *outputs* by simple stacking of the individual single input-single output FRF estimates, but it is more difficult to estimate frequency response matrices (FRM) for systems with multiple inputs.

It is seen that the estimation of frequency response matrices with multiple inputs require, multiple experiments (one independent experiment for each input) (Pintelon & Schoukens, 2012, p. 64). With an approach similar to the estimation of the initial and final conditions, the FRM with multiple inputs can be directly estimated from a *single* experiment. The method is based on local polynomial approximations of the frequency responses over neighbouring frequencies and is thus named local polynomial method (LPM) (Pintelon et al., 2010a, 2010b); the specific variant used in this thesis is the *fast local polynomial method*

(fast LPM). The LPM is the first method that provides frequency response matrices with full frequency resolution from a single experiment. The LPM is derived in detail in section 2.5, the statistical distribution of its estimates is analysed in section 2.6.

Both, the transient LPM and the fast LPM, are pretty easy to use. They require few user choices and are robust to them. As shown in chapter 3 on the basis of Monte Carlo simulations, quite good estimates can be provided with standard settings. This makes the estimators very well suited for online applications.

As a summary, the main advantageous of the LPM methods are:

- The initial and final conditions are explicitly estimated.
- The first two periods of data can be included in the estimation without introducing systematic errors.
- The fast local polynomial method is the first algorithm that can estimate frequency response matrices with full frequency resolution from a single experiment.
- The local polynomial methods are pretty easy to use.

2.1.2.2 Stability Analysis Based on Estimates

In the second part of this chapter (sections 2.7 and 2.8) the estimated system is analysed for (robust) stability. Based on the stability criteria, the confidence level of the largest uncertainty that is robust stable is computed. This confidence level is applied in chapter 4 to monitor the integrity of a multiple input/multiple output flight control system, i.e. it measures the probability that the system behaves as intended (here: to be stable). The algorithm is applied to the FAT aircraft simulation model described in appendix A.

The monitoring algorithm is based on two well-known stability criteria, namely the H_∞-*criterion* (Skogestad & Postlethwaite, 2005, pp. 306–308) and *structured singular values* (Skogestad & Postlethwaite, 2005, pp. 311–321) that are both introduced in section 2.7. The stability criteria test all possible realizations of the frequency response contained in the uncertainty region for stability. They further provide a scaling factor κ that describes how much larger the uncertainty could be, before the stability criteria fail - obviously, robust stability is given if the scaling factor is larger than one. With this scaling factor, the maximum uncertainty that satisfies the stability criterion (just no more) can be computed for every analysed frequency.

In section 2.8 the criteria are adjusted to the specifics of the LPM estimate. In particular, the confidence regions are transformed in an uncertainty model that can be used with robust stability criteria.

In section 2.8.4 it is further shown that the scaling factor κ can be related to the confidence level p of the confidence regions. This relation allows to compute the (maximum) confidence level that results in robust stability for every analysed frequency; it is thus named *confident stability level*. Under the assumption of independence, the frequency-by-frequency information can be summarized in a single confident level for the entire frequency range.

This measure provides the total probability that the system is stable with respect to the measurement uncertainty, directly and solely based on measured data. This direct monitoring approach has several advantages:

- The FRM with its uncertainty model is the most fundamental description of the system estimate available from the measurements. Applying the stability criteria directly on the FRM, without the estimation of a parametric model, avoids additional

assumptions on the systems structure that can lead to (overly) conservative assumptions about parameter uncertainty.
- It is difficult to assess if the model structure assumptions are valid or not. Leaving this step out, simplifies the integrity monitoring.
- The monitoring algorithm requires little knowledge of the underlying dynamics. For the signal design, only information about the approximate eigenfrequencies of the relevant modes (to set the frequency range of interest) and their rough damping (to set the required frequency resolution) are required. If this information is inaccurate, the algorithm still works fine, but the result may be not optimal.
- The monitoring algorithm is fully independent of the actual (control-) system implementation. This adds additional diversity as it avoids the issue of common errors that affect other monitoring methods like voting between redundant systems.
- The robust stability criteria fit well to the estimation algorithm introduced in the first part of the chapter and can be easily combined in an online framework that can provide a continuous integrity monitoring during flight testing.
- As the fast LPM provides estimates of the full frequency response matrix, the monitoring can easily be applied to multiple input systems.

2.2 Preliminaries

2.2.1 General System Structure

Throughout this thesis, systems are described by transfer functions, that are point wise described by frequency response functions / frequency response matrices. The underlying systems have the general shape shown in Figure 2-2a (open loop system), where $u(t)$ is the system input, $y(t)$ the system output and G_{yu} the system transfer function. In Figure 2-2b, the system is extended by input noise $v_u(t)$ and output noise $v_y(t)$, Figure 2-2c shows a closed loop system with controller K, reference signal $r(t)$ and control error $e(t)$. Throughout the thesis, the general structures from Figure 2-2 are adjusted as required.

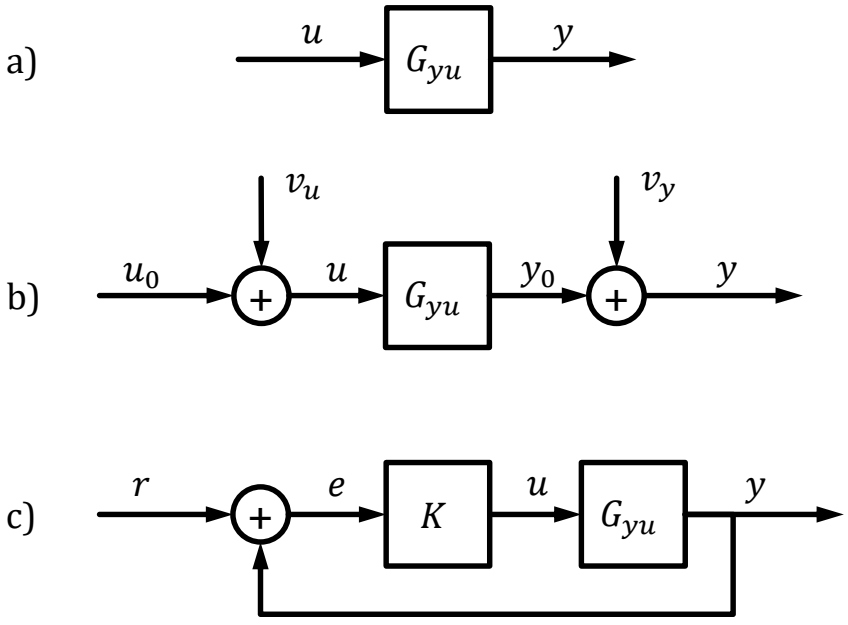

Figure 2-2: General block diagram of systems: open loop (a), open loop with noise (b), closed loop system (c). The signals dependence on time is dropped for clarity.

2.2.2 Sampling of Time Domain Data

Physical systems are continuous in time. For processing in computers, continuous signals are measured at discrete epochs. Only these discrete values are stored and processed, while the signal behaviour between consecutive measurements is unknown. In general, signals are measured at equidistant time steps with size $\frac{1}{f_s}$, where f_s is called *sampling frequency* and is usually given in units of Hz. The regular sampling has computational advantages, as it allows for very efficient computation of discrete Fourier transforms (DFTs) with the help of Fast Fourier Transforms (FFTs). Throughout this thesis it is assumed that signals are measured with constant sampling frequency. It is further assumed that all time domain signals are real valued.

Throughout this thesis ordinary frequency f and angular frequency ω are used side by side. While angular frequency is mostly used in chapter 2, ordinary frequency is more often used in sections 3 and 4. As both frequencies are related by

$$\omega = 2\pi f \tag{2.11}$$

the expressions can be easily converted.

2.2.2.1 Band Limited Signals

The discrete signal processing obviously discards parts of the continuous signal. For a correct processing, assumptions about the intersample behaviour must be made. One such assumption is that signals are *band limited*[7]. This means that the auto power spectra $S_{xx}(\omega)$ of the (random) signals are zero for frequencies above some maximum frequency ω_{max}, i.e.

$$S_{xx}(\omega) = 0 \; \forall \; |\omega| \geq \omega_{max} \tag{2.12}$$

where ω_{max} is called bandwidth[8] of the signal. Equation (2.12) may be analogously formulated in terms of ordinary frequency with bandwidth $f_{max} = \frac{\omega_{max}}{2\pi}$. The auto power spectrum $S_{xx}(\omega)$ is defined as

$$S_{xx}(\omega) = \lim_{T\to\infty} \frac{1}{T} \mathbb{E}\left\{ \left(X_T^{[i]}(j\omega) \right) \left(X_T^{[i]}(j\omega) \right)^H \right\}, \tag{2.13}$$

where $X_T^{[i]}(j\omega) = \int_0^T x^{[i]}(t) e^{-j\omega t} dt$ are finite time fourier transforms of i independent realizations of a continuous time, stationary ergodic random process $x(t)$ and the expectation $\mathbb{E}\{\cdot\}$ is computed over the realizations i (Bendat & Piersol, 1971/2010).

As shown by (Shannon, 1949), band limited signals can be fully reconstructed from the discrete observations if f_{max} (or ω_{max}) is smaller than half the sampling frequency; due to its importance in signal processing, half the sampling frequency is often called *Nyquist frequency*, in honour of Harry Nyquist (1889 – 1976).

$$f_{max} \leq \frac{f_s}{2} \tag{2.14}$$

[7] An alternative intersample assumption is the *zero-order hold*-assumption, i.e. signals are assumed to be piecewise constant. As shown in Pintelon and Schoukens (2012, pp. 498–512), the zero-order hold assumption has practical disadvantages compared to the band limited assumption.

[8] It is noted that this definition is different from the use in control design.

2.2.2.2 EFFECT OF SAMPLING ON FOURIER SPECTRA

The sampling of a continuous time domain signal can be modelled as a multiplication with an impulse train, sometimes called Dirac comb; an impulse train is a periodically repeated Dirac impulse with period $\Delta t = \frac{1}{f_s}$ (Brigham, 1974, pp. 83–87). The Dirac impulse is denoted by $\delta(t)$ and is defined by $\delta(0) = \infty$, $\delta(t) = 0$ for $t \neq 0$ and $\int_{\infty}^{\infty} \delta(x)dx = 1$. The multiplication with a Dirac comb is thus given by

$$x(t_n) = x(t) \cdot \sum_{n=-\infty}^{\infty} \delta(t - n\Delta t) = x(t) \cdot \mathfrak{d}_{\Delta t}(t), \tag{2.15}$$

where $\mathfrak{d}_{\Delta t}(t) = \sum_{n=-\infty}^{\infty} \delta(t - n\Delta t)$ denotes the Dirac comb with sampling time Δt and $x(t)$ is the continuous time signal. $x(t_n)$ denotes the (still continuous) sampled signal that is nonzero only for $t_n = n\Delta t$ with $n \in \mathbb{Z}$. It is common to restrict $x(t_n)$ to its nonzero values and to normalize Δt, resulting in a discrete time signal $x[n]$, with

$$x[n] = x(n\Delta t), \qquad n \in \mathbb{Z} \tag{2.16}$$

As for the Laplace transform, the Fourier transform of the product of two signals equals the convolution of their respective Fourier transforms.

$$\mathcal{F}\{x(t) \cdot \mathfrak{d}_{\Delta t}(t)\} = \mathcal{F}\{x(t)\} * \mathcal{F}\{\mathfrak{d}_{\Delta t}(t)\} \tag{2.17}$$

As shown in (Papoulis, 1962, pp. 44–45), the Fourier series of an impulse train $\mathfrak{d}_{\Delta t}(t)$ with period Δt is also an impulse train but with impulse distance $\frac{1}{\Delta t}$, i.e. the impulse spacing in time and frequency domain are inverses.

$$\mathcal{F}\{\mathfrak{d}_{\Delta t}(t)\} = \mathfrak{d}_{\frac{1}{\Delta t}}(j\omega) \tag{2.18}$$

This relation can be written analogously in terms of (ordinary) sampling frequency f_s or angular sampling frequency ω_s. Thus equation (2.17) becomes

$$\mathcal{F}\{x(t) \cdot \mathfrak{d}_{\Delta t}(t)\} = X(j\omega) * \mathfrak{d}_{\omega_s}(j\omega) \tag{2.19}$$

On the right hand side, the Fourier transform $X(j\omega)$ is convolved with a Dirac comb. An important property of the Dirac impulse (and an alternative way to define it, see (Papoulis, 1962, p. 270)) is the property

$$\int_{-\infty}^{\infty} f(\tau)\delta(\tau)\, d\tau = f(0) \tag{2.20}$$

where $f(\tau)$ is an arbitrary function, continuous at the origin, cmp. (Papoulis, 1962, p. 270). From this property follows, that a convolution with a Dirac impulse results in the original function

$$\begin{aligned} f(\tau) * \delta(\tau) &= \int_{-\infty}^{\infty} f(\mathcal{T})\delta(\tau - \mathcal{T})\, d\mathcal{T} \\ &= f(\tau) \end{aligned} \tag{2.21}$$

For a Dirac impulse $\tilde{\delta}(\tau) = \delta(\tau - T)$ that is shifted by T follows directly

$$\int_{-\infty}^{\infty} f(\tau)\tilde{\delta}(\tau)\, d\tau = f(T) \tag{2.22}$$

and the convolution with a shifted Dirac impulse results in a shift of the original signal

$$f(\tau) * \tilde{\delta}(\tau) = \int_{-\infty}^{\infty} f(\mathcal{T})\tilde{\delta}(\tau - \mathcal{T})\, d\mathcal{T} = f(\tau - T) \tag{2.23}$$

With these results, the convolution on the right hand side of equation (2.19) can be further analysed. As shown above, the convolution with a *single* shifted Dirac impulse shifts the original signal in time or frequency. The convolution with an impulse *train* (which is the sum of many shifted Dirac impulses) results in the sum of many shifted repetitions of the original signal. The effect of the convolution with a Dirac comb on the Fourier transform is visualized in Figure 2-3: The original spectrum $X(j\omega)$ is shown as solid line. The dirac comb is indicated by orange arrows. Each element of the comb shifts the original signal by ω_s, so that the entire signal $\tilde{X}(j\omega)$ (shown as dashed line) is a periodic repetition of the original spectrum. Thus, transforming the Fourier transform of the infinite long, sampled signal $x(t_k)$ to the frequency domain results in

$$\tilde{X}(j\omega) = \mathcal{F}\{x(t_n)\} = \sum_{m=-\infty}^{\infty} X(j\Omega_m)\Big|_{\Omega_m = \omega - m\omega_s} \tag{2.24}$$

where $X(j\Omega_m) = \mathcal{F}\{x(t)\}$ is the spectrum of the original, unsampled signal $x(t)$. The sum on the right hand side is a periodic repetition of $X(j\Omega_k)$ with period ω_s.

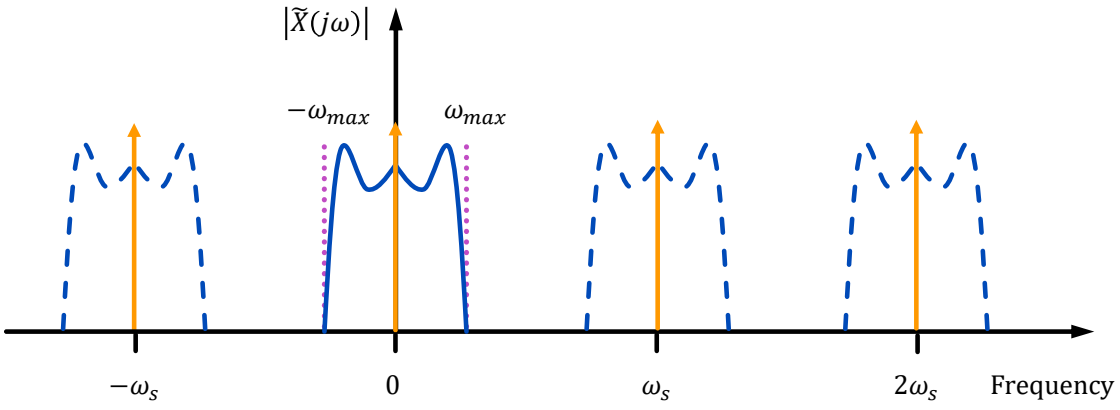

Figure 2-3: The Fourier spectrum $|\tilde{X}(j\omega)|$ of a sampled signal (dashed line) results from the convolution of the original spectrum $X(j\omega)$ (solid line) with the dirac comb (orange arrows): The convolution with the impulse comb result in a periodic repetition of the original spectrum.

Figure 2-3 shows the magnitude spectrum of a *band limited* sampled signal. For band limited signals with bandwidth smaller than the Nyquist frequency (i.e. $\omega_{max} < \frac{\omega_s}{2}$), the repetitions do not overlap, as the distance between neighbouring impulses is larger than the bandwidth of the original signal. Due to the band limitation, any spectral content outside the original signal bandwidth $[-\omega_{max}, \omega_{max}]$ is only due to the effect of sampling and hence should in general be discarded in the context of system identification.

If the signal bandwidth is larger than the Nyquist frequency (or if the signal is not band limited at all), the repeated spectra overlap, resulting in *Aliasing*, i.e. high frequency content is mapped to low frequency regions (Brigham, 1974, pp. 80–83). To avoid aliasing, the sampling frequency must be at least twice the signal bandwidth. Guidelines for aircraft system identification recommend a sampling frequency about 25 times larger than the maximum frequency of interest to avoid numerical inaccuracies. (Tischler & Remple, 2006, p. 90)

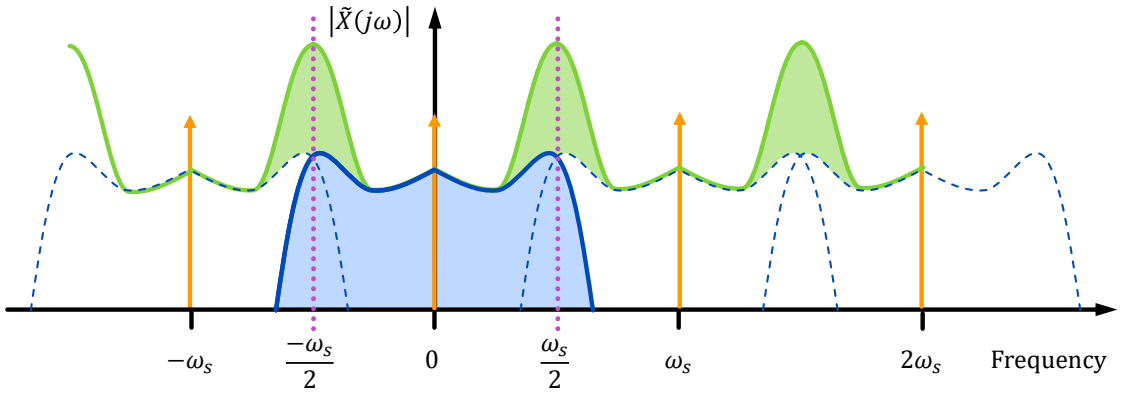

Figure 2-4: If the signal bandwidth is larger than $\frac{\omega_s}{2}$, the periodically repeated spectra $X(j\Omega_m)$ overlap (=Aliasing). The resulting spectrum (green) is very different from the original spectrum (blue).

2.2.2.3 Effect of Sampling on Frequency Response Estimates

To study the effect of sampling on ETFE's, in equation (2.24) the term for $m = 0$ is separated from the sum, and equation (2.9) is rewritten as

$$\hat{G}_{BL}(\mathrm{j}\omega) = \frac{\tilde{Y}(j\omega)}{\tilde{U}(j\omega)} = \frac{Y(j\omega) + \sum_{m=-\infty, m\neq 0}^{\infty} Y(j\Omega_n)\big|_{\Omega_m=\omega-m\omega_s}}{U(j\omega) + \sum_{m=-\infty, m\neq 0}^{\infty} U(j\Omega_n)\big|_{\Omega_m=\omega-m\omega_s}}, \tag{2.25}$$

where $Y(j\omega)$ and $U(j\omega)$ are the spectral contributions of the $m = 0$-term, while the two sums contain all other terms. If the signals $u(t)$ and $y(t)$ are measured with appropriate anti-alias filters with a cut-off-frequency well below $\frac{\omega_s}{2}$, the input and output signals can be safely assumed to be band limited and the only contributions in the frequency range from $\frac{-\omega_s}{2} < \omega < \frac{\omega_s}{2}$ stem from the $Y(j\omega)$ and $U(j\omega)$, while the two sums $\sum_{m=-\infty, m\neq 0}^{\infty} Y(j\Omega_n)\big|_{\Omega_m=\omega-m\omega_s}$ and $\sum_{m=-\infty, m\neq 0}^{\infty} U(j\Omega_n)\big|_{\Omega_m=\omega-m\omega_s}$ are mere artefacts from sampling.

This shows, that sampling has no effect on the ETFE within the frequency range given by $|\omega| < \left|\frac{\omega_s}{2}\right|$, if the input and output signals are properly band limited. The ETFE $\hat{G}_{BL}(j\omega)$ from band limited, sampled signals (indicated by the subscript $(\cdot)_{BL}$) coincide with the ETFE $\hat{G}(j\omega)$ from continuous signals within the bandwidth of the signals (Pintelon & Schoukens, 2012, pp. 498–512), i.e.

$$\hat{G}_{BL}(j\omega) = \hat{G}(j\omega), \text{ for } |\omega| < \left|\frac{\omega_s}{2}\right| \tag{2.26}$$

While this result may seem trivial, it is relevant when compared to e.g. the zero-order hold assumption, where (2.26) does not hold. (Pintelon & Schoukens, 2012, pp. 498–512)

2.2.3 Effect of Windowing

For computer based signal processing, the measurement records must be restricted to a finite length; otherwise infinite memory would be required to store the experiment data. The restriction to a finite observation length is mathematically described by a multiplication with a window function. Window functions are zero outside the observation interval and nonzero during the experiment. Without loss of generality it is assumed that the window function is zero for $t < 0$ and $t \geq T_{win}$ where T_{win} is the window length. For discrete signals, T_{win} is a multiple of the sampling time Δt, i.e. $T_{win} = N \cdot \Delta t$, where N is the number of time domain data samples contained in the window function.

The nonzero part of the window function can be shaped in many ways to weigh the measurements. A detailed analysis of several window functions is found in (Harris, 1978). Within this thesis only rectangular window functions $w(t)$ are used; they are defined in the time domain by

$$w(t) = \begin{cases} 1/T_{win}, & \text{if } 0 \leq t < T_{win} \\ 0, & \text{otherwise} \end{cases} \tag{2.27}$$

The Fourier transform of $w(t)$ results from the transform of a rectangular window function that is symmetric around zero (see Råde, Westergren, & Vachenauer, 2000, p. 315, F48) and a time shift by $T/2$ (see Råde et al., 2000, p. 313, F7) and is given by

$$W(j\omega) = e^{\frac{-j\omega T_{win}}{2}} \cdot \operatorname{sinc}\left(\frac{\omega T_{win}}{2}\right) \tag{2.28}$$

where $\operatorname{sinc}(x) = \frac{\sin(x)}{x}$ is the cardinal sine function, steadily continued at 0, i.e. $\operatorname{sinc}(0) = 1$, see also (Pintelon & Schoukens, 2012, p. 37)

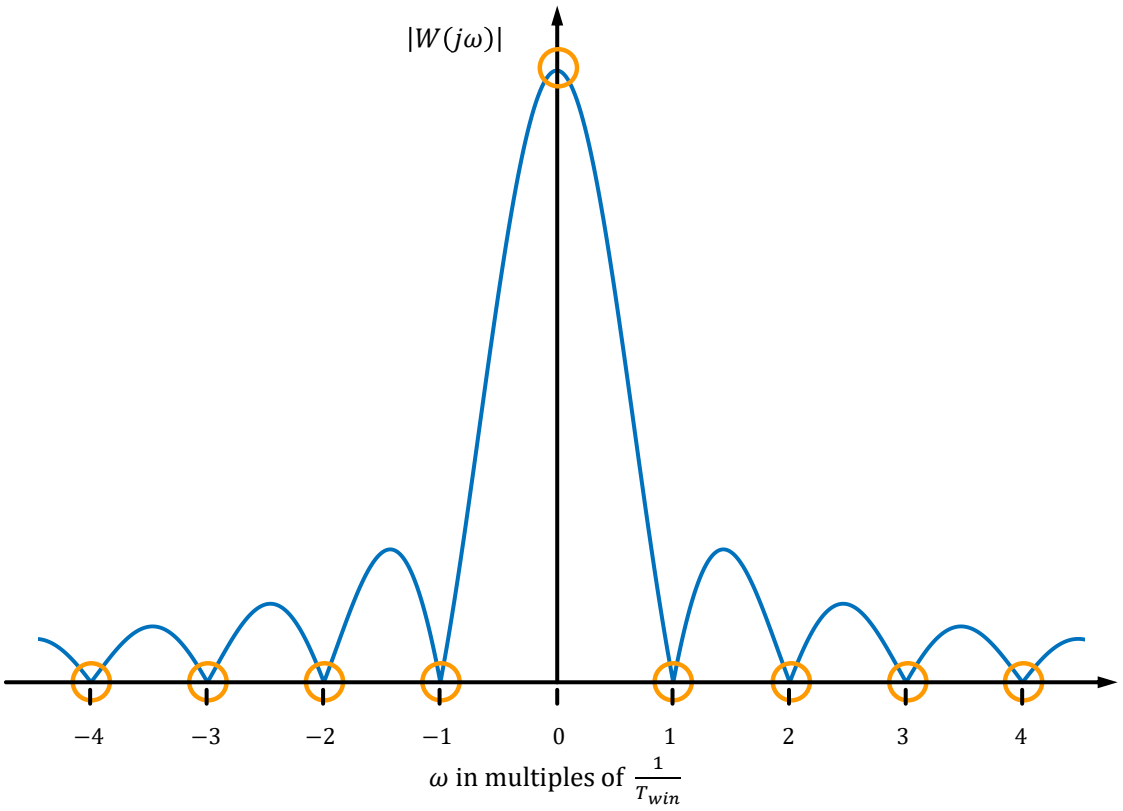

Figure 2-5: The Fourier transform $W(j\omega)$ of a rectangular window function is zero for $\omega_k = \frac{k}{T_{win}}$ (orange circles) with integer k, $k \neq 0$.

Analogously to the discussion of the effect of sampling on signal spectra in section 2.2.2.2, the multiplication of a signal $x(t)$ with a window function $w(t)$ corresponds to a convolution of the respective Fourier transforms $X(j\omega)$ with $W(j\omega)$ in the frequency domain.

$$\mathcal{F}\{x(t) \cdot w(t)\} = X(j\omega) * W(j\omega) \tag{2.29}$$

Due to the convolution, the original spectrum of $X(j\omega)$ can be disturbed or "smeared" such that signal energy is "moved" from its original frequency to other frequency regions; this effect is called spectral leakage (Brigham, 1974, pp. 99–108). Brigham further shows that no leakage occurs if full periods of a periodic signal are observed.

In frequency domain system identification spectral leakage can be a major error source (Pintelon & Schoukens, 2012, p. 60). To avoid it, it is strongly recommended to use periodic excitation signals and measure integer numbers of full periods (Pintelon & Schoukens, 2012, p. 58). For periodic signals, the spectrum $X(j\omega)$ is nonzero only for discrete frequencies, namely integer multiples of the period length. The effect of this line spectrum, consisting of spikes at the respective harmonics, on the convolution in equation (2.29) is similar to the effect of sampling (see section 2.2.2.2) and results in a repetition of the window function with a frequency shift of $\frac{1}{T_{win}}$. However the zeros of sinc $\left(\frac{\omega T_{win}}{2}\right)$ coincide with the harmonics of the periodic signal. Thus, the frequencies of interest $\omega_k = \frac{k}{T_{win}}$ are just at the zeros of sinc $\left(\frac{\omega T_{win}}{2}\right)$. As a result, the spectrumis not affected by leakage.

Figure 2-6 shows a simple example. The signal spectrum contains only two harmonics with $\omega = 0$ and $\omega = \frac{2}{T_{win}}$. Dashed lines show the convolution of each harmonic with the windofunction, centered at $\omega = \frac{0}{T_{win}}$ and $\frac{2}{T_{win}}$ respectively. The sum, i.e. the convolution $X(j\omega) * W(j\omega)$ is shown as solid line. It is seen that $X(j\omega) * W(j\omega)$ is zero for all multiples of $\frac{1}{T_{win}}$ except 0 and 2. Thus, the spectrum at ω_k is free of leakage. If the DFT is computed at any other frequency spectral leakage occurs.

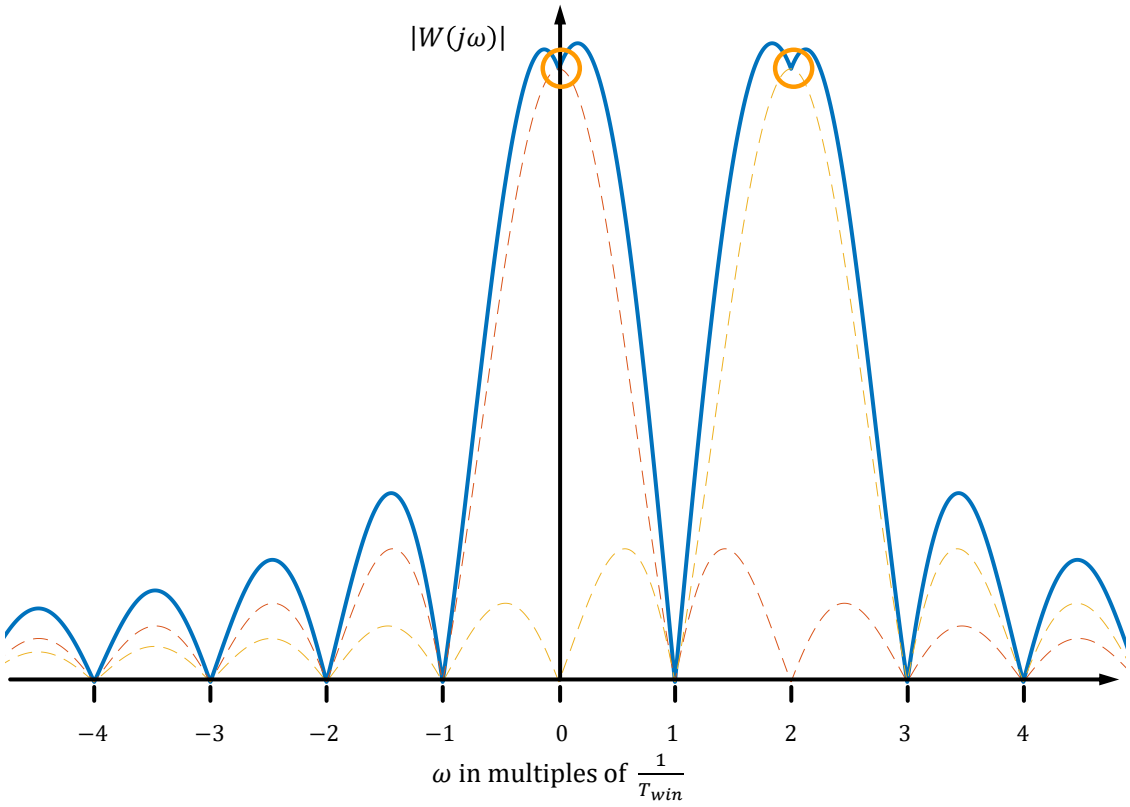

Figure 2-6: For periodic signals, the frequency content is concentrated at discrete frequencies. The convolution with a rectangular window with T_{win} equal to a multiple of the signal frequency results in a spectrum without leakage.

2.2.4 Discrete Frequency Resolution

For processing in digital computers, also the number of frequencies must be restricted to a finite number of discrete frequencies. It is common to select a regular frequency grid with frequency spacing $\Delta f = \frac{1}{T_{win}}$, so that the spectrum is computed solely at discrete frequencies f_k with

$$f_k = \frac{k}{T_{win}}, \qquad k \in \{0, 1, \dots, F-1\} \tag{2.30}$$

i.e. at the integer multiples to the fundamental harmonic $f_1 = \frac{1}{T_{win}}$ (Brigham, 1974, 140-146). From equation (2.30) follows that the frequencies f_k are equally spaced with a frequency resolution $\Delta f = \frac{1}{T_{win}}$.

In principle, the number of frequencies F can be chosen arbitrarily. However from the sampling theorem (Shannon, 1949) follows that for $F = \frac{N}{2}$ the original, real valued signal can be *exactly* reconstructed from the Fourier coefficients[9]. That means that the Fourier coefficients for frequencies $f_k, k \in \{0, \dots, F-1\}$ contain the *entire* signal information of the sampled signal. It follows that computing a larger number of frequencies (i.e. $F > \frac{N}{2}$) does not add more information about the signal.

It is noted that the restriction to a finite, regular frequency grid can be interpreted as sampling and windowing in the frequency domain. If DFT coefficients are transformed back to the time domain (inverse DFT), the effect of the above steps on the time domain signal need to be considered, analogously to sampling and windowing in the time domain.

The selection of equation (2.30) has important advantages: Foremost it helps to avoid leakage when combined with periodic excitations, see section 2.2.3. It further eases the efficient computation due to the use of FFT algorithms, that are especially efficient when the DFT is computed for this frequency grid. The computational effort to compute a N point DFT at F frequencies increases as $\mathcal{O}(F \cdot N)$ with a standard DFT; with FFT algorithms, the effort to compute an N point DFT at $F = N$ frequencies[10] increases as $\mathcal{O}(N \cdot \log(N))$ (Frigo & Johnson, 2005), which makes a great difference for large N.

Comparing the computational effort shows, that for F larger than $\log(N)$ it tends to be more efficient to use a full N point FFT instead of a standard DFT, even if many of the computed frequencies are discarded later.

Within this thesis the number of time domain samples N is in the order of 10^6; hence for $F \gtrsim 14$, it can be expected that a full N sample FFT is computational more efficient than a standard DFT. As this condition is fulfilled in all experiment of this thesis, standard full N point FFTs are applied throughout this thesis. All DFT's are computed with MATLAB's `fft` function, that is based on the FFTW-library (Frigo & Johnson, 2005; The Mathworks, 2017a).

One notable FFT algorithm is the Chirp-z transform (CZT) (Rabiner, Schafer, & Rader, 1969). The CZT can compute the DFT for an arbitrary number of equally spaced frequencies within

[9] For complex valued signals, $F = N$ frequencies are required. The additional frequencies are usually considered as *negative* frequencies with $f_k = \frac{k}{T_{win}}$ with $k \in \{-F+1, \dots, -1\}$.

[10] FFT algorithms are generally designed to support complex input signals and thus return positive and negative frequencies. For real valued signals, the negative frequencies are complex conjugates of the positive ones ($X(-f_k) = \overline{X(f_k)}$) and are discarded.

a user defined frequency range. This allows to "zoom" into certain frequency ranges, which is useful for some applications like image reconstruction (Takaya, Ma, Shimizu, Kitama, & Mikami, 1990) or radar signal processing (Martin, 2005). The CZT has also been used for system identification (Tischler, 1987), as it offers more flexibility compared to conventional FFT algorithms. The CZT allows to compute the DFT also for frequency grids with a frequency resolution $\Delta f < \frac{1}{T_{win}}$ (Tischler, 1987). However, doing so results in spectral leakage, ruining the beneficial properties of periodic excitation signals, compare section 2.2.3.

2.2.5 Discrete Fourier Transform

For sampled, finite length signals, the Fourier transform computed for an equidistant, discrete set of frequencies results in the discrete Fourier transform (DFT) (Brigham, 1974). For discrete frequencies $\omega_k = \frac{2\pi k}{T_{win}}$, with $T_{win} = N \cdot \Delta t$ and $t = n\Delta t$ the continuous Fourier transform of a regularly sampled signal is related to the DFT as

$$\begin{aligned}\mathcal{F}\{x(t) \cdot \mathfrak{d}_{\Delta t} w_{T_{win}}(t)\} &= \int_{-\infty}^{\infty} x(t) \cdot \mathfrak{d}_{\Delta t}(t) \cdot w_{T_{win}}(t) \cdot e^{-j\omega_k t} dt \\ &= \int_{0}^{T_{win}} x(t) \cdot \mathfrak{d}_{\Delta t}(t) \cdot e^{-j\omega_k t} dt \\ &= \int_{0}^{N\Delta t} x(n\Delta t) \cdot \mathfrak{d}_{\Delta t}(n\Delta t) \cdot e^{\frac{-j2\pi kn\Delta t}{N\Delta t}} dn \\ &= \sum_{n=0}^{N} x[n] \cdot e^{\frac{-j2\pi kn}{N}}\end{aligned} \tag{2.31}$$

Different scaling factors of the DFT are common: in this thesis, the DFT is scaled with $\frac{1}{\sqrt{N}}$, in accordance with (Pintelon & Schoukens, 2012, p. 39). Thus, the DFT is given by

$$X(k) = \frac{1}{\sqrt{N}} \sum_{n=0}^{N-1} x[n] \cdot e^{\frac{-j2\pi kn}{N}}, \qquad k \in \{0, 1, \dots, N-1\} \tag{2.32}$$

where $x[n]$ is the discrete signal, N the number of samples, k the respective harmonic and $\frac{1}{\sqrt{N}}$ a scaling factor. In the context of frequency response function estimation, the scaling has no influence on the FRF estimates, as both, the input and output signal are scaled equally, cmp. the definition of the ETFE in equation (2.9). However, the scaling is relevant for the variance/covariance estimates and the deduced confidence regions.

The DFT is a special case of the more general z-transform (Ragazzini & Zadeh, 1952), introduced in equations (2.6) and (2.7), with $z = e^{\frac{j2\pi k}{N}}$. Due to its relation, the DFT inherits the computational rules for transforms of sums, multiplications and convolutions from the z-transform.

2.2.6 Empirical Transfer Function Estimate

The straight forward method to estimate the frequency response function $\hat{G}_{yu}$ is the empirical transfer function estimate (ETFE) (Ljung, 2009, p. 173), introduced in equation (2.9). In the current section, the simple ETFE is extended to periodic excitation signals that allow for a reduction of the effect of noise.

2.2.6.1 ESTIMATE FROM PERIODIC DATA

If periodic excitation signals are used (which is generally recommended), the accuracy of the simple ETFE can be increased by averaging over multiple periods.

$$\hat{G}_{yu}(j\omega_k) = \frac{\hat{Y}(k)}{\hat{U}(k)} \tag{2.33}$$

where $\hat{U}$ and $\hat{Y}$ are the sample means

$$\hat{U}(k) = \frac{1}{M}\sum_{l=1}^{M} U^{[l]}(k) \tag{2.34}$$

and

$$\hat{Y}(k) = \frac{1}{M}\sum_{l=1}^{M} Y^{[l]}(k) \tag{2.35}$$

of the DFT transforms of the independent data sub records

$$U^{[l]}(k) = \mathrm{DFT}\big(u^{[l]}(n)\big) \tag{2.36}$$

and

$$Y^{[l]}(k) = \mathrm{DFT}\big(y^{[l]}(n)\big) \tag{2.37}$$

For noisy input and output signals $U = U_0 + V_U$, $Y = Y_0 + V_Y$, where U_0, Y_0 are the undisturbed signals and V_U, V_Y denote the respective noise components, the ETFE

$$\hat{G}_{yu}(j\omega_k) = \frac{Y_0 + V_Y}{U_0 + V_U} \tag{2.38}$$

is biased due to the effect of the input noise V_U (Pintelon & Schoukens, 2012, p. 53). To analyse the bias error, equation (2.38) is developed in a Taylor series; here only the first term is shown.

$$\hat{G}_{yu}(j\omega_k) = G_0(j\omega_k)\left(1 + \frac{V_Y(k)}{Y_0(k)}\right)\left(1 - \frac{V_U(k)}{U_0(k)} + \left(\frac{V_U(k)}{U_0(k)}\right)^2\right) + \text{h.o.t.} \tag{2.39}$$

For Gaussian noise[11], that is independent from the input and output signals, the Taylor series converges to the true value $G_0(j\omega)$ if $\left|\frac{V_U(k)}{U_0(k)}\right| < 1$. However, a part of the signal noise $V_U(k)$ will violate this condition; as a consequence, the input signal should be checked for outliers, that can violate this condition. For uncorrelated input-output noise the relative bias $b(k)$ is given by (Pintelon & Schoukens, 2001)

$$\frac{b(k)}{G_0(j\omega_k)} = -e^{\left(\frac{-|U_0(k)|^2}{\sigma_U^2(k)}\right)}, \tag{2.40}$$

where $\sigma_U^2(k)$ is the variance of the noise $V_U(k)$. For correlated noise, the bias and variance of the ETFE can be computed explicitly under the assumption of normally distributed noise (Pintelon & Schoukens, 2001); the bias and variance are respectively given by

$$b_{\hat{G}}(k) = (-1)\left(\rho_{V_Y V_U}(k) \cdot \frac{|U_0(k)|/\sigma_U(k)}{|Y_0(k)|/\sigma_Y(k)}\right) e^{\frac{-|U_0|^2}{\sigma_U^2}} \tag{2.41}$$

where $\rho_{V_Y V_U}(k)$ denotes the correlation coefficient of the normalized input and output errors V_U/U_0 and V_Y/Y_0 , that is given by (see Pintelon & Schoukens, 2001)

[11] A detailed introduction of the noise properties is found in section 2.6.1.

$$\rho_{V_Y V_U}(k) = \frac{\sigma^2_{YU}(k)}{\sigma_U(k)\sigma_Y(k)} e^{-j\angle G_0(j\omega_k)}, \tag{2.42}$$

In both cases, the bias is a function of the signal-to-noise ratios. Table 2-1 gives an overview of the expected bias for some signal-to-noise ratios. The values for correlated noise assume a (worst case) correlation of -1 and identical signal-to-noise ratios for the input and output signals. It is seen, that the ETFE bias is smaller than 10^{-4} for SNRs of about 10 dB and thus can often be neglected.

For Gaussian noise, the covariance of the estimate $\hat{G}_{yu}$ is given by

$$\hat{\sigma}^2_{\hat{G}}(k) \approx \left|\frac{\hat{G}_{yu}(j\omega_k)}{M}\right| \left(\left|\frac{\hat{\sigma}^2_U(k)}{\hat{U}(k)}\right|^2 + \left|\frac{\hat{\sigma}^2_Y(k)}{\hat{Y}(k)}\right|^2 - 2\mathrm{Re}\left(\frac{\hat{\sigma}^2_{YU}(k)}{\hat{Y}(k)\,\overline{\hat{U}(k)}}\right)\right) \tag{2.43}$$

(Pintelon & Schoukens, 2012, p. 51). The approximation is due to the use of sample (co)variances given by equations (2.44) to (2.46), instead of the exact (unknown) (co)variances.

$$\hat{\sigma}^2_U(k) = \frac{1}{M-1}\sum_{l=1}^{M}\left|U^{[l]}(k) - \hat{U}(k)\right|^2 \tag{2.44}$$

$$\hat{\sigma}^2_Y(k) = \frac{1}{M-1}\sum_{l=1}^{M}\left|Y^{[l]}(k) - \hat{Y}(k)\right|^2 \tag{2.45}$$

$$\hat{\sigma}^2_{YU}(k) = \frac{1}{M-1}\sum_{l=1}^{M}\left(Y^{[l]}(k) - \hat{Y}(k)\right)\left(\overline{U^{[l]}(k) - \hat{U}(k)}\right) \tag{2.46}$$

In equation (2.43), the three terms in the sum are basically inverse signal-to-noise ratios. It is thus clear, that the estimation uncertainty is directly related to the signal-to-noise ratio.

Table 2-1: Bias for several signal-to-noise ratios.

SNR	SNR in dB	b (uncorrelated)	b (correlated)
1	0	0.367	0.736
2	6.02	0.0183	0.0366
3.1	10	$4.54 \cdot 10^{-5}$	$9.08 \cdot 10^{-5}$
5	13.9	$1.38 \cdot 10^{-11}$	$2.77 \cdot 10^{-11}$
10	20	$3.72 \cdot 10^{-44}$	$7.44 \cdot 10^{-44}$

2.2.6.2 Discrete Frequency Resolution

The ETFE in equation (2.33) requires that $\hat{U}(k)$ is different from zero, otherwise, the fraction $\frac{\hat{Y}(k)}{\hat{U}(k)}$ is not defined. In experiments, it must be ensured, that every considered frequency k is properly excited, i.e. $\hat{U}(k_{exc}) \neq 0$, where k_{exc} denotes the excited frequencies.

Without further assumptions on the system, the ETFE does not provide information about the system behaviour at non-excited frequencies $k_{non} \neq k_{exc}$, $k_{non} \in \mathbb{R}$, where the inequality includes two important cases:

a) k is not an integer: As shown in section 2.2.4, non-integer frequencies k cause spectral leakage. As a result, the DFT is limited to integer k (i.e. $k \in \mathbb{Z}_0$) and it follows immediately, that also the ETFE is computed only for integer k.
b) If k is an integer, but the respective frequency is not excited by the input signal, the ETFE is not defined, as the denominator becomes zero.

As a consequence, the estimation of frequency response functions from DFT's gives only information about the transfer function at excited discrete frequencies. The system behaviour at intermediate (non-integer) frequencies and non-excited integer frequencies is generally not known.

Throughout this thesis, frequency response functions are computed for discrete frequencies only, i.e. $k \in \mathbb{Z}_0$. If required, the system behaviour at intermediate frequencies (i.e. $k \notin \mathbb{Z}_0$) is considered separately.

2.2.6.3 Indirect Estimate From Closed Loop Data

As shown in equation (2.41) estimates that are subject to correlated input and output noise are biased. The maximum bias occurs for $\rho_{V_U,V_Y} = -1$, which is typically given for closed loop systems (Pintelon & Schoukens, 2001). The bias can however be avoided, if the undisturbed reference signal $r(t)$ that drives the closed loop is exactly known, cmp. Figure 2-2c for the closed loop system structure.

The so called *indirect estimate* (Pintelon & Schoukens, 2012, pp. 61–62) is based on the estimation of the FRF $\hat{G}_{ur}$ from the reference signal to the noisy input signal and $\hat{G}_{yr}$ from the reference signal to the output signal. Each FRF is estimated separately, e.g. with the ETFE (equation (2.9) or (2.33)). For simplicity both FRF's can be estimated in a single estimation step by collecting the input- and output DFT spectra in a single variable $Z(k) = \begin{bmatrix} Y(k) \\ U(k) \end{bmatrix}$. Estimating the FRF from $R(k)$ to $Z(k)$ results in $\hat{G}_{zr}(j\omega_{kP}) = \begin{bmatrix} \hat{G}_{yr}(j\omega_{kP}) \\ \hat{G}_{ur}(j\omega_{kP}) \end{bmatrix}$ and in a covariance matrix estimate $\hat{C}_{vec(\hat{G}_{zr})}$. As shown in (Pintelon & Schoukens, 2012, p. 62), the open loop dynamics $\hat{G}_{yu}$ are computed from $\hat{G}_{zr}$ as

$$\hat{G}_{yu} = \hat{G}_{yr}(j\omega_{kP}) \cdot \hat{G}_{ur}^{-1}(j\omega_{kP}), \tag{2.47}$$

Where $\hat{G}_{ur}$ must be invertible. With a first order Taylor approximation the covariance matrix of $\hat{G}_{yu}$ from equation (2.47) is given in (Pintelon & Schoukens, 2012, p. 273) by

$$\hat{C}_{vec(\hat{G}_{yu})} \approx \left(\hat{G}_{ru}^{-T} \otimes \left[I_{n_{out}}, -\hat{G}\right]\right) \hat{C}_{vec(\hat{G}_{rz})} \left(\hat{G}_{ru}^{-T} \otimes \left[I_{n_{out}}, -\hat{G}\right]\right)^H \tag{2.48}$$

2.2.6.4 Multiple Input Systems

The ETFE is restricted to estimate single input systems. If applied to a multiple input system, the ETFE would be underdetermined. From an engineering point of view this means, that the effect of multiple, simultaneous excitations cannot be attributed to the respective input signal. If additional, but unknown, inputs are present, the ETFE will be biased. Three approaches to circumvent this problem are common:

- **Superpose single input dynamics from separate experiments**: For linear systems with multiple inputs, a straight forward method is to estimate the dynamics for each input separately and superpose the respective single input dynamics. This procedure requires independent experiments (one for each input) and the non-identified inputs must be zero. The latter can be difficult to achieve in flight tests,

e.g. when additional inputs are required to keep the aircraft in trim conditions (Tischler & Remple, 2006, pp. 229–258).

- **Split frequency content**: The multiple input problem can be resolved when each input is assigned a set of individual frequencies. In a two input example the odd harmonics ($k = 1, 3, 5, \ldots$) could be excited by input one, even harmonics ($k = 2, 4, 6, \ldots$) by input two; as every harmonic is excited only by one input, the ETFE is well defined and the response is attributed to the correct input. The approach is applied e.g. in (Morelli, 2003) and works very well with multisine inputs, where the spectral content of each signal can be precisely defined. With these zippered multisines, frequency response functions for multiple input systems can be estimates from a single experiment, but at the cost of a reduced frequency resolution. Furthermore, for any single frequency, the response is known only for a single input, while the effect of the others is not identified.
- **Spectral methods with uncorrelated signals**: With spectral methods, based on conditioned spectral density functions (Bendat & Piersol, 1971/2010, pp. 201–248), the effect of multiple input signals can be separated, if the excitations signals are uncorrelated. In theory this spectral approach can identify the full frequency response matrix from a single experiment. In practice, it is difficult to achieve good accuracy in all responses (Tischler & Remple, 2006, pp. 247–248). Hence, it is recommended to perform separate experiments, where the focus is on the accurate estimation of a single input.

As a summary it is stated that none of these approaches can provide frequency response matrices for multiple input systems with full frequency resolution and good accuracy in all responses.

2.2.7 Summary

In the preceding section the ETFE was introduced as the primary non-parametric estimator of frequency response functions. With proper signal processing, aliasing and leakage can be fully avoided and the ETFE provides accurate estimates of the frequency response functions from system's steady-state response to a periodic excitation signal.

If the input signal is disturbed by noise, the estimate is biased. For closed loop systems, an unbiased estimate can be computed if the reference signal is known without error. The variance in the FRF estimate depends on the signal-to-noise ratio of the input- & output signals and the noise correlation. It can be reduced when periodic excitations are used the input- and output- DFTs are averaged over multiple periods.

Two major drawbacks of the ETFE remain:

- The ETFE requires the steady-state response: The ETFE is biased if the transients from the initial values have not died out. The standard approach to discard the first two periods is costly, especially when the settling time of relevant modes is large (which can be in the order of minutes for the Dutch roll and the phygoid).
- None of the methods can estimate the frequency response matrix with full frequency resolution and with good accuracy from a single experiment.

In the following sections novel approaches for both issues are presented, that are based on local polynomial approximations (Pintelon et al., 2010a, 2010b). In sections 2.3 and 2.4 the effect of unknown initial and final values is approached. In section 2.5 an alternative estimator for multiple input systems is introduced.

2.3 Extended Transfer Function Model

As introduced in the beginning of this chapter, the ETFE $Y_{DFT}(j\omega)/U_{DFT}(j\omega)$ is different from the transfer function given by z-transforms due to the effect of unknown initial and final conditions. To understand this effect, it is recalled that the system response $y[n]$ of any discrete time LTI system to a given input signal $u[n]$ is a convolution of the input signal with the systems impulse resonse $g[n]$ given by

$$\begin{aligned} y[n] &= \sum_{k=-\infty}^{\infty} u[k] \cdot g[n-k]\,, \\ &= u[n] \cdot g[n] + u[n-1]g[n-1] + \cdots \end{aligned} \tag{2.49}$$

Thus, the system response is a sum of impulse responses, that are shifted by time (due to the convolution) and weighted by the respective input signal. This relation is visualized in Figure 2-7; the top plot shows (schematically) an input signal. At every epoch n, the input $u[n]$ "triggers" an impulse response that is scaled with the amplitude $u[n]$. The system response is the sum of all impulses that were triggered in the past and is shown in the middle plot, where three exemplary impulse responses are indicated. When the response signal is measured only for a finite time interval, indicated by the violet box, and unknown outside, some parts of the responses are cut off.

The first exemplary impulse response is partly contained in the measurement interval, but the corresponding input impulse is not contained in the measurement interval. Thus, the output signal contains components without a corresponding input.

Analogously, at the end of the measurement interval, the response is cut off, but the corresponding input is fully contained in the data. Now, the input signal contains components that miss the corresponding response. These missing parts due to finite measurement interval make up the initial and final conditions.

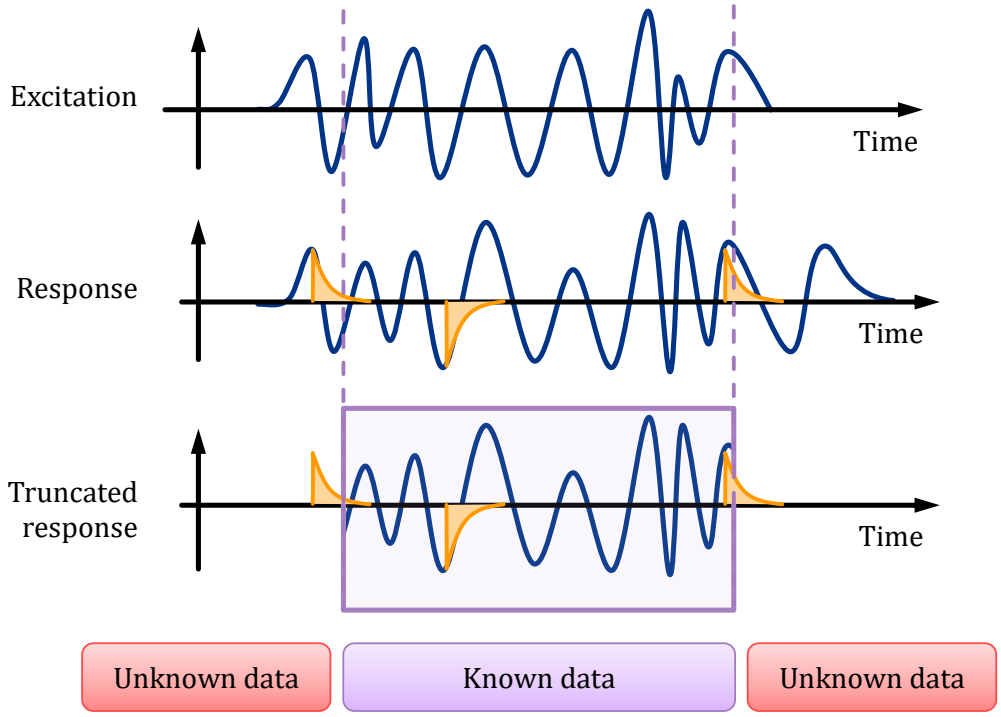

Figure 2-7: Relation of the system response to the input signal : The system response (middle) is related to the input signal (top) by its impulse response (indicated in orange). When only a finite number of data is known (indicated by the violet box), parts of the impulse response are cut off.

To derive a model that accounts for the initial and final conditions, the transfer function model from equation (2.9) is rewritten in the form

$$Y_{DFT}(j\omega) \approx G_{0,yu}(j\omega)U_{DFT}(j\omega), \tag{2.50}$$

and will be extended with an additional term $T(j\omega)$ that accounts for the initial and final values, cmp. equation (2.81). The extended transfer function model (ETFM) was proposed in (Pintelon et al., 1997); it is derived from the system's difference equation (2.51) (respectively from its z-transform (2.52)) and is (in contrast to equation (2.50)) an exact relation of the input-/output DFTs to the system transfer function $G_{0,yu}(j\omega)$.

$$\sum_{p=0}^{n_a} a_{\mathrm{p}} y[n-\mathrm{p}] = \sum_{q=0}^{n_b} b_q u[n-q], \quad \text{with } n = -\infty, \cdots, -1, 0, 1, \cdots, \infty. \tag{2.51}$$

$$A(z^{-1})Y(z) = B(z^{-1})U(z) \tag{2.52}$$

For the derivation of the ETFM, the z-transform is adjusted to explicitly takes the unknown initial and final conditions into account. It is assumed that the input and output signals are known exactly for the time interval $[0, (N-1)]$ and are unknown outside this interval.

To deal with the unknown data when transforming (2.51) the one-sided z-transform at $n = 0$ with unknown initial conditions is derived (section 2.3.1). Analogously, the one-sided z-transform at $t = N$ with unknown final conditions is derived to cope with unknown final conditions (section 2.3.2). Subtracting the latter from the modified z-transform account for initial conditions, result in a finite length z-transform that accounts for initial and final conditions. Applying the derived z-transforms to the system difference equation (2.51) (sections 2.3.2 and 2.3.4) leads to the ETFM (section 2.3.5). The following derivation is an extended version of the derivation in (Pintelon et al., 1997).

2.3.1 One Sided Z-transform With Unknown Initial Conditions

The derivation of the ETFM starts from the definition of the one-sided Z-transform (equation (2.53). For signal processing purposes it is common to ignore non-zero parts of the transformed signal $x[n]$ for $n < 0, n \in \mathbb{Z}$, cmp. (Oppenheim et al., 1997, p. 790)[12]. As shown in the beginning of this section, it is exactly this part that is relevant for the initial conditions. To be more precise, the initial conditions at $n = 0$ of the difference equation (2.51), are a function of the past data $u[n], y[n]$ for $n < [-r: -1]$. For physical systems, r equals the denominator grade n_a. Thus n_a samples of the past input and output signals are required to describe the initial conditions exactly.

The aim of this section is to explicitly include and separate the contribution of the unknown past data on the z-transform $X(z)$. This is achieved by a time shift and a splitting of the transform in two separate sums. The derivation starts from the standard, one-sided z-transform

$$X(z) = \sum_{n=0}^{\infty} x[n]z^{-n}. \tag{2.53}$$

If the past r samples were known, they could be easily included in (2.53) by a shift of the time vector by r samples, resulting in

[12] For linear systems, this is identical to the assumption that the initial values are zero.

$$X_p(z) = \sum_{n=0}^{\infty} x[n-r]z^{-n}, \tag{2.54}$$

where the subscript p indicates that past data is included, cmp. steps 1 and 2 in Figure 2-8. To separate the contributions of (unknown) past data (before $n = 0$) and known data (starting at $n = 0$), the summation is split in two parts; the first ranges from $n = [0; r-1]$ (including the past data), the second from $n = [r; \infty[$, (cmp. step 3 in Figure 2-8)

$$X_p(z) = \sum_{n=0}^{r-1} x[n-r]z^{-n} + \sum_{n=r}^{\infty} x[n-r]z^{-n} \tag{2.55}$$

Finally, the summation indices are replaced: In the first summation $l = n - r$ is introduced and in the second summation $m = n - r$. Factoring out z^{-r} and changing the sign of l gives

$$\begin{aligned} X_p(z) &= \sum_{l=-r}^{-1} x[l]z^{-(l+r)} + \sum_{m=0}^{\infty} x[m]z^{-(m+r)} \\ &= z^{-r}\left(\sum_{l=-r}^{-1} x[l]z^{-l} + \sum_{m=0}^{\infty} x[m]z^{-m}\right) \\ &= z^{-r}\left(\underbrace{\sum_{m=0}^{\infty} x[m]z^{-m}}_{X(z)} + \underbrace{\sum_{l=1}^{r} x[-l]z^{l}}_{X_1(z)}\right), \end{aligned} \tag{2.56}$$

which corresponds to equation (3) in (Pintelon et al., 1997), cmp. step 4 in Figure 2-8. Equation (2.56) can be written shorter as

$$\sum_{n=0}^{\infty} x[n-r]z^{-n} = z^{-r}\big(X(z) + X_1(z)\big) \tag{2.57}$$

with

$$X(z) = \sum_{m=0}^{\infty} x[m]z^{-m} \tag{2.58}$$

and

$$X_1(z) = \sum_{l=1}^{r} x[-l]z^{l} \tag{2.59}$$

where the term X_1 contains the initial conditions, i.e. the contributions of the past data to $X_p(z)$, and $X(z)$ is a standard one-sided z-transform, starting at $n = 0$ and extending to infinity. Thus, the transformation (2.57) requires infinite data, that cannot be provided by experiments; this problem is tackled in section 2.3.2.

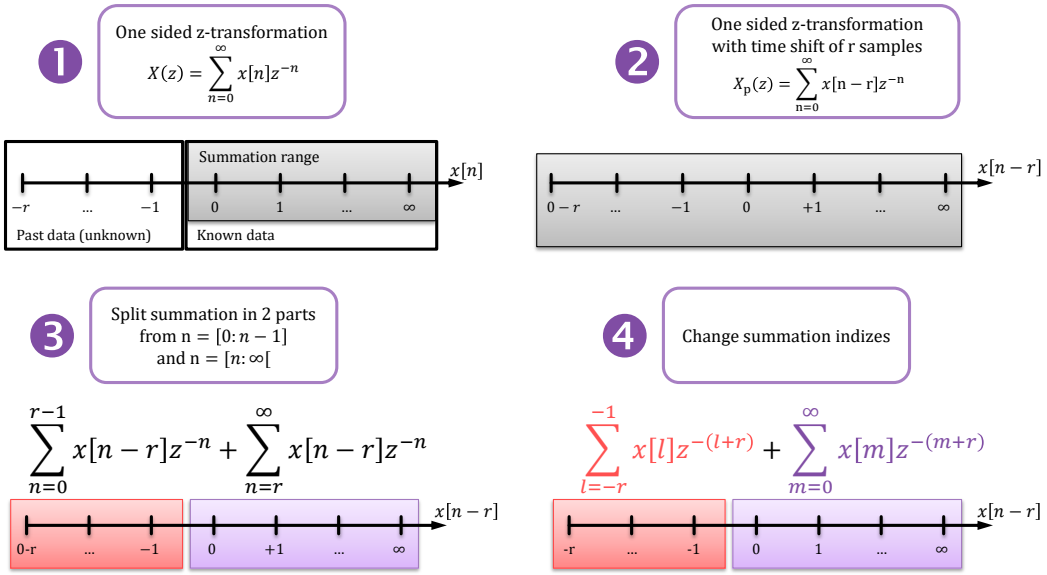

Figure 2-8: Derivation of the z-transform with unknown initial conditions.

2.3.2 Transformation of Difference Equation With Unknown Initial Conditions

In sections 2.3.1 the z-transform was extended to include the effect of unknown initial conditions. The modified transform is now applied to the difference equation; the transformation is analogously to the standard z-transform (cmp. equations (2.51), (2.52)). Applying equation (2.57) on the difference equation (2.51) results in

$$\begin{aligned} a_0 \cdot z^{-0}\big(Y(z) + Y_1(z)\big) + \cdots + a_{n_a} \cdot z^{-n_a}\big(Y(z) + Y_1(z)\big) \\ = b_0 \cdot z^{-0}\big(U(z) + U_1(z)\big) + \cdots + b_{n_b} \cdot z^{-n_b}\big(U(z) + U_1(z)\big) \end{aligned} \tag{2.60}$$

or shorter

$$A(z^{-1}) \cdot \big(Y(z) + Y_1(z)\big) = \mathrm{B}(\mathrm{z}^{-1}) \cdot \big(U(z) + U_1(z)\big) \tag{2.61}$$

with U_1, Y_1 from equation (2.59). The $U_1(z)$ and $Y_1(z)$ terms can be combined in a single term $T_1(z)$ that describes the initial conditions, i.e. the contributions of the unknown past data to the system difference equation:

$$A(z^{-1})Y(z) = B(z^{-1})U(z) + T_1(z), \tag{2.62}$$

with
$$\mathrm{T}_1(z) = \mathrm{B}(\mathrm{z}^{-1})U_1(z) - A(z^{-1})Y_1(z) \tag{2.63}$$

The term T_1 is derived in detail in appendix C.1 and is given by

$$\begin{aligned} T_1(z) &= \sum_{q=0}^{n_b} b_q z^{-q} \cdot U_1(z) - \sum_{p=0}^{n_a} a_p z^{-p} \cdot Y_1(z) \\ &= [\dots] \\ &= \sum_{q=0}^{n_b} \sum_{n=1}^{q} b_q\, u[-n] z^{n-q} - \sum_{p=0}^{n_a} \sum_{n=1}^{p} a_p\, y[-n] z^{n-p}, \end{aligned} \tag{2.64}$$

It is once more noted that $U(z), Y(z)$ are standard one-sided z-transforms. Thus, equation (2.62) requires infinite long data sets.

2.3.3 One Sided Z-transform With Unknown Final Conditions

In section 2.3.1 the z-transform is extended to account for the contributions of unknown initial values. The resulting transform requires infinite data, that cannot be provided from real measurements. To limit the transformation to a finite number of samples, the transform (2.57) is applied to the unknown future data, starting at $n = N$. The result is then subtracted from X_p (see sections 2.3.5), resulting in a finite length transform that accounts for the initial and final conditions.

The approach is similar as for initial conditions. The final conditions at the end of the available data set, i.e. after N samples, depend on the last r samples before N. Due to the finite number of known samples, however a part of the system response is cut off and is not contained in the available data set. This missing signal part is summarized in the final conditions.

The derivation of the one-sided z-transform that accounts for final conditions follows the same lines as for the initial conditions. As before, the z-transform of a time shifted signal is split in two contributions, but the known and unknown parts are swapped. Further the z-transform now starts from $n = N$, i.e. at the end of the known data set. Thus equation (2.54) becomes (cmp. steps 1 and 2 in Figure 2-9)

$$X(z) = \sum_{n=N}^{\infty} x[n-r]\ z^{-n} \tag{2.65}$$

Again, the summation is split in two parts, the first with $n = [N; N+r-1]$, the second with $n = [N+r; \infty[$, cmp. step 3 in Figure 2-9.

$$X_f(z) = \sum_{n=N}^{N+r-1} x[n-r]z^{-n} + \sum_{n=N+r}^{\infty} x[n-r]z^{-n} \tag{2.66}$$

Here the first sum includes known data, while the second contains the unknown future data; the subscript f indicates that future data is included. Replacing $l = -n + N + r$, $m = n - r$ and factoring out z^{-r} and z^{-N} results in

$$\begin{aligned} X_f(z) &= z^{-r}\left(z^{-N}\sum_{l=1}^{r} x[N-l]z^{l} + \sum_{m=N}^{\infty} x[m]z^{-m}\right) \\ &= z^{-r}\left(\tilde{X}(z) + z^{-N}X_2(z)\right), \end{aligned} \tag{2.67}$$

with

$$\tilde{X}(z) = \sum_{m=N}^{\infty} x[m]z^{-m} \tag{2.68}$$

and

$$X_2(z) = \sum_{l=1}^{r} x[N-l]z^{l} \tag{2.69}$$

Cmp. step 4 in Figure 2-9. $\tilde{X}$ is a one-sided z-transform starting at $m = N$ (the tilde indicates the non-standard starting value) that includes the contribution of the unknown future data to X_f, while X_2 contains the contribution of the known data to X_f.

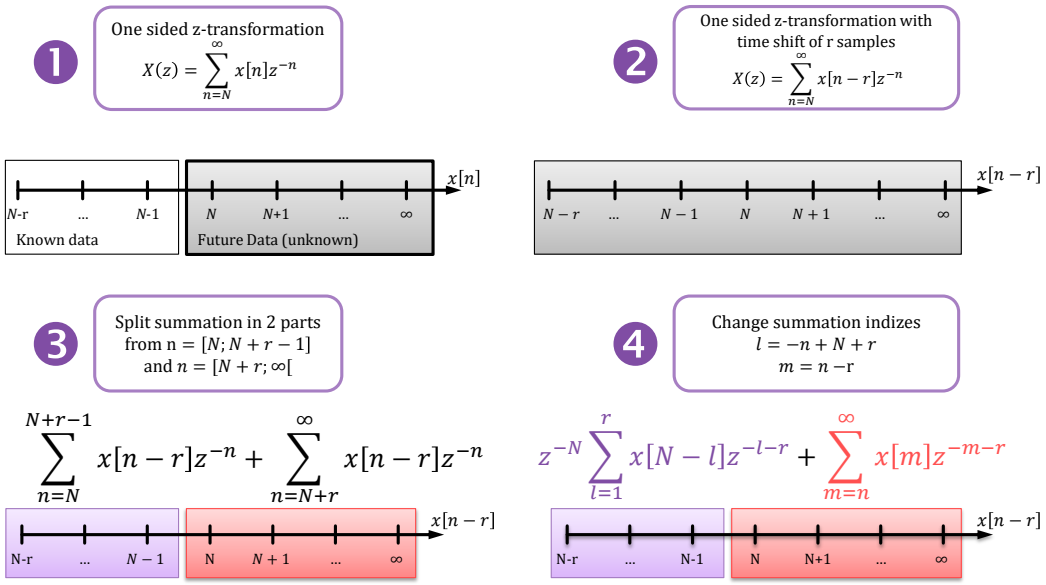

Figure 2-9: Derivation of the z-transform with unknown final conditions.

2.3.4 Transformation of Difference Equation With Unknown Final Conditions

Applying the modified transform (2.67), that accounts for unknown future values, on the difference equation (2.51) results in

$$\begin{aligned} &a_0 \cdot z^{-0}\left(\tilde{Y}(z) + z^{-N}\, Y_2(z)\right) + \cdots + a_{n_a} \cdot z^{-n_a}\left(\tilde{Y}(z) + z^{-N}\, Y_2(z)\right) \\ &= b_0 \cdot z^{-0}\left(\tilde{U}(z) + z^{-N}\, U_2(z)\right) + \cdots + b_{n_b} \cdot z^{-n_b}\left(\tilde{U}(z) + z^{-N}\, U_2(z)\right) \end{aligned} \tag{2.70}$$

Or shorter

$$A(z^{-1}) \cdot \left(\tilde{Y}(z) + z^{-N}\, Y_2(z)\right) = \mathrm{B}(z^{-1}) \cdot \left(\tilde{U}(z) + z^{-N}\, U_2(z)\right) \tag{2.71}$$

Where $\tilde{U}(z), \tilde{Y}(z)$ are one-sided z-transforms that require infinite data. Combining U_2 and Y_2 in a single term results in

$$A(z^{-1})\tilde{Y}(z) = B(z^{-1})\tilde{U}(z) + z^{-N}T_2(z^{-1}) \tag{2.72}$$

with

$$T_2(z) = \mathrm{B}(z^{-1})U_2(z) - A(z^{-1})Y_2(z) \tag{2.73}$$

As shown in appendix C.1, the term T_2, fully expanded, is given by

$$T_2(z) = \sum_{q=0}^{n_b}\sum_{n=1}^{q} b_q u[N-n]z^{n-q} - \sum_{p=0}^{n_a}\sum_{n=1}^{p} a_p\, y[N-n]z^{n-p}, \tag{2.74}$$

2.3.5 Extended Transfer Function Model

2.3.5.1 Finite Length z-Transform

In the further derivation of the ETFM, the results from equations (2.57) (initial values) and (2.67) (future data) are combined. The derivation utilizes that $X(z)$ and $\tilde{X}(z)$ have different summation ranges, but are otherwise identical, thus

$$\begin{aligned} X(z) - \tilde{X}(z) &= \sum_{m=0}^{\infty} x[m]z^{-m} - \sum_{m=N}^{\infty} x[m]z^{-m} \\ &= \sum_{m=0}^{N-1} x[m]z^{-m} \end{aligned} \tag{2.75}$$

is a finite length z-transform and results in the DFT for $z = e^{-j\omega}$. Figure 2-10 visualizes this result; $X(z)$ is a one-sided z-transform with initie length, starting at $n = 0$; similarly, $\tilde{X}(z)$ is an infinite sum that starts at $n = N$. As they are otherwise identical sums, their difference is a finite length sum.

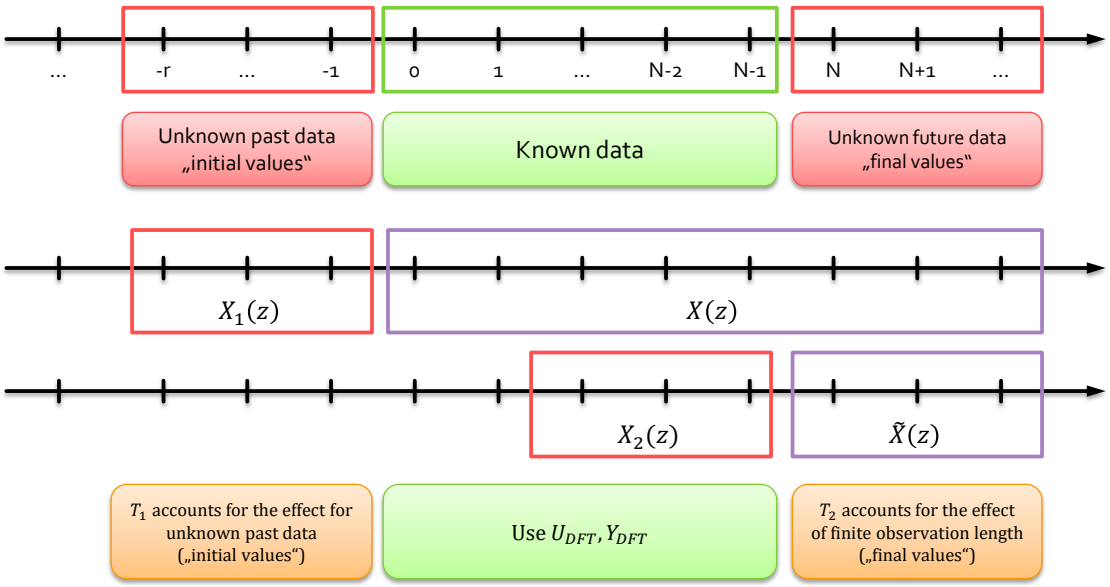

Figure 2-10: Schematic of the transforms with initial and final conditions.

Figure 2-10 gives further insight in the role of $X_1(z)$ and $X_2(z)$: As stated before, the initial values depend on past samples, that are not included in the known data set, indicated by the red rectangle $X_1(z)$. A non-zero input at e.g. $x[-1]$ will result in a response that (partly) extends into the measured data range $n = [0: N-1]$. So, the system response is partly contained in the Y_{DFT}, but the corresponding input is not part of U_{DFT}. This disparity obviously results in erroneous input-/ output-transfer function results.

Similarly, at the end of the available data set, a part of the system response is cut off. The missing part is a function of the preceding samples, i.e. of the last samples that are known, indicated by the red rectangle $X_2(z)$. Here, the known input at e.g. $u[N-1]$ is contained in the input DFT, but the response extends over the measured data set. Thus a part of the response will be cut off and is missing in Y_{DFT}, while the corresponding excitation is contained in U_{DFT}.

When the steady-state response of a system to a periodic excitation is measured, the missing part of the system response at the end of the known data set is identical to the additional part at the beginning; thus X_1 and X_2 compensate each other.

From this interpretation further follows, that the effect of initial and final conditions is specific for system responses and the modified z-transforms have no general meaning beyond their application to input and output signals of LTI systems.

2.3.5.2 Discrete Time Systems

To derive the ETFM, equation (2.72) is subtracted from (2.62):

$$A(z^{-1})Y(z) - A(z^{-1})\tilde{Y}(z) = B(z^{-1})U(z) - B(z^{-1})\tilde{U}(z) + T_1(z) - z^{-N}T_2(z^{-1}), \quad (2.76)$$

$$A(z^{-1})\left(Y(z) - \tilde{Y}(z)\right) = B(z^{-1})\left(U(z) - \tilde{U}(z)\right) + \left(T_1(z) - z^{-N}T_2(z^{-1})\right), \quad (2.77)$$

With equation (2.75) the result can be expanded as

$$\sum_{p=0}^{n_a} a_p z^{-p}\left(\sum_{n=0}^{N-1} y[n]z^{-n}\right) = \sum_{q=0}^{n_b} b_q z^{-q}\left(\sum_{n=0}^{N-1} u[n]z^{-n}\right) + T_1(z^{-1}) - z^{-N}T_2(z^{-1}), \quad (2.78)$$

where $\sum_{n=0}^{N-1} y[n]z^{-n}$ and $\sum_{n=0}^{N-1} u[n]z^{-n}$ are finite length z-transforms. With $z^{-1} = e^{j\omega_k}$, $\omega_k = \frac{2\pi k}{N}$, $k = 0,1,\dots,F-1$, where F is the number of frequencies, the finite length z-transforms become discrete Fourier transforms and the equation results in

$$A(j\omega_k)Y_{DFT}(k) = B(j\omega_k)U_{DFT}(k) + T(j\omega_k) \quad (2.79)$$

with

$$T = T_1(z^{-1}) - z^{-N}T_2(z^{-1}) \quad (2.80)$$

where $T(j\omega_k) = \mathrm{T}_1(j\omega_k) - (j\omega_k)^{-N}T_2(j\omega_k)$ summarizes the transient terms. The resulting transfer function $G(j\omega_k)$ is derived by division with $A(j\omega_k)$

$$Y_{DFT}(k) = G(j\omega_k)\, U_{DFT}(k) + T_G(j\omega_k) \quad (2.81)$$

where the transient term T_G is given by

$$T_G(j\omega_k) = \frac{T(j\omega_k)}{A(j\omega_k)} \quad (2.82)$$

Equation (2.81) is called extended transfer function model (ETFM). It is an exact relation of the *input-/output-DFTs* and the *system transfer function* for discrete-time LTI systems (Pintelon et al., 1997). The ETFM holds for arbitrary excitations (either periodic or non-periodic) and accounts for the effect of non-steady state conditions. The term T_G is a linear function of the difference between the initial and final conditions of the system and is called *equivalent initial condition*. As explained already before, T_G is zero for periodically excited systems under steady state conditions if an integer number of full periods is observed, as in that case T_1 and T_2 cancel each other (Pintelon & Schoukens, 2012, pp. 185–188).

From equation (2.81) follows that the transfer function $G_{0,yu}$ is related[13] to the DFT spectra of the input and output signals by

$$G(j\omega_k) = \frac{Y_{DFT}(k)}{U_{DFT}(k)} - \frac{T_G(j\omega_k)}{U_{DFT}(k)} \quad (2.83)$$

[13] In contrast to equation (2.50), this is an exact relation.

2.3.5.3 CONTINUOUS TIME SYSTEMS

When applied to continuous systems, equation (2.81) must be extended by an additional error term $\widetilde{\Delta}(j\omega_k)$. This additional term is called residual alias error and represents the errors due to sampling of continuous signals, cmp section 2.2.2. With the additional term equation (2.81) results in

$$Y(k) = G_{yu}(j\omega_k)\, U(k) + T_G(j\omega_k) + \widetilde{\Delta}(j\omega_k) \tag{2.84}$$

In (Pintelon & Schoukens, 2012, pp. 212–216) it is shown that $T_G(j\omega_k)$ and $\widetilde{\Delta}(j\omega_k)$ both tend to zero as $\mathcal{O}(N^{-1/2})$; hence $\widetilde{\Delta}(j\omega_k)$ cannot be neglected with respect to (w.r.t.) $T_G(j\omega_k)$. In practical applications $\widetilde{\Delta}(j\omega_k)$ can be approximated well with a polynomial (Pintelon et al., 1997). The estimation of this polynomial can be combined with the estimation of $T_G(j\omega_k)$ by adjusting the estimate $\hat{T}_G(j\omega_k)$ (Pintelon & Schoukens, 2012, pp. 186–188). In the following, $\widetilde{\Delta}(j\omega_k)$ is generally included in $T_G(j\omega_k)$.

2.3.5.4 ETFM WITH NOISE

In many cases, the input or output signals are not known exactly, but are disturbed by measurement noise. To include the input and output noise in the ETFM two noise terms are added.

$$Y(k) + V_Y(k) = G_{yu}(j\omega_k)\left(U(k) + V_u(k)\right) + T_G(j\omega_k) \tag{2.85}$$

For a simplified analysis, the noise term can be summarized in a single term $V(k)$, resulting in the output error model structure.

$$Y(k) = G_{yu}(j\omega_k)\, U(k) + T_G(j\omega_k) + V(k) \tag{2.86}$$

This output error model is used for the analysis of the ETFM and its properties. It is also the basis for the derivation of the local polynomial method.

2.3.6 PROPERTIES OF THE EXTENDED TRANSFER FUNCTION MODEL

Equation (2.82) shows that $T_G(j\omega_k)$ has the same poles as G_{yu}. Hence $T_G(j\omega_k)$ can be described by a rational form with polynomials of degree $n_a - 1$, i.e. with same order as the system dynamics. Further $T_G(j\omega_k)$ is a smooth function of frequency; however it may vary significantly (over frequency) if G_{yu} contains lightly damped poles. Other properties of the ETFM are noted in (Pintelon et al., 1997) and are summarized here:

- The extended transfer function model is valid for unstable systems[14]. To run experiments with unstable systems, a stabilizing controller may be required.
- The transient term is a smooth function of frequency. The smoothness property is exploited in section 2.4 to compute estimates of T_G from local polynomial approximations.
- Close to lightly damped poles (i.e. at resonance frequencies) T_G can vary rapidly. In such cases a polynomial approximation can be biased.

For the derivation of the ETFM the input and output signals were assumed to be known exactly for the observed time interval and unknown otherwise. It was shown that the unknown initial states and the unknown final states result in an additional term T_G that represents the difference of the initial and final conditions.

[14] As the z-transform does also exist for exponentially increasing sinusoids, the derivation can be extended to unstable systems.

In the following sections, an algorithm for the estimation of $T_G(j\omega_k)$ is introduced. It is based on periodic excitations and the observation of full signal periods (at least two periods are required).

2.4 Estimation of Transient Term From Periodic Data

As outlined in the beginning of chapter 2, the transient term, representing the equivalent initial and final conditions, can be explicitly estimated. The estimation approach shown in this section was developed in (Pintelon & Schoukens, 2012, pp. 248–263) and is based on periodic excitations. In section 2.5. the estimation of the transient term is combined with FRF estimators, which are thus able to estimate frequency response functions without errors due to non-zero initial and final conditions.

The estimation approach is based on the well-known property of LTI systems, that the steady-state response to a periodic input signal is also periodic and has the same period. The second property can be utilized to estimate the transient term from periodic input data. To do so, the system is excited with a periodic signal and multiple consecutive periods of the system response are measured (section 2.4.1). This allows to split the response data in two datasets: The first set contains all harmonics that are excited by the input signal. The second set contains only harmonics that are not excited by the input signal (sections 2.4.2). The latter is used to estimate the transient effect and the noise at the excited harmonics based on a local polynomial approximation (section 2.4.3). When the transient term is removed from the input-/output DFT spectra, only the periodic signal parts remain; they are the basis for the FRF estimation in section 2.5

In (Pintelon & Schoukens, 2012) several variants of this algorithm are introduced. The one presented here is based on periodic excitations and is called *fast LPM*. A related algorithm that handles arbitrary excitation signals is described in (Pintelon & Schoukens, 2012, pp. 227–248) and is named *arbitrary LPM*. For periodic data, the fast LPM results in more accurate FRF estimates. Thus the arbitrary LPM is not used in this thesis.

2.4.1 Periodic Input Signal

The input signal $u[n]$ is periodic with a period of N samples. To avoid leakage, only full periods of $u[n]$ are observed, i.e. the entire observation length is an integer multiple of N. As introduced in section 2.2.5, the DFT is computed for the harmonics of the observation length. Figure 2-11 shows the first three harmonics $U(1)$ in blue, $U(2)$ in pink and $U(3)$ in green.

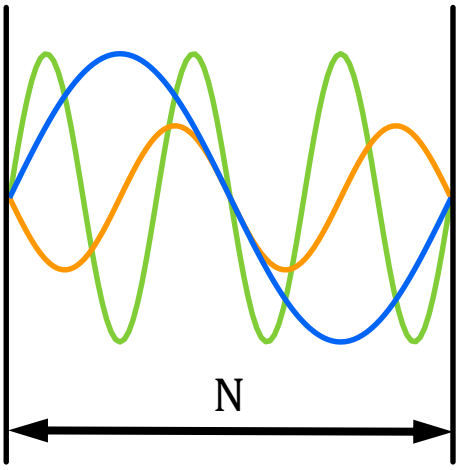

Figure 2-11: First harmonics when *N* samples are observed.

When multiple periods are observed, the individuals periods are denoted by $u^{[l]}[n]$, where $l = 1,2,\dots,P$ is the number of the respective period and P the total number of periods. The entire dataset containing all periods is denoted by $u^{[:]}[n]$. In the absence of noise, any single period $u^{[l]}[n]$ is equal to the first one, i.e. $u^{[l]}[n] = u^{[1]}[n]$ and hence $U^{[l]}(k) = U^{[1]}(k)$.

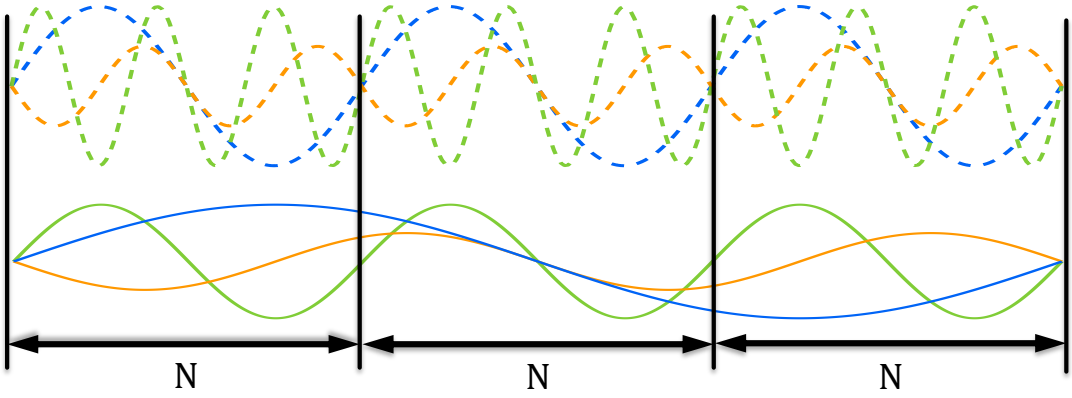

Figure 2-12: Harmonics when 3 periods are observed.

The DFT $U^{[:]}$ of the *entire* dataset has a P-time finer frequency resolution compared to $U^{[1]}(k)$, as the (total) observation length is increased by a factor of P. The frequency content is not changed by observing multiple periods of $u[n]$; in the absence of input noise, the "additional" frequencies of the DFT spectrum due to the longer observations length are all zero, cmp. Table 2-2. Hence, the DFT $U^{[:]}(m)$ of multiple periods relates to the DFT $U^{[1]}(k)$ of a single period as

$$U^{[:]}(m) = \begin{cases} U^{[1]}(k), & m = Pk \\ 0, & m \neq Pk \end{cases} \tag{2.87}$$

with $k \in [0,\dots,F-1]$ where F denotes the number of frequencies and P the number of observed periods. In the following sections, the spectra are split in a set of *excited* frequencies with $m = Pk$ and a set of *non-excited* frequencies with $m \neq Pk$:

$$\begin{aligned} U_{exc} &= U^{[:]}(m), & m &= Pk \\ U_{non} &= 0, & m &\neq Pk \end{aligned} \tag{2.88}$$

The resulting mapping of the respective harmonics to U_{exc} and U_{non} is summarized in Table 2-2.[15] The relation of harmonics and observation length is visualized in Figure 2-12 for an example with three periods: The first three harmonics $U^{[:]}(1)$ (blue), $U^{[:]}(2)$ (orange) and $U^{[:]}(3)$ (green) of the entire dataset are shown as solid lines, the first three harmonics of each period are shown as dashed lines. It is seen that $U^{[1]}(1)$ coincides with $U^{[:]}(3)$. The harmonics $U^{[:]}(1)$ and $U^{[:]}(2)$ however are not contained in $U^{[1]}$. This ensures that $U^{[:]}(1)$ and $U^{[:]}(2)$ are not excited by the periodic signal. For linear systems any signal content in non-excited harmonics is thus due to noise or transient effects.

[15] For the remainder of section 2.4 and for the derivation of the local polynomial methods in section 2.5 it is assumed that all harmonics $U^{[1]}(k)$ are excited. As it will be seen in section 3.2.5, this can be relaxed, resulting in additional freedom for experiment design.

Table 2-2: Comparison of frequencies contained in $U^{[1]}$ and $U^{[:]}$ for three periods ($P = 3$).

$U^{[1]}(k)$	k			1			2			3	…	$\frac{n}{2}$
	ω_k			$\frac{1}{T}$			$\frac{2}{T}$			$\frac{3}{T}$	…	$\frac{n}{2T}$
$U^{[:]}(m)$	m	1	2	3	4	5	6	7	8	9	…	$\frac{3n}{2}$
	ω_m	$\frac{1}{3T}$	$\frac{2}{3T}$	$\frac{3}{3T}$	$\frac{4}{3T}$	$\frac{5}{3T}$	$\frac{6}{3T}$	$\frac{7}{3T}$	$\frac{8}{3T}$	$\frac{9}{3T}$	…	$\frac{n}{2T}$
U_{exc}				x			x			x	…	
U_{non}		x	x		x	x		x	x		…	

2.4.2 System Response to Periodic Signal

Under steady state conditions, the response of a linear system to a periodic input signal as described in section 2.4.1 contains only signal energy at the excited harmonics $m = Pk$. The system response $Y(m)$ is given by

$$Y(m) = G_{yu}(j\omega_m)\, U(m) \tag{2.89}$$

Analogously to equation (2.88), also $Y(m)$ is split in two datasets

$$\begin{aligned} Y_{exc}(m) &= Y^{[:]}(m) \\ &= G(j\omega_m)\, U^{[:]}(m) \end{aligned} \tag{2.90}$$

where $m = Pk$ and Y_{non}

$$\begin{aligned} Y_{non}(m) &= Y^{[:]}(m) \\ &= 0 \end{aligned} \tag{2.91}$$

with $m \neq Pk$. This result shows, that under steady state conditions and in the absence of noise, the non-excited harmonics $Y_{non}(m), m \neq Pk$ of the measured response are exactly zero.

2.4.2.1 Non-Steady State Conditions With Noise

As shown in section 2.3.5 under non-steady state conditions the system response is described by the ETFM, equation (2.84),

$$Y(m) = G_{yu}(j\omega_m)\, U(m) + T_G(j\omega_m) \tag{2.92}$$

$T_G(j\omega_m)$ is a broadband signal, i.e. in general $T_G(j\omega_m)$ (including $\widetilde{\Delta}(j\omega_m)$ for continuous systems) is different from zero, independent of frequency.

$$T_G(j\omega_m) \neq 0 \tag{2.93}$$

Hence under non-steady state conditions equation (2.90) becomes

$$Y_{exc} = G_{yu}(j\omega_m)\, U(m) + T_G(j\omega_m), \qquad m = Pk \tag{2.94}$$

and equation (2.91) becomes

$$Y_{non} = T_G(j\omega_m), \qquad m \neq Pk \tag{2.95}$$

This shows that under non-steady state conditions, the non-excited harmonics of the output signal Y_{non} contain only the transient term T_G.

2.4.2.2 NOISE

As noise is generally non-periodic, its noise spectrum cannot be split in excited and non-excited sets of frequencies. In general, noise is a broadband signal, so that all harmonics of the system output $Y^{[:]}$ may contain noise. With the additional noise terms, equations (2.90) and (2.91) extend to

$$Y_{exc} = G_{yu}(j\omega_m)\, U(m) + T_G(j\omega_m) + V(m), \qquad m = Pk \tag{2.96}$$

and

$$Y_{non} = T_G(j\omega_m) + V(m), \qquad m \neq Pk \tag{2.97}$$

In presence of noise, the response Y_{non} from non-steady state measurements contains two signal contributions, namely the transient term T_G and noise V.

2.4.2.3 SUMMARY

As derived above, the system response $Y^{[:]}(m)$ can be split in two data sets Y_{exc} and Y_{non}. Y_{exc} contains all harmonics that are excited by the input signal $U^{[l]}$, whereas Y_{non} contains only harmonics that cannot be excited by the periodic input signal. As shown in equation (2.97), Y_{non} contains only contributions from the transient term T_G, and noise V.

2.4.3 LOCAL POLYNOMIAL APPROXIMATION OF TRANSIENT TERM

As shown in section 2.4.2 the system response of an LTI system to a periodic input can be split in two sets of excited (Y_{exc}) and non-excited harmonics (Y_{non}). The excited set in (2.96) contains contributions from the system response GU, the transient term T_G and noise V. To compute accurate estimates of G_{yu}, the contribution of T_G to Y_{exc} must be accounted for.

To do this, T_G at the *excited* harmonics is estimated. The estimate is based on the *non-excited* data set: As shown above, the non-excited data set contains only the transient term and noise. Both terms have different behaviour over frequency. While the transient term T_G is a *smooth* function of frequency, the noise V *varies wildly* with frequency. This different behaviour over frequency can be easily exploited: The smooth part, i.e. the transient term T_G, is modelled with local polynomials; the residuals constitute the noise V. With this approach, T_G is easily accessible.[16]

The local polynomials are developed at every excited frequency, with its supporting points (non-excited harmonics only) distributed left and right of the harmonic of interest. Based on the local polynomial approximation, an estimate of the transient at the excited harmonic is computed (sections 2.4.3.1 to 2.4.3.3).

Removing the estimated transient term from Y_{exc} results in the input- and output DFT spectrum sample mean $\hat{Y}(kP)$ (section 2.4.3.4). While the polynomial fit contains the smooth signal part, the residuals contain the wildly varying part. As the varying part is noise, an estimate of the noise covariance matrix can be computed from them (section 2.4.3.5). The estimation algorithm can be applied to the input- *and* output DFT spectrum; if the

[16] An alternative approach to estimate T_G is part of the arbitrary local polynomial method, that is shortly discussed in section 2.5.9.1. It puts restrictions on the excitation signal U, so that GU varies wildly over frequency and T_G is the only smooth function of frequency.

signals contain no transients or noise, the estimation will return the unchanged signals. For convenience both spectra may be stacked on top of each other to form a single variable $Z(k)$ with

$$Z(k) = \begin{bmatrix} Y^{[:]}(k) \\ U^{[:]}(k) \end{bmatrix} \tag{2.98}$$

2.4.3.1 LOCAL POLYNOMIAL APPROXIMATION

The signal Z is locally approximated with polynomials of degree R. The polynomials approximate the signal as function of frequency in the vicinity of each excited frequency. At each excited frequency kP, a separate polynomial is created. The general ansatz has the shape

$$Y(k + r_i) = \Theta_0 \cdot (r_i)^0 + \Theta_1 \cdot (r_i)^1 + \Theta_2 \cdot (r_i)^2 + \cdots + \Theta_{R+1} \cdot (r_i)^{R+1} \tag{2.99}$$

where the numbers r_i, $i = 1,2, \dots, n$ are the first n elements of the set $\mathbb{Z}^+ \setminus \{kP | k \in \mathbb{Z}^+\}$, i.e. the neighbouring, non-excited harmonics next to kP.

Figure 2-13 shows a schematic of the polynomial approximation with eight supporting points (i.e. $n = 4$) symmetrically distributed around kP (indicated by the gray arrow) and with three periods of data ($P = 3$). The supporting points are only non-excited harmonics; excited harmonics are left out. The approximated polynomial function is shown as a continuous line (orange), the discrete noise terms as green arrows. In this example the transient term is approximated with a quadratic polynomial with $R = 2$.

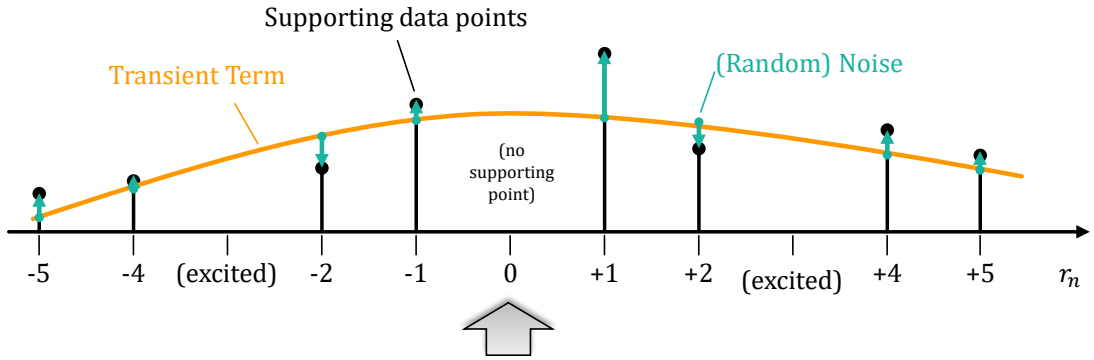

Figure 2-13: Local polynomial approximation of transient term and noise. The supporting data points are only non-excited frequencies; data at excited harmonics (here -3, 0 and 3) is not used.

The polynomial approximation is applied to every signal in Z. Each element of $Z(k)$ is approximated by a polynomial and the polynomial ansatz can be written in matrix form as

$$Z_n = \hat{\Theta}\, K_n \tag{2.100}$$

where Z_n contains the DFT coefficients of the input and output signals from the $2n$ neighboring non-excited harmonics next to kP, distributed around k

$$Z_n = [Z(kP - r_n),\ \dots, Z(kP - r_1), Z(kP + r_1), \dots, Z(kP + r_n)] \tag{2.101}$$

The matrix K_n contains the polynomial basis vectors for all frequencies

$$K_n = [K(kP - r_n),\ \dots, K(kP - r_1), K(kP + r_1), \dots, K(kP + r_n)] \tag{2.102}$$

where $K(kP \pm r_n)$ is defined as

$$K(kP \pm r_i) = \begin{bmatrix} 1 \\ (\pm r_i) \\ \vdots \\ (\pm r_i)^R \end{bmatrix} \tag{2.103}$$

Hence Z_n is a $(n_{out} + n_{in}) \times 2n$ matrix, $\widehat{\Theta}$ is of dimension $(n_{in} + n_{out}) \times (R+1)$ and the size of K_n is $(R+1) \times 2n$.

The value of n is selected depending on the number of estimated variables and the degrees of freedom of the noise covariance estimate, see section 2.4.3.5. For a system with two inputs, three outputs, approximated with 2nd order polynomials ($R = 2$), the matrices Z_n, K_n and Θ have the following shape:

$$Z_n = \begin{bmatrix} Y_1(-n), & \dots, & Y_1(-1), & Y_1(1), & \dots, & Y_1(+n) \\ Y_2(-n), & \dots, & Y_2(-1), & Y_2(1), & \dots, & Y_2(+n) \\ Y_3(-n), & \dots, & Y_3(-1), & Y_3(1), & \dots, & Y_3(+n) \\ U_1(-n), & \dots, & U_1(-1), & U_1(1), & \dots, & U_1(+n) \\ U_2(-n), & \dots, & U_2(-1), & U_2(1), & \dots, & U_2(+n) \end{bmatrix} \tag{2.104}$$

$$K_n = \begin{bmatrix} 1 & 1 & \dots & 1 & 1 & \dots & 1 & 1 \\ (-r_n)^1 & (-r_{n+1})^1 & \dots & (-1)^1 & (1)^1 & \dots & (r_{n-1})^1 & (r_n)^1 \\ (-r_n)^2 & (-r_{n+1})^2 & \dots & (-1)^2 & (1)^2 & \dots & (r_{n-1})^2 & (r_n)^2 \end{bmatrix} \tag{2.105}$$

$$\Theta = \begin{bmatrix} \Theta_{y_1,g_0} & \Theta_{y_1,g_1} & \Theta_{y_1,g_2} \\ \Theta_{y_2,g_0} & \Theta_{y_2,g_1} & \Theta_{y_2,g_2} \\ \Theta_{y_3,g_0} & \Theta_{y_3,g_1} & \Theta_{y_3,g_2} \\ \Theta_{u_1,g_0} & \Theta_{u_1,g_1} & \Theta_{u_1,g_2} \\ \Theta_{u_2,g_0} & \Theta_{u_2,g_1} & \Theta_{u_2,g_2} \end{bmatrix} \tag{2.106}$$

2.4.3.2 Border Effect

At the boundaries of the excited frequency range it may not be possible to select the non-excited frequencies symmetrically around kP, (e.g. as r_i is larger than kP). In this case r_i is shifted by p harmonics, resulting in

$$\tilde{r}_i = r_i + p, \qquad i = 1,2,\dots,n \tag{2.107}$$

The border effect increases the variance of the estimate $\widehat{\Theta}$. Accordingly, the variance increase is in the order of magnitude of

$$\frac{\hat{\sigma}^2_{border}}{\hat{\sigma}^2} \approx \mathcal{O}\left(\frac{n + |p|}{n}\right)^{R+1} \tag{2.108}$$

where R is the order of the estimated polynomials. The maximum effect is in the order of 2^{R+1} for the first and last DFT frequency (Pintelon & Schoukens, 2012, p. 233).

2.4.3.3 Least Squares Solution

Equation (2.100) is solved for $\widehat{\Theta}$ in the least squares sense.

$$\hat{\Theta} = Z_n K_n^H (K_n K_n^H)^{-1} \tag{2.109}$$

The first column of $\widehat{\Theta}$ contains the polynomials' constant terms; they are estimates of the transient term $\hat{T}_Z$ at kP.

$$\hat{T}_Z(j\omega_{kP}) = \hat{\Theta}_{[:,1]} \tag{2.110}$$

With equation (2.110) an estimate of the transient term can be computed for every excited frequency.

The polynomial interpolation is repeated for each excited frequency. From Figure 2-13 it becomes clear, that in general the interpolation range of neighboured excited frequencies will overlap; as a result, the estimates $\hat{\theta}$ at neightboring frequencies (e.g. at kP and $(k+1)P$) are correlated.

2.4.3.4 *Input- & Output DFT Spectrum Sample Mean*

Removing the transient term estimate $\hat{T}_Z$ from the input and output DFT spectra results in the sample mean of the input-output spectra over P periods (cmp. Pintelon & Schoukens, 2012, p. 251).

$$\hat{Z}(kP) = Z(kP) - \hat{T}_Z(j\omega_{kP}) \tag{2.111}$$

2.4.3.5 *Noise Covariance Estimate*

The sample noise covariance $\hat{C}_Z^{noise}(kP)$ estimate at the excited harmonics is computed from $\widehat{\Theta}$ as

$$\hat{C}_Z^{noise}(kP) = \frac{1}{q^{noise}}\left(Z_n - \widehat{\Theta}K_n\right)\left(Z_n - \widehat{\Theta}K_n\right)^H \tag{2.112}$$

with

$$q^{noise} = 2n - (R+1) \tag{2.113}$$

the number of degrees of freedom of the least squares residuals, where $2n$ denotes the number of data lines used for the estimation and R the order of the polynomial. It is noted that equation (2.112) assumes the true noise covariance matrix being constant over the frequency range of the local polynomial. If this assumption does not hold, the covariance estimate can be biased.

In equation (2.111), the sample mean $\hat{Z}$ is computed by subtraction of $\hat{T}_Z$ from Z, where $\hat{T}_Z$ is an estimate of the true T_Z based on noisy data. Thus, it also contains a noise contribution, that is (inadvertently) subtracted from Z. Thus, the sample covariance $\hat{C}_{\hat{Z}}^{noise}$ of the sample mean is slightly larger than $\hat{C}_Z^{noise}$. As derived in (Pintelon & Schoukens, 2012, pp. 274–275), their relation is given by

$$\hat{C}_{\hat{Z}}^{noise}(kP) = \mu_{poly}\hat{C}_Z^{noise}(kP) \tag{2.114}$$

with

$$\mu_{poly} = 1 + \left\|\Sigma_K^{-1}V_{K[1,:]}^H\right\|_2^2 \tag{2.115}$$

where $\|x\|_2$ indicates the 2-norm of x, $x_{[1,:]}$ denotes the first row of x and $U_K\Sigma_K V_K^H$ is the singular value decomposition of K_n^H. The factor μ_{poly} quantifies the increase in noise variance of the sample mean $\hat{Z}(kP)$ with respect to the uncorrected DFT spectrum $Z(kP)$ (Pintelon & Schoukens, 2012, pp. 250–251).

The degrees of freedom of the sample noise covariance matrices are set by q^{noise}. To ensure that $\hat{C}_{\hat{Z}}^{noise}(kP)$ has the same rank as the true noise covariance $C_Z^{noise}(kP)$, the condition $q^{noise} \geq n_{out} + n_{in}$ must be fulfilled, i.e. q^{noise} (and hence the degrees of freedom of $\hat{C}_Z^{noise}(kP)$) must be equal or larger to the sum of input and output signals. In any case $P = 2$ periods of data are sufficient for the estimation (Pintelon & Schoukens, 2012, p. 252).

2.4.4 Summary

In this section, it was shown the DFT spectrum from multiple periods of periodic data can be split in two sets of excited and non-excited harmonics. The non-excited harmonics contain only noise and the transient term and is used to estimate the transient term and the noise covariance at the excited harmonics.

This is achieved by a local polynomial approximation of the transient term, based on non-excited harmonics only. As the transient term is a smooth function over frequency, it is closely approximated by the polynomials. Whereas noise is a random function over frequency and amounts to the residuals. As noted before, it is implicitly assumed that the noise covariance is constant over the frequency range of the local polynomials, eventually leading to biased covariance estimates, if the assumption does not hold.

The transient term describes the effect of the initial and final conditions on the DFT spectra. After removing the transient term, only the periodic components remain in the spectra $\hat{Z}$, cmp. equation (2.111). Thus FRF estimates based on $\hat{Z}$ are not affected by non-zero initial- and final conditions.

2.5 Local Polynomial Methods

In section 2.4, a method for the estimation of the transient part in input- and output DFT spectra with local polynomials was introduced. The algorithm is based on input and output data of at least two periods of a periodic excitation signal. After removing the transient part (e.g. due to non-zero initial or final conditions) from the input- and output DFT spectra, the remaining signals are periodic; for single input systems, the frequency response function $\hat{G}_{yu}$ can then be estimated directly from $\hat{Z}(kP)$ (computed in eq. (2.111)) with the ETFE (eq. (2.9)). This algorithm is called *transient local polynomial method* (Monteyne et al., 2012) and is described in section 2.5.1.

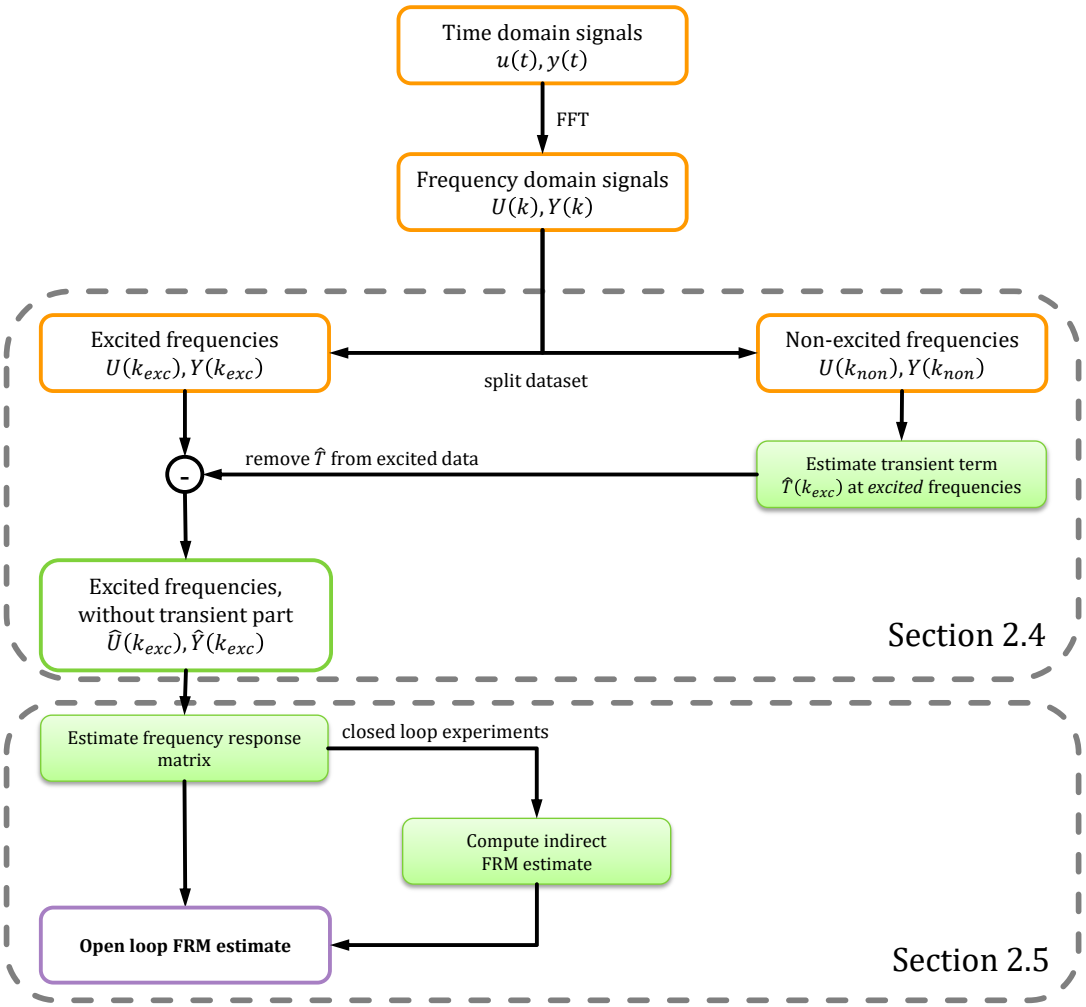

Figure 2-14: Schematic workflow of the fast local polynomial method.

For multiple input systems, the ETFE, and thus also the transient LPM, is underdetermined. Classical approaches for MIMO systems require multiple experiments (Bendat & Piersol, 1971/2010; Tischler & Remple, 2006) or are based on zippered multisines (Morelli, 2003), resulting in reduced frequency resolution for the individual input-/output pairs. To overcome these limitations, (Pintelon et al., 2010a, 2010b) proposed to approximate the FRF with local polynomials. The resulting algorithm is called *fast local polynomial method* (fast LPM); its algorithm is described in section 2.5.2 and 2.5.3. The fast LPM is closely related to the estimation of the transient term and estimates the MIMO response with full frequency resolution from the set of *excited* frequencies; Figure 2-14 shows the schematic workflow of the fast LPM; the parts of the algorithm that are introduced in section 2.4 and 2.5 are highlighted. Equation (2.82) shows that the transient term has the same poles as the system; hence the system dynamics can be modelled with local polynomial approximations of similar order as the transient term (Pintelon & Schoukens, 2012, pp. 258–263).Figure 2-12As transient effects can be removed in advance, the both algorithms can be applied to data that contains transient components. This includes e.g. the first two periods of a periodic excitation signal that often need to be removed when classical FRF estimation algorithms are applied (Bailey & Markofski, 2001).

Figure 2-15 shows the block diagram of a typical closed loop estimation model structure with linear plant, controller and actuator that drives the system. The respective signals are: reference excitation signal $r(t)$, plant input $u_1(t)$, plant output $y_1(t)$, generator noise $v_g(t)$, process noise $v_p(t)$, measurement noise of the input $v_u(t)$ and measurement noise of the output $v_y(t)$. The open loop transfer function of the plant is thus given by

$$G_{yu}(j\omega_k) = \frac{Y(k)}{U(k)} - \frac{V(k)}{U(k)} \tag{2.116}$$

The general task of the identification algorithm is to find an open loop plant dynamics estimate $\hat{G}_{yu}$ and its sample covariance estimate $\hat{C}_{vec(\hat{G})}$. The noise covariance $\hat{C}_{\hat{Z}}$ of the input and output signals and the transient term $\hat{T}$ are estimated in advance as shown in section 2.4, based on non-excited frequencies.

The estimate can either be based on open loop or closed loop experiments. In the latter case, consistent estimates can be computed with the indirect estimate (section 2.5.6).

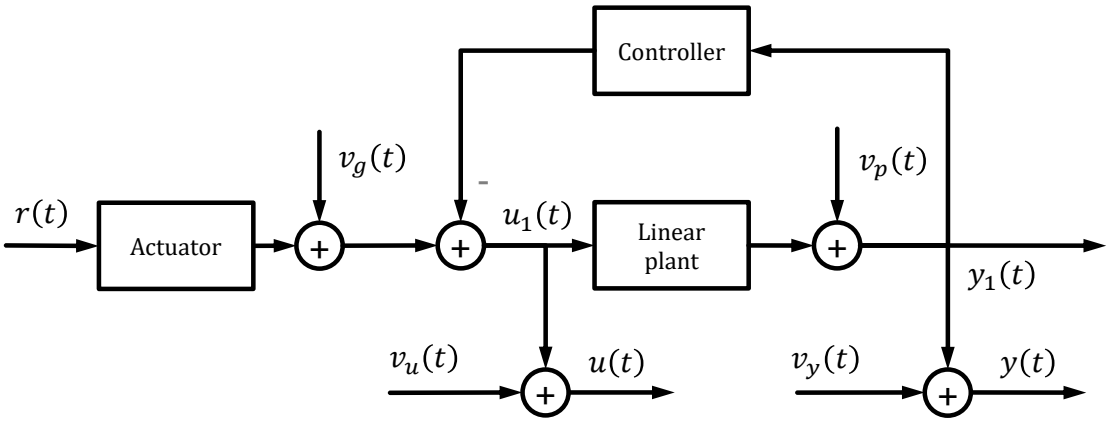

Figure 2-15: Block diagram of the estimated system.

2.5.1 Single Input Frequency Response Function Estimates

For single input systems, $\hat{G}_{yu}$ can be directly estimated from (2.116) with sample input-/output DFT spectra $\hat{U}$, $\hat{Y}$ from section 2.4. The resulting algorithm is called transient local polynomial method (transient LPM or tLPM) (Monteyne et al., 2012). It is a straight forward extension of the ETFE with the estimation of the transient term introduced in sections 2.3 and 2.4.

2.5.1.1 Transient Local Polynomial Method

The transient LPM is based on multiple periods of the input-/output data of an LTI system to a periodic excitation signal. In the first step, the transient part in the input and output spectra $U(k), Y(k)$ is estimated and removed as described in sections 2.3 and 2.4. Thus the transient signal parts are removed and the system need not be operated in steady state.

After the transient term is removed, the remaining sample spectra $\hat{U}(k), \hat{Y}(k)$ contain only the periodic components. Thus the FRF can be estimated directly from $\hat{U}(k), \hat{Y}(k)$ without being affected by non-zero initial and final conditions:

$$\hat{G}_{tLPM}(j\omega_k) = \frac{\hat{Y}_{DFT}(k)}{\hat{U}_{DFT}(k)} \tag{2.117}$$

Equation (2.117) is identical to the ETFE introduced in equation (2.33). It thus has the same statistical properties.

2.5.1.2 Effect of Noise

The effect of noise on the ETFE has been discussed already in section 2.2.6; it is summarized here for the output error model (OE). As shown in (Monteyne et al., 2012), the sample noise covariance $\hat{C}_{\hat{G}_{tLPM}}(k)$ of $\hat{G}_{tLPM}(j\omega_k)$ is given for the output error model as

$$\hat{C}_{\hat{G}_{tLPM}}(k) = \frac{\hat{C}_Z^{noise}(k)}{|U(k)|^2} \tag{2.118}$$

where $\hat{C}_Z^{noise}$ is the estimated noise covariance from equation (2.112) that is computed during the estimation of the transient term and $U(k)$ the undisturbed excitation signal. The sample covariance $\hat{C}_{\hat{G}_{tLPM}}$ is based on the residuals of the local polynomial fit of the transient term. As a consequence, the noise covariance estimate $\hat{C}_{\hat{G}_{tLPM}}$ is correlated over frequency.

2.5.1.3 Summary

The transient LPM is an extension of the ETFE. It has the advantage that it gives unbiased results from periodic input data, even if data from the first two periods are used. In principle, two periods are sufficient for the estimation; additional periods help to reduce the effect of noise. For the estimation of the transient term, it is assumed that the transient term is a smooth function of frequency and can be approximated with local polynomial functions[17]. As for the ETFE, the estimation of multiple input systems requires multiple independent experiments. The transient LPM computes the FRF estimates for each frequency independently; no averaging or smoothing over adjacent frequencies is applied.

When compared to the fast LPM introduced in section 2.5.2, this has the advantage, that the transient LPM does not suffer from a bias at lightly damped poles (Monteyne et al., 2012).

[17] This basically means that the frequency resolution must be fine enough that the polynomials follow the shape of the transient term.

2.5.2 Multiple Input Estimates

For multiple input systems the direct estimation of the frequency response matrix from a single experiment is not possible. This can be seen from the dimensions of the respective signals:

$$\underbrace{Y(k)}_{[n_{out}\times 1]} = \underbrace{G(j\omega_k)}_{[n_{out}\times n_{in}]}\ \underbrace{U(k)}_{[n_{in}\times 1]} \tag{2.119}$$

For MIMO systems $\hat{G}_{yu}$ is of dimension $n_{out} \times n_{in}$, and contains $n_{out} \cdot n_{in}$ unknown variables. Equation (2.119) however provides only n_{out} independent equations. Hence it becomes obvious, that with a single experiment, equation (2.119) is underdetermined and additional information (usually independent repeated experiments) is required to result in a well determined set of equations.

The fast local polynomial method circumvents this problem by including additional *frequencies*. To do so, the systematic change of $G(j\omega_k)$ over frequency is modelled with local polynomials. Each polynomial is supported by $2n_E + 1$ frequencies. As the number of polynomial parameters is smaller than $2n_E + 1$, a proper choice of n_E assures that the

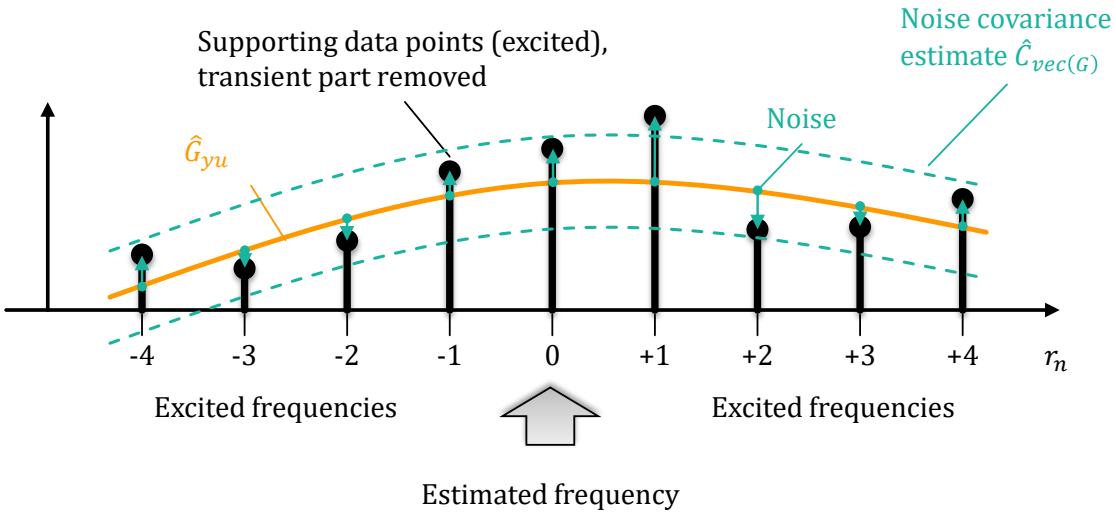

Figure 2-16: Local polynomial approximation of FRF.

resulting set of equations is well determined. The general shape of the local polynomial approximation around $G(j\omega_k)$ is

$$G(r) = \Psi_0 \cdot (r)^0 + \Psi_1 \cdot (r)^1 + \cdots + \Psi_R \cdot (r)^R \tag{2.120}$$

where $G(r)$ is the transfer function, $\Psi_g,\ g \in \{0, 1, \ldots, R\}$ the polynomials coefficients and r the distance from the center frequency $j\omega_k$. Inserting the polynomial approximation in the input-/output relation (2.119) results in [18]

$$\begin{aligned} Y(k+r) = {} & \Psi_0 \cdot (r)^0 \cdot U(k+r) + \Psi_1 \cdot (r)^1 \cdot U(k+r) + \cdots \\ & + \Psi_R \cdot (r)^R \cdot U(k+r) \end{aligned} \tag{2.121}$$

The polynomial approximation of G_{yu} thus follows the same algorithm used for the estimation of the transient term in section 2.4.3. It is based on equation (2.122), where the

[18] Following the nomenclature rules, the frequency index $(j\omega_k)$ used for systems is now replaced by the frequency index (k) for signals.

first term $\frac{Y(k)}{U(k)}$ is a smooth function of frequency and is approximated around the discrete frequency k with local polynomials with the general shape

$$G_{yu}(j\omega_k) = \frac{Y(k)}{U(k)} - \frac{V(k)}{U(k)} \tag{2.122}$$

The noise contribution $\frac{V(k)}{U(k)}$ varies wildly with frequency; its estimate is based on the residuals of the local polynomial approximation. The polynomials supporting points are excited frequencies only. In matrix form, the polynomials are defined as

$$Y_{n_E} = \widehat{\Psi} L_{n_E} \tag{2.123}$$

where Y_{n_E} contains the output DFT spectra at the supporting points, $\widehat{\Psi}$ contains the polynomial coefficients and L_{n_E} combines the structure of the polynomials and the input DFT spectra at the supporting points.

In detail, the matrices are defined as

$$Y_{n_E} = \left[Y\left((k - r_{n_E})P\right), \dots, Y(kP), \dots, Y\left((k + r_{n_E})P\right)\right] \tag{2.124}$$

$$L_{n_E} = \left[L\left((k - r_{n_E})P\right), \dots, L(kP), \dots, L\left((k + r_{n_E})P\right)\right] \tag{2.125}$$

with

$$L\big((k \pm r_i)P\big) = \begin{bmatrix} 1 \\ (\pm r_i) \\ (\pm r_i)^2 \\ \vdots \\ (\pm r_i)^R \end{bmatrix} \otimes U\big((k \pm r_i)P\big) \tag{2.126}$$

where $Y\left((k \pm r_{n_E})P\right)$ and $U\left((k \pm r_{n_E})P\right)$ are the DFT coefficients of the output- and input spectra at the excited harmonics. The harmonics $(k \pm r_{n_E})P$ refer to the entire data set of P periods and are chosen such that $kP \pm r_i = 1,2, \dots, n_E$ are the next neighbouring excited harmonics of $U^{[:]}$; finally $\otimes$ denotes the Kronecker matrix product.

If follows that Y_{n_E} is a $(n_{out}) \times (2n_E + 1)$ matrix, L_{n_E} is $(R+1)n_{in} \times (2n_E + 1)$ and $\widehat{\Psi}$ is of dimension $(n_{out}) \times (R+1)n_{in}$, cmp. (Pintelon & Schoukens, 2012, p. 258).

The number n_E of supporting data points around kP is selected such that the least squares problem is well determined and its residuals have sufficient degrees of freedom. A lower bound for n_E is given in (Pintelon & Schoukens, 2012) by

$$n_E \geq \text{ceil}\left(\frac{1}{2} \cdot \{(n_{out} + m) + (R+1)\big(n_{in} + n_{in,add}\big) - 1\}\right) \tag{2.127}$$

where n_{in} and n_{out} are the number of input and output signals, R the plynomials order and ceil$(\cdot)$ the ceiling function; $n_{in,add}$ is one, if the transient term has not been removed before and is estimated together with $\hat{G}_{yu}$ and zero otherwise, which is usually the case.[19] The value of m affects the degrees of freedom of the covariance matrix $\hat{C}_{\hat{G}}$ estimate and can be set by the user as required: for $m = 1$ the inverse $\hat{C}_{\hat{G}}^{-1}$ of the DFT sample total covariance matrix estimate exists; for $m = 2$ also $\hat{C}_{\hat{G}}^{-2}$ exists; if neither is needed, m can be set to zero, reducing

[19] Pintelon and Schoukens (2012) show that it is possible to estimate the transient term together with $\hat{G}_{yu}$, by including additional terms in Ψ and L_{n_E}. In this thesis however the estimation is always based on at least two periods and thus the transient term can be removed in advance.

the local polynomial frequency range. The same conditions apply for the existence of the inverses of $\hat{C}_{vec(\hat{G})}$ (Pintelon & Schoukens, 2012, pp. 232, 253-260).

For a system with two inputs, three outputs, approximated with 2nd order polynomials ($R = 2$), the matrices Y_{n_E}, L_{n_E} and $\widehat{\Psi}$ have the following shape:

$$Y_{n_E} = \begin{bmatrix} Y_1(-n_E), & \dots, & Y_1(0), & \dots, & Y_1(+n_E) \\ Y_2(-n_E), & \dots, & Y_2(0), & \dots, & Y_2(+n_E) \\ Y_3(-n_E), & \dots, & Y_3(0), & \dots, & Y_3(+n_E) \end{bmatrix} \tag{2.128}$$

$$L_{n_E} = \begin{bmatrix} 1 \cdot U_1(-n_E) & 1 \cdot U_1(-n_E+1) & \dots & 1 \cdot U_1(n_E) \\ 1 \cdot U_2(-n_E) & 1 \cdot U_2(-n_E+1) & \dots & 1 \cdot U_2(n_E) \\ (-n)^1 \cdot U_1(-n_E) & (-n+1)^1 \cdot U_1(-n_E+1) & \dots & (n)^1 \cdot U_1(n_E) \\ (-n)^1 \cdot U_2(-n_E) & (-n+1)^1 \cdot U_2(-n_E+1) & \dots & (n)^1 \cdot U_2(n_E) \\ (-n)^2 \cdot U_1(-n_E) & (-n+1)^2 \cdot U_1(-n_E+1) & \dots & (n)^2 \cdot U_1(n_E) \\ (-n)^2 \cdot U_2(-n_E) & (-n+1)^2 \cdot U_2(-n_E+1) & \dots & (n)^2 \cdot U_2(n_E) \end{bmatrix} \tag{2.129}$$

$$\Psi = \begin{bmatrix} \Psi_{Y_1,g_0,U_1} & \Psi_{Y_1,g_0,U_2} & \Psi_{Y_1,g_1,U_1} & \Psi_{Y_1,g_1,U_2} & \Psi_{Y_1,g_2,U_1} & \Psi_{Y_1,g_2,U_2} \\ \Psi_{Y_2,g_0,U_1} & \Psi_{Y_2,g_0,U_2} & \Psi_{Y_2,g_1,U_1} & \Psi_{Y_2,g_1,U_2} & \Psi_{Y_2,g_2,U_1} & \Psi_{Y_2,g_2,U_2} \\ \Psi_{Y_3,g_0,U_1} & \Psi_{Y_3,g_0,U_2} & \Psi_{Y_3,g_1,U_1} & \Psi_{Y_3,g_1,U_2} & \Psi_{Y_3,g_2,U_1} & \Psi_{Y_3,g_2,U_2} \end{bmatrix} \tag{2.130}$$

where U_a, Y_b denote the DFT coefficients of the a'th input and b'th output channel respectively; Ψ_{Y_a,g_c,U_b} is the g_c'th coefficient of the polynomial of the transfer function that relates the input U_b to the output Y_b.

For a three by two system (3 outputs, 2 inputs), this results in 18 unknown parameters. If the covariance is not estimated ($m = 0$), the number of supporting points is at least four ($n_E \geq 4$), cmp. (2.127). If the covariance is estimated, too, $n_E \geq 5$ and Y_{n_E} is at least of dimension 3×11, L_{n_E} is 6×11 and Ψ_{n_E} a 3×6 matrix.

2.5.3 Least Squares Solution

Provided that n_E is chosen large enough, equation (2.123) is overdetermined and can be solved for $\widehat{\Psi}$ in a least squares sense.

$$\widehat{\Psi} = \hat{Y}_{n_E} L_{n_E}^H \left(L_{n_E} L_{n_E}^H \right)^{-1} \tag{2.131}$$

For the reliable estimation, $L_{n_E} L_{n_E}^H$ must have full rank; this is the case if the input signals $U_i(k)$, $i = 1, \dots, n_{in}$ are uncorrelated[20]. The first n_{in} columns of $\widehat{\Psi}$ contain the polynomials' constant terms. They are the estimates of the FRF at kP.

$$\hat{G}_{yu}(j\omega_{kP}) = \widehat{\Psi}_{[:,1:n_{in}]} \tag{2.132}$$

Due to the local interpolation, estimates of $\hat{G}$ at adjacent frequencies are correlated. The correlation length is measured in excited frequency bins and equals $n_E + 1$.

2.5.4 Bias Error of $\widehat{G}_{YU}$

In (Pintelon & Schoukens, 2012) possible bias errors in LPM estimates are analysed. The following sources for bias errors are studied:

- noisy input, noisy output case
- estimation errors in $\hat{T}_G$

[20] For multisine inputs (section 3.2.5) the correlation of the phase angles can be tested with the circular correlation coefficient.

- non-steady state conditions
- polynomial interpolation errors

Noisy input, noisy output case: Analogously to the ETFE, the LPM estimate can be biased, when the input signal is noisy or depends on process noise due to a feedback loop. The bias can be avoided when an indirect estimate is computed, cmp. sections 2.2.6.3, 2.5.6 and (Pintelon & Schoukens, 2012).

Estimation errors in $\hat{T}_G$: The estimate $\hat{T}_G$ that is removed from the signals can be errorneous, resulting in the residual system leakage error. For *steady-state responses* to periodic signals, the residual system leakage error is zero (cmp. section 2.3.5.2). For *non-steady state conditions* an estimation error remains. It vanishes asymptotically for $PN \to \infty$, i.e. for infinite long measurements with infinite fine frequency resolution (Pintelon & Schoukens, 2012, p. 278). For finite length measurements, it results in the plant leakage error, that introduces a bias in $\hat{G}_{yu}$; for the fast LPM used in this thesis, the plant leakage bias can be neglected with respect to the polynomial interpolation error. (Pintelon & Schoukens, 2012, p. 260)

Polynomial interpolation errors: Around lightly damped poles, the fitted polynomials cannot accurately follow the true frequency response function. This results in an interpolation error, that can be the main systematic error source. In (Pintelon & Schoukens, 2012, p. 260) it is shown that this is the case when the signal-to-noise ratios are larger than 10 dB. In this section, the polynomial interpolation error is discussed in more detail.

2.5.4.1 Polynomial Interpolation Bias

In the frequency range around lightly damped poles and zeros, the polynomial fit cannot follow the variation of FRF over frequency. This is due to the large curvature of the true (rational) frequency response function that occurs at the resonance peaks. As shown in (Schoukens, Vandersteen, Pintelon, Emedji, & Rolain, 2012), the maximum interpolation error occurs at resonance peaks, i.e. at complex pole pairs of the transfer function.

The principle of the interpolation error is illustrated in Figure 2-17: It shows the $\pm$3dB region around the resonance peak of a lightly damped PT2-system (blue, solid line) with eigenfrequency ω_0 and damping ζ[21]. Within the 3dB frequency range, the magnitude $|G(j\omega)|$ is larger than approximately $0.708 \cdot |G(j\omega_N)|$, i.e. the magnitude drops by about 30% from its peak value.

The FRF is approximated with a second order polynomial (orange, dashed line), based on 7 supporting points in the range of $0.8\,B_{3dB}$, where $B_{3dB} \approx 2\zeta\omega_0$. The fitting range is indicated by bold lines. At frequency ω_N, the magnitude of the polynomial fit is 0.989 instead of the true value of 1. This error of about 1.1% (or equivalently -0.097 dB) is the polynomial interpolation bias.

The polynomial interpolation bias is a consequence of the large curvature of the frequency response function. It is thus expected, that the interpolation error is largest in the frequency regions of the FRF that have largest curvature – thus at the resonance peak.

In the following subsections, upper bounds for the estimation error are analysed. The numerical examples are based on polynomial fits on a perfectly known system.

[21] Lightly damped PT2 system peak at $\omega_n = \omega_0\sqrt{1-\zeta^2}$. The 3dB frequency range is given approximately by $\pm\zeta\omega_0$

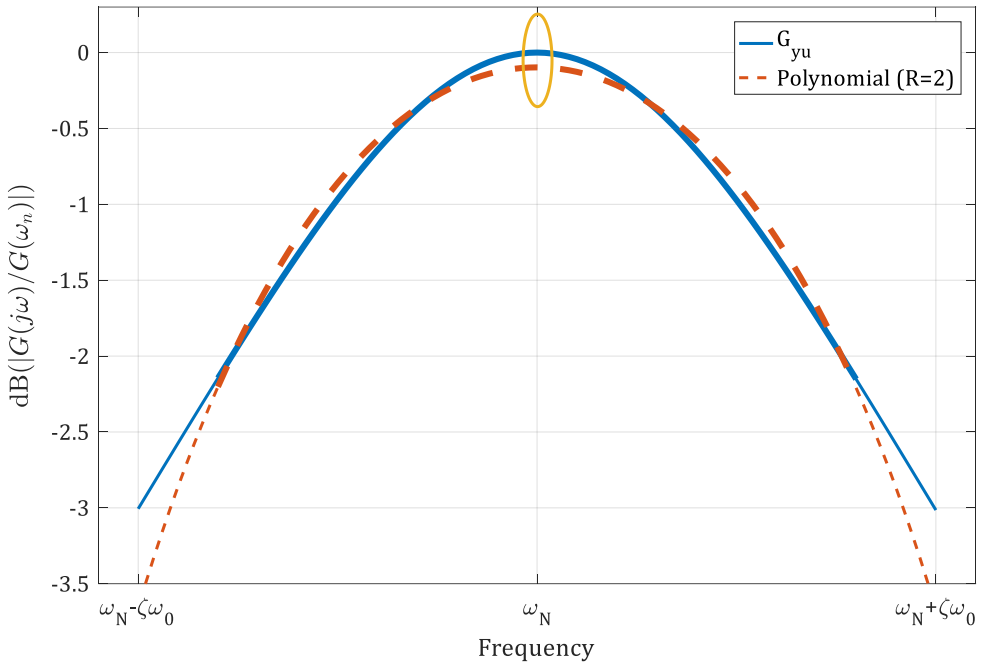

Figure 2-17: Polynomial interpolation error for lightly damped systems: In the vicinity of lightly damped poles, the polynomial fit (dashed) cannot follow the curvature of the true system (solid). This results in the polynomial interpolation error. The maximum interpolation error is observed directly at the highlighted resonance peak and is highlighted.

2.5.4.2 Maximum Polynomial Interpolation Bias

A detailed analysis of the maximum interpolation error introduced by the local polynomial approximation of a PT2-system is found in (Schoukens et al., 2012). The study is based on a partial fraction decomposition of a normalized PT2-transfer function.

The paper shows that the maximum interpolation error occurs at the natural frequency $\omega_N = \omega_0\sqrt{1-\zeta^2}$.[22] For (very) lightly damped poles, the square root is close to one ($\sqrt{1-\zeta^2} \approx 1$) and the resonance frequency approximately equals the eigenfrequency ($\omega_N \approx \omega_0$).

Schoukens et al. show that for lightly damped poles ($\zeta < 0.25$) the interpolation error is governed by the polynomial degree R, and depends on the damping ζ and eigenfrequency ω_0 of the pole. At frequency ω_0 only the *imaginary* part of G_{yu} affects the bias, while its real part has no effect due to symmetry considerations. For this case (PT2-system at resonance peak), the maximum interpolation error b_{int} can be computed analytically from a Taylor series expansion of the transfer function: The local polynomial approximation of order R covers all contributions up to the R'th order. The interpolation error is then governed by the next higher order term $R+1$.

The PT2-frequency response around its resonance peak is approximately an even function. As a consequence, the increase in accuracy when changing the order from $R = 2$ to $R = 3$ is only small, compared to the increase from $R = 3$ to $R = 4$. This has two consequences:

- The further analysis is limited to even R's.
- The interpolation error is practically governed by the second higher order term, i.e by the $R + 2$ term.

[22] Note on nomenclature: In the original paper, the resonance frequency is denoted with ω_n (which corresponds to ω_0 in this thesis).

According to (Schoukens et al., 2012), the interpolation bias is thus limited by

$$\begin{aligned}\tilde{b}_{int} &= \tilde{\alpha}_{R+2}\left(\frac{B_{lpm}}{B_{3dB}}\right)^{R+2}\mathrm{Im}\big(G(\omega_0)\big)\\ &= \tilde{\alpha}_{R+2}\left(\frac{2n_e\cdot\Delta f_{exc}}{2\zeta\omega_0}\right)^{R+2}\mathrm{Im}\big(G(\omega_0)\big)\end{aligned} \tag{2.133}$$

where $B_{lpm} = (2n_e + 1)\cdot\Delta f_{exc}$ is the frequency range of the polynomial fit; $(2n_e + 1)$ is the number of supporting points in the polynomial estimate, with n_e following equation (2.127), and Δf_{exc} is the frequency spacing between excited frequencies, R the polynomial order, $B_{3dB} = 2\zeta\omega_0$ is the approximate 3-dB frequency range of the PT2-system and $\mathrm{Im}\big(G(\omega_0)\big) = |G_{max}|$ its peak magnitude (Schoukens et al., 2012). For the PT2-system considered by Schoukens et al., $\mathrm{Im}\big(G(\omega_0)\big) = |G_{max}|$ and (2.133) can be rewritten as

$$\begin{aligned}\tilde{b}_{int} &= \tilde{\alpha}_{R+2}\left(\frac{B_{lpm}}{B_{3dB}}\right)^{R+2}|G_{max}|\\ &= \tilde{\alpha}_{R+2}\left(\frac{(2n_e+1)\cdot\Delta f_{exc}}{2\zeta\omega_0}\right)^{R+2}|G_{max}|,\end{aligned} \tag{2.134}$$

which is the form actually presented in (Pintelon & Schoukens, 2012). The constant factor $\tilde{\alpha}_{R+2}$ is specific for the order R; for its computation only the *imaginary* part $\mathrm{Im}(G)$ is considered:

$$\tilde{\alpha}_{R+2} = \tilde{b}(\omega_0)\left(\frac{B_{lpm}}{B_{3dB}}\right)^{-R-2}\mathrm{Im}\big(G(\omega_0)\big)^{-1} \tag{2.135}$$

Table 2-3 lists numerically computed values for $R = 2, 4, 6$; odd orders are skipped. The numerical approach is shortly described in appendix C.2.

Table 2-3: Values of $\tilde{\alpha}_{R+2}$ for some R.

R	α_{R+2}
2	0.0857
4	$8.65\cdot10^{-6}$
6	$4.86\cdot10^{-9}$

As pointed out by Schoukens et al., equation (2.135) relies on the symmetry and anti-symmetry of the real and imaginary parts. In the following section, this effect is studied with numerical examples.

2.5.4.3 Effect of Non-Symmetric Frequency Distribution

When the supporting points of the polynomial are not symmetric around the resonance peak, the symmetry requirements of equation (2.135) are violated - its effect on the bias (and $\tilde{\alpha}_{R+2}$) is the topic of this subsection.

To study the effect of non-symmetrical supporting points, the interpolation range is shifted by a random number $\delta\omega$ in the range $[-B_{lpm}: B_{lpm}]$; thus, the polynomials are developed in the frequency range $[\omega_N + \delta\omega - B_{lpm} : \omega_N + \delta\omega + B_{lpm}]$, cmp. Figure 2-18.

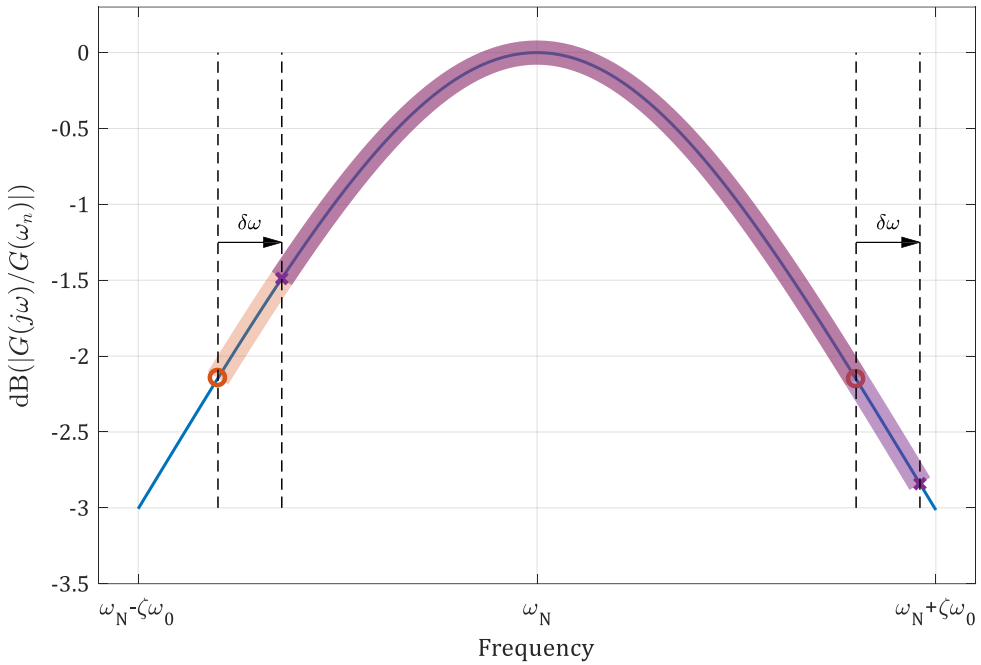

Figure 2-18: Centred (orange) and shifted (violet) interpolation frequency range.

Figure 2-19 shows the resulting $\tilde{\alpha}_{2+2}$ for 500 repeated polynomial fits to PT2 systems with random damping ζ in the range from 0 to 0.8. For each system, 50 different frequency shifts $\delta\omega$ are computed; the results for zero shift ($\delta\omega = 0$) are highlighted. The following observations can be made from Figure 2-19:

a) The coefficient $\tilde{\alpha}_4$ is constant for dampings $0 < \zeta < 0.25$.
b) The coefficient $\tilde{\alpha}_{R+2}$ increases for larger dampings
c) The maximum interpolation error occurs at the resonance peak, i.e. for $\delta\omega = 0$ (these values are highlighted).

All three observations are in accordance with the results presented in (Schoukens et al., 2012)[23], where it is further noted that the increase is related to the neglected influence of the real part of G.

For many applications, the increase of $\tilde{\alpha}$ for well damped systems is irrelevant, as the interpolation bias will be generally smaller for well damped systems, cmp. equation (2.133) where the effect of ζ in the denominator outweighs the increase of $\tilde{\alpha}$ for higher dampings. However, the error statistics of $\hat{G}$ that are analysed in section 2.6 are affected by the bias and the estimate provided by (2.133) will be systematically too small for larger damped systems.

[23] In the paper of Schoukens et al. (2012), the DC-gain is fixed to 1; the peak magnitude G_{max} is thus a function of ζ with $G_{max} = G_{DC}/2\zeta$. Figure 3 of the paper shows the relation E/EG of the true error E and the error estimate EG. It is seen that for $G_{max} \approx$ 6dB (this corresponds to $\zeta = 0.25$), the estimate becomes too small.

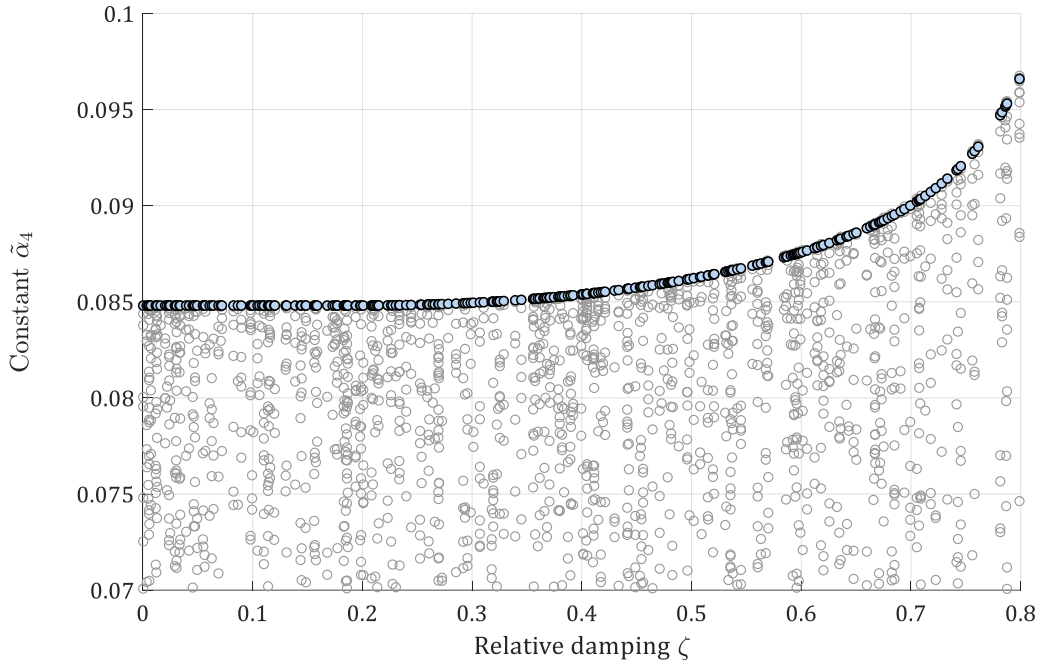

Figure 2-19: Constant $\tilde{\alpha}_4$ for imaginary part of PT2 systems with damping in the range from 0 to 0.8.

2.5.4.4 Magnitude Interpolation Error

The foregoing interpolation error model is heavily based on the symmetry of the real part around the resonance peak. A very similar model, that does *not* rely on this symmetry is given by equations (2.136) and (2.137). It follows the same approach, but the constant term α (without tilde) is defined in a slightly different way:

$$\begin{aligned} b_{int} &= \alpha_{R+2}\left(\frac{B_{lpm}}{B_{3dB}}\right)^{R+2}|G_{max}| \\ &= \alpha_{R+2}\left(\frac{2n_e\cdot\Delta f_{exc}}{2\zeta\omega_0}\right)^{R+2}|G_{max}| \end{aligned} \tag{2.136}$$

with

$$\alpha_{R+2} = b(\omega_0)\left(\frac{B_{lpm}}{B_{3dB}}\right)^{-R-2}|G(\omega_0)|^{-1} \tag{2.137}$$

The difference to the approach shown in (Schoukens et al., 2012) is, that the estimation error magnitude $|b_{int}|$ is modelled, instead of $\mathrm{Im}(b_{int})$. Albeit this is only a small notational change, equation (2.137) models the interpolation error as function of $|G(\omega_0)|$ and thus does not rely on the symmetry of the real part. To distinguish both approaches, b_{int} from equation (2.136) is denoted as interpolation *magnitude* error.

The Monte Carlo simulations from section 2.5.4.3 are repeated with the new error estimate. Figure 2-20 shows the resulting constant α_4 for the interpolation magnitude errors b_{int} computed from 500 simulations with randomized damping ζ from 0 to 0.8 with 50 different $\delta\omega$.

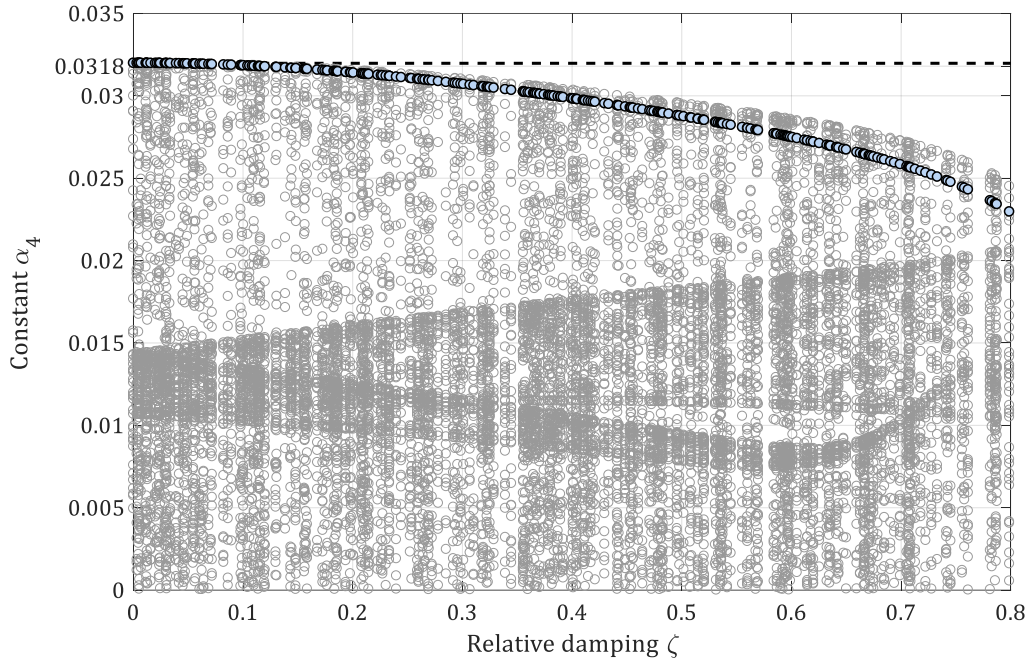

Figure 2-20: Constant α_4 for magnitude of PT2 systems (damping from 0 to 0.8).

As before, the results at the peak frequency ($\delta\omega = 0$) are highlighted. It is seen from Figure 2-20 that…

- α_4 varies with damping.
- Its maximum value is 0.0318.
- The maximum is reached for $\delta\omega = 0$ and $\zeta \to 0$.
- For larger damping coefficients (up to $\zeta = 0.8$), α_4 becomes *smaller*.

Thus, the maximum magnitude interpolation error $|b_{int}|$ is bounded by equation (2.133) with $\alpha_4 = 0.0318$. This maximum interpolation error is valid for $\zeta < 0.8$, which extends the useful range of the estimate to systems with larger damping. It is noted that the 3dB-frequency is always computed as $B_{3dB} = 2\zeta\omega_0$, regardless of the true 3-dB frequency range. For higher order polynomials the resulting values for α_R are found in Table 2-4. Comparing Table 2-3 and Table 2-4 shows a much slower convergence of the error (expressed in the magnitude of α_{R+2}) that is in accordance with the analysis in (Schoukens et al., 2012).

Table 2-4: Values of α_{R+2} for some R.

R	α_{R+2}
2	0.0318
4	$6.67 \cdot 10^{-3}$
6	$1.46 \cdot 10^{-3}$

As an intermediate result it is noted that the interpolation bias b_{int} *can* be estimated. For lightly damped systems ($\zeta < 0.25$) Schoukens et al. give an upper bound, that is based on symmetry consideration.

- It is shown in section 2.5.4.2 that the newly introduced bound holds also if the interpolation range is not symmetric around ω_n.
- For damping coefficients $0.25 < \zeta < 0.8$ the formula by Schoukens et al. can result in too small results.

- A new estimate in terms of magnitude is introduced in section 2.5.4.4.
- It is shown that this alternative estimate gives reliable interpolation bias estimates also for $\zeta < 0.8$, thus extending the validity of the estimate to systems with more damping.
- It is shown that the scale factors α differ for both approaches. Numerical values are presented for selected polynomial orders and it is seen that the magnitude based estimation formula converges considerably slower. As a consequence, also the asymptotic estimates for $\zeta \to 0$ differ (the estimate by Schoukens et al. is tighter, due to the symmetry considerations)

2.5.4.5 Reducing the Polynomial Interpolation Bias

Equation (2.133) shows that the interpolation bias is a function of polynomial order R and polynomial frequency range B_{lpm}. For experiment design, it is useful to study the effect of both quantities on b_{int}. The polynomial order R has dependencies with numerous other quantities, including the number of supporting points n_E and thus also with B_{lpm}. Therefore, the effect of changes of R on the estimation bias b_{int} is complex and must be considered on a case-by-case basis.

The effect of B_{lpm} on the interpolation bias is more obvious: Reducing B_{lpm} also reduces the bias. The local polynomial frequency range B_{lpm} basically depends on the number of supporting points n_E and the excitation frequency resolution Δf_{exc} and is typically given by $B_{lpm} = \Delta f_{exc}(2n_E + 1)$ (Schoukens et al., 2012). For n_E there is a lower limit, since the least-squares problem (2.146) must not be under-determined. As it is advisable to choose n_E small to avoid correlation over frequency, there is usually little space to reduce n_E and only the excitation frequency resolution Δf remains as design parameter.

2.5.4.6 Requirements on Minimum Frequency Resolution

With the error response function $|\varepsilon_b(G)| = \frac{b_{int}}{|G_{max}|}$ introduced later in section 3.3.2 and with the polynomial frequency range $B_{lpm} = \Delta f_{exc} \cdot (2n_E + 1)$ (see section 2.5.3), equation (2.133) can be solved for the excitation frequency response Δf_{exc}, resulting in

$$\Delta f_{exc} = \frac{B_{3dB}}{2n_E + 1} \left(\frac{|\varepsilon_b(G)|}{\alpha_{R+2}} \right)^{-(R+2)} \tag{2.138}$$

This is a lower limit for the coarsest frequency resolution of the excitation signal, that reduces the relative bias to the accepted level $|\varepsilon_b(G)|$. The corresponding observation length is the inverse of the frequency resolution Δf_{exc}[24] and is thus given by

$$T_{meas} = \frac{2n_E + 1}{B_{3dB}} \left(\frac{|\varepsilon_b(G)|}{\alpha_{R+2}} \right)^{(R+2)} \tag{2.139}$$

T_{meas} is a lower limit for the minimum observation length that is required to reduce the bias to the acceptale limit $|\varepsilon_b(G)|$. It is in practice an important quantity for experiment design. In the online application shown in chapter 4, the minimum observation length corresponds to the length of the moving window.

[24] The relation of Δf_{exc} to the required measurement time follows the same line of reasoning as for the DFT frequency resolution in section 2.2.4.

For the PT2-system shown in (Schoukens et al., 2012), the 3-dB frequency range is given by $B_{3dB} = 2\zeta\omega_0$, where ζ is the damping of the PT2-system. With typical SISO standard settings (i.e. $n_E = R + 1$), the polynomial frequency range B_{lpm} is $2R + 3$. For simplicity it is assumed that a relative bias $|\varepsilon| = \alpha_{R+2}$ is considered as acceptable[25]; then the required measurement time T_{meas} is given by

$$T_{meas} = \frac{(2R+3)\pi}{2\zeta\omega_0} \tag{2.140}$$

and the corresponding frequency resolution is

$$\Delta f_{exc} = \frac{2\zeta\omega_0}{(2R+3)\pi} \tag{2.141}$$

2.5.4.7 Estimation of the Magnitude Interpolation Error

Equation (2.133) can be further used to estimate the (maximum) interpolation error based on the LPM estimate; in this case, the LPM-frequency range $B_{lpm} = (2n_E + 1)\Delta f_{exc}$, the polynomial order R and $\tilde{\alpha}_{R+2}$ are known; $|G_{max}|$ is replaced with $|\hat{G}|$, i.e. the magnitude of the FRF estimate at the frequency of interest. The 3db-frequency range , i.e. the frequency range in that the magnitude drops by 3dB, is approximated based on the curvature of the local polynomial from equation (2.121). For quadratic polynomials, this results in

$$k\Psi_0 = \Psi_2\tilde{B}_{3dB}^2 + \Psi_1\tilde{B}_{3dB} + \Psi_0 \tag{2.142}$$

where $k = -3\text{dB} \approx \frac{1}{\sqrt{2}}$. The equation can be solved for $\tilde{B}_{3dB}$ with the quadratic formula.

$$\tilde{B}_{1/2} = \frac{-\Psi_1 \pm \sqrt{{\Psi_1}^2 - 4\,(1-\mathrm{k})\Psi_0\Psi_2}}{2\Psi_2} \tag{2.143}$$

The 3dB-frequency range estimate is then given by

$$\hat{B}_{3dB} = \left|\tilde{B}_1 - \tilde{B}_2\right| \tag{2.144}$$

and the interpolation bias estimate $\hat{b}_{int}$ results in

$$\hat{b}_{int}(k) = \tilde{\alpha}_{R+2}\left(\frac{(2n_E+1)\Delta f_E}{\hat{B}_{3dB}}\right)^{R+2}\left|\hat{G}(j\omega_k)\right|, \tag{2.145}$$

As the interpolation bias depends primarily on the curvature of the frequency response, it has proven its worth to discard the linear term Ψ_1 in equation (2.142). The bias estimate $\hat{b}_{int}$ is used later to correct the confidence regions for the interpolation bias, see section 2.6.5.

2.5.5 Sample Covariance of GYU

The sample total covariance estimate of the FRM estimate $\hat{G}_{yu}$ is computed from the residuals of the least squares fit in (2.131) and is given by

$$\hat{C}_{vec(\hat{G})}(kP) = \frac{1}{q}\left(\hat{Y}_{n_E} - \hat{\Psi}L_{n_e}\right)\left(\hat{Y}_{n_E} - \hat{\Psi}L_{n_e}\right)^H \tag{2.146}$$

with

$$q = 2n_E + 1 - (R+1)n_{in} \tag{2.147}$$

[25] In Schoukens et al. (2012) the guideline for T_{meas} is motivated slightly differently, based on requirements on the relative bandwidths. The result is however the same.

where q is the number of degrees of freedom (dof) of the least squares residuals, $2n_E + 1$ the number of supporting points for the polynomials, R the polynomials' order and n_{in} the number of input signals, cmp. (Pintelon & Schoukens, 2012, p. 230). $\hat{Y}_{n_e}$ is the output DFT after removing the transient term, cmp. eq. (2.111), $\hat{\Psi}$ are the polynomial coefficients from the least squares fit, eq. (2.131), and L_{n_e} the regressor matrix, cmp. eq. (2.125) with (2.126). For MIMO systems, the frequency response matrix $\hat{G}$ is vectorised, by stacking its colums on top of each other, as indicated by $vec(\hat{G})$.

The statistical properties of $\hat{C}_{vec(\hat{G})}$ depend on the properties of the disturbing noise; both are discussed in detail in section 2.6. It is shown there, that the estimate $\hat{G}$ can often be assumed to be Gaussian distributed. It then follows directly, that the sample covariance matrix $\hat{C}_{vec(\hat{G})}$ from equation (2.146) is complex Wishart[26] distributed with q degrees of freedom, see (Pintelon & Schoukens, 2012, pp. 236–237) and section 2.6.2.4. The sample total covariance $\hat{C}_{vec(\hat{G})}(kP)$ includes the influence of noise and stochastic nonlinear distortions.

The variance of a single element of $vec(\hat{G}_{yu})$ is given by the respective diagonal element of $\hat{C}_{vec(\hat{G})}$. Its standard deviation is given by

$$\hat{\sigma}_{vec(\hat{G}),[i]}(k) = \sqrt{\hat{C}_{vec(\hat{G}),[i,i]}} \tag{2.148}$$

2.5.6 Indirect Estimate from Closed Loop Data

For plants with input- and output noise, the LPM estimate introduced in sections 2.5.1 and 2.5.2 may be not consistent. As for the ETFE, the bias is caused by the input noise (Pintelon & Schoukens, 2012, pp. 240–241). Unbiased, consistent estimates of open loop plant dynamics can still be estimated from closed loop experiments by indirect estimates, if the reference signal $r(t)$ that drives the closed loop system is known without error. The procedure is analogous to the ETFE, cmp. section 2.2.6.3.

The indirect estimate can be conveniently computed by stacking Y and U on top of each other, resulting in a single vector $Z = [Y, \quad U]^T$. As already shown in section 2.2.6.3, the FRM estimate $\hat{G}_{zr} = \begin{bmatrix} \hat{G}_{yr} & \hat{G}_{ur} \end{bmatrix}^T$ then provides the FRMs required for the indirect estimate

$$\hat{G}_{yu} = \hat{G}_{yr}(j\omega_{kP}) \cdot \hat{G}_{ur}^{-1}(j\omega_{kP}), \tag{2.149}$$

with covariance estimate $\hat{C}_{vec(\hat{G}_{yu})}$

$$\hat{C}_{vec(\hat{G}_{yu})} = \left(\hat{G}_{ru}^{-T} \otimes \left[I_{n_{out}}, -\hat{G}\right]\right)\hat{C}_{vec(\hat{G}_{rz})}\left(\hat{G}_{ru}^{-T} \otimes \left[I_{n_{out}}, -\hat{G}\right]\right)^H \tag{2.150}$$

2.5.7 Stochastic Nonlinear Disturbances and Covariance Estimate

The fast LPM consists of two local polynomial fits, where the residuals of both fits provide information about the noise contributions, cmp. equations (2.112) from section 2.4.3.5 and (2.146) from section 2.5.5.

For indirect estimates $\hat{G}_{zr}$ of a nonlinear plant, both estimates are related to each other; as both are computed in different ways, their difference provides additional information about the system noise. This relation is discussed in detail in (Pintelon & Schoukens, 2012, 119-150, 240-243, 250-261) and is shortly summarized here.

[26] The Wishart distribution is a multiple dimensions generalization of the χ^2-distribution.

The response of a nonlinear system to a sine input may contain additional harmonics beside the excitation frequency (Pintelon & Schoukens, 2012, p. 74). Hence the response to an input signal as described in section 2.4.1 can contain any harmonics. Extending this idea to signals that contain multiple harmonics, leads to an additional term Y_S that describes the nonlinear effects (Pintelon & Schoukens, 2012, pp. 119–150). This nonlinear stochastical disturbance is added to the input-output relation eq. (2.90), resulting in

$$Y_{exc} = G_{yu}(j\omega_m)\, U(m) + T_G(j\omega_m) + Y_S(m) + V(m),\ m = Pk \tag{2.151}$$

and equation (2.91) becomes

$$Y_{non} = T_G(j\omega_m) + Y_S(m) + V(m),\ m \neq Pk \tag{2.152}$$

respectively. The covariance of the stochastic nonlinear disturbance can be estimated from equations (2.114) and (2.146); they provide estimates of the sample noise covariance and the sample total covariance of the input-output DFT spectra $Z(kP)$. In (Pintelon & Schoukens, 2012, p. 241) it is shown, that their difference is an estimate of the covariance of the stochastic nonlinear distortions Z_s. The sample covariance estimate of the nonlinear stochastic distortion $\hat{C}_{Z_S}$ is given as

$$\hat{C}_{Z_s}(kP) = \frac{1}{P}\left(\hat{C}_{\hat{Z}}(kP) - \hat{C}_{\hat{Z}}^{noise}(kP)\right) \tag{2.153}$$

where $\hat{C}_{\hat{Z}}$ is computed from equation (2.146), where Y is replaced by Z and U by R, and $\hat{C}_{\hat{Z}}^{noise}$ from equation (2.112). Experiments indicate that for the given application (see sections 3 and 4), the nonlinear stochastic distortions are small compared to the total covariance $\hat{C}_{\hat{Z}}$. Hence the analysis concentrates on total covariance $\hat{C}_{\hat{Z}}$ and nonlinear stochastic distortions are not further considered.

2.5.8 Properties of Fast LPM Estimates

The properties of the fast LPM estimate are summarized for different conditions:

Input noise & closed loop experiments: The LPM estimate is generally biased if the input signal is noisy; in this respect the LPM is not different from the ETFE. If the reference signal $r(t)$ is available, the indirect FRM can be computed, resulting in an unbiased estimate of the plant dynamics. This holds independent of the input- and output noise correlation and thus extends directly to estimates from closed loop experiments.

Multiple input systems: To estimate frequency response *matrices*, i.e. dynamics of multiple input systems, each input must be excited with an independent random phase signal. Further the number of excited data points n_E in equation (2.123) must be adjusted to account for the increased number of unknowns. FRM estimates are generally biased due to the polynomial interpolation. If integer numbers of full periods are observed, the interpolation bias is the only bias source. An estimation formula for the maximum interpolation error is provided. For SISO systems unbiased estimates can be computed with the transient LPM, see section 2.5.1.

Nonlinear dynamics: In presence of nonlinearities, the fast LPM algorithm computes the best linear approximation (BLA) of the nonlinear dynamics (Pintelon & Schoukens, 2012, pp. 258–260). The nonlinearities are described by the nonlinear stochastic disturbance.

Non-steady state conditions: The first step of the fast LPM algorithm is the estimation of the transient part in the DFT spectra. This compensates the effect of non-steady state conditions in the estimates; hence the local polynomial methods can be applied to the first periods of data, that are otherwise have to be removed.

2.5.9 VARIANTS OF THE LPM AND RELATED METHODS

The LPM is a quite young method and new variants are steadily developed. Several alternatives and improvements have been suggested, mainly to improve the accuracy of the FRF estimated. This section gives a short overview of some variants.

2.5.9.1 TRANSIENT LPM

The transient LPM (Monteyne et al., 2012) is described in detail in the section 2.5.1. It combines the ETFE from periodic excitations (section 2.2.6) with the estimation of the transient term from periodic data (section 2.4). As the estimation is identical to the ETFE, it requires multiple experiments for multiple input systems.

2.5.9.2 FAST METHOD, ROBUST METHOD AND ARBITRARY LPM

In (Pintelon & Schoukens, 2012) three further variants of the LPM are introduced:

- Fast Method for periodic inputs
- Robust Method for periodic inputs
- LPM for arbitrary or random inputs

The fast method is described in section 2.5.2 of this thesis. The robust method differs from the fast LPM in the way the experiments are conducted: While the fast method is based on *one* experiment that excites all inputs at the same time, the robust method requires individual experiments for each input. As these individual experiments are time consuming, the fast method is preferred in the context of online estimation.

The LPM for arbitrary or random inputs uses a different algorithm to estimate the transient term and does not benefit from the advantages of periodic signals. As a consequence, its covariance is larger than for the fast LPM. In aircraft applications with automatic flight control systems periodic excitations can be easily realized. As the fast LPM computes more accurate estimates, it is thus preferred over the arbitrary LPM algorithm.

2.5.9.3 LOCAL RATIONAL METHOD

The local rational method (LRM) approximates the transient term and the FRF with local rational models instead of polynomials. This extends the LPM, as the numerator and denominator of the transfer function are approximated with separate polynomials. Thus, the LRM is essentially a Padé approximation of the FRF (Baker & Graves-Morris, 2010). Local rational models have the advantage, that they can follow the actual FRF more closely, especially around lightly damped poles, but are more sensitive to noise (McKelvey & Gúerin, 2012).

Their major drawback is, however, that the Padé approximation does not converge reliable: Even for single input systems, the approximation may not converge, e.g. when an estimated pole is close to a supporting point. In such cases, the estimates can deviate far from the true data. For multiple input systems, where multidimensional Padé approximations are required, this applies all the more (Baker & Graves-Morris, 2010, pp. 443–465). As a summary, the local Padé approximation *can* be more accurate than a local polynomial fit, but there is no guarantee for it. This may be acceptable for offline use, where the user can easily cross check the estimation results – but it is not an option for online applications, where no user interaction is possible. Thus, the polynomial approach is preferred in this thesis for its better stability.

2.5.9.4 LOCAL POLYNOMIAL METHOD WITH CONSTRAINTS

The LPM algorithm solves a series of independent least squares approximations, one for every frequency. (Gevers et al., 2011) show that neighbouring least squares problems are interrelated due to the overlap of the local polynomials and that this relation can be used to reduce the mean square estimation errors.

(Gevers et al., 2011) discuss different approaches how the relation can be included in the estimate and propose constraints for the estimation parameters as the preferred method. The resulting algorithm is thus called *local polynomial method with constraints* (LPMC) (Gevers et al., 2011). The LPMC can be implemented in a two-step approach: In the first step, the standard LPM is applied. In the second step, a similar least squares problem is solved, however it is now extended with the weighted constraints, resulting in a multiobjective least squares problem. As for the normal LPM method, the approach is applied to every excited frequency. Thus, the computational effort of the LPMC roughly doubles, compared to the normal LPM.

In the practical part of this thesis (chapters 3 and 4) it is seen that the fast LPM can achieve very accurate estimation results. The improved accuracy of the LPMC does not outweigh the increased computational effort; thus the LPMC is not used in this thesis.

Although not considered in (Gevers et al., 2011), the LPMC could in principle be combined with the LRM, leading to a "local rational method with constraints" (LRMC).

2.5.9.5 TRIMM

The Transient Impulse Response Modelling Method (TRIMM) was developed in (Hägg, Hjalmarsson, & Wahlberg, 2011) and was later given its name (Hägg & Hjalmarsson, 2012). A comparison shows that TRIMM may require longer computation time than LPM (Gevers, Hägg, Hjalmarsson, Pintelon, & Schoukens, 2012). As fast computations are necessary for online applications, the LPM algorithm was preferred over the TRIMM algorithm in this thesis.

2.5.10 SUMMARY

In this section two algorithms for the estimation of frequency response matrices have been introduced. They are both based on periodic excitations and require at least two periods of data. Consistent open loop estimates from closed loop data can be computed from indirect estimates if the reference input is known without error. The effect of initial- and final conditions (transient part) is removed in advance as described in section 2.4. It remains the periodic signal part that is the basis for the FRF / FRM estimation.

For single input systems, the *transient LPM* provides a simple and direct way to estimate frequency response functions. It is a straight forward combination of the ETFE with the transient estimation. Due to its close relation, the transient LPM has basically the same properties as the ETFE introduced in section 2.2.6. In particular, the transient LPM requires multiple experiment to estimate multiple input frequency response matrices with full frequency resolution (one experiment for each input).

Alternatively, *multiple input* FRMs can be computed with full frequency resolution from a *single* experiment if the FRM is locally approximated with polynomials (*fast LPM*). As noted before, this is a unique feature of the fast LPM. The algorithm is basically the same as for the estimation of the transient term. Its statistical properties (bias and variance) are discussed in detail: It is seen that the primary bias source is the interpolation bias. As shown in (Schoukens et al., 2012) for PT2 systems, the interpolation bias is worst at resonance

frequencies of lightly damped poles. The upper limit given in (Schoukens et al., 2012) is extended to magnitude and phase presentation and numerical values for the factor α_R are presented. The worst case interpolation bias provides a limit for the required frequency resolution that is useful for the experiment design.

Both algorithms, transient LPM and fast LPM, provide sample covariance matrices $\hat{C}_{vec(\hat{G})}$ of the estimated responses. They are the basis for the computation of confidence regions that is detailed in the following section.

2.6 Estimated Confidence Region of FRF-Estimates

In this section, the effect of noise on FRF estimates is analysed. The analysis starts with general assumptions on the noise properties and an examination of the effect of noise on DFT spectra (section 2.6.1). The effect of signal noise on FRF estimates is studied for the estimators used in this thesis and an approximation of the probability density function with a Gaussian distribution is introduced (section 2.6.2). The Gaussian approximation is the basis to derive general conditions for ellipsoidal shaped confidence regions (section 2.6.3), that contain the true value of the estimate with given probability. For multidimensional estimates, the resulting high dimensional ellipsoids are difficult to interpret. It is common to derive simultaneous confidence regions, that are simpler to interpret (section 2.6.3.4). When applied to frequency response estimates (section 2.6.3.5), it is seen that the simultaneous confidence regions of a single estimate are circular shaped (section 2.6.5).

The noise is modelled in the time domain by real valued random signals. It is seen that the DFT of real valued random signals results in complex random variables. Appendix B.2 provides a short introduction of complex random variables, some important properties and relevant distribution functions. For more general introductions to multivariate statistics, the reader is referred to (Johnson & Wichern, 2007) and (Härdle & Simar, 2015). An extensive presentation of complex random variables is provided in (Picinbono, 1993).

2.6.1 Distribution of Noise in Frequency Domain

2.6.1.1 Discrete Fourier Transform of Filtered White Noise

Within this thesis, any noise signal $v[n]$ is assumed to be filtered white noise that can be described by the simple noise model

$$v[n] = H(z^{-1})e[n] \tag{2.154}$$

where $H(z)$ is a stable linear filter and e$[n]$ is a band limited discrete white noise process[27]. This noise model describes coloured noise $v[n]$, that is shaped with the filter $H(z^{-1})$. While equation (2.154) is a time domain representation, this section discusses the statistical noise properties after the transformation to the frequency domain.

It is assumed that the sampled sequence $e[n]$ is independent and identically distributed (iid). The statistical properties of the DFT $E(k)$ of $e[n]$ with $k = 1, 2, \dots, \frac{N}{2} - 1$ (i.e. without DC and Nyquist frequency) are then analysed for three different cases; they have in common that $E(k)$ is independent over frequency k, i.e. $E(k_1)$ and $E(k_2)$ are statistically independent for $k_1 \neq k_2$. The respective distributions differ, depending on the properties of $e[n]$ (Pintelon & Schoukens, 2012, pp. 227, 601):

[27] See appendix B.1 for a definition of band limited white noise.

(a) $\boldsymbol{e[n]}$ **has *finite second order moments*:** If the noise process $e[n]$ has finite second order moments, its DFT spectrum $E(k)$ is uncorrelated over frequency k and circular complex distributed for any number of samples N.

(b) $\boldsymbol{e[n]}$ **has existing *moments of any order***: If $e[n]$ has existing moments of any order, $E(k)$ is *asymptotically* for $N \to \infty$, independent over k, circular complex normally distributed.

(c) $\boldsymbol{e[n]}$ **is *Gaussian* distributed:** If $e[n]$ is Gaussian distributed, $E(k)$ is independent over frequency k, circular complex *normally* distributed for any N.

For cases (b) and (c), the effect of a linear filter $H(z^{-1})$ on the DFT of $v[n]$ can be determined analytically. Case (b) is considered in (Pintelon & Schoukens, 2012, p. 601); it is proven that the DFT $V(k)$ of filtered iid noise $v[n] = H(z^{-1})e[n]$, with stable $H(z^{-1})$ is also asymptotically for $N \to \infty$ independent, circular complex normally distributed.

For case (c), it is a well-known property, that a Gaussian distributed input $E(k)$ to a linear system results in a Gaussian output $V(k)$, cmp. (Papoulis & Pillai, 2002, pp. 398–399). It follows that for Gaussian noise $e[n] \in \mathbb{N}(0, \sigma^2)$, the DFT coefficients $V(k)$ are also circular complex normally distributed with

$$V(k) \in \mathbb{N}^c\left(0, \sigma_k^2\right), \qquad \forall\, k \in \mathbb{Z}^+ \tag{2.155}$$

where $\sigma_k^2 = \frac{\sigma^2}{T_s} \cdot \left|H\left(z_k^{-1}\right)\right|^2$ with σ^2 the variance of the band limited white noise process $e[n]$ and T_s the discrete sampling time; the superscript in $\mathbb{N}^c$ indicates the complex normal distribution.

2.6.1.2 Noise Properties of Input- and Output Signals

The general result of (2.155) is transferred to the input and output noise of estimated systems: When the input and output signals of an estimated system are disturbed by filtered Gaussian white noise, the DFT spectra V_U and V_Y of the input- and output noise are circular complex normally distributed with

$$\mathbb{E}\{V_U(k)\} = 0 \tag{2.156}$$

$$\mathbb{E}\{V_Y(k)\} = 0 \tag{2.157}$$

$$\mathbb{E}\{|V_U(k)|^2\} = \sigma_U^2(k) \tag{2.158}$$

$$\mathbb{E}\{|V_Y(k)|^2\} = \sigma_Y^2(k) \tag{2.159}$$

$$\mathbb{E}\{V_Y(k)\bar{V}_U(k)\} = \sigma_{YU}^2(k) = \bar{\sigma}_{UY}^2(k) \tag{2.160}$$

$$\mathbb{E}\{V_Y(k)V_U(k)\} = 0 \tag{2.161}$$

where $k = 1, 2, \ldots F$.

Equations (2.156) to (2.161) can be verbalized as

- $V_U(k)$ and $V_Y(k)$ are zero mean (eq. (2.156),(2.157))
- $[V_U(k), \quad V_Y(k)]^T$ is a circular random vector (eq. (2.158) to (2.161)).

The assumption of filtered white noise is often a good model that can be applied to many real world effects, cmp. (Dryden, 1943; IEEE, 1997). In the practical part of this thesis in chapters 3 and 4, the disturbances are modelled as filtered Gaussian noise and the respective DFT coefficients of the disturbing noise $V(k)$ are thus circular complex Gaussian distributed.

2.6.2 Distribution of Frequency Response Estimates

As introduced in 2.2.6, noise results in uncertainty in FRF estimates; both, the noise and the uncertainty of the estimate, are described mathematically by random variables. The most complete description of a random variable is its probability density function (pdf), that describes the probability that the realization of the process takes a certain value (Bendat & Piersol, 1971/2010, p. 45).

In this section, the probability density function of frequency response estimates is analysed. The analysis is based on the assumption of filtered Gaussian noise (case (c) in 2.6.1). For non-Gaussian noise with existing moments of any order, the derivation holds asymptotically for $N \to \infty$.

The analysis starts with the exact probability density function of the empirical transfer function estimate. The exact pdf is then approximated with a Gaussian distribution, that can be analysed more easily. Based on the Gaussian approximation, the pdfs of the sample mean and sample covariance of an ETFE are introduced. The results are then extended to LPM estimates.

2.6.2.1 Exact Probability Density Function of ETFE

In (Pintelon et al., 2003) exact and approximated probability density functions for FRF estimates for systems with input and output noise are derived. The noise (described in the time domain) is assumed to be filtered white, zero-mean normally distributed. For this case, equations (2.156) to (2.161) hold. The input and output noise can be correlated. For the analysis of the probability density functions, the ETFE

$$\hat{G}_{yu}(j\omega_k) = \frac{Y_0(k) + V_Y(k)}{U_0(k) + V_U(k)} \tag{2.162}$$

is rewritten in terms of normalized errors $\tilde{u} = \frac{V_U}{U_0}$, $\tilde{y} = \frac{V_Y}{U_0}$, where U_0, Y_0 are the true input/output signals.

$$\hat{G}_{yu}(j\omega_k) = \frac{Y_0(k)\left(1 + \frac{V_Y(k)}{Y_0(k)}\right)}{U_0(k)\left(1 + \frac{V_U(k)}{U_0(k)}\right)} = G_0 \frac{1+\tilde{y}}{1+\tilde{u}}, \tag{2.163}$$

where $G_0 = \frac{Y_0}{U_0}$ is the true FRF. Dividing both sides with G_0 results in the normalized FRF estimate $g = \frac{\hat{G}}{G_0}$, given by

$$\begin{aligned} g &= \frac{\hat{G}_{yu}}{G_0} \\ &= \frac{1+\tilde{y}}{1+\tilde{u}}, \end{aligned} \tag{2.164}$$

Its probability density function (pdf) $p(g)$ is given in (Pintelon et al., 2003) as

$$p(g) = \frac{1}{\pi a(g)}\left(\frac{\sigma_{\tilde{u}}^2\sigma_{\tilde{y}}^2\,(1-|\rho|^2)}{a(g)} + \left|\frac{b(g)}{a(g)} + 1\right|^2\right) e^{\frac{-|g-1|^2}{a(g)}} \tag{2.165}$$

with
$$a(g) = \sigma_{\tilde{y}}^2 + |g|^2\sigma_{\tilde{u}}^2 - 2\sigma_{\tilde{y}}\sigma_{\tilde{u}}Re(\rho\bar{g}) \tag{2.166}$$

and
$$b(g) = (g-1)\left(\bar{\rho}\sigma_{\tilde{y}} - \bar{g}\sigma_{\tilde{u}}\right)\sigma_{\tilde{u}} \tag{2.167}$$

where $\sigma_{\tilde{u}}^2, \sigma_{\tilde{y}}^2, \sigma_{\tilde{y}\tilde{u}}^2$ denote the (co)variances of the normalized errors and $\rho = \sigma_{\tilde{y}\tilde{u}}^2/\left(\sigma_{\tilde{u}}\sigma_{\tilde{y}}\right)$ is the corresponding correlation coefficient, cmp. (Pintelon & Schoukens, 2012); the bar (as in $\bar{\rho}$ and $\bar{g}$) denotes the complex conjugate.

To compute confidence regions for $\hat{G}$, equation (2.165) must be (numerically) integrated. This is computationally involved and not well suited for online applications. Instead, the true pdf is approximated with a Gaussian distribution, that can be analysed more easily.

2.6.2.2 Gaussian Approximation of ETFE

The pdf in equation (2.165) reduces to a Gaussian distribution if the input signal is noise free, i.e. $\sigma_{\tilde{u}}^2 = 0$. For sufficient signal-to-noise ratio in the input signal, the true pdf can be closely approximated by a Gaussian distribution function, i.e. it is assumed that the estimation error $\hat{G}(j\omega_k) - G_0(j\omega_k)$ is circular complex normally distributed with zero mean and covariance matrix $C_{vec(G)}$. The approximation can be derived by a Taylor series expansion of equation (2.162) as shown in appendix B.3, or – more detailed – from the true pdfs, see (Pintelon et al., 2003).

2.6.2.3 Conditions for Gaussian Approximation

The Gaussian approximation is considered valid for input signal-to-noise ratios (SNRu) larger than 40 dB; this condition can be relaxed to 20dB, when the input U is checked for outliers (Pintelon et al., 2003): For the given noise assumptions it is possible (albeit unlikely) that $U = U_0 + V_U$ becomes zero or close to zero. The Taylor approximation in B.3 is then no longer converging. It is thus necessary to ensure that $|U|$ is larger than a minimum threshold and remove outliers that violate the condition. With the definition of $SNR_U = |U_0(k)|/\sigma_U(k)$ the criterion $SNR_U \geq 20dB$ results in

$$\frac{|U_0(k)|}{\sigma_U(k)} \geq 20dB \tag{2.168}$$

where $\sigma_U(k) = \sqrt{\mathbb{E}\{|V_U(k)|^2\}}$. In terms of magnitude, equation (2.168) is equivalent to

$$\frac{|U_0(k)|}{\sigma_U(k)} \geq 10 \tag{2.169}$$

or

$$\sigma_U(k) \leq \frac{|U_0(k)|}{10} \tag{2.170}$$

2.6.2.4 Distribution of Sample Mean and Sample Covariance Matrix

As it is well known, the sample mean and unbiased sample (co-)variance of two random processes $x(k)$, $y(k)$, computed from P independent realizations $x^{[l]}, l = 1, \dots, P$ and $y^{[m]}, m = 1, \dots, P$, respectively, are defined as

$$\hat{x}(k) = \frac{1}{P}\sum_{l=1}^{P} x^{[l]}(k) \tag{2.171}$$

$$\hat{C}_x(k) = \frac{1}{P-1}\sum_{l=1}^{P}\left(x^{[l]}(k) - \hat{x}(k)\right)\left(x^{[l]}(k) - \hat{x}(k)\right)^H \tag{2.172}$$

$$\hat{C}_{xy}(k) = \frac{1}{P-1}\sum_{l=1}^{P}\left(x^{[l]}(k) - \hat{x}(k)\right)\left(y^{[l]}(k) - \hat{y}(k)\right)^H \tag{2.173}$$

where $\hat{x}(k)$ is the sample mean, $\hat{C}_x(k)$ the sample variance and $\hat{C}_{xy}(k)$ the sample covariance respectively (Johnson & Wichern, 2007, pp. 6–8).

The definitions of the sample mean and sample covariance apply for univariate (scalar) random variables, as well as for multivariate random vectors. They further can be applied to both, real- and complex valued random vectors (Giri, 1965).

UNIVARIATE NORMAL DISTRIBUTION

If $x(k)$ is an univariate *normally distributed* random process with mean μ_x and variance σ_x^2 it is denoted as $x(k) \in \mathbb{N}(\mu_x, \sigma_x^2)$. Its sample mean and sample variance are respectively

$$\hat{x}(k) \in \mathbb{N}\left(\mu_x(k), \frac{\sigma_x^2(k)}{P}\right) \tag{2.174}$$

and

$$\hat{C}_x(k) \in \frac{\sigma_x^2}{P-1}\chi^2(P-1) \tag{2.175}$$

distributed (Johnson & Wichern, 2007, pp. 173–174). The χ^2-distribution with $P-1$ degrees of freedom in equation (2.175) is equivalent to an univariate Wishart distribution with $P-1$ degrees of freedom and associated parameter matrix 1, denoted as $\mathbb{W}^1(P-1, 1)$. Including the scaling factor $\frac{\sigma_x^2}{P-1}$ in the Wishart-distribution, equation (2.175) can be rewritten equivalently as

$$\hat{C}_x(k) \in \mathbb{W}^1\left(P-1, \frac{\sigma_x^2(k)}{P-1}\right) \tag{2.176}$$

MULTIVARIATE NORMAL DISTRIBUTION

This result can be extended to multivariate circular complex normally distributed processes: for an n-variate[28] random process $\boldsymbol{x}(k) \in \mathbb{N}^{c,n}\left(\boldsymbol{\mu_x}(k), \boldsymbol{C_x}(k)\right)$[29], the sample mean $\hat{\boldsymbol{x}}(k)$ and its sample covariance matrix $\widehat{\boldsymbol{C}}_{\boldsymbol{x}}$ are respectively

$$\hat{\boldsymbol{x}}(k) \in \mathbb{N}^{c,n}\left(\boldsymbol{\mu_x}(k), \frac{\boldsymbol{C_x}(k)}{P}\right) \tag{2.177}$$

$$\widehat{\boldsymbol{C}}_{\boldsymbol{x}}(k) \in \mathbb{W}^{c,n}\left(P-1, \frac{\boldsymbol{C_x}(k)}{P-1}\right) \tag{2.178}$$

distributed (Giri, 1965), where $\mathbb{W}^{c,n}(m, \boldsymbol{C})$ denotes an n-variate complex Wishart-distribution with m degrees of freedom and associated parameter matrix $\boldsymbol{C}$.

APPLICATION TO FREQUENCY RESPONSE ESTIMATES

When these results are applied to the Gaussian approximation of the ETFE estimates $\hat{G}_{ETFE}$ derived in section 2.6.2.2, it follows that

$$\widehat{\boldsymbol{G}}_{ETFE}(k) \in \mathbb{N}^{c,n}\left(\boldsymbol{G}(k), \frac{\boldsymbol{C_G}(k)}{P}\right) \tag{2.179}$$

and

$$\widehat{\boldsymbol{C}}_{\widehat{\boldsymbol{G}},ETFE}(k) \in \mathbb{W}^{c,n}\left(P-1, \frac{\boldsymbol{C_G}(k)}{P-1}\right) \tag{2.180}$$

[28] To better distinct the univariate and multivariate case, in *this* section vectors and matrices are in bold print.
[29] The superscript *c* indicates a circular complex distributions; the superscript *n* indicates the dimension of the vector.

2.6.2.5 DISTRIBUTION OF LPM ESTIMATES

The foregoing derivation of the pdf of $\hat{G}$ is valid for the ETFE. It can be extended to local polynomial estimates, computed either with the transient LPM or the fast LPM.

The transient LPM introduced in section 2.5.1 is an direct extension of the ETFE. The only difference is the estimation and correction of the transient term: While the ETFE requires steady state response data, the tLPM actively removes transient signal parts. Besides this preprocessing of the input and output DFT spectra, the estimation of the frequency response function is identical. The derivation of sections 2.6.2.2 to 2.6.2.4 can thus be extended directly to the transient LPM estimates. It follows that the input and output noise V_U, V_Y after the estimation of the transient term are circular complex normally distributed. As a direct consequence, the Gaussian approximation introduced in section 2.6.2.2 holds also for transient LPM estimates. The transient LPM averaged computed from P periods of data has the distribution

$$\widehat{\boldsymbol{G}}_{tLPM}(k) \in \mathbb{N}^{c,n}\left(\boldsymbol{G}(k), \frac{\boldsymbol{C_G}(k)}{P}\right) \tag{2.181}$$

and

$$\widehat{\boldsymbol{C}}_{\widehat{\boldsymbol{G}},tLPM}(k) \in \mathbb{W}^{c,n}\left(P-1, \frac{\boldsymbol{C_G}(k)}{P-1}\right). \tag{2.182}$$

The fast LPM algorithm utilizes a different estimation approach. It is based on least squares fits of circular complex normally distributed data. The residuals of least squares fits to normally distributed data are also normally distributed; thus, the Gaussian approximation also holds for fast LPM estimates (Pintelon & Schoukens, 2012, pp. 236–264) and the sample covariance matrix estimate $\hat{C}_{vec(\hat{G})}$ is (under the assumption of Gaussian noise, see section 2.6.1) complex Wishart distributed. By contrast to the ETFE and the tLPM, the fit is computed over neighbouring frequencies, not over independent realizations. Therefore, the number of periods P is replaced by the number of frequencies $2n_E$ in the least squares fits and the distributions result in

$$\widehat{\boldsymbol{G}}_{fastLPM}(k) \in \mathbb{N}^{c,n}\left(\boldsymbol{G}(k), \frac{\boldsymbol{C_G}(k)}{2n_{in}n_{out}}\right) \tag{2.183}$$

and

$$\widehat{\mathbf{C}}_{\widehat{\mathbf{G}},\mathrm{fastLPM}}(\mathrm{k}) \in \mathbb{W}^{\mathrm{c,n}}\left(\mathrm{q}, \frac{\mathbf{C_G}(\mathrm{k})}{\mathrm{q}}\right) \tag{2.184}$$

with true mean value $G(k)$, true covariance matrix C_G[30]; n_{in}, n_{out} are the number of system input and outputs, respectively, and q is given in equation (2.147) as

$$q = 2n_E + 1 - (R+1)n_{in} \tag{2.185}$$

where R is the polynomial order and n_E the number of supporting points, cmp. (Pintelon & Schoukens, 2012, 237, 258). The number of degrees of freedom q results from the number of supporting points $2n_E + 1$, minus the number of estimated polynomial parameters $(R+1)n_{in}$.

As a summary, FRF estimates from all three algorithms that are discussed in this thesis (ETFE, transient LPM, fast LPM) can be assumed to be circular complex normally distributed; the corresponding sample covariance matrix $\hat{C}_{vec(\hat{G})}$ is complex Wishart distributed.

[30] In this context, possible estimation biases, in the fast LPM estimates are neglected.

2.6.3 Confidence Regions of Gaussian Random Variables

As shown in the preceding section, the frequency response function estimates from all three algorithms are (approximately) Gaussian distributed. In this section, confidence regions for the estimate $\hat{G}$ are introduced. They are based on the Gaussian approximation and thus can be applied to all three estimation algorithms. The introduction starts from a univariate example that is then generalized to multivariate complex distribution functions.

The computation of confidence regions for $\hat{G}$ is carried out analogously to the computation of confidence regions for normally distributed mean values, that is well covered in the statistics literature, see e.g. (Johnson & Wichern, 2007, pp. 210–233) or (Härdle & Simar, 2015, pp. 210–231).

2.6.3.1 Confidence Regions for Univariate Normally Distributed Random Variables

When based on sample means and sample variance of a normally distributed random variable, the confidence bounds for the sample mean can be derived from the student's t-distribution (Gosset, 1908). The resulting t-test compares the sample mean to the population mean, based on the population sample variance; thus, the tested null-hypothesis is that the sample mean $\hat{x}$ is equal to the true (population) mean μ_0 (Johnson & Wichern, 2007, p. 210). For normally distributed random variables, the statistic

$$t = \sqrt{n}\,\frac{\hat{x} - \mu_0}{\hat{\sigma}_x} \tag{2.186}$$

is t-distributed with $n-1$ degrees of freedoms (i.e. $t \in \mathbb{t}(n-1)$), where $\hat{x}$ is the sample mean, μ_0 the true mean and $\hat{\sigma}_x$ the sample standard deviation (Johnson & Wichern, 2007, pp. 210–211). The null hypothesis of the t-test is that the estimate $\hat{x}$ is equal to the true value μ_0. It is not rejected at level α if

$$\left|\sqrt{n}\,\frac{\hat{x} - \mu_0}{\hat{\sigma}_x}\right| \leq \mathbb{t}^{-1}\left(\frac{1-\alpha}{2}, n-1\right) \tag{2.187}$$

Equivalently, confidence regions around $\hat{x}$ that contain the true value μ_0 with probability $p = 1-\alpha$ are given by

$$\hat{x} - \frac{\hat{\sigma}_x}{\sqrt{n}}\,\mathbb{t}^{-1}\left(\frac{1-\alpha}{2}, n-1\right) \leq \mu_0 \leq \hat{x} + \frac{\hat{\sigma}_x}{\sqrt{n}}\,\mathbb{t}^{-1}\left(\frac{1-\alpha}{2}, n-1\right) \tag{2.188}$$

(Johnson & Wichern, 2007, p. 211), where $\mathbb{t}^{-1}(\frac{1-\alpha}{2}, n-1)$ is the student's t inverse cumulative distribution function[31] with $n-1$ degrees of freedom for the corresponding propability $\frac{1-\alpha}{2}$; the factor $\frac{1}{2}$ distributes the confidence region symmetrically to both tails.

The principle of the t-test is shown in Figure 2-21. The figure shows 10 repeated experiments. Each experiment contains 20 samples from a standard normal distribution (grey circles)[32]. For each experiment, the sample mean (rectangle) and its 90%-confidence region (vertical bar), computed from equation (2.188), are shown. It is seen that the true mean ($\mu_0 = 0$) is contained in the confidence regions for 9 out of 10 experiments; this coincides with the 90%-confidence level.

[31] Note the nomenclature: Differing from the general rule, here $\mathbb{t}$ (lower case) denotes the *cdf* of the student-t distribution.

[32] The vertical axis is pruned for better readability; samples outside the [-2; 2] range are not shown.

For the further derivation of multivariate confidence regions, equation (2.186) is squared;

$$t^2 = (\hat{x} - \mu_0)\left(\frac{\hat{\sigma}_x^2}{n}\right)^{-1}(\hat{x} - \mu_0) \tag{2.189}$$

t^2 is a $\mathbb{t}^2$- distributed random variable, where $\hat{x} - \mu$ is the normally distributed estimation error and $\hat{\sigma}_x^2$ the χ^2-distributed covariance estimate with n degrees of freedom.The corresponding test statistic is

$$(\hat{x} - \mu_0)\left(\frac{\sigma_x^2}{n}\right)^{-1}(\hat{x} - \mu_0) \leq \mathbb{t}^{-2}\left(\frac{1-\alpha}{2}, n-1\right) \tag{2.190}$$

It will be seen in the following sections, that the statistics and the corresponding tests for the multivariate cases have the same general shape as equations (2.189) and (2.190).

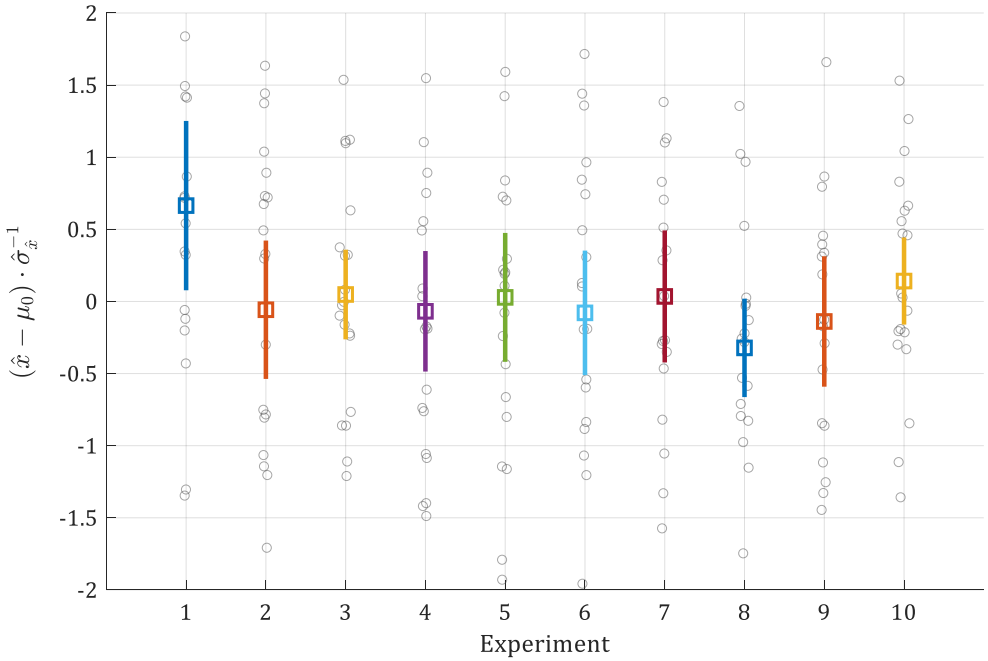

Figure 2-21: Confidence intervals for sample mean.

2.6.3.2 *Extension to Multivariate Case*

In equation (2.189), $\hat{x} - \mu_0$ is a normally distributed random variable (rv) and $\hat{\sigma}_x^2$ is χ^2-distributed. Following (Johnson & Wichern, 2007, p. 213), the statistic of t^2, i.e. of equation (2.189), can be rewritten as

$$t^2 = \begin{pmatrix}\text{normal}\\ \text{distr. rv}\end{pmatrix}\left(\frac{\text{(scaled) } \chi^2 \text{ rv.}}{\text{dof}}\right)^{-1}\begin{pmatrix}\text{normal}\\ \text{distr. rv}\end{pmatrix} \tag{2.191}$$

i.e. the squared normally distributed random variable is divided by its scaled χ^2-distributed sample covariance. This formulation can be extended to the multivariate case: The random vector is then multivariate normally distributed, its sample covariance matrix is Wishart distributed, cmp. equations (2.177) and (2.178). The resulting test statistic T^2 has the shape

$$T^2 = \begin{pmatrix}\text{multivariate}\\ \text{normal}\\ \text{distr. rv}\end{pmatrix}^T\left(\frac{\text{Wishart random}}{\text{dof}}\right)^{-1}\begin{pmatrix}\text{multivariate}\\ \text{normal}\\ \text{distr. rv}\end{pmatrix} \tag{2.192}$$

where T^2 follows the Hoteling's T^2-distribution (Hotelling, 1931) which is closely related to the F-distribution, cmp. (Härdle & Simar, 2015, pp. 219–224). The resulting test statistic for multivariate estimates is the F-test

$$\left(\hat{X} - \mathrm{M}_0\right)^H \hat{C}_{\hat{X}}^{-1} \left(\hat{X} - \mathrm{M}_0\right) \leq \frac{n_X(n-1)}{(n-n_X)} \mathbb{F}^{-1}(1-\alpha, n_X, n-n_X) \tag{2.193}$$

where $\hat{X}$ is the normally distributed random vector with n_X elements, M_0 its true mean value, $\hat{C}_{\hat{X}}^{-1}$ its sample covariance matrix with n degrees of freedom, and $\mathbb{F}^{-1}(1-\alpha, n_X, n-n_X)$ the F-distributions inverse cumulative distribution function for probability $1-\alpha$ and parameters n_X and $n-n_X$. The comparison with equation (2.190) shows the similar shape of the univariate t-test and the multivariate F-test.

Table 2-5 compares the univariate and multivariate distributions of the sample mean, the sample (co-) variance and the resulting test statistics for the computation of confidence regions.

Table 2-5: Comparison of statistics for univariate and multivariate normal random variables.

	univariate	**multivariate**
Distribution of sample mean	Normal distribution	Normal distribution
Distribution of sample covariance	χ^2-distribution	Wishart distribution
Test statistic for confidence regions	Student t-distribution	F-distribution

2.6.3.3 Example: Confidence Ellipsoid of Bivariate Random Vector

For multivariate Gaussian random variables, the most compact confidence regions are ellipsoids (Härdle & Simar, 2015, pp. 219–224). Figure 2-22 shows a scatter plot with samples of a bivariate Gaussian random vector $z = [x,\ y]^T$ with its 95%-confidence ellipsoid (orange, bold line). The marginal distributions are indicated with thin violet lines. The dashed lines indicate the bounds of the 95% confidence ellipsoid; they correspond to the simultaneous 95% confidence regions, introduced later in section 2.6.3.4.

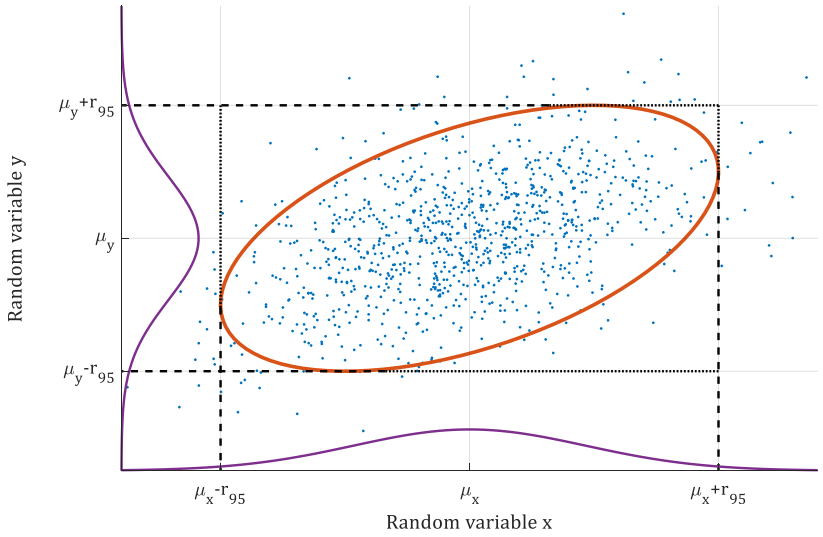

Figure 2-22: Confidence ellipsoid of a normally distributed bivariate distribution (x,y) (orange) with marginal distributions (violet) and marginal 95% confidence radii (black dashed).

2.6.3.4 SIMULTANEOUS CONFIDENCE REGIONS

For multivariate distributions, the analysis of ellipsoidal confidence regions like equation (2.193) can be cumbersome. For a simpler analysis, simultaneous confidence bounds are computed. They describe the maximum expansion of the confidence ellipsoid along the coordinate axis. In Figure 2-22 simultaneous confidence regions are shown as black dashed lines. They form a *confidence rectangle* that inscribes the confidence ellipsoid. Simultaneous confidence regions for a single element of the random vector hold, whatever value the other elements take.

In the statistics literature, simultaneous confidence regions are often derived by a more general approach: It computes simultaneous confidence regions for an arbitrary linear combination of the elements of the random vector. The linear combination is described by a projection vector a, that is multiplied with the random vector. With the bivariate example $\mathrm{z} = [\mathrm{x},\ \mathrm{y}]^{\mathrm{T}}$ from section 2.6.3.3, simultaneous confidence bounds for y can be computed with a projection vector $a = [0,\quad 1]^T$, where

$$y = a^T z \tag{2.194}$$

In the following, this approach is applied to derive simultaneous confidence regions for the elements of the FRF estimate $\hat{G}(j\omega_k)$. The derivation is based on the generalized Cauchy-Schwarz Inequality and is described in many textbooks on multivariate statistics, cf. e.g. (Anderson, 2003, pp. 178–179; Härdle & Simar, 2015, pp. 219–224; Johnson & Wichern, 2007, pp. 220–231). With a projection vector a, the test statistic of the F-test in equation (2.193) results in

$$\left(a^T(z-\mu_z)\right)^H\left(a^T\hat{C}_{\hat{z}}a\right)^{-1}\left(a^T(z-\mu_z)\right) \leq \frac{n_z(n-1)}{(n-n_z)}\mathbb{F}^{-1}(1-\alpha, n_z, n-n_z) \tag{2.195}$$

where n_z is 1 and n the number of degrees of freedom of the covariance matrix.

The simultaneous confidence regions from (2.205) can be quite conservative. To show this, we have a second look at Figure 2-22, which is repeated here for convenience (Figure 2-23); the confidence ellipse (orange) and the simultaneous confidence regions (green) are highlighted. It is clearly seen that the simultaneous confidence rectangle (green) includes a larger area and thus includes the true value with larger confidence. The design confidence level $p = 1-\alpha$ in equations (2.193) and (2.195) is however identical; the simultaneous confidence regions are thus conservative. The effect is emphasized for higher dimensional cases.

2.6.3.5 BONFERRONI-METHOD FOR SINGLE ELEMENTS

As shown above, simultaneous confidence regions are in general conservative. An alternative approach that can provide tighter rectangular confidence regions is the Bonferroni method (Dunn, 1961), named after and based on the Bonferroni inequality (Bonferroni, 1935; Bonferroni, 1936). Especially if the number of non-zero elements in the projection vector a is small, the Bonferroni method can provide tighter estimates than the F-test (National Institute of Standards and Technology [NIST], 2018, sec. 7.4.7.3).

Recalling the (univariate) t-test from equation (2.188), and the F-test for simultaneous confidence regions from equation (2.195),

$$(\hat{x}-\mu_0)\left(\frac{\sigma_{\hat{x}}^2}{n}\right)^{-1}(\hat{x}-\mu_0) \leq\ \mathbb{t}^{-2}\left(\frac{1-\alpha}{2}, n-1\right) \tag{2.196}$$

$$\left(a^T(X-\mathrm{M}_0)\right)^H\left(a^T\hat{C}_{\hat{X}}a\right)^{-1}\left(a^T(X-\mathrm{M}_0)\right)\leq\frac{n_X(n-1)}{(n-n_X)}\mathbb{F}^{-1}(1-\alpha,n_X,n-n_X) \qquad (2.197)$$

the Bonferroni method is a sort of mixture of both, as it combines the left hand side of simultaneous confidence regions with the statistic of the t-test:

$$\left(a^T(X-\mathrm{M}_0)\right)^H\left(a^T\left(\frac{\hat{C}_X}{n}\right)a\right)^{-1}\left(a^T(X-\mathrm{M}_0)\right)\leq\mathbb{t}^{-2}\left(\frac{1}{2}\left(1-\frac{\alpha}{n_X}\right),n-1\right) \qquad (2.198)$$

where $\hat{X}$ is the normally distributed random vector with n_X elements, M_0 its true mean value, $\hat{C}_{\hat{X}}^{-1}$ its sample covariance matrix with n degrees of freedom. (Johnson & Wichern, 2007, p. 232). Equation (2.198) can be written equivalently in terms of the F-distribution[33],

$$\left(a^T(X-\mathrm{M}_0)\right)^H\left(a^T\left(\frac{\hat{C}_X}{n}\right)a\right)^{-1}\left(a^T(X-\mathrm{M}_0)\right)\leq c\mathbb{F}^{-1}\left(1-\frac{\alpha}{n_X},1,n-1\right) \qquad (2.199)$$

with scaling factor $c=\frac{n_X(n-1)}{(n-n_X)}$. The comparison of equations (2.197) and (2.199) shows the different ways, how the multivariate case is accounted for: In the case of simultaneous confidence levels, the first parameter n_X is increased, while the Bonferroni intervals adjust the confidence level $p=1-\frac{\alpha}{n_X}$, keeping the first parameter of the F-distribution equal to one.

As shown above, rectangular confidence regions are advantageous, as they provide simultaneous confidence regions, i.e. they hold for each element of the estimate, irrespective of the values of other elements. This makes them easy to use, especially for high dimensional problems. However, the shown approach introduces significant conservatism; the Bonferroni method can often provide tighter rectangular confidence regions, cmp. Figure 2-23.

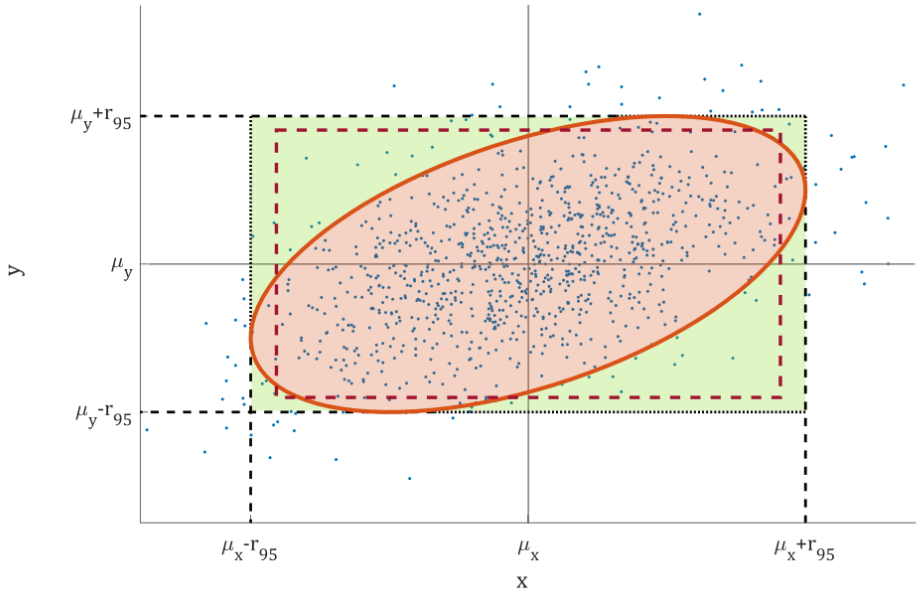

Figure 2-23: Comparison of simultaneous confidence regions (green) with confidence ellipsoid (orange). Bonferroni intervals are indicated as dark red, dashed rectangle.

[33] Note that the F-distribution is one sided (different from the t-distribution). The probability level p is thus not divided by 2.

2.6.4 Confidence Regions for FRM Estimates

The confidence regions derived in section 2.6.3 are now applied to the Gaussian approximations of the frequency response estimates, that have been introduced before in section 2.6.2.2.

2.6.4.1 Multivariate Confidence Regions For Frequency Response Estimates

In section 2.6.2 it was shown that the estimate (i.e. the sample mean) $\hat{G}(j\omega_k)$ is (approximately) normally distributed and its sample covariance matrix is Wishart distributed. Thus, confidence regions for $\hat{G}(j\omega_k)$ can be constructed from Hotelling's T^2-statistic (Anderson, 2003, p. 179) or from the related F-distribution (Härdle & Simar, 2015, pp. 219–220). The test statistic is shown in equation (2.200): if the inequality holds, the vector X is inside the confidence region with confidence level p.

$$\left(X - vec\left(\hat{G}\right)\right)^H \hat{C}_{vec(\hat{G})}^{-1} \left(X - vec\left(\hat{G}\right)\right) \leq \frac{n_1 q}{n_2} \mathbb{F}^{-1}(p, n_1, n_2) \tag{2.200}$$

where $X - vec\left(\hat{G}\right)$ is the difference of a vector and the estimated frequency response, $\hat{C}_{vec(\hat{G})}$ the sample covariance matrix of $vec\left(\hat{G}\right)$ (from (2.146)) with q degrees of freedom (see (2.147)). $\mathbb{F}^{-1}(p, n_1, n_2)$ denotes the inverse cumulative distribution function of an F-distributed random variable with parameters n_1 and n_2 for the corresponding probability level p; the inverse cumulative distribution function corresponds to the $100 \times p$ percentile[34]. n_1 and n_2 are given by

$$n_1 = 2n_{in}n_{out} \tag{2.201}$$

and

$$n_2 = 2q - 2n_{in}n_{out} + 2, \tag{2.202}$$

i.e. n_1 is the number of degrees of freedom of the estimate $\hat{G}$; n_2 results from the number of degrees of freedom q of the covariance matrix and n_1. Note that the parameters n_1 and n_2 include an additional factor 2 compared to the real case, that accounts for the additional degrees of freedom due to the complex distribution of $\hat{G}$ (Giri, 1965; Pintelon & Schoukens, 2012, p. 573).

It must be further ensured that the parameter n_1 and n_2 are true positive integers, as otherwise $\mathbb{F}^{-1}(p, n_1, n_2)$ does not exist: The covariance of the F-distribution is defined only for $n_2 > 4$. Hence the degree of freedom q in equation (2.202) must be sufficiently large, cf. sections 2.5.1 and 2.5.2, particularly equation (2.127).

2.6.4.2 Simultaneous Confidence Regions of FRM Estimates

When applied to frequency response matrix estimates, the vectorized matrix $\mathrm{vec}(\hat{\mathrm{G}})$ and its sample covariance estimates $\hat{\mathrm{C}}_{\mathrm{vec}(\hat{\mathrm{G}})}$ are inserted in equation (2.195), resulting in

$$\left(a^T\left(X - vec\left(\hat{G}\right)\right)\right)^H \left(a^T \hat{C}_{vec(\hat{G})} a\right)^{-1} \left(a^T\left(X - vec\left(\hat{G}\right)\right)\right) \leq \frac{n_1 q}{n_2} \mathbb{F}^{-1}(p, n_1, n_2) \tag{2.203}$$

with $n_1 = 2n_{in}n_{out}$ and $n_2 = 2q - 2n_{in}n_{out} + 2$ from equations (2.201), (2.202) and q the number of degrees of freedom of the covariance matrix estimate. With $c = \frac{n_1 q}{n_2}$ and $\mathbb{F}^{-1}(\sim) = \mathbb{F}^{-1}(p, n_1, n_2)$ confidence intervals for $\hat{g} = a^T vec\left(\hat{G}\right)$ are given by

$$\hat{g} - \sqrt{c\ \mathbb{F}^{-1}(\sim)\ a^T \hat{C}_{vec(\hat{G})} a}\ \leq\ \hat{g}\ \leq \hat{g} + \sqrt{c\ \mathbb{F}^{-1}(\sim)\ a^T \hat{C}_{vec(\hat{G})} a} \tag{2.204}$$

[34] Note that p is in the range from 0 to 1; with $p = 0.9$, the $100 \times p$ percentile contains 90% of all values.

a^T can be chosen as the columns of the identity matrix to derive simultaneous confidence regions for single elements of $\hat{G}$: With a being zero except for $a_{[i]} = 1$, the term $a^T \hat{C}_{vec(\hat{G})} a$ in (2.204) reduces to $\hat{C}_{vec(\hat{G}),[i,i]}$, i.e. diagonal elements of $\hat{C}_{vec(\hat{G})}$. Hence the simultaneous confidence interval for a single element of $vec(\hat{G})$ depends only on its respective variance; the numerical values of the off-diagonal elements of $\hat{C}_{vec(\hat{G})}$ (i.e. the covariances) do not influence the simultaneous confidence regions:

$$X_{[i]} - \sqrt{c\ \mathbb{F}^{-1}(\sim)\hat{C}_{vec(\hat{G}),[i,i]}} \leq vec(\hat{G})_{[i]} \leq X_{[i]} + \sqrt{c\ \mathbb{F}^{-1}(\sim)\hat{C}_{vec(\hat{G}),[i,i]}} \qquad (2.205)$$

This includes, that confidence regions for $X_{[b]},\ X_{[c]}, b \neq c$, are statistically independent[35], which is the basic reason for the simpler handling of simultaneous confidence regions.

2.6.4.3 Bonferroni-Type Confidence Intervals for FRM Estimates

For complex random variables, the Bonferroni approach from equation (2.199) needs to be slightly adjusted, as each complex random variable has two degrees of freedom (real part and imaginary part). As a consequence, the confidence intervals follow an F-distribution with parameters 2 and $2q$ (Pintelon & Schoukens, 2012, p. 237). The confidence intervals for a *single element* of the $n_{out} \times n_{in}$ matrix $\hat{G}_{yu,[i,j]}$ with confidence level $p = 1 - \alpha$ are thus given by

$$\frac{\left|vec(\hat{G}_{[i]}) - vec(G_{0,[i]})\right|^2}{\hat{C}_{vec(\hat{G}),[i]}} \leq \mathbb{F}^{-1}\left(1 - \frac{\alpha}{n_{in}n_{out}}, 2, 2q\right), \qquad (2.206)$$

where $\left|vec(\hat{G}_{[i]}) - vec(G_{0,[i]})\right|$ is the magnitude of the estimation error of the i'th element of $vec(\hat{G})$ with $\hat{C}_{vec(\hat{G}),[i,i]}$ the respective diagonal entry of the sample covariance matrix with q degrees of freedom, see section 2.5.4.7 and (Pintelon & Schoukens, 2012, pp. 51, 237), and $1 - \frac{\alpha}{n_{in}n_{out}}$ the Bonferroni-correction of the confidence level; the scaling factor $n_X(n-1)/(n-n_X)$ in equation (2.197), that relates the F- and the t^2-distribution, is in this case equal to 1 and vanishes, cmp. (Pintelon & Schoukens, 2012, p. 237).

2.6.5 Confidence Regions for Single Elements of $\hat{G}_{yu}$

2.6.5.1 Confidence Regions for Unbiased Estimates

The confidence intervals computed in equation (2.206) are circular shaped, as they depend only on the magnitude of the error and not on its phase. For a single element of the estimated frequency response matrix $\hat{G}_{[i,j]}$, the confidence regions are circles, centred at $\hat{G}_{[i,j]}$ with radius $r_{p,[i,j]}$. For simpler indexing, the formula for r_p is given in terms of $vec(\hat{G})_{[i]}$, i.e. with respect to the vectorised matrix:

$$r_{p,[i]}(k) = \sqrt{\mathbb{F}^{-1}(p, 2, 2M-2)\ \hat{C}_{vec(\hat{G}),[i,i]}(k)}, \qquad (2.207)$$

where p denotes the confidence level, i.e. the 100p%- percentile contained inside the confidence region. The circular confidence regions extend symmetrically along the real and imaginary axis and contain the real value of $\hat{G}$ with probability p, where $0 \leq p \leq 1$.

The standard deviation of a single element of the frequency response function is given by

[35] It is noted that the confidence regions are nevertheless correlated if the covariance matrix estimates $\hat{C}_{vec(\hat{G})}(k)$ are correlated over frequency, as is the case for the fast LPM.

$$\hat{\sigma}_{vec(\hat{G}),[i]}(k) = \sqrt{\hat{C}_{vec(\hat{G}),[i,i]}} \tag{2.208}$$

For a single element of $\hat{G}_{yu}$, equation (2.207) can be rewritten in terms of standard deviation with simpler indexing, where $\hat{\sigma}_{\hat{G}}(k)$ is the square root of the respective covariance matrix element:

$$r_p(k) = \hat{\sigma}_{\hat{G}}(k)\sqrt{\mathbb{F}^{-1}(p, 2{,}2M-2)} \tag{2.209}$$

It is noted that $r_p(k)$ depends linearly on $\hat{\sigma}_{\hat{G}}(k)$ (or $\sqrt{\hat{C}_{vec(\hat{G}),[i,i]}(k)}$ respectively) and $\sqrt{\mathbb{F}^{-1}(p, 2, 2M-2)}$. This property is used in section 2.8.3 to compute confident stability measures. The confidence regions do not account for the estimation bias of $\hat{G}_{yu}$; in section 2.8.4 a correction based on estimated confidence levels is introduced.

It is noted that for large M's, the F-distribution in equation (2.209) can be approximated by a logarithm as $r_p(k) = \hat{\sigma}_{\hat{G}}(k)\sqrt{-\ln(1-p)}$. For $p = 0.95$, this gives approximate confidence regions $r_{0.95} \approx \hat{\sigma}_{\hat{G}}(k)\sqrt{3}$; thus, the 95%-confidence regions have a radius of approximately $1.73\ \hat{\sigma}_{\hat{G}}$.[36]

2.6.5.2 *Confidence Regions for Biased Estimates*

The derivation of the confidence regions is assumes that the estimate $\hat{G}$ is unbiased. As shown in section 2.5.4, the fast LPM is prone to an interpolation bias. The observed estimation errors $\left|\hat{G} - G_0\right|$ are thus larger than expected from the noise analysis. To account for this additional error, equation (2.209) is extended with the bias estimate (section 2.5.4.7), resulting in

$$\tilde{r}_p(k) = r_p(k) + \hat{b}_{int}(k) \tag{2.210}$$

To verify the reliability of the confidence regions $\tilde{r}_p(k)$, the cumulative distribution function (cdf) of $\left|\left|\hat{G} - G_0\right| - \hat{b}\right|^2 / \hat{\sigma}_{\hat{G}}^2(k)$ is computed for multiple independent experiments and compared to the analytical $\mathbb{F}(2, 2M-2)$-distribution, see section 5.3.

2.6.6 Summary

The noise in this thesis is modelled as filtered, discrete time band limited white noise. This approach covers a wide class of noise models and includes typical models for turbulence and gyroscope noise, that are the primary noise sources considered in this thesis.

The effect of such noise (also for correlated input- and output noise) on the ETFE is described by the pdf of the estimate and is known analytically. For practical reasons, the pdf is approximated by a Gaussian distribution. The approximation can be applied when the signal-to-noise ratios in the input signal are better than 20dB.

Based on the Gaussian approximation, confidence regions are derived. The most compact confidence regions are ellipsoids, that are hardly comprehensible for high dimensional estimates. Thus, simultaneous confidence regions are derived, that are conservative, as they neglect the covariance between estimates, but simpler to apply. For a single estimate, i.e. for a single element of $\hat{G}_{yu}$, less conservative confidence regions are computed with an

[36] This is not to be confused with the well known $\pm 2\sigma$-rule for real normally distributed random variables.

approach similar to the Bonferroni method; these confidence regions are circular shaped. When the fast LPM is used, a correction of the confidence regions for the interpolation bias is provided.

This concludes the first part of chapter 2 (spanning sections 2.3 to 2.6), in which the estimation of frequency response functions was analysed. With the transient local polynomial method and the fast local polynomial method, two improved estimators were introduced that explicitly account for non-zero initial and final conditions and thus can be applied to the first two periods of data. With the fast local polynomial method, a novel estimator was introduced, that allows to estimate frequency response *matrices* for multiple input systems with full frequency resolution from a *single* experiment.

In the second part of chapter 2 (sections 2.7 and 2.8), the focus is on stability analysis, solely based on the estimated dynamics. In section 2.7 the robust stability criteria are introduced, in section 2.8 they are applied and adjusted to a 3-input-3-output system, that is further analysed in chapter 4.

2.7 Preliminaries on Robust Stability Analysis

In the field of robust control uncertainty is defined as the difference between the actual system and the model of the system. As any model is a simplified image of reality (Ljung, 2009), no model can exactly match the reality. The robust control approach is based on uncertainty models, that quantify this (mis-) match of the (nominal) model with reality. The general idea is that the uncertainty describes a set of models that include the true system dynamics. The robust control approach ensures design goals for all systems in the uncertainty set, thus including the true system – the controller is then robust stable with respect to the model uncertainty. The robust control framework is well covered in the literature, e.g. in (Skogestad & Postlethwaite, 2005), (Zhou, Doyle, & Glover, 1996) or (Levine, 1999); aircraft applications are covered e.g. in (Stevens & Lewis, 2003).

The frequency domain is well suited to describe model uncertainties, as it provides very simple means of uncertainty models (Skogestad & Postlethwaite, 2005). Frequency domain uncertainties can be easily added to nominal models as additional additive or multiplicative terms. With suitable transformations it is possible to find sufficient stability criteria for linear systems with uncertainties. Those criteria are based on singular values and the small gain theorem (Postlethwaite, Edmunds, & MacFarlane, 1981).

In the section at hand, the general uncertainty model is described and stability criteria for uncertain systems are introduced. The description is widely based on (Skogestad & Postlethwaite, 2005), where more details can be found.

2.7.1 Modelling Uncertainty of Linear Systems

The frequency domain is very well suited to describe neglected or unknown dynamics, allowing for uncertainty descriptions that are simple and still realistic. This makes the frequency domain useful for robust control, i.e. for control of uncertain systems. As it is shown later, the frequency-domain approach for robust control can be very well combined with the estimation of frequency response functions shown in sections 2.5 and 2.6.

The basic idea in robust control is to check if the design specifications (e.g. stability criteria) are satisfied even for the worst-case uncertainty. To do so, it is assumed that the dynamics of the nominal plant are described by a set of possible LTI systems with a fixed linear controller. All possible realizations form the uncertainty set Π, where the nominal plant transfer function $G(s)$ is contained in Π, i.e. $G(s) \in \Pi$. Following the nomenclature of

(Skogestad & Postlethwaite, 2005), within this chapter particular realizations of $G(s)$ are denoted with subscript p, e.g. $G_p(s)$.

To describe uncertainties mathematically, norm-bounded uncertainty descriptions are used. That means, the set Π is generated from a nominal plant $G(s)$ by adding H_∞-norm bounded perturbations Δ, where H_∞-norm of Δ is less than or equal to 1 (Skogestad & Postlethwaite, 2005, p. 294). The perturbations are formulated in the Fourier domain, i.e. the Laplace operator is replaced by the complex frequency $j\omega$, cmp. (Skogestad & Postlethwaite, 2005, p. 294)

$$\|\Delta(j\omega)\|_\infty \leq 1 \tag{2.211}$$

In the block diagram, the uncertainty block is either parallel to or in series with the respective nominal block, leading to additive or multiplicative uncertainties; within this thesis, only additive uncertainties are used.

2.7.1.1 Additive Uncertainty

A disc shaped uncertainty region may be generated by an additive complex norm-bounded perturbation around a nominal plant G. In terms of Fourier transforms, the set Π_A of an uncertain system is given by

$$\Pi_A:\ G_p(j\omega) = G(j\omega) + w_A(j\omega)\Delta_A(j\omega);\ \ \|\Delta_A(j\omega)\| \leq 1\ \forall\omega, \tag{2.212}$$

where the subscript A indicates an additive uncertainty.

$\Delta_A(j\omega)$ attains all possible values with $\|\Delta_A(j\omega)\|_\infty \leq 1$ and describes a disc with radius 1 with its centre at the origin of the complex plain. The factor $w_A(j\omega)$ can be interpreted as a weighting that shapes the uncertain as a function of frequency. As only the magnitude of $w_A(j\omega)$ matters, the uncertainty $\Delta_A(j\omega)$ is generally chosen to be stable and minimum phase. (Skogestad & Postlethwaite, 2005, pp. 260–262)

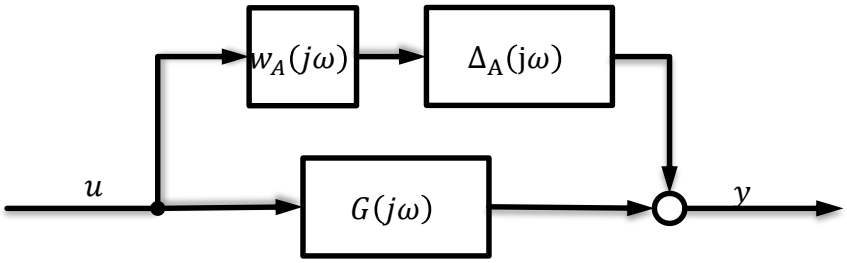

Figure 2-24: Schematic of additive uncertainty of $G(s)$.

2.7.1.2 Parametric and Nonparametric Uncertainties

In the literature, uncertainties are sometimes distinguished in parametric and non-parametric uncertainties. This classification refers to $w(j\omega)$: For parametric uncertainties, $w(j\omega)$ is described by a parametric model, e.g. a transfer function. For nonparametric uncertainties $w(j\omega)$ is a nonparametric function, e.g. a frequency response function. Within this thesis only non-parametric uncertainties are used, as those can be modelled directly from the FRF measurements.

2.7.1.3 Structured and Unstructured Uncertainties

When multiple independent sources of uncertainty $\Delta_{[i,j]}(j\omega)$ are combined, they can be arranged in an uncertainty matrix. If multiple, independent uncertainties are present in the model, the matrix $\Delta(j\omega)$ will be a diagonal matrix, with each nonzero element $\Delta_{[i,i]}$ being a norm bounded uncertainty by itself.

$$\Delta(s) = \begin{bmatrix} \Delta_{11} & & 0 \\ & \ddots & \\ 0 & & \Delta_{nn} \end{bmatrix} \tag{2.213}$$

Such an uncertainty is called structured, as the H_∞-boundedness is applied to individual matrix elements, i.e. $\left\|\Delta_{[i,j]}\right\|_\infty < 1$, resulting in a mathematical structure of the uncertainty model. By contrast, uncertainty models, where the boundedness criterion is applied to the entire matrix (i.e. $\|\Delta\|_\infty < 1$), are called unstructured.

2.7.2 General Model Configuration for Uncertain Systems

Standard forms have been established for stability analysis and control design of uncertain systems. They are based on the general control configuration, shown in Figure 2-25. Its basic idea is to separate the uncertainty from the plant dynamics and the controller. For better readability, the dependence on frequency is dropped.

2.7.2.1 General Control Configuration

The general control configuration has been introduced by (Doyle, 1983, 1984). Its idea is to separate the plant, the controller and the uncertainty in individual blocks, as shown in Figure 2-25. Due to its generality the general control configuration forms a widely used framework for the analysis and synthesis of robust control systems (Doyle, 1983; Levine, 1999).

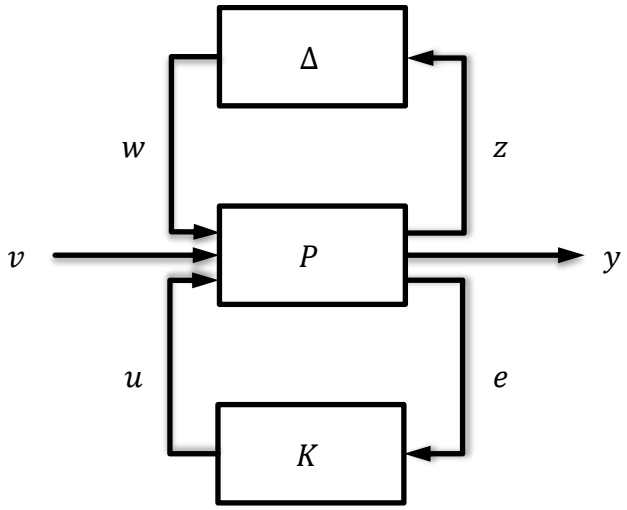

Figure 2-25: Block diagram of general control configuration

As shown in Figure 2-25, the plant outputs *e* and *z* are fed back to P, via K and Δ respectively. The block diagram corresponds to a set of equations, where (2.214) describes the plant, (2.215) the lower feedback loop with the controller and (2.216) the upper feedback loop with the perturbation.

$$\begin{bmatrix} z \\ y \\ e \end{bmatrix} = P \begin{bmatrix} w \\ v \\ u \end{bmatrix} = \begin{bmatrix} P_{11} & P_{12} & P_{13} \\ P_{21} & P_{22} & P_{23} \\ P_{31} & P_{32} & P_{33} \end{bmatrix} \begin{bmatrix} w \\ v \\ u \end{bmatrix} \tag{2.214}$$

$$u = Ke \tag{2.215}$$

$$w = \Delta z \tag{2.216}$$

The individual components of P can be derived from the system's block diagram. Figure 2-26 shows a closed loop system with negative feedback and a weighted additive uncertainty. The respective signals and blocks are listed in Table 2-6.

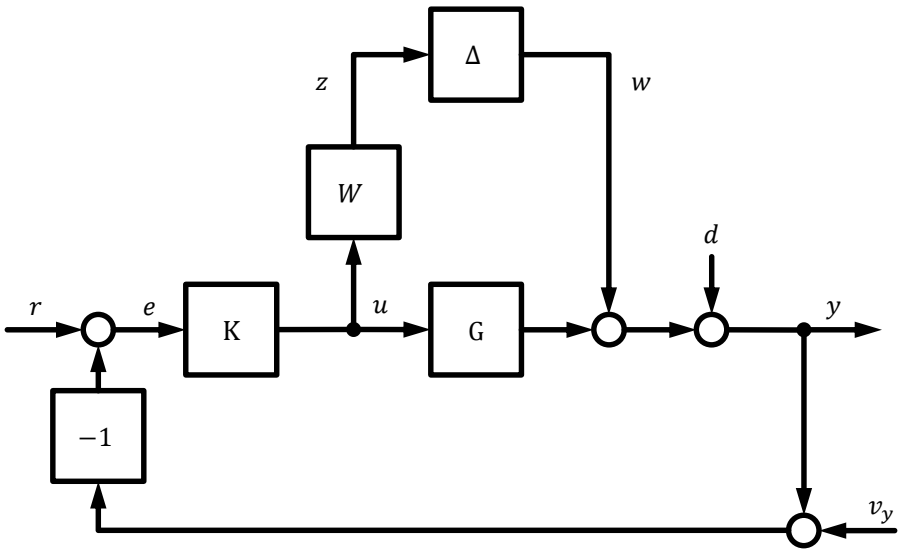

Figure 2-26: Block diagram of a closed loop system with additive uncertainty

Table 2-6: Signals and Blocks in general closed loop system.

Symbol	Description
$\boldsymbol{K}$	Controller
$\boldsymbol{G}$	Nominal plant
$\boldsymbol{W}$	Weighting of uncertainty
$\boldsymbol{\Delta}$	Additive uncertainty
$\boldsymbol{r}$	Reference input
$\boldsymbol{e}$	Controller input
$\boldsymbol{u}$	Controller output, plant input
$\boldsymbol{v_y}$	Measurement noise
$\boldsymbol{d}$	Disturbance
$\boldsymbol{y}$	Control error
$\boldsymbol{z}$	Weighted uncertainty input
$\boldsymbol{w}$	Uncertainty output

To transform the closed loop system into general control configuration, the outputs z, y and e are used; the inputs are u, v, and w, where v contains the reference input, noise and disturbances:

$$v = \begin{bmatrix} d \\ v_y \\ r \end{bmatrix} \tag{2.217}$$

The transfer dynamics from u, v, w to z, y, e can be derived from Figure 2-26; with identity and zero matrices of suitable size, denoted by I and 0 respectively, they result in

$$\begin{bmatrix} z \\ y \\ e \end{bmatrix} = \begin{bmatrix} 0 & 0 & 0 & 0 & W \\ I & I & 0 & 0 & G \\ -I & -I & -I & +I & -G \end{bmatrix} \begin{bmatrix} w \\ d \\ v_y \\ r \\ u \end{bmatrix} \tag{2.218}$$

To rewrite equation (2.218) in the general control configuration, the respective elements are found by comparing equation (2.218) with (2.214):

$$\begin{aligned} &P_{11} = 0, \quad && P_{12} = [0 \quad 0 \quad 0], \quad && P_{13} = W, \\ &P_{21} = I, \quad && P_{22} = [I \quad 0 \quad 0], \quad && P_{23} = G, \\ &P_{31} = -I, \quad && P_{32} = [-I \quad -I \quad +I], \quad && P_{33} = -G \end{aligned} \tag{2.219}$$

A more formal framework to compute P and M from general block diagrams are linear fractional transforms (LFT); details can be found in (Doyle, 1984) or (Zhou et al., 1996).

2.7.2.2 NΔ-STRUCTURE

For stability analysis, the general control configuration can be reduced to the $N\Delta$-structure. For stability analysis, the controller is fixed. Hence it can be included in the model plant. The resulting model is based on the general control configuration; however, it contains only the plant and the uncertainty block. Figure 2-27 shows the block diagram with the plant model N and the uncertainty block Δ.

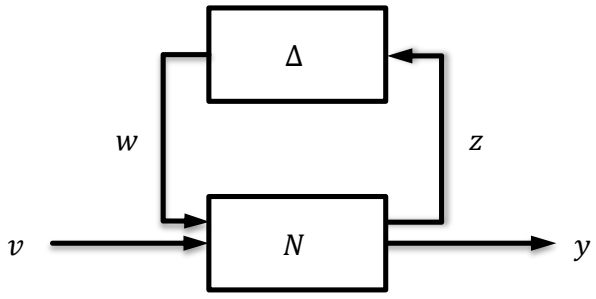

Figure 2-27: Block diagram of $N\Delta$-structure for robust analysis.

The transfer function of the $N\Delta$-structure is

$$\begin{bmatrix} z \\ y \end{bmatrix} = N \begin{bmatrix} w \\ v \end{bmatrix} = \begin{bmatrix} N_{11} & N_{12} \\ N_{21} & N_{22} \end{bmatrix} \begin{bmatrix} w \\ v \end{bmatrix} \tag{2.220}$$

For the system of Figure 2-26 with an additive uncertainty, the elements N_{11} and N_{12} are shown in terms of the P-matrix; the derivation is shown in appendix C.4.

$$N_{11} = P_{11} + P_{13}\,(I - KP_{33})^{-1}\,KP_{31} \tag{2.221}$$

$$N_{12} = P_{12} + P_{13}\,(I - KP_{33})^{-1}\,KP_{32} \tag{2.222}$$

2.7.2.3 $M\Delta$-Structure

For the analysis of robust stability, only the N_{11} term is relevant and the $N\Delta$-structure can be further reduced to the $M\Delta$-structure, shown in Figure 2-28, where $M = N_{11}$ (Skogestad & Postlethwaite, 2005, p. 292). In the $M\Delta$-structure the external input v and output y are discarded and M equals the transfer function G_{zw}, relating the perturbation output and input.

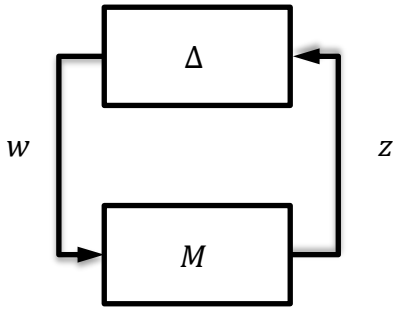

Figure 2-28: Block diagram of $M\Delta$-structure for robust analysis.

With equation (2.221), the transfer function G_{zw}, relating the perturbation output and input, is given by

$$M = (P_{11} + P_{13}\,(I - KP_{33})^{-1}\,KP_{31})\,w \tag{2.223}$$

Inserting equation (2.219), M finally results in

$$M = -W\,(I + KG)^{-1}\,K \tag{2.224}$$

where W denotes the weighting matrix of the uncertainty, I the identity matrix of suitable size, K the controller and G the system dynamics; the matrices M, W, K and G can be functions of frequency. Within this thesis it is assumed that $(I + KG)^{-1}$ exists. It is further noted that a scaling of the uncertainty W with a scalar a also affects M linearly.

2.7.3 Robust Stability of Uncertain Systems

In robust stability (RS) analysis it is examined, whether the uncertain system remains stable for all allowed perturbations, i.e. for all plants in the uncertainty set. The RS approaches applied in this thesis are based on a nominal plant. The nominal plant does not contain uncertainties and is required to be stable (nominal stability), with or without a controller.

In the following section, criteria are shown that ensure robust stability for the entire uncertainty set.

2.7.3.1 H_∞-Criterion for Robust Stability

Based on the small gain theorem Skogestad and Postlethwaite show that robust stability is ensured for a nominal stable system $M(j\omega)$ and stable perturbations $\Delta(j\omega)$ with $\|\Delta\|_\infty \leq 1$,

if
$$\|M(j\omega)\|_\infty < 1 \;\; \forall\, \omega \in \mathbb{R} \tag{2.225}$$

where $M(j\omega)$ is the transfer function of the $M\Delta$-structure derived in section 2.7.2.3 and $\|M(j\omega)\|_\infty$ denotes its infinity-norm, see (Skogestad & Postlethwaite, 2005, p. 306). Inserting equation (2.224) (and dropping the frequency argument) results in

$$\|-W\,(I + KG)^{-1}\,K\|_\infty < 1 \tag{2.226}$$

2.7.3.2 Structured Singular Value Criterion for Robust Stability

For structured uncertainties, (Skogestad & Postlethwaite, 2005) further show a tighter robust stability criterion. It is based on structured singular values and is applied to the same uncertain system $M(j\omega)$ as the H_∞-criterion. The difference between the two criteria is in the structure of the uncertainty, as the structured singular value criterion exploits the internal structure of the uncertainty, see section 2.7.1.3 and (Skogestad & Postlethwaite, 2005, pp. 309–311) for details. Structured singular values are often denoted with mu, Mu or μ. In this thesis, they are denoted with ssv(·) to avoid disambiguities with the mean value.

The structured singular value is introduced in (Packard & Doyle, 1993) as the inverse of the minimum factor κ_m that makes $\det(I - \kappa_m M\Delta) = 0$, i.e.

$$\mathrm{ssv}(M)^{-1} = \min\{\bar{\sigma}_{max}(\Delta) \mid \det(I - M\Delta) = 0\}, \tag{2.227}$$

where Δ is a structured uncertainty with $\bar{\sigma}_{max}(\Delta) \leq 1$. It is noted that κ_m is a function of frequency. Similarly to the H_∞-criterion, for a stable system $M(j\omega)$ and a stable uncertainty $\Delta(j\omega)$ with maximum singular value $\bar{\sigma}_{max}\big(\Delta(j\omega)\big) \leq 1$, the $M\Delta$-system is stable if and only if

$$\mathrm{ssv}\big(M(j\omega)\big) < 1 \tag{2.228}$$

Inserting equation (2.224) results in the robust stability criterion

$$\mathrm{ssv}(-W\,(I + KG)^{-1}\,K) < 1 \tag{2.229}$$

The numerical computation of structured singular values is computationally involved. Approximations are available (Young & Doyle, 1990; Young, Newlin, & Doyle, 1992), but they still take more computational effort than the H_∞-norm.

2.7.3.3 Maximum Stable Uncertainty

In the literature, the robust stability criteria are usually introduced in terms of the H_∞-norm or the structured singular value μ (here denoted as ssv). Analogously, both criteria can be formulated in terms of their inverses, usually denoted with κ. To distinguish the criteria, κ_{H_∞} and κ_{ssv} are introduced respectively as

$$\kappa_{H_\infty}(j\omega) = \frac{1}{\|M(j\omega)\|_\infty} \tag{2.230}$$

$$\kappa_{ssv}(j\omega) = \frac{1}{ssv\big(M(j\omega)\big)} \tag{2.231}$$

In the following, κ will be used to compute the maximum uncertainty that can be tolerated by the given controller, before the system gets unstable. The approach follows the alternative definition of the structured singular value introduced in (Safonov, 1982); it results in

$$\kappa_{H_\infty}(j\omega) > 1, \ \forall\, \omega \tag{2.232}$$

and

$$\kappa_{ssv}(j\omega) > 1, \ \forall\, \omega \tag{2.233}$$

as robust stability criteria, respectively. In the thesis at hand, the robust stability criteria (2.106) and (2.107) in terms of κ are more convenient, as they directly provide the maximum uncertainty that can be tolerated by a given controller: With the multiplication rules for scalar multiplication of matrix norms, multiplication of the uncertainty W_Δ in equation (2.224) with a scalar factor a gives

$$\begin{aligned}\left\|(aW_\Delta)\left(I+K\hat{G}_{yu}\right)^{-1}K\right\|_\infty &= |a|\left\|W_\Delta\left(I+K\hat{G}_{yu}\right)^{-1}K\right\|_\infty \\ &= |a|\cdot\|M\|_\infty\end{aligned} \tag{2.234}$$

With the definition of κ, the equation can be rewritten as

$$\left\|(aW_\Delta)\left(I+K\hat{G}_{yu}\right)^{-1}K\right\|_\infty = |a|\cdot\left(\kappa_{H_\infty}\right)^{-1} \tag{2.235}$$

This shows that for the given model structure, $\|M\|_\infty$ is linear in W_Δ and thus the marginal case for the scaled uncertainty where $\left\|(aW_\Delta)\left(I+K\hat{G}_{yu}\right)^{-1}K\right\|_\infty = 1$ will be reached for

$$a = \kappa_{H_\infty}^{-1}a \tag{2.236}$$

In other words, the marginal uncertainty $W_{\Delta,\kappa}$ that fulfils the robust stability criterion (2.252) just no more, is given by

$$W_{\Delta,\kappa} = \kappa_{H_\infty}\,W_\Delta \tag{2.237}$$

For the structured singular value criterion the same result holds; it is a direct consequence of the definition of the structured singular value (Safonov, 1982). Thus for the structured singular value criterion, the marginal uncertainty $W_{\Delta,\kappa}$ is given by

$$W_{\Delta,\kappa} = \kappa_{ssv}\,W_\Delta \tag{2.238}$$

It is noted that the marginal uncertainty case, i.e. for $W_{\Delta,\kappa} = \kappa_{H_\infty}W_\Delta$, the RS criterion is not fulfilled any more. For simplicity, in the course of this thesis, the marginal case is denoted as the maximum uncertainty, keeping in mind, that for RS the actual uncertainty W_Δ must be *smaller* than $W_{\Delta,\kappa}$.

2.7.3.4 Nominal Stability

The nominal system is called nominally stable, if it is stable (or stabilized by the controller) without the model uncertainty. (i.e. with $\Delta = 0$). Both, the H-infinity and the structured singular value criterion, are based on the assumption that $M(j\omega)$ is nominal stable.

For parametric models, the nominal stability can be proven with classical stability measures, e.g. by pole-zero analysis. For estimated, nonparametric models as introduced in section 2.5, the proof of nominal stability is more involved. To show nominal stability a two-step approach is introduced:

- In the first step the robust stability of the estimated dynamics $\hat{G}_{yu}$ (without uncertainty) with respect to a stable reference model G_n is shown, where the uncertainty is based on the magnitude estimation error $\left|G_n - \hat{G}_{yu}\right|$.
- In the second step, $\hat{G}_{yu}$ is known to be stable and is used as nominal model. The uncertainty is based on the sample covariance estimate $\hat{C}_{vec(\hat{G})}$ and circular confidence regions $\hat{r}_p$ respectively.

The nominal model G_n must be known to be stable in advance; for parametric models G_n stability can be shown e.g. by classical pole-zero analysis. The full approach is shown in detail in section 2.8.3.

2.8 Stability of Estimated Systems $\hat{G}_{yu}$

To analyse stability of the estimated system, the robust stability criteria introduced in section 2.7 are applied to the estimates from section 2.5 and 2.6. The estimation algorithm provides the estimated frequency response matrix $\hat{G}_{yu}$, its covariance matrix $\hat{\sigma}_{\hat{G}_{yu}}$, confidence regions r_p and estimates of the bias $\hat{b}$. The RS criteria test, if all system realization inside the confidence region $\hat{r}_p$ are stable or not. If RS is given, it can be stated, that the true system is robust stable with probability p. Thus, the size of the uncertainty is directly linked to a confidence level. For the maximum uncertainty that is robust stable, the corresponding confidence level is called *confident stability level* (CSL). It is used in chapter 5 as a measure of system integrity.

In the preceding section, robust stability criteria based on H_∞ and structured singular values have been introduced. They are based on a general closed loop system model structure with additive uncertainty parallel to the plant. In section 2.8.1, the robust stability criteria are adjusted to a model with three inputs and three outputs, as it is later used in chapters 4 and 5. The uncertainty model is transformed to the $M\Delta$-structure (section 2.8.1). The robust stability criteria are then applied twice to show robust stability of the estimate $\hat{G}_{yu}$ w.r.t. its uncertainty model (section 2.8.2) and nominal stability of $\hat{G}_{yu}$ with respect to a given, nominal plant model G_n that is known to be stable (section 2.8.3).

The frequency response estimates describe the system dynamics only for discrete frequencies; the consequences for the stability criteria are discussed in section 2.8.4. In section 2.8.5 confidence levels are computed, based solely on the frequency response estimates, that describe the probability that the true system to be robust stable.

2.8.1 Uncertainty Model of Estimated System

2.8.1.1 Model Structure

The FRF estimation in section 2.5 assumes a model structure as shown in Figure 2-15. For further analysis, the model is simplified and adjusted: In the experimental part of this thesis in chapters 3 to 5, the reference signal $r(t)$, the controller input $y_1(t)$ and the controller output $u_1(t)$ are assumed to be known exactly as in typical flight test experiments they are processed digitally; the measurement noise is thus summarized in v_p and the terms $m_u(t)$ and $m_y(t)$ are removed. The reference signal is infused directly to the controller (no additional actuator). The model is further transformed to the standard control configuration with unity feedback. The resulting model is shown in Figure 2-29: G contains the aircraft dynamics, control surface actuators and sensor dynamics. K contains the fixed, known linear controller[37].

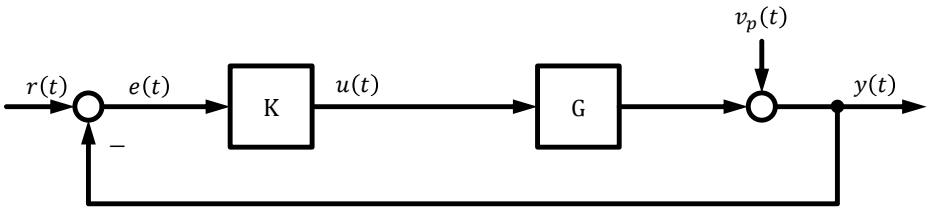

Figure 2-29: Block diagram of aircraft with unit feedback controller.

[37] Here, „fixed“ is used in the sense of time-invariant and for delimitation from the robust control design, where the controller varies. Different from the given example, the controller gains $K(s)$ can be functions of frequency.

2.8.1.2 UNCERTAINTY MODEL

As $\hat{G}_{yu}$ is estimated, it includes measurement errors. As shown in section 2.6 the resulting simultaneous confidence regions are circles with radii $r_p(k)$. The radius is a linear function of the diagonal elements of the cross covariance matrix $\hat{C}_{vec(\hat{G})}$. To include the estimation uncertainty in the model, the block diagram in Figure 2-29 is extended with an additive, weighted perturbation block. The resulting uncertainty then contains the true model with probability p.

The confidence intervals hold simultaneously with given probability. This corresponds to independent perturbations of the elements of $\widehat{\mathrm{G}}_{\mathrm{yu}}$. Independent perturbations of $\widehat{\mathrm{G}}_{\mathrm{yu}}$ are modelled by diagonal perturbation matrices Δ_G with dimension $(n_{in} \cdot n_{out}) \times (n_{in} \cdot n_{out})$ with $n_{in} \cdot n_{out}$ nonzero elements along the diagonal. Each diagonal element corresponds to the perturbation of the respective element of the $n_{out} \times n_{in}$ matrix $\hat{G}_{yu}$.

$$\Delta_G(j\omega) = \begin{bmatrix} \Delta_1(j\omega) & & 0 \\ & \ddots & \\ 0 & & \Delta_{n_{in} \cdot n_{out}}(j\omega) \end{bmatrix} \tag{2.239}$$

As introduced in section 2.7.1, the perturbation Δ_G is normalized, so that it describes circular discs with radius 1:

$$\|\Delta_G(j\omega)\|_\infty \leq 1 \tag{2.240}$$

To map the perturbation to the correct input and output, two additional matrices S and T are required. S has dimension $(n_{in} \cdot n_{out} \times n_{in})$ and maps the input signal $U(k)$ to the respective perturbations, while T is a $(n_{out} \times n_{in} \cdot n_{out})$ matrix and maps the perturbation to the respective output signal $Y(k)$.

For a (3×3) system, S is selected as

$$\mathrm{S} = \begin{bmatrix} 1 & & \\ 1 & & 0 \\ 1 & & \\ & 1 & \\ & 1 & \\ & 1 & \\ & & 1 \\ 0 & & 1 \\ & & 1 \end{bmatrix} \tag{2.241}$$

And T as

$$\mathrm{T} = \begin{bmatrix} 1 & 0 & 0 & 1 & 0 & 0 & 1 & 0 & 0 \\ 0 & 1 & 0 & 0 & 1 & 0 & 0 & 1 & 0 \\ 0 & 0 & 1 & 0 & 0 & 1 & 0 & 0 & 1 \end{bmatrix} \tag{2.242}$$

So that the matrix product $T \cdot S$ results in a matrix of ones

$$\begin{bmatrix} 1 & 1 & 1 \\ 1 & 1 & 1 \\ 1 & 1 & 1 \end{bmatrix} = \mathrm{TS} \tag{2.243}$$

This selection sorts the uncertainties first by the input signal, then by the output signal. With this order, $\Delta_G(j\omega)$ can be written as

$$\Delta_{\mathrm{G}} = \mathrm{diag}\left(\Delta_{[1,1]}, \Delta_{[2,1]}, \Delta_{[3,1]}, \Delta_{[1,2]}, \Delta_{[2,2]}, \ldots, \Delta_{[n_{out},n_{in}]}\right) \tag{2.244}$$

where $diag\left(\Delta_{[1,1]}, \dots, \Delta_{[n_{out},n_{in}]}\right)$ is a block diagonal matrix with elements $\Delta_{[y,u]}$, where the indices y and u denote the perturbation of the respective elements of $\hat{G}_{yu}$, i.e. $\Delta_{[2,1]}$ is the perturbation of the FRF from input 1 to output 2 respectively.

The same transformation is applied to the system matrix $\hat{G}_{yu}$. The transformation does not change the system dynamics, but is required to disturb each element in $\hat{G}_{yu}$ independently. This leads to a diagonal system matrix $\hat{G}_{yu,diag}$ with elements as shown in equation (2.245), where the index yu in $\hat{G}_{yu}$ is dropped to save space and $\hat{G}_{[i,j]}$ denotes the element in the i-th row and the j-th column of $\hat{G}_{yu}$.

$$\hat{\mathrm{G}}_{\mathrm{diag}} = \mathrm{diag}\left(\hat{G}_{[1,1]}, \hat{G}_{[2,1]}, \dots, \hat{G}_{[n_{out},1]}, \hat{G}_{[1,2]}, \dots, \hat{G}_{[n_{out},2]}, \dots, \hat{G}_{[n_{out},n_{in}]}\right) \tag{2.245}$$

or in other terms

$$\hat{\mathrm{G}}_{\mathrm{diag}} = \mathrm{diag}\left(\mathrm{vec}\left(\hat{G}_{yu}\right)\right) \tag{2.246}$$

The resulting system is fully described by the block diagram in Figure 2-30.

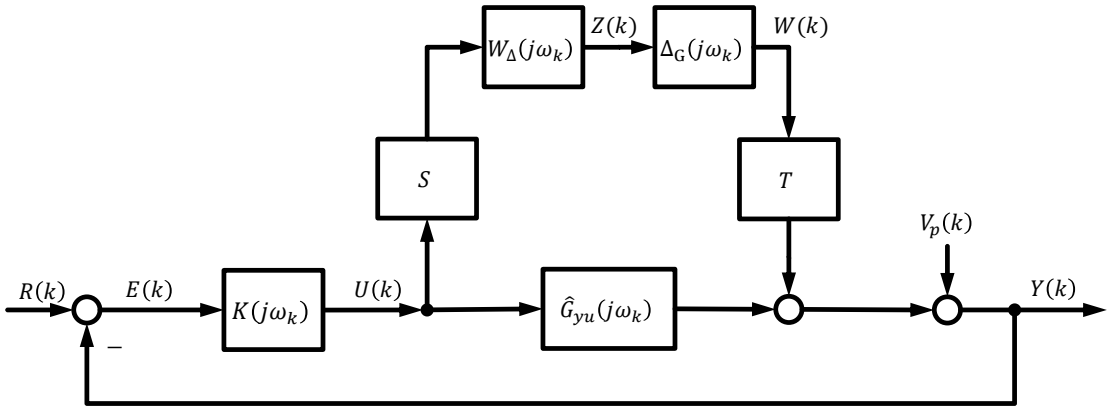

Figure 2-30: Block diagram of estimated AC dynamics with additive uncertainty.

2.8.1.3 Weighting Matrix

The weighting W describes the size of the respective uncertainty. For the FRF estimates these are the respective diagonal elements of the covariance estimate $\hat{C}_{vec(\hat{G})}$. For unbiased estimates $\hat{G}_{yu}$ the uncertainty $W_\Delta(j\omega_k)$ equals the standard deviation $\hat{\sigma}_{\hat{G}}(k)$ from equation (2.148)

$$W_\Delta(k) = \hat{\sigma}_{\hat{G}}(k) \tag{2.247}$$

For biased estimates, $W_\Delta(k)$ is

$$W_\Delta(k) = \hat{\sigma}_{\hat{G}}(k) + \hat{b}_{\hat{G}} \tag{2.248}$$

where $\hat{b}_{\hat{G}}$ is the bias estimate introduced in section 2.5.4. This 1σ-uncertainty contains the true model with about 63% probability (cmp. section 2.6.5)

2.8.1.4 MΔ-Structure of Estimated Model

In section 2.7.2.3, the $M\Delta$ structure is derived for a general closed loop system with additive uncertainty. For further analysis the model in Figure 2-30 is transformed to the general control configuration. With the estimated dynamics $\hat{G}_{yu}$, the diagonal weighting matrix W_Δ and the mapping for independent uncertainties S and T, equations (2.218) and (2.219) result in

$$\begin{bmatrix} Z(k) \\ Y(k) \\ E(k) \end{bmatrix} = \begin{bmatrix} 0 & 0 & 0 & 0 & W_\Delta(k) \cdot S \\ T & I & 0 & 0 & G_{yu}(k) \\ -T & -I & 0 & +I & -G_{yu}(k) \end{bmatrix} \begin{bmatrix} W(k) \\ V_p(k) \\ 0 \\ R(k) \\ U(k) \end{bmatrix} \tag{2.249}$$

and

$$\begin{aligned} P_{11} &= 0, & P_{12} &= [0 \quad 0 \quad 0], & P_{13} &= W_\Delta(k) \cdot S, \\ P_{21} &= T, & P_{22} &= [I \quad 0 \quad 0], & P_{23} &= G_{yu}(k), \\ P_{31} &= -I, & P_{32} &= [-I \quad 0 \quad +I], & P_{33} &= -G_{yu}(k), \end{aligned} \tag{2.250}$$

With the additional mapping for a diagonal uncertainty, the M-matrix from equation (2.224) results in

$$M = -SW_\Delta \left(I + K\hat{G}_{yu}\right)^{-1} KT \tag{2.251}$$

2.8.2 Robust Stability of Estimated System

To show robust stability of the estimated model M, the robust stability criteria are applied to the uncertain model introduced in section 2.8.1. In Figure 2-31, the estimated FRF $\hat{G}_{yu}$ is drawn as blue line, the uncertainty W_Δ is indicated by the blue surface with dashed bounds. Robust stability is shown for any realization of G inside the dashed bounds.

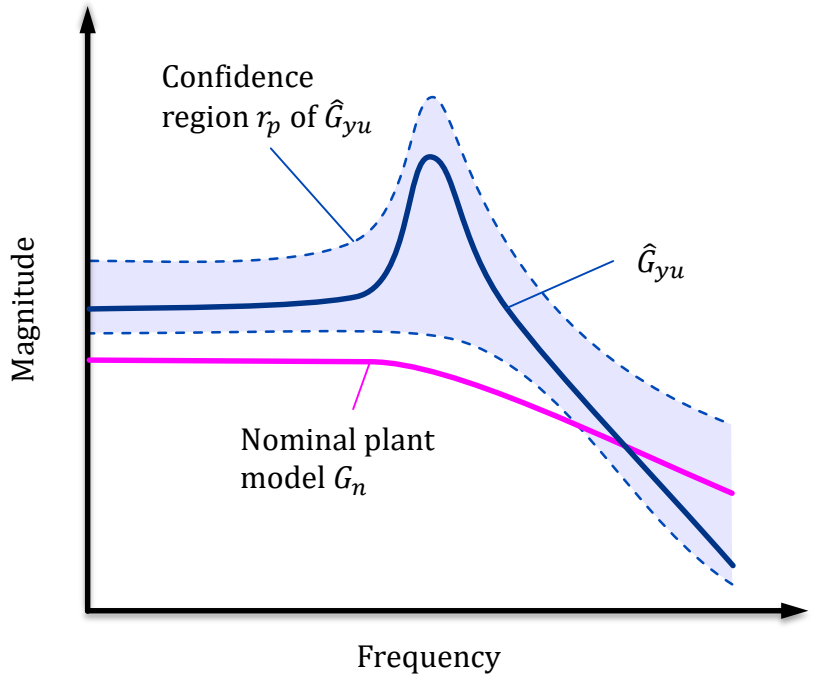

Figure 2-31: Magnitude plot with nominal model G_n, estimated model $\hat{G}_{yu}$ and confidence region r_p .

2.8.2.1 H_∞-CRITERION

Applying the robust stability criterion from (2.225) on equation (2.251) and disregarding the negative sign which does not affect the H_∞-norm, the resulting stability criterion for the system of Figure 2-30 is

$$\left\| SW_\Delta(j\omega_k)\left(I + K\hat{G}_{yu}(j\omega_k)\right)^{-1} KT \right\|_\infty < 1 \tag{2.252}$$

In the experimental part of this thesis, the numerical values of $\left\| SW_\Delta(j\omega_k)\left(I + K\hat{G}_{yu}(j\omega_k)\right)^{-1} KT \right\|_\infty$ cover a wide range of values. For better readability the values are converted to dB. With the conversion to dB, the criterion for stability is

$$dB\left(\left\| SW_\Delta(j\omega_k)\left(I + K\hat{G}_{yu}(j\omega_k)\right)^{-1} KT \right\|_\infty\right) < 0 \tag{2.253}$$

For the H_∞-criterion follows from equation (2.252) with equation (2.230) that κ_{H_∞} is given by

$$\kappa_{H_\infty}(k) = \frac{1}{\left\| SW_\Delta(j\omega_k)\ \left(I + K\hat{G}_{yu}(j\omega_k)\right)^{-1} KT \right\|_\infty} \tag{2.254}$$

where $\left\| SW_\Delta(j\omega_k)\ \left(I + K\hat{G}_{yu}(j\omega_k)\right)^{-1} KT \right\|_\infty$ is a scalar function of frequency.

2.8.2.2 STRUCTURED SINGULAR VALUE-CRITERION

Analogously, inserting M from equation (2.252) into the structured singular value criterion from section 2.7.3.2 results in

$$ssv\left(SW_\Delta(j\omega_k)\ \left(I + K\hat{G}_{yu}(j\omega_k)\right)^{-1} KT\right) < 1 \tag{2.255}$$

Or given in terms of dB:

$$dB\left(ssv\left(SW_\Delta(j\omega_k)\ \left(I + K\hat{G}_{yu}(j\omega_k)\right)^{-1} KT\right)\right) < 0 \tag{2.256}$$

The maximum scaling κ_{ssv} of the uncertainty that results in marginal stability is given by

$$\kappa_{ssv}(k) = ssv\left(SW_\Delta(j\omega_k)\ \left(I + K\hat{G}_{yu}(j\omega_k)\right)^{-1} KT\right)^{-1} \tag{2.257}$$

2.8.3 NOMINAL STABILITY OF ESTIMATED SYSTEM

To show nominal stability of $\hat{G}_{yu}$, the stability criterion from section 2.8.2 is applied again: It is assumed that a nominal plant model G_n is available and G_n is stabilized by the given controller K. As an example G_n could be a parametric plant model as they are commonly used for control design. Stability of G_n can be shown e.g. by classical pole zero analysis. If the uncertainty equals the difference $\left|\hat{G}_{yu}(j\omega) - G_n(j\omega)\right|$, it is ensured that $\hat{G}_{yu}$ is (marginally) contained in the uncertainty regions and the robust stability critertia can be applied. Figure 2-32 illustrates the approach: The nominal plant model G_n is shown as a pink line, $\hat{G}_{yu}$ is shown as blue line. The uncertainty region is shown as pink surface and stretches symmetrically around G_n.

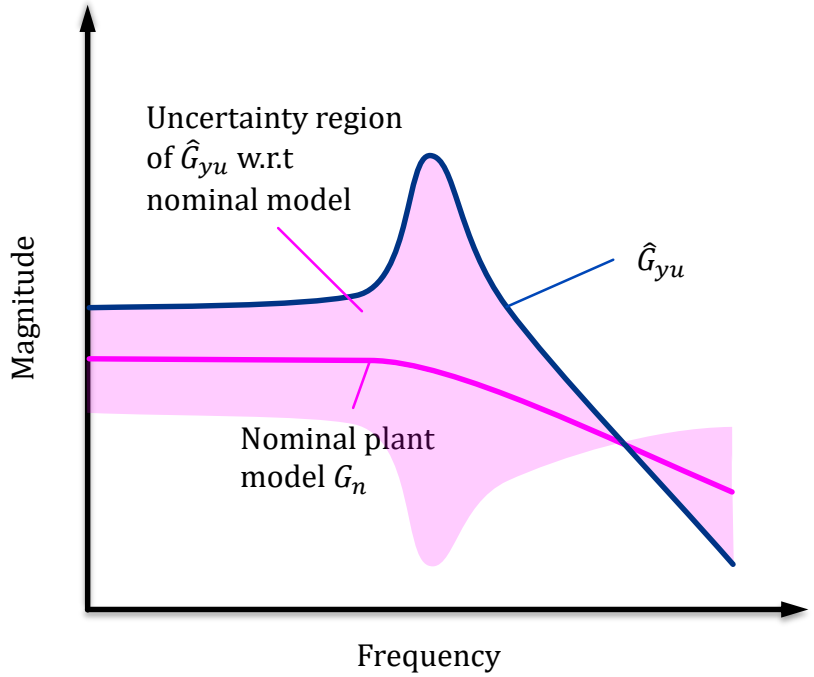

Figure 2-32: Magnitude plot of nominal model with uncertainty set Π_{G_n}.

The uncertainty set Π_{G_n} needs to be chosen such, that the estimate $\hat{G}_{yu}$ is certainly contained, i.e. equation (2.258) needs to be fulfilled.

$$\hat{G}_{yu}(j\omega) = G_n(j\omega) + W_{G_n}(j\omega)\Delta_{G_n}(j\omega) \tag{2.258}$$

Δ_{G_n} has the same shape as Δ_G in section 2.8.1 and $W_{G_n}(j\omega)$ is chosen as the difference of G_n and $\hat{G}_{yu}$. As the weighting W_{G_n} requires no phase information, it can be selected as

$$W_{G_n}(j\omega) = \left|\hat{G}_{yu}(j\omega) - G_n(j\omega)\right| \tag{2.259}$$

Note that for each frequency, the uncertainty region stretches symmetrically above and below G_n. With equation (2.252) nominal stability of $\hat{G}$ w.r.t. the nominal model G_n is achieved for

$$\left\| SW_{G_n}\,(I + KG_n)^{-1}\,KT \right\|_\infty < 1 \tag{2.260}$$

or in terms of κ for

$$\kappa_{H_\infty}(k) > 1 \tag{2.261}$$

i.e. nominal stability is given, if $\kappa_{H_\infty,nom}(k) > 1$. Then equation (2.260) ensures nominal stability of $\hat{G}_{yu}$ and $\hat{G}_{yu}$ is nominally stable w.r.t. the nominal plant G_n. Equation (2.260) can analogously be formulated in terms of $\kappa_{ssv,nom}(k)$.

2.8.4 Inter-Grid Behaviour

The frequency response function estimates describe the system dynamics only at a discrete frequency grid (usually the FFT grid). The estimates do not provide information about the FRF between these frequencies; thus, the intergrid behaviour must be considered separately. In this section, a limit for the intergrid error is derived, based on assumptions of the worst case damping of an intergrid resonance peak.

Intergrid Error Estimate

Due to its finite frequency resolution, the FRF estimate could miss an extremely lightly damped resonance peak, if a very narrow peak is just between two analysed frequencies. Figure 2-33 shows this as a schematic: Along the x-axis, the figure shows the continuous frequency f, the y-axis shows the FRF magnitude. The FRF $\hat{G}(k)$ is estimated only at the discrete frequencies f_{k_1} and f_{k_2}; they are shown as blue balls[38]. The FRF is a smooth function and with a sufficiently fine frequency resolution, the true FRF will be close to the lines elements that connect the discrete point estimates (shown in the figure as blue lines).

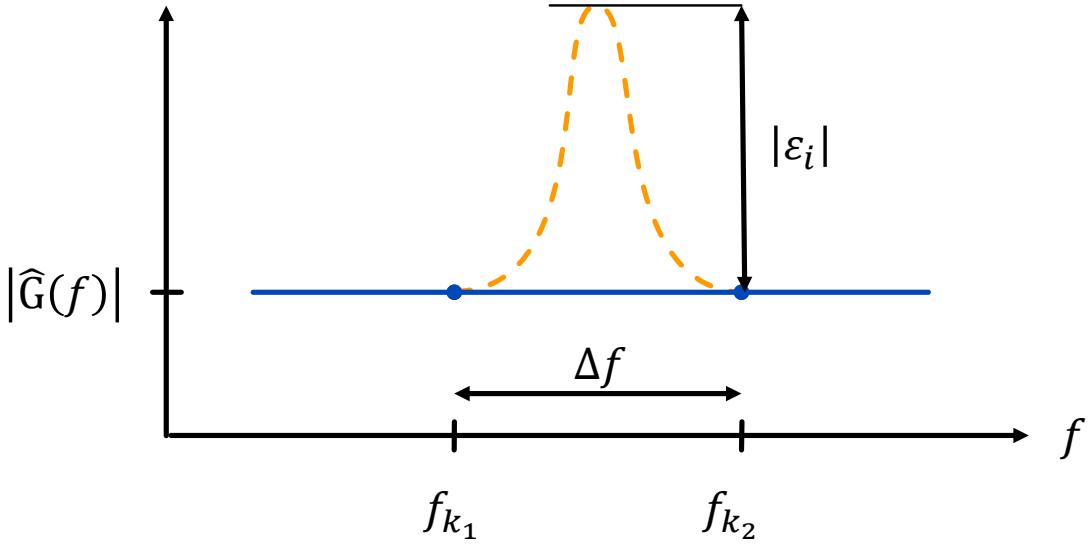

Figure 2-33: Schematic of intergrid error due to discrete frequency resolution.

However, the FRF estimate provides *no information* about the true FRF dynamics at inter-grid frequencies $f \neq f_k$. An extremely lightly damped pole (indicated by the orange, dashed line) would be missed. It is thus clear, that the intergrid dynamics must be accounted for in the robust stability criteria. To do so, the intergrid error $|\varepsilon_i|$ is estimated as function of the frequency resolution. The estimate is derived based on the $3dB$-frequency range of the resonance peak; it can be computed analogously for other intergrid error levels, cmp. Figure 2-35.

As shown in section 2.5.4, the damping and the 3dB-bandwith of a resonance peak are directly related to the frequency resolution and the estimation error: The $3dB$-frequency range around the peak is given by $2\zeta\omega_0$ (or $4\pi\zeta f_0$ in terms of normal frequency); in the example of Figure 2-33, the resonance peak lies at $f_0 = f_{k_1} + \frac{\Delta f}{2}$.

[38] For simplicity $\hat{G}$ is here shown here as a horizontal line.

With a frequency resolution $\Delta f = B_{3dB}$, the relative intergrid error ε_i is thus 3dB. The damping ζ_{3dB} of the resonance peak that results in a relative magnitude error ε_i of $3dB$ is thus a function of frequency resolution and is given by

$$\begin{aligned} \zeta_{3dB} &= \frac{\Delta f}{2\omega_0} \\ &= \frac{\Delta f}{4\pi f_0} \end{aligned} \tag{2.262}$$

For a given frequency resolution, any resonance peak with a damping $\zeta_{peak} > \zeta_{3dB}$ will result in a maximum intergrid error $|\varepsilon_i(G)|$ smaller than 3dB. The possible relative intergrid error $|\varepsilon_b(G)|$ is accounted for in the robust stability test, analogously to the interpolation bias. This ensures that the robust stability criterion also accounts for the intergrid dynamics of the system.

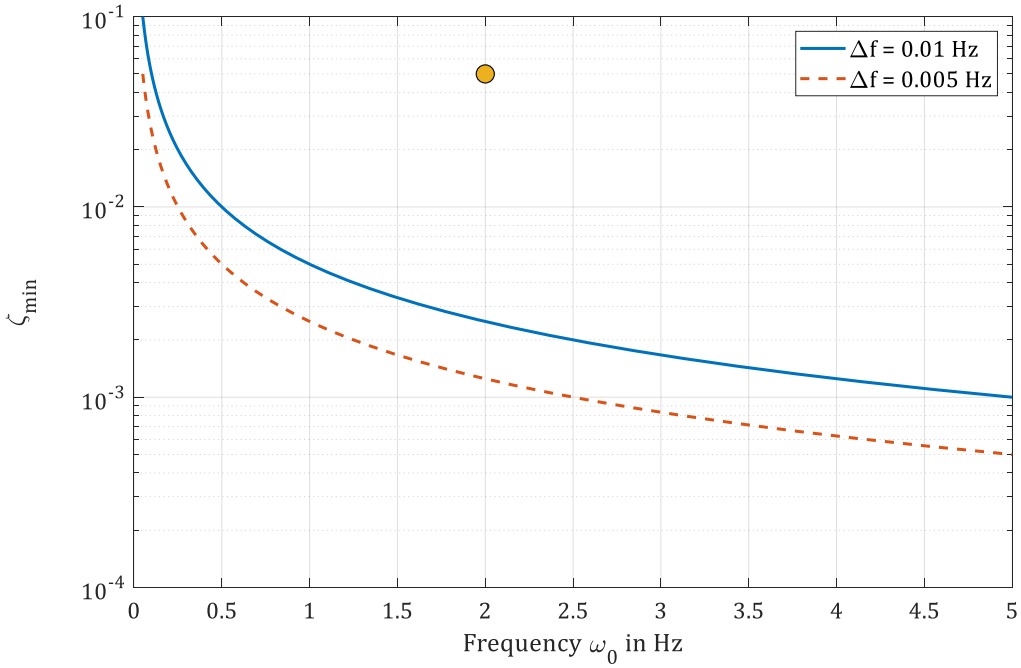

Figure 2-34: Damping coefficient that results in a 3dB intergrid error as function of ω_0

Figure 2-34 shows the resulting damping coefficient ζ_{3dB} for the frequency resolutions applied in chapters 4 and 5. In the given context of flight control design applications, the unknown dynamics are primarily elastic or aeroelastic modes. In (Stengel, 2004, p. 564) it is noted that the (first) aeroelastic modes have typical eigenfrequencies around 2 Hz and damping coefficients ζ_a[39] in the order of 0.05; the point $\omega_0 = 2$ Hz, $\zeta = 0.05$ is highlighted in Figure 2-34 with a yellow circle. It is seen from the figure, that the selected frequency resolutions are much finer, so that the intergrid error due to an aeroelastic mode with $\omega_0 = 2$ Hz, $\zeta = 0.05$ would be clearly smaller than 3dB magnitude.

For smaller intergrid error levels, the resulting relation between intergrid error, damping coefficient and frequency resolution is visualized in Figure 2-35: The contour lines show the relative frequency resolution $\frac{\Delta f}{f_0}$, that ensures, that any resonance peak due to a pole pair

[39] The damping of aeroelastic modes varies due to the (nonstationary) airflow around the wing. Depending on airspeed, the damping coefficients during flight can be reduced.

with minimum detected damping ζ_{det} results in a magnitude intergrid error smaller than b_i. For the frequency resolution of 0.005, accounting for an intergrid error of 5% includes the worst case intergrid dynamics of poles with damping larger than 0.008.

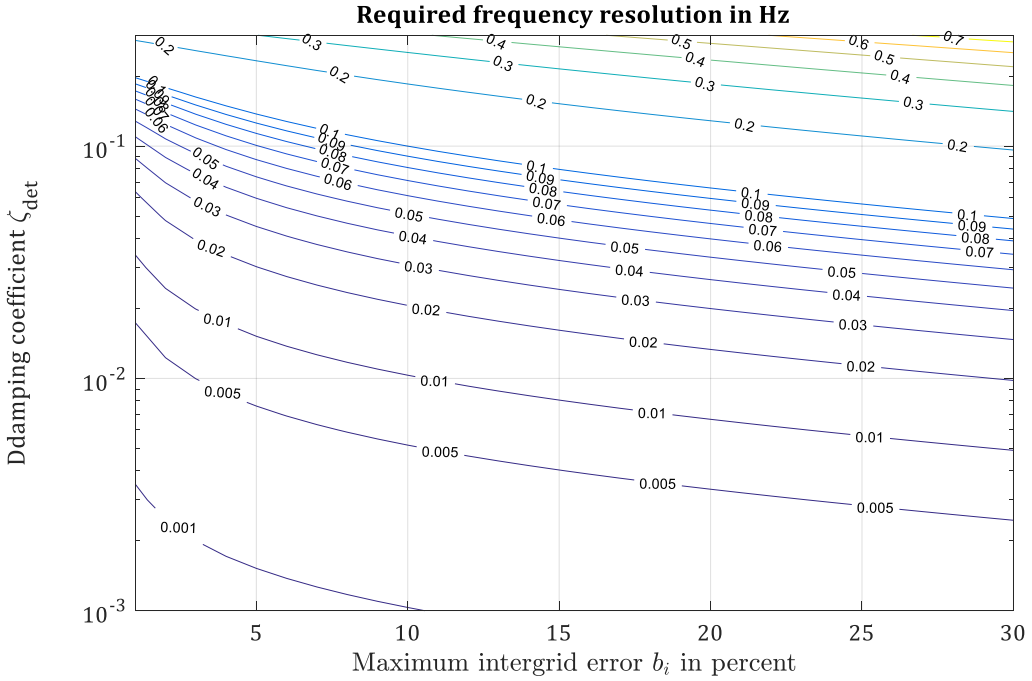

Figure 2-35: Contour plot of the minimum relative frequency resolution, that limits the maximum intergrid error, as function of the damping coefficient.

CORRECTION OF STABILITY CRITERION

The estimated intergrid error ε_i is accounted for by shifting the frequency response by $\hat{\varepsilon}_i$. The principle is shown in Figure 2-36; adding the intergrid error $\hat{\varepsilon}_i$ shifts the FRF estimate from the solid blue line to the blue dash-dotted line. The mathematical representation is shown in section 2.8.5, where the intergrid error ε_i is included in the robust stability criterion analogously to the bias estimate ε_b.

It is noted that this worst case assumption is only based on magnitude errors; in reality, a resonance peak would also influence the phase. If this was considered, the intergrid error estimate would be even smaller.

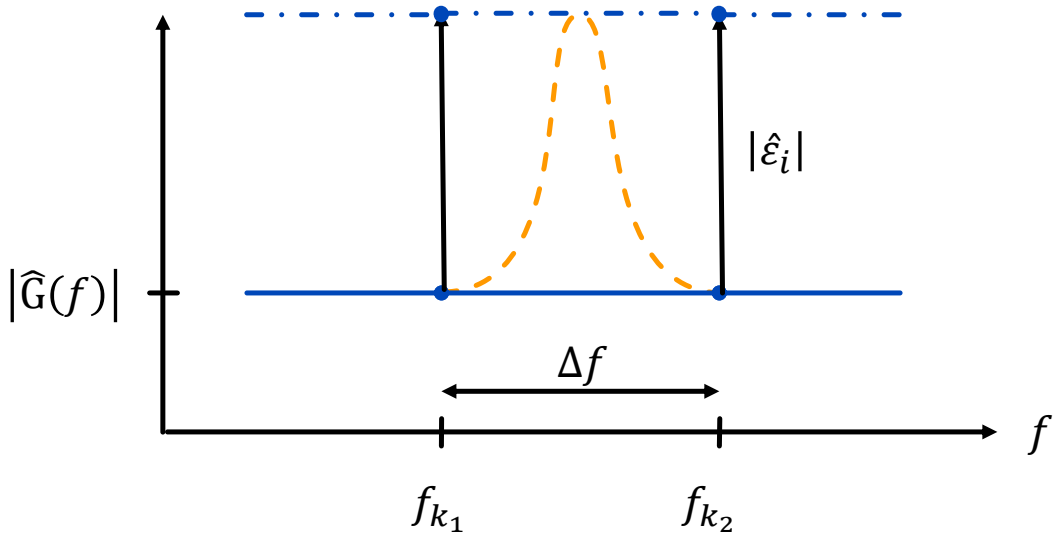

Figure 2-36: Correction of frequency response estimate for intergrid error estimate $\hat{\varepsilon}_i$.

2.8.5 Confidence Level for Robust Stability

We now come back to the stability of the uncertain system, that was analysed in sections 2.7.3. and 2.8.2. As shown there, the robust stability criteria (2.237) and (2.238) return the scaling factor κ of the maximum uncertainty $W_{\hat{G},\kappa}$ that is marginal stable. In this chapter it is shown, how κ and $W_{\hat{G},\kappa}$ can be related to confidence regions r_{p_κ} that coincide with each other. The resulting p_κ is the probability that the estimated system $\hat{G}_{yu}$ is not unstable. Depending on whether the estimate is unbiased (e.g. for the test of nominal stability) or biased (for robust stability), different relations for p_κ result.

2.8.5.1 Confidence Levels Without Bias

Both, the uncertainty W_Δ and the confidence regions r_p are circular with radii that are functions of standard deviation $\hat{\sigma}_{\hat{G}}$, see (2.247) and (2.209). Thus the uncertainty can be related to the confidence level by

$$W_{\Delta,\kappa} = r_{p_\kappa} \tag{2.263}$$

where $W_{\Delta,\kappa}$ is the maximum uncertainty and r_{p_κ} is the confidence region with equal size. Inserting the maximum instability from equation (2.237) or (2.238) and the circular confidence regions from (2.209), results in

$$\kappa \cdot \hat{\sigma}_{\hat{G}} = \sqrt{\mathbb{F}^{-1}(p_\kappa, 2, 2M-2)} \cdot \hat{\sigma}_{\hat{G}} \tag{2.264}$$

where p_κ denotes the confidence level that has the same size as the maximum uncertainty $W_{\Delta,\kappa}$. The equation can be solved for the $\mathbb{F}^{-1}$-function

$$\mathbb{F}^{-1}(p_\kappa\,, 2, 2M-2) = \kappa^2 \tag{2.265}$$

and finally for p_κ

$$p_\kappa = \mathbb{F}(\kappa^2, 2, 2M-2) \tag{2.266}$$

2.8.5.2 Confidence Levels With Bias and Intergrid Error

If the uncertainty contains parts that are not a function of $\hat{\sigma}_{\hat{G}}$, like a bias and the intergrid error, the computation of p_κ must be adjusted. In this case, the initial uncertainty model is the sum of the bias/intergrid error and the sample standard deviation $\hat{\sigma}_{\hat{G}}$.

$$W_\Delta = \hat{b}_{\hat{G}} + \hat{\sigma}_{\hat{G}} \tag{2.267}$$

With the additional term, equation (2.263) results in

$$W_{\Delta,\kappa}(k) = \kappa(k)\left(\hat{b}_{\hat{G}}(k) + \hat{\sigma}_{\hat{G}}(k)\right), \tag{2.268}$$

where $W_{\Delta,\kappa}$ describes the maximum uncertainty, that ensures robust stability. For biased estimates, the confidence regions are extended by the bias estimate., resulting in

$$r_p = \sqrt{\mathbb{F}^{-1}(p_\kappa, 2, 2M-2)} \cdot \hat{\sigma}_{\hat{G}} \; + \; \hat{b}_{\hat{G}} \tag{2.269}$$

Setting r_p equal to $W_{\Delta,\kappa}$ results in

$$\sqrt{\mathbb{F}^{-1}(p_\kappa, 2, 2M-2)} \cdot \hat{\sigma}_{\hat{G}} \; + \; \hat{b}_{\hat{G}} = \kappa(k)\left(\hat{b}_{\hat{G}}(k) + \hat{\sigma}_{\hat{G}}(k)\right) \tag{2.270}$$

Solving for p_κ results in

$$p_\kappa = \mathbb{F}\left(\frac{\left(\kappa\left(\hat{b}_{\hat{G}} + \hat{\sigma}_{\hat{G}}\right) - \; \hat{b}_{\hat{G}}\right)^2}{\hat{\sigma}_{\hat{G}}^2}, 2, 2M-2\right) \tag{2.271}$$

It is noted that the bias estimate $\hat{b}_{\hat{G}}$ may be larger than the maximum uncertainty $W_{\Delta,\kappa}$. This is the case if the uncertainty contribution of the bias alone is sufficient to break the robust stability criterion. If so, p_κ is obviously zero.

2.8.5.3 Total Confidence Level

To assess the confidence in stability of the entire system, nominal stability and robust stability must be considered. For any estimate that does not fulfil nominal stability, its confidence is set to zero.

$$p_{tot} = \begin{cases} 0, & \kappa_{nom} \leq 1 \\ p_\kappa, & \kappa_{nom} > 1 \end{cases} \tag{2.272}$$

The total confidence level can be extended with additional requirements. An example is the minimum signal-to-noise ratio of 20 dB, that is required for the Gaussian approximation of the ETFE (section 2.6.2).

2.8.5.4 Stability Over Frequency Range

The foregoing analysis studies single frequencies only. When multiple frequencies in a frequency range B are combined, their joint probability distribution is sought. For independent random variables, this is just the product of the respective probabilities.

As shown in section 2.6, the simultaneous confidence intervals are independent of each other. However, due to the local approximations in the LPM algorithm, estimates at neighbouring frequencies are correlated over frequency. This affects the FRM estimates, covariance estimates and also confidence levels p_{max}. If it is nevertheless assumed that the estimates at neighbouring frequencies are independent, the confidence level for an entire frequency range B containing frequencies $\omega_{b_1}, \dots, \omega_{b_n}$ can be computed from $p_{max}(\omega_k)$ as

$$p_{max}(B) = \prod_{k=b_1}^{b_n} p_\kappa(\omega_k) \tag{2.273}$$

Figure 5-10 shows a histogram of $p(B)$, computed with structured singular values, where B equals the FRoI. In this example, for 26% of the simulations the confidence level $p(B)$ is larger than 99% and 60% have a confidence level larger than 90%. In 4 simulations $p(B)$ is zero due to large bias estimates.

2.8.6 Summary

The frequency response estimates introduced in section 2.4 are suited excellently for the stability analysis with robust control methods. As shown in this section, the robust stability criteria (section 2.7), combined with with frequency response estimates (section 2.5) work hand in hand to assess the system stability. The stability criterion is applied twice:

- To show robust stability of the estimate with respect to its estimation uncertainty, described by the (co-) variance estimate $\hat{C}_{vec(\hat{G})}$, that is due to measurement noise (turbulence, sensor noise, etc.) (section 2.8.2).
- To show nominal stability of the estimated FRF $\hat{G}$ with respect to the nominal model G_{nom} that must be known to be stable, see section 2.8.3.

Based on the Gaussian approximation of the pdf of $\hat{G}$ (cmp. section 2.6), a confidence level is computed; for every excited frequency, it provides a measure of the probability that the true system is robust stable. The algorithm is applied on a discrete frequency grid; the extension to intermediate frequencies behaviour is discussed.

2.9 SUMMARY OF THEORETICAL PART

In the second part of chapter 2, robust stability criteria are combined with frequency response function estimates. The robust stability criteria are derived for a system with three inputs and three outputs (MIMO), as it is used later in chapters 4 and 5. The stability criteria are adjusted to include the interpolation bias (2.5.4, 2.6.5.2). Confidence levels for robust stability are computed; they provide a measure of the probability that the true system is robust stable.

The computed simultaneous confidence regions are in principle independent of each other.This includes especially, that confidence regions for different frequencies are statistically independent. In fact, the frequency response estimates and the respective covariance estimates are correlated due to the polynomial fits.

When the correlation is neglected, i.e. if it is assumed that estimates at different frequencies *are* statistically independent, the per frequency confidence levels can be combined to make statements on the probability of robust stability p_{max} of an entire frequency range. The resulting confidence level p_{max} is used in section 4 to monitor the system integrity.

3 SINGLE INPUT FREQUENCY RESPONSE ESTIMATION

The local polynomial methods introduced in section 2.5 feature the explicit estimation of initial and final conditions. The general advantage of this approach over traditional methods like the ETFE is shown in (Gevers et al., 2011; Pintelon & Schoukens, 2012). The focus in this chapter is on the advantages of the LPM for aircraft applications.

The main advantages of the local polynomial methods are twofold:

- The explicit estimation of corresponding initial and final conditions allows to estimate frequency responses from the first two periods.
- The fast local polynomial method can estimate frequency response matrices with full frequency resolution.

The analysis starts in chapter 3 with a comparison of the three considered estimators, based on FRF estimates of a single input system; the focus is on the effect that the estimation of the initial and final condition has on frequency response estimates.

In chapter 4 the fast LPM is applied to a multiple input system and the confident stability measures introduced in section 2.8 are applied to assess the confident stability measure.

3.1 INTRODUCTION AND OUTLINE

Common non-parametric estimation methods for flight dynamics identification in the frequency domain either ignore (Tischler & Remple, 2006) non-zero initial and final conditions or estimate only one of them (Klein & Morelli, 2006) (initial conditions). In this section, the effect of the explicit estimation of the initial and final conditions is examined and the three estimators introduced in this thesis are compared.

The advantageous of the local polynomial methods are demonstrated on simulated flight tests of the longitudinal dynamics of the Flying Autonomous Testbed (FAT) aircraft. The simulation model of the FAT has been developed at the Institute of Flight System Dynamics at Technical University Munich (TUM-FSD). The simulation includes light turbulence and sensor noise.

The LPM algorithm can estimate the open loop frequency response from open loop and closed loop experiments, where the closed loop identification is generally more difficult; thus the focus here is on closed loop experiments. Albeit the controller is known, the knowledge is not used for the estimation.

It is generally assumed that the aircraft can be excited with computer generated input commands. This is essential to apply periodic signals, as a pilot can never exactly repeat a signal multiple times. In aircraft with automated flight control systems the available actuators and sensors of the automated flight control system can be utilized. The computer generated excitation signal is then injected to the flight control computer as reference signal. Hence no additional sensors or actuators are required.

In section 3.2 a simulation model and the experimental conditions are described. In section 3.3 the analysis criteria are introduced; they are used in section 3.4 to compare the different estimators. The LPM user choices and their effect on FRF estimates are shortly discussed in section 3.5.

3.2 Experimental Setup

3.2.1 The Flying Autonomous Testbed (FAT)

The estimation algorithms are applied to estimate the FRF of a simulation model of the Flying Autonomous Testbed (FAT) test aircraft (Figure 3-1). The FAT is an unmanned and remote controlled test aircraft that was developed at the Institute of Flight System Dynamics (TUM-FSD) in cooperation with the Institute of Aircraft Design (TUM-LLS) of the Technical University of Munich (TUM).

The FAT has a length of three meters, its wingspan is five meters and it weighs 23 kg. It is powered by an electric motor that drives one single push propeller. It features a V-tail that combines rudder and elevators (so called ruddervators). The V-tail has a total of four control surfaces, two on each fin, that can be deflected independently. The respective deflections are a combination of the rudder and elevator commands. The ailerons are traditional style and are deflected corresponding to the roll command.

Figure 3-1: The FAT at its maiden flight, by courtesy of the Institute of Aircraft Design (LLS), TU Munich.

For the test runs, the simulation model is excited with a computer generated signal. For all experiments a simple rate control algorithm with constant gain is used. Hence the excitation signal corresponds to a commanded angular rate. All signals are stored with a sampling rate of 50 Hz. All signals are assumed to be regularly sampled.

The primary focus is on the input-output dynamics from the control inputs to the kinematic angular rates. These input/output pairs are of special importance for traditional flight control systems, where the rotational dynamics are the innermost control loop and hence must be stable

3.2.2 Plant Dynamics Model

The simulation model features nonlinear equations of motion, aerodynamics based on flight test data, sensor and actuator models. Figure 3-2 shows a bode diagram of the primary input / output responses. The relevant longitudinal and lateral poles and zeros are highlighted with arrows (ZR: zero in yaw response r_K ($\zeta_c \rightarrow r_K$), DR: Dutch roll, RM: roll mode, PH: phygoid, SH: short period); the eigenfrequencies, time constants and damping coefficients are found in appendix A.

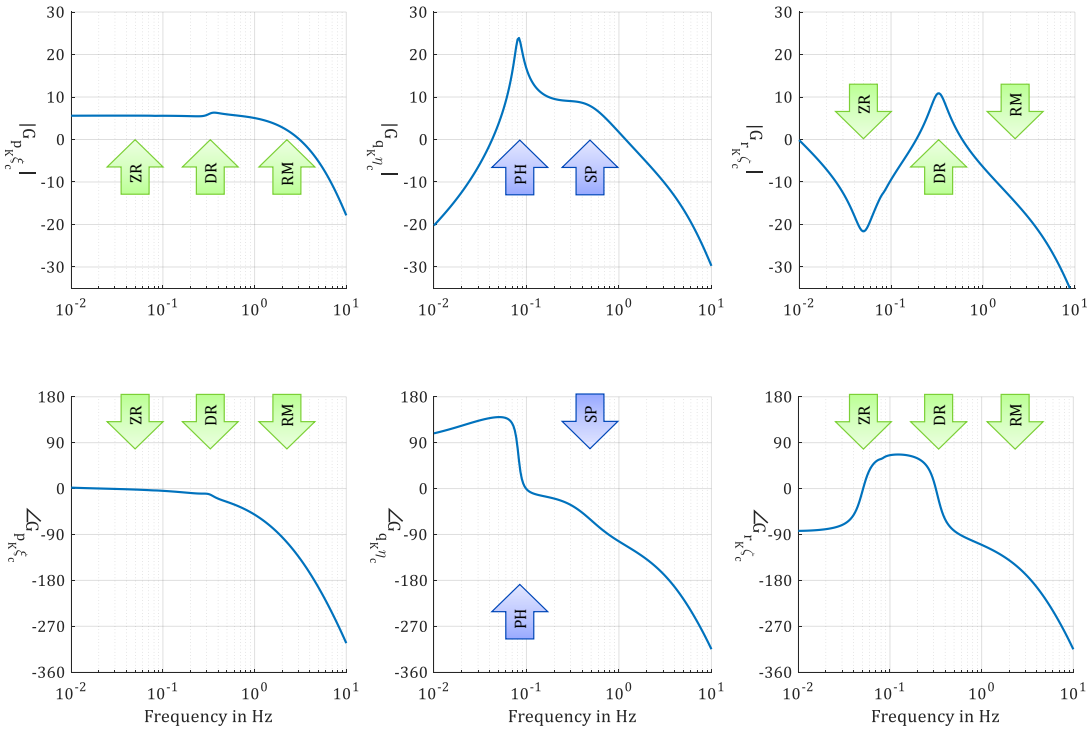

Figure 3-2: Primary responses of FAT with relevant eigenmodes.

The actuator dynamics are described in appendix A.2. The full MIMO bode diagram with all input/output pairs is shown in the appendix (Figure A-1).

The simulation results in section 3.4.1 are based on the linearized dynamics of the nonlinear model. For the nonlinear, longitudinal simulations in section 3.4.2, the lateral states are fixed. In chapter 4, the full, nonlinear simulation model is used.

3.2.3 Flight Control System

The model includes a simple flight controller with constant proportional gains. The controller is a rate controller, i.e. the rotational rates of the rigid body are fed back. The gains are fixed and are set to $0.5\frac{1}{rad/sec}$, i.e. a rotational rate command of 1 rad/sec results in a normalized excitation of 50% of the maximum deflection. This corresponds to 20 deg deflection of the control surfaces. It is noted that the estimation is independent of the controller and can be applied whether or not the controller is known.

The controller includes a turn coordinator. During the experiments, significant bank angles can occur. The turn coordinator commands the corresponding yaw rate that results in a coordinated turn. Doing so, the yaw rate due to bank angle can be subtracted from the observed yaw rate. The remaining part is only due to the actual yaw excitation ζ_c.

For a coordinated turn with bank angle Φ, the resulting yaw rate is

$$r_K = \dot{\Psi}\cos(\Phi)\cos(\theta) \approx \dot{\Psi}cos(\Phi) \tag{3.1}$$

This results in

$$r_{K,ct} = \frac{m}{V_k}\sin(\Phi) \tag{3.2}$$

where $r_{K,ct}$ is the yaw rate required for a coordinated turn, Φ the kinematic roll angle, Θ the kinematic pitch angle, m the aircraft mass, V_k the kinematic speed with reference to the

inertial frame and Ψ the turn rate. The yaw rate resulting from (3.2) is added to the feedback signal, cmp. Figure 3-4. Thus the yaw dynamics are estimated for a coordinated turn.

If Φ is small, equation (3.2) can be simplified with the small angle approximation. The resulting block diagram from roll command ξ_c to yaw rate r_K is shown in Figure 3-3. The corresponding additional transfer function is given by

$$G_{r_K\xi_c} = \frac{Km}{V_K} \cdot \frac{1}{s} G_{r_K\zeta} G_{p\xi} \tag{3.3}$$

As can be seen from equation (3.2) the turn coordination results in a nonlinear control law. The effect of the turn coordination on the FRF is shortly discussed in the appendix A.6.

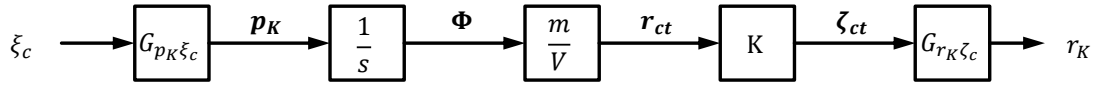

Figure 3-3: Block diagram of turn coordinator dynamics with small angle approximation.

The above derivation of the turn coordination control law is based on rotational rates $[p_K,\ r_K]_B$ given in the body-frame. As the simulation models optionally accounts for sensor misalignment errors, kinematic rotational rates p_K, q_K, r_K of the body frame are replaced by kinematic rotational rates p_S, q_S, r_S of the IMU-frame[40] as needed. The entire flight control design is shown in Figure 3-4, where the output y and the roll angle Φ are provided by the attitude heading reference system (AHRS). The closed loop FRM G_{ry} with and without the turn coordinator is shown in the appendix as bode plots, cf. Figure A-6.

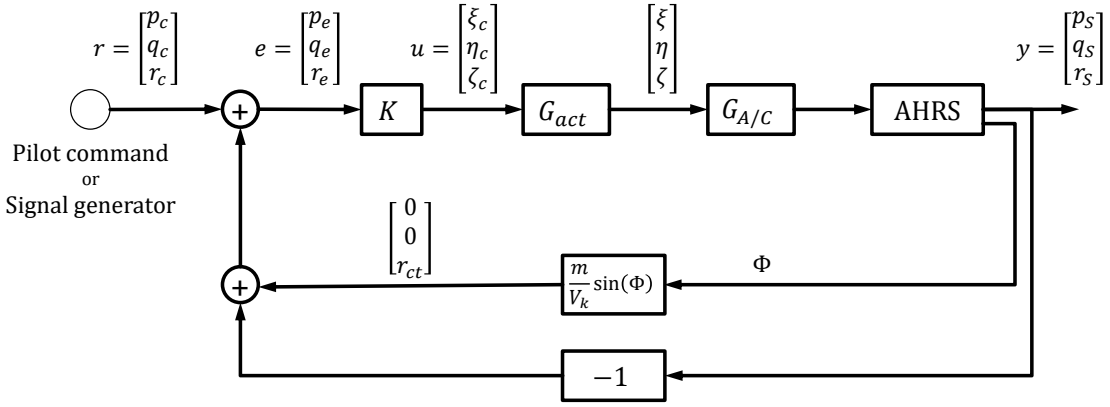

Figure 3-4: Block diagram of FCS with turn coordination.

3.2.4 Flight Conditions and Simulation Settings

The simulations start in trimmed straight level flight at an altitude of 610 meters and with a kinematic velocity of 24 m/sec. Constant wind is not considered at all, as it has no influence on the estimation result[41]. The test flights are simulated with light turbulences (Dryden, 1943). The sensors represent a generic tactical grade IMU that is described in appendix A.5.

The simulation model is implemented in Simulink. It is integrated with Simulink's ode4 solver. The aircraft dynamics are simulated with a simulation step size of 0.02 sec (50 Hz); the sensor model is simulated with a smaller step size of 0.005 sec (200 Hz).

[40] Compare appendix A.5 and the aircraft nomenclature rules in the beginning of this thesis.
[41] Constant wind influence only the DC-frequency which is not considered in the LPM algorithm.

In the following analyses, the largest frequency of interest is 5 Hz; the simulation rate is 10 times larger. Thus, the sampling theorem holds (requires factor 2), but the guideline by Tischler and Remple (factor 25, cmp section 2.2.2.2) is not met. Experiments with smaller step size of 0.005 sec for the entire aircraft dynamics showed no differences in the FRM estimates, indicating that the simulation step size of 0.02 seconds is sufficient to avoid numerical effects.

3.2.5 Excitation Signal, Frequency Range and Frequency Resolution

In all simulations, the exact reference signal is available for the later estimation. Random phase multisines are used in all experiments[42]. Each excited frequency has the same amplitude.

3.2.5.1 Frequency Range of Interest

Within this thesis, to different frequency ranges are analysed: In chapter 3, the different estimators are compared. As the ETFE and the transient LPM are only suited for single input systems, chapter 3 is restricted to the longitudinal motion and only the pitch frequency response is estimated. For concise results, the excitation is limited to 20 frequencies linearly distributed in the range from 0.05 Hz to 1 Hz. This range includes the short period mode (at 0.48 Hz). The Phygoid (at 0.082 Hz) is contained in the frequency range, but its resonance peak is not resolved by the too coarse frequency resolution. As shown in Figure 3-6, the frequency resolution of 0.05 Hz is coarser than recommended for the fast LPM. This is on purpose to show the detrimental effect of too coarse frequency resolutions on the FRF estimates.

In chapter 4 a wider frequency range with finer frequency resolution is analysed to show the full potential of the LPM to estimate frequency response matrices for a large number of frequencies. The frequency resolution is adjusted over the frequency range to account for the time constants of the respective modes; cmp. section 3.2.5.4.

3.2.5.2 Eigenmodes of the FAT

The frequency range of interest is determined by the minimum and maximum frequencies that are relevant for the respective task. For the FAT the intended task is to analyse stability based on estimated FRM's and the respective uncertainty regions.

Based on FCS handling quality criteria, all relevant modes must be stable (Department of Defense, 1997). The relevant modes (i.e. poles) are

- Short period
- Phygoid
- Dutch roll

Modes with low eigenfrequency frequency (large time constant) may be slightly instable, as slow modes can be stabilized manually by the pilot. Hence the spiral mode is not of interest. Further zeros are of secondary interest, as they do not affect stability.

As shown in appendix A.1 the longitudinal modes lie approximately between 0.1 Hz and 0.5 Hz. The lateral modes (except spiral mode) lie between 0.33 and 3 Hz. In the following chapters, different frequency ranges are analysed:

[42] Different crest factor optimized signals have been tested. For a fixed signal, the deviation of the aircraft from its trim point is not random and results in systematic errors that would distort the Monte Carlo results.

- In chapter 3, the focus is on the comparison of the different estimators. For a clean overview, the number of frequencies is kept low. The focus is on longitudinal dynamics in the frequency range from 0.15 Hz to 1 Hz, including the short period.
- In chapter 4, a larger frequency range is studied to show effects that are specific for the fast LPM. The analysed frequencies range from 0.05 Hz to 5 Hz, including all oscillating modes.
- In chapter 5 the frequency range is selected as 0.29 Hz to 2.9 Hz, so that the phygoid mode is not contained in the FRoI.

In Figure 3-5 shows the eigenfrequencies of the oscillating eigenmodes for typical aircraft and for the FAT.

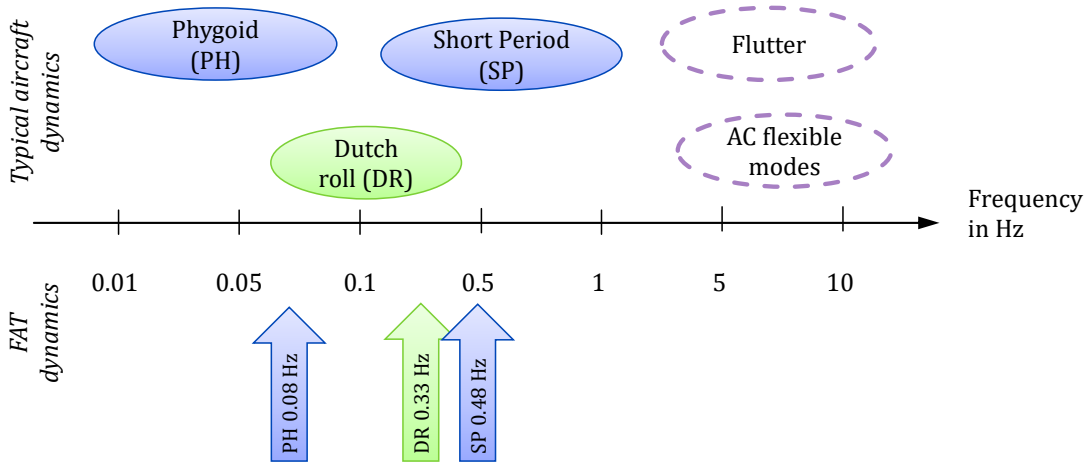

Figure 3-5: Frequency range of oscillating AC eigenmodes.

3.2.5.3 Recommended Frequency Resolution

As introduced in section 2.5.4, the fast LPM algorithm can be biased near lightly damped poles. The relative bias is a function of excitation frequency resolution and damping. Equation (2.138) sets an upper limit; for coarser frequency resolutions the bias may exceed the tolerated level $|\varepsilon_b(G)|$. As lightly damped poles are a worst case condition, the recommended measurement times T_{meas} (and the resulting frequency resolution Δf_{exc}) introduced in section 2.5.4.6 can be used as a general guideline for the signal design. In Table 3-1 the measurement times and frequency resolutions for the poles of the FAT are shown for a tolerated bias $|\varepsilon_b(G)|$ of about 3% (i.e. for $\varepsilon_b = \alpha_R$) and second order fits ($R = 2$). It is seen that the recommended frequency resolution for the relevant modes (Phygoid, Dutch roll, Short Period) range from $1.33 \cdot 10^{-3}$ Hz to 0.067 Hz. The respective measurement times range from 14.9 seconds to 750 seconds.

Table 3-1: Recommended measurement times and frequency resolutions for FAT eigenmodes

Mode	$\boldsymbol{\omega_0}$ in Hz	$\boldsymbol{\zeta_0}$	$\boldsymbol{T_{meas}}$ **in sec**	$\boldsymbol{\Delta f}$ **in Hz**
Spiral mode	$0.68 \cdot 10^{-3}$	-	$> 10^4$	$< 10^{-3}$
Phygoid	0.082	0.077	750	$1.33 \cdot 10^{-3}$
Dutch roll	0.33	0.18	78.3	0.013
Short period	0.48	0.66	14.8	0.067
Roll motion	2.3	-	2.1	0.48
Actuators	6.4	0.9	0.8	1.2

3.2.5.4 CUSTOMIZED FREQUENCY RESOLUTION

In chapter 4 the focus is on a signal with modified frequency resolution is used. The focus is on accurate estimation of Dutch roll, short period and roll dynamics. With the data from Table 3-1 a signal with reduced number of frequencies is constructed. It is based on a linearly spaced signal with frequency resolution of 0.005 Hz by dropping selected frequencies. The remaining frequency subset ensures sufficient frequency resolution for all relevant modes. This procedure allows to thin the frequency resolution where possible and simultaneously ensures that the remaining frequencies are still multiples of the base frequency.

Figure 3-6 shows frequency resolutions Δf as function of frequency f in double logarithmic scale. Linear distributed frequencies show up as horizontal lines. Exponential distributed frequencies show up as diagonal lines due to the log-log scale. The eigenmodes from Table 3-1 and the respective required frequency resolution are indicated with blue circles; for better legibility the single data points are connected by a dotted line. The linear frequency distribution used in chapter 3 is shown as orange solid line, the finer frequency resolution used in chapter 4 is shown as yellow line. The customized frequency resolution for chapter 5 is shown as violet line. The figure gives a graphical representation of the frequency response requirements; if the frequency resolution is below the required resolution, the fast LPM bias is small.

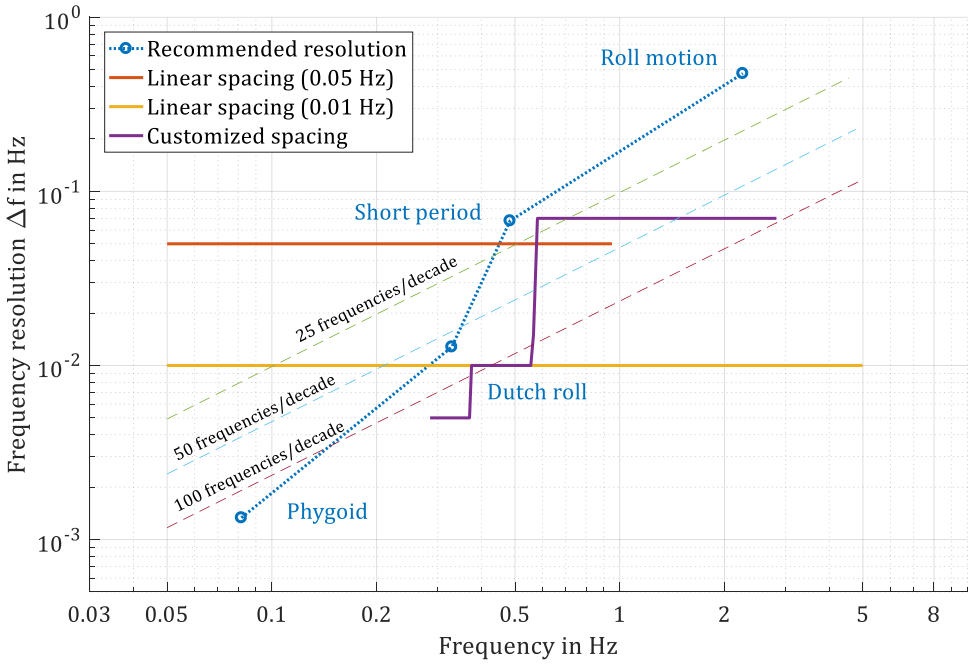

Figure 3-6: Frequency resolution as function of frequency.

3.2.6 LPM USER CHOICES

In general, two full periods of the excitation signal are observed. The local polynomials are of order 2 and the parameter m (see section 2.5.2, eq. (2.127)) is set to 2, so that confidence regions can be computed.

3.2.7 ESTIMATION TASK

The estimation goal is the open loop frequency response function of the aircraft dynamics G_{yu}, i.e. the plant dynamics without the controller. The input signal contains the roll, pitch

and yaw command. The commands are mapped to the respective surfaces, where the ailerons are controlled by the roll command and the ruddervator by the combined pitch and yaw command. The signals are normalized to the range $[-1,1]$, where ± 1 corresponds to full deflection of the respective control surfaces. The normalized signals have no unit.

The system outputs are rigid body angular rates $(\vec{\omega}_K^{IB})_B = [p_K \quad q_K \quad r_K]_B^T$, where p_K is the kinematic roll rate, q_K the kinematic pitch rate and r_K the kinematic yaw rate or measured rotational rates $(\vec{\omega}_K^{IB})_S = [p_S \quad q_S \quad r_S]^T$ respectively. All rotational rates are given in rad/sec, unless specified otherwise. In sum, the entire FRM has unit $\left(\frac{\text{rad}}{\text{sec}}\right)^{-1}$.

The transfer function from normalized input commands to rotational rates depend significantly on aerodynamic speed. To account for aircraft speed changes in linear models of AC dynamics, it is common to compute non-dimensional coefficients, where rotational rates are scaled with speed and a characteristic length (Etkin & Reid, 1996, pp. 115–117). Within this thesis, dimensional estimates are used. However, speed changes during the experiments are accounted for by scaling the transfer function estimate to match the trim speed dynamics

$$\hat{G} = \tilde{G} \cdot \frac{|V_{trim}|}{|V_{mean}|} \tag{3.4}$$

where $\hat{G}$ is the corrected estimate, $\tilde{G}$ is the unscaled estimate, V_{trim} the trim speed and V_{mean} the mean aerodynamic speed, averaged over the experiment duration.

The estimated FRM is the open loop transfer function G_{yu} that describes the dynamics from commanded control surface deflections $u = [\xi_c,\ \eta_c,\ \xi_c]^T$ to the rotational rates $y = [p_K,\ q_K,\ r_K]^T$. As shown in Figure 3-7 the estimated FRM G_{yu} contains actuator dynamics, aircraft rigid body dynamics and sensor dynamics.

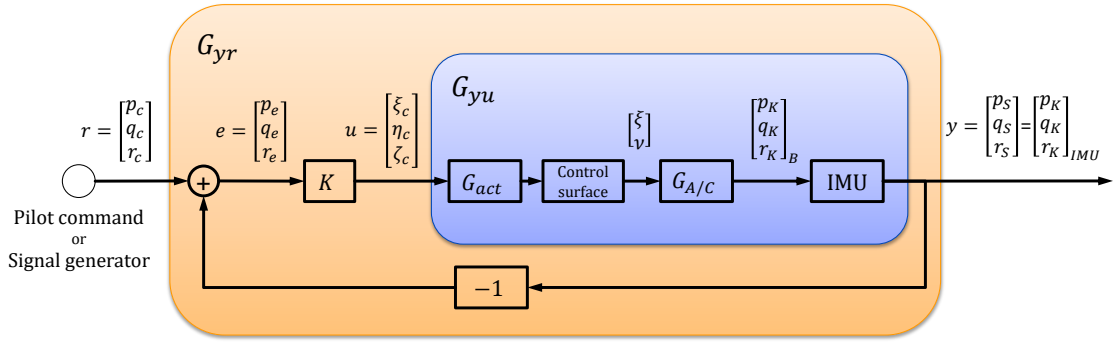

Figure 3-7: Block diagram of estimated system.

For better overview, the frequency response matrix elements are grouped in three categories: primary (or on-axis), secondary and cross coupling responses. The mapping is shown in Figure 3-8. It is seen that the primary responses contain the main lateral and longitudinal rotational responses. The secondary responses contain the lateral off-axis dynamics, while the cross coupling responses contain the lateral-longitudinal coupling responses.

Output \ Input	ξ	η	ζ
p_K	Primary, on-axis response	Cross coupling responses	Secondary response
q_K	Cross coupling responses	Primary, on-axis response	Cross coupling responses
r_K	Secondary response	Cross coupling responses	Primary, on-axis response

Figure 3-8: Frequency response group mapping.

3.3 Accuracy Measures for FRF Estimates

The estimated FRMs $\hat{G}$ are compared to an analytically linearized reference model G_0. The reference model is computed with Simulink's linearization utilities, that are contained in Simulink Control Design, see (The Mathworks, 2017c). The deviation of the estimates from the nominal dynamics is described by several quantities, that are introduced in the following section.

3.3.1 Absolute Error

In the following analyses, two different error measures are used. These are absolute errors and error response functions. The true absolute error is defined as $\hat{G} - G_0$, the absolute sample error is $\hat{G} - \tilde{G}$, where $\tilde{G}$ is the mean estimate of $\hat{G}$. The absolute error magnitude $\left|\hat{G} - G_0\right|$ is especially relevant for the statistical analyses in chapter 4; the absolute error phase $\angle\left(\hat{G} - G_0\right)$ is statistically uniformly distributed[43] and thus bears little additional information. It is noted that the magnitude of the absolute error $\left|\hat{G} - G_0\right|$ must not be confused with the error of magnitudes $\left|\hat{G}\right| - |G_0|$.

3.3.2 Error Response Function

The error response function (erf) of the estimated FRF $\hat{G}$ is a complex function and contains the relative magnitude error and the absolute phase error. It is denoted by $\varepsilon\left(\hat{G}\right)$ and its magnitude $\varepsilon\left(\left|\hat{G}\right|\right)$ is defined as the magnitude ratio of the estimate w.r.t. the analytical value:

$$\varepsilon\left(\left|\hat{G}(\omega_k)\right|\right) = \frac{\left|\hat{G}(\omega_k)\right|}{|G_0(\omega_k)|} \tag{3.5}$$

If specified in dB, the ratio (3.5) results in the difference in magnitude:

$$\varepsilon\left(\left|\hat{G}(\omega_k)\right|\right)_{db} = \left|\hat{G}(\omega_k)\right|_{db} - |G_0(\omega_k)|_{db} \tag{3.6}$$

The erf phase error $\varepsilon\left(\angle\hat{G}\right)$ is defined as the absolute error of the estimate w.r.t. the analytical value:

$$\varepsilon\left(\angle\hat{G}(\omega_k)\right) = \angle\hat{G} - \angle G_0 \tag{3.7}$$

[43] It is assumed that $\hat{G}$ is circular complex distributed.

Confidence regions of the erf are scaled as required. The confidence regions for phase angles and lower magnitude bound may be undefined, if the confidence region includes the origin of the complex plain.

3.3.3 Maximum Unnoticed Additional Dynamics

Based on flight simulator experiments, Wood and Hodgkinson analysed the effect of differences in aircraft pitch rate response on the handling quality rating of pilots. Based on these experiments, upper and lower bounds for the maximum unnoticed additional dynamics (MUADs) of pitch response functions were defined, where unnoticed means that the pilot handling quality rating is not changed (Wood & Hodgkinson, 1980). MUADs became part of the MIL-HDBK-1797 (Department of Defense, 1997).

The experiments showed, that pilots are especially sensitive to additional dynamics in the frequency range of pilot's crossover frequency[44]. Hence MUADs are tighter around the typical pilot cross over frequency and wider at lower and higher frequencies. MUADs are defined in terms of error response functions, i.e. the magnitude error in dB and the absolute phase errors. Figure 3-9 shows the upper and lower bounds; the nominal dynamics with 0 dB magnitude error and 0 degree phase error are plotted as dashed black line.

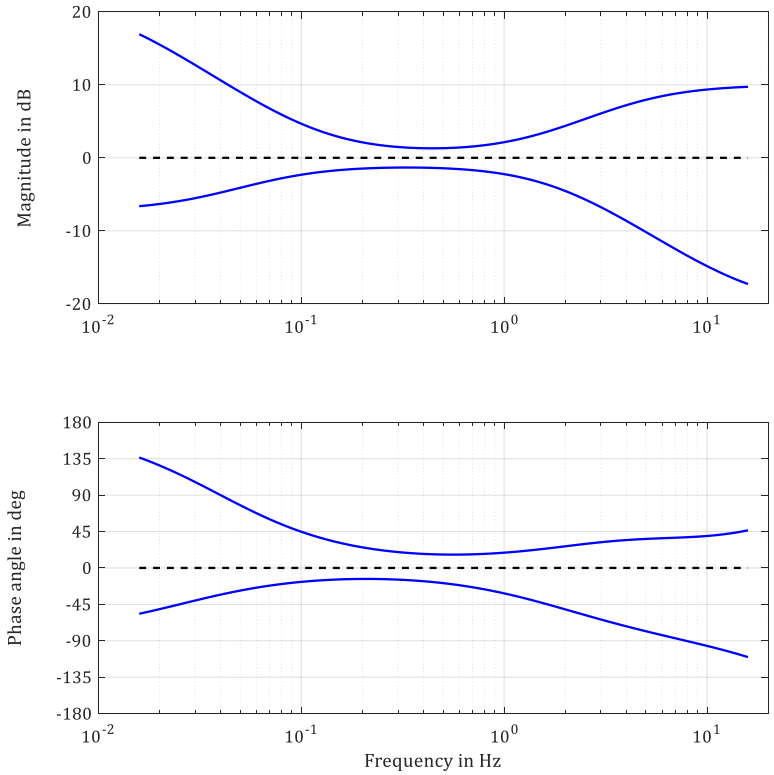

Figure 3-9: Maximum unnoticed additional dynamics (MUADs).

When applied to system identification results, the MUADs can be interpreted as upper and lower bounds for the pitch rate error response function as function of frequency; if the pitch response estimation error function remains within the boundaries, the estimated dynamics will be judged by pilots with the same handling quality rating as the nominal model.

[44] For further details on pilot behaviour modelling see McRuer (1974)

3.3.4 Cost Function

To quantify the accuracy of the matches over all frequencies, a quadratic cost function is used. It is based on the cost function in (Tischler & Remple, 2006) and is formulated in terms of magnitude and phase errors. The cost function $CF(\hat{G}, G_0)$ is defined as

$$CF(\hat{G}, G_0) = \frac{20}{n_\omega} \sum_{k=1}^{n_\omega} W_{mag} \cdot \left(\mathrm{dB}(|\hat{G}(\omega_k)|) - \mathrm{dB}(|G_0(\omega_k)|) \right)^2 + W_{angle} \cdot \left(\angle \hat{G}(\omega_k) - \angle G_0(\omega_k) \right)^2 \tag{3.8}$$

where n_ω is the number of frequencies, $|\hat{G}(\omega_k)|$ and $|G_0(\omega_k)|$ the FRF's magnitude, $\angle \hat{G}(\omega_k)$ and $\angle G_0(\omega_k)$ the FRF's phase angle and W_{mag}, W_{angle} weighting factors, with magnitudes given in dB and phase angles in degree. The cost function is zero, if the estimate perfectly matches the real dynamics. With equations (3.6) and (3.7) the cost function is rewritten as

$$CF(\hat{G}, G_0) = \frac{20}{n_\omega} \sum_{k=1}^{n_\omega} W_{mag} \cdot \left(\varepsilon(|\hat{G}(\omega_k)|) \right)^2 + W_{angle} \cdot \left(\varepsilon \left(\angle \hat{G}(\omega_k) \right) \right)^2 \tag{3.9}$$

Common weighting factors are

$$W_{mag} = 1 \tag{3.10}$$

$$W_{angle} = 0.01745 \tag{3.11}$$

such that 1 dB magnitude error has the same effect as 7.57 deg phase error. In parametric system identification, this cost function is used as optimization criterion for parameter estimation. (Tischler & Remple, 2006, p. 280)

As a guideline for flight-dynamics modelling Tischler and Remple state that an acceptable match is achieved with cost functions values below 100. Cost functions below 50 result in a match that can be hardly distinguished from flight data (Tischler & Remple, 2006, p. 280). It is noted that these guidelines do not account for the frequency dependence of pilot sensitivity to additional dynamics, as is the case for MUADs.

3.4 Comparison of Estimators

The effectivity of the transient term estimation (section 2.4) is shown on the basis of repeated simulations with different random phase excitations signals. The comparison in section 3.4.1 is based on linear model of the pitch rate dynamics $G_{q\eta}$. As the focus is on the effect of the initial- and final conditions, no noise is added to the model. The system is excited with a random phase multisine that consists of 18 frequencies linearly spaced from 0.15 Hz to 1 Hz, with a frequency resolution of 0.05 Hz; one period takes 20 seconds and two full periods are observed. The simulation starts in rest, i.e. initial conditions are zero.

The conditions are chosen such, that the only variation is due to the non-steady state conditions at the beginning of the simulation. Hence, the differences in the estimates are only due to the effect of the transient term. The same conditions are simulated in section 3.4.2 with the nonlinear simulation model.

3.4.1 Effectivity of Transient Term Estimation

Figure 3-10 shows a scatter plot of the normalized relative magnitude estimation error from 20 repeated experiments. The mean value, averaged over 20 experiments is marked with a square, its respective 90% confidence interval from the student's t-test is indicated by the

dashed lines. The ETFE is shown in blue, the transient LPM is orange, the fast LPM is shown in yellow. The normalization is selected such that the true value is at zero.

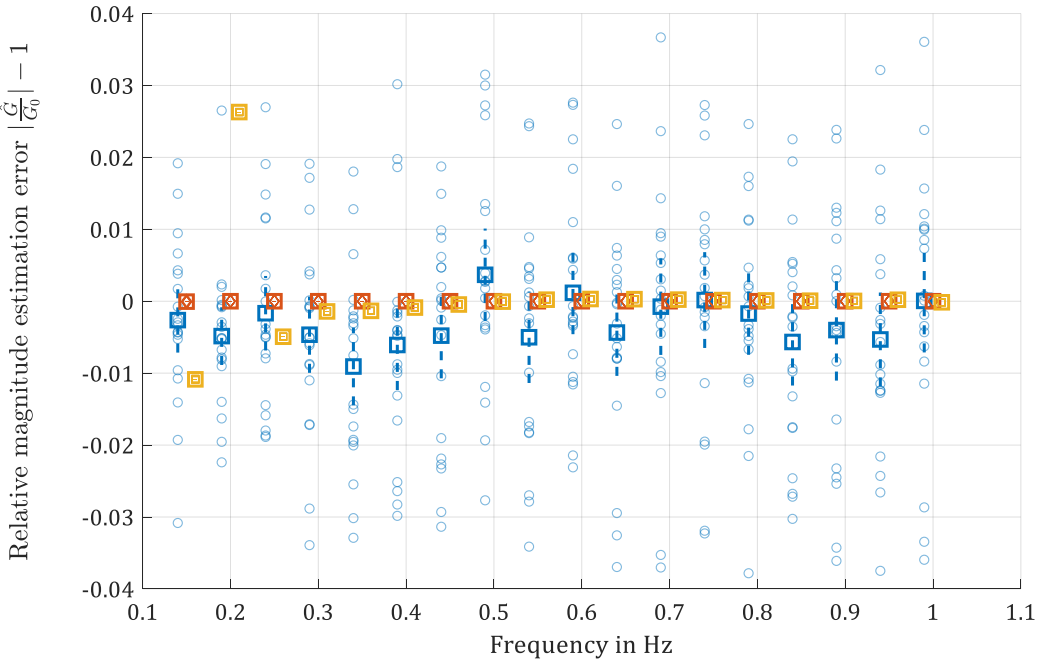

Figure 3-10: Normlized relative magnitude estimation error (ETFE: blue, tLPM: orange, fastLPM: yellow).

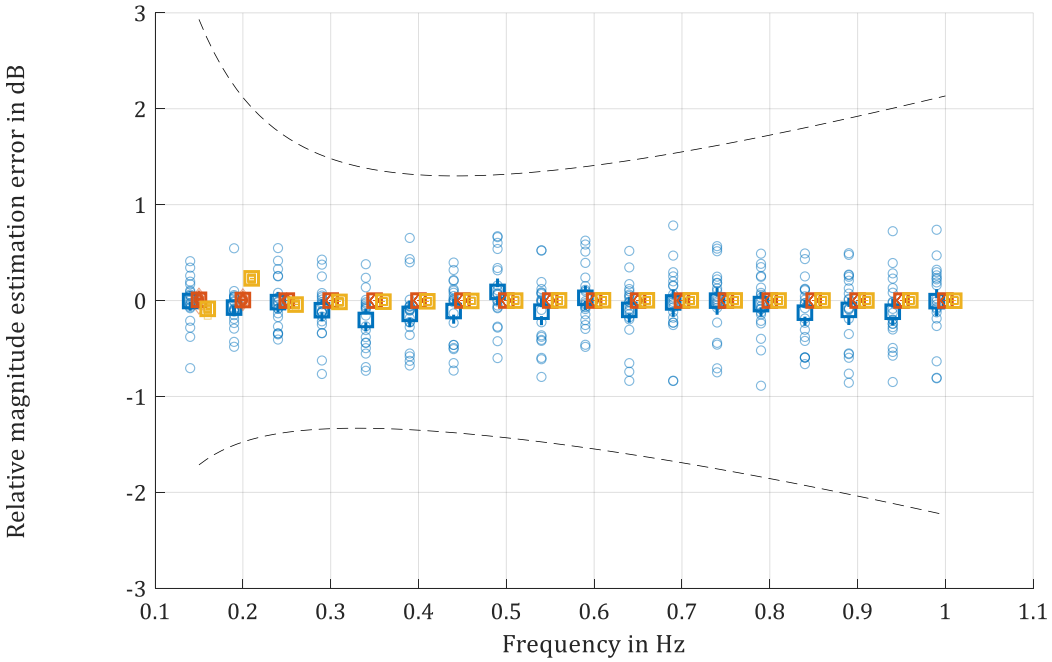

Figure 3-11: Relative magnitude estimation error in dB with MUAD bounds (ETFE: blue, tLPM: orange, fastLPM: yellow, MUAD: black dashed lines).

In Figure 3-11 the same results are shown scaled in dB and are compared to the MUAD bounds (shown as black dashed lines)[45]. It is seen that the estimates remain well inside the MUAD bounds.

Table 3-2 and Table 3-3 show the mean estimation error and the 90% confidence ranges for selected frequencies. It is seen, that the transient and fast LPM estimates vary much less than the ETFE (by several orders of magnitude); this shows how effective the estimation of the transient term is.

A closer look reveals that the true value is included in the confidence intervals for the ETFE and the transient LPM in about 85% of the experiments respectively; this is in good accordance with the proposed confidence level (90%). The results for the fast LPM are generally very accurate, but show a bias at low frequencies, especially at 0.15 Hz and 0.2 Hz. This is due to the interpolation bias and the border effect; both effects are discussed later in more detail later, see sections 4.2 and 4.3.

Table 3-2: Absolute value of the mean relative estimation error in dB.

Frequency (Hz)	0.2	0.4	0.6	0.8	1.0
ETFE	0.043	0.054	0.009	0.016	0.001
tLPM	$< 10^{-4}$	$< 10^{-4}$	$< 10^{-4}$	$< 10^{-4}$	$< 10^{-4}$
fastLPM	0.226	0.008	0.003	0.001	0.001

Table 3-3: Confidence range (90%) for relative magnitude errors in dB.

Frequency (Hz)	0.2	0.4	0.6	0.8	1.0
ETFE	0.085	0.137	0.126	0.129	0.159
tLPM	0.009	$< 10^{-3}$	$< 10^{-4}$	$< 10^{-4}$	$< 10^{-4}$
fastLPM	0.004	$< 10^{-3}$	$< 10^{-4}$	$< 10^{-4}$	$< 10^{-3}$

3.4.2 Nonlinear Simulation

For comparison, the same simulations are repeated with the nonlinear simulation model. The respective result is shown in Figure 3-12. It is clearly seen that the nonlinear simulation results in additional estimation errors, that can be several times larger than the random error due to the nonzero initial and final conditions (c.f. the different scaling of the y-axis). Once more, the estimation errors are compared to the MUAD bounds (Figure 3-13). It is seen that the additional variance has a similar size as the MUAD bounds; that means that the effect of the variation is so large that a pilot would decrease the handling quality rating.

The close relation of aerodynamic forces and moments to dynamic pressure and thus airspeed suggests, that the additional variation of the estimates is caused by the changes of airspeed. To quantify this relation, and thus the effect of speed changes on the FRF estimates, requires the identification a parameter varying model (Goos, 2016), which is not covered in this thesis.

[45] The scaling in dB is a nonlinear function that affects the estimates' statistical distribution; thus, the confidence intervals computed from the student's t-test cannot be applied to the values in dB.

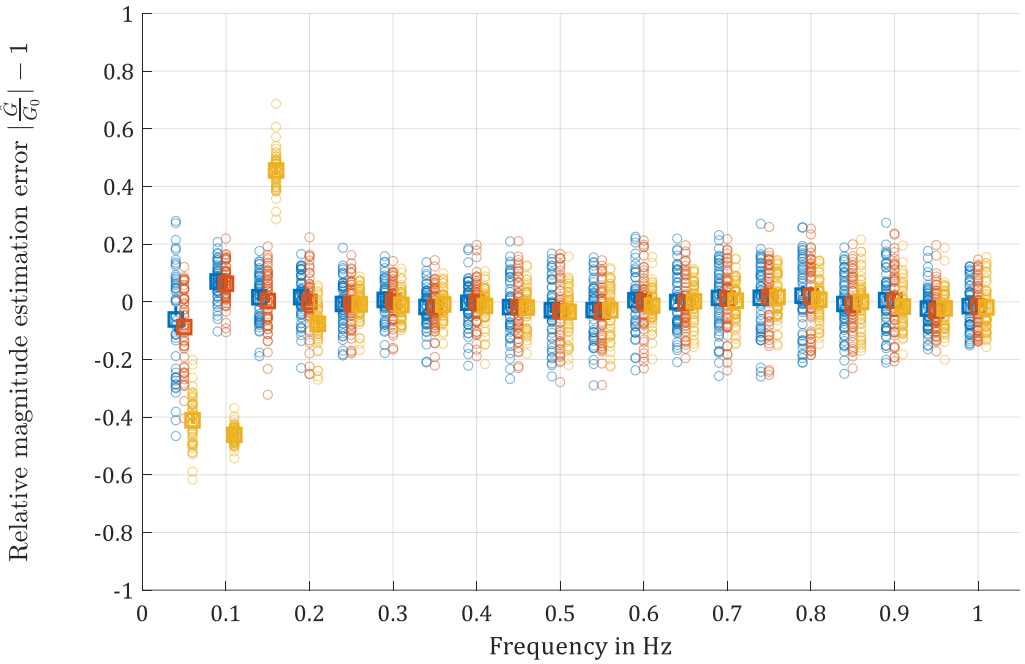

Figure 3-12: Normalized relative magnitude estimation error (ETFE: blue, tLPM: orange, fastLPM: yellow) for nonlinear simulation.

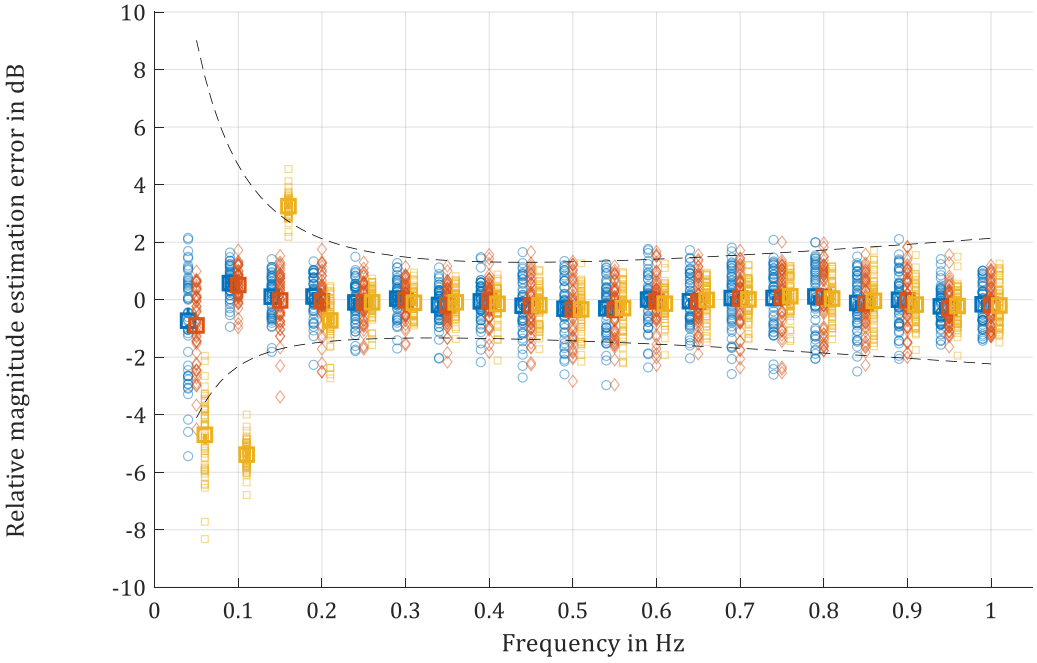

Figure 3-13: : Relative magnitude estimation error in dB with MUAD bounds (ETFE: blue, tLPM: orange, fastLPM: yellow) with nonlinear model.

With additional noise (light turbulence), the estimation errors of all estimators are further increased, as shown in Figure 3-14 and Figure 3-15 respectively.

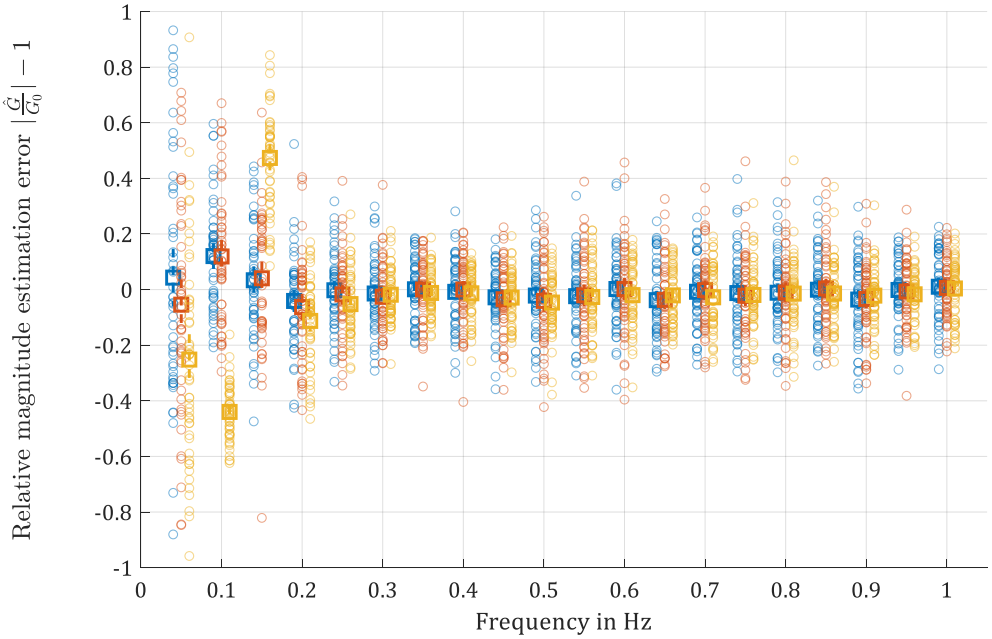

Figure 3-14: Relative magnitude estimation error (ETFE: blue, tLPM: orange, fastLPM: yellow) with nonlinear model and light turbulence.

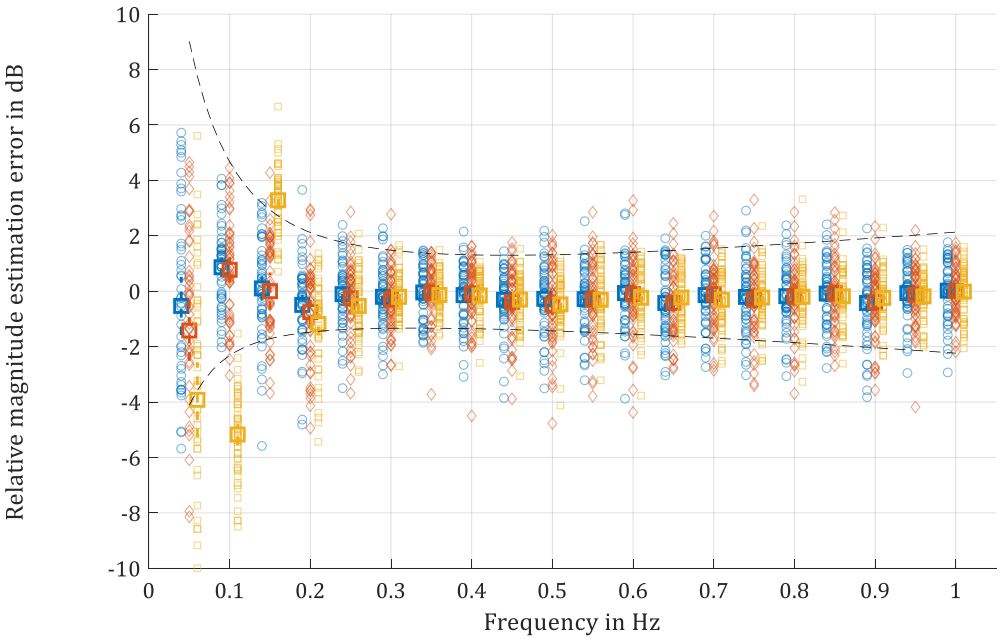

Figure 3-15: Relative magnitude estimation error in dB with MUAD bounds (ETFE: blue, tLPM: orange, fastLPM: yellow) with nonlinear model and light turbulence.

In the nonlinear case, the ETFE and the transient LPM show very similar results; this is due to the close relation of the two estimators. The fast LPM shows slightly smaller variation, but at low frequencies (0.05 to 0.15 Hz) it is severely biased (about 40% relative error); the bias is caused by the coarse frequency resolution, cmp. sections 2.5.4; the bias on fast LPM estimates is further analysed in section 5.3.1.

All estimators show much larger estimation errors than in the linear case. This is due to the additional errors, that are introduced by the nonlinear simulation, especially by the deviation from its trim speed, cmp. section 3.2.7. When compared to e.g. general aviation

aircraft, the FAT is a small and very light vehicle that flies at rather low speed. Both makes the aircraft sensitive to turbulence. A similar analysis by the author of this thesis, that is based on a general aviation aircraft, is presented in (Merkl & Holzapfel, 2018); it suggests that the nonlinear effects are especially pronounced for the FAT. The simulation results emphasize that nonlinear effects must be considered in the experiment design to achieve good signal-to-noise ratios that ensure more accurate estimation results, cmp. chapters 4 and 5.

A more detailed analysis of the variance of the respective estimates is difficult, as the analytical terms have entirely different shapes, see (Pintelon & Schoukens, 2012, pp. 237–269), where a qualitative comparison is provided. Omitting a detailed analysis, it is stated that the simulation results presented in this section are in accordance with the general trends shown by Pintelon and Schoukens.

3.5 LPM User Choices

The LPM algorithm requires user choices for the number of observed periods P, the polynomial order R and for q, the number of degrees of freedom of $\hat{C}_{vec(\hat{G})}$. While the first two are directly set by the user, the dof's are set by with the parameter m in equation (2.127). In this section, the effect of the three parameters P, R and m is shortly discussed.

Number of periods P: The fast LPM algorithm requires data with at least two full periods of the excitation signal. With additional periods, more non excited frequencies are available to estimate the noise and transient term, see section 2.4: If the number of supporting points n in the polynomial approximation (see section 2.4.3) is unchanged, the frequency range $P \pm r_n$ includes fewer excited frequencies. As a result, the correlation of the noise covariance estimate is reduced. As shown in this thesis, accurate results can be achieved with two periods of data; the effect of noise can be further reduced, when more periods are observed. This result is in accordance with the recommendations in (Pintelon & Schoukens, 2012).

Polynomial order R: The user must set the order R of the polynomials that are used to approximate the transient term and the FRM. As discussed in (Pintelon & Schoukens, 2012, p. 231), quadratic polynomials (i.e. $R = 2$) are often a good compromise, while higher order polynomials can reduce the bias at low damped poles. As shown in section 2.5.4, the bias is a function of frequency resolution and polynomial order; equation (2.133) can be used to estimate the effect of higher order polynomials on the bias of the FRM estimates. As shown by Schoukens et al., even degrees are most suitable. Within this thesis, all estimates were computed with quadratic polynomials. The benefits of higher order polynomials should be examined on a case –by-case basis.

Degrees of freedom of covariance matrix estimate q: The dofs of the covariance matrix estimate $\hat{C}_{vec(\hat{G})}$ are selected according to equation (2.127). To ensure the existence of the covariance of the F-distribution, the parameter m is chosen as 2, cmp. section 2.5.2. As pointed out in (Pintelon & Schoukens, 2012, p. 230), the number of degrees of freedom q should be generally as small as possible.

In summary the conducted experiments[46] show that standard settings for the LPM parameters are sufficient to achieve accurate estimation results. This renders the LPM a very robust method that is also well suited for online applications, where the experimenter has to set all parameters in advance.

[46] Only a part of the simulation results is presented here.

3.6 SUMMARY

The comparison of the ETFE, the transient LPM and the fast LPM estimates shows the advantages and the effectivity of the transient term estimation. The effect of non-zero initial and final conditions was shown with Monte Carlo simulations of a linear plant model without noise. The local polynomial methods estimate the initial and final conditions accurately and provide accurate FRF estimation results also from the first two periods of data. A comparison with non-linear simulation results show, that the effect of non-zero initial conditions can be covered by noise and nonlinear effects.

In both cases, fairly good estimation results were achieved with standard settings for the local polynomial user choices. This is a significant advantage especially compared to the commonly used spectral methods. Spectral Methods are sometimes considered "*more art than science*" (Tischler & Remple, 2006, p. 145), as they are quite sensitive to the many user choices that are related to the sampling, filtering and the proper choice of window functions. The local polynomial methods, however, are less sensitive to the few required user choices and even with standard settings fairly good estimation results can be achieved.

4 MULTIPLE INPUT FREQUENCY RESPONSE ESTIMATION

The unique feature of the fast local polynomial method is the estimation of frequency response matrices with full frequency resolution from one single experiment, where full frequency resolution means, that all FRFs have the same frequency resolution. With previous methods, multiple experiments (one for each input) were required (ETFE and spectral methods) or the frequency resolution was different for each control input (in the case of zippered multisines). To make this advance possible, the frequency responses are approximated with local polynomials.

As a preparation for the computation of confident stability levels in chapter 5, the general accuracy of the fast local polynomial method is analysed. The focus is on the interpolation bias and the border effects. To show the overall performance of the estimates, a wide frequency range, covering two decades, is analysed. The chapter starts with the description of the analysed flight condition(section 4.1). In section 4.2 the systematic estimation errors are analysed and compared to the bias estimate that was derived in section 2.5.4. The (co-) variance estimates are analysed in section 4.3.

4.1 SIMULATION SETUP

4.1.1 FREQUENCY RANGE AND FREQUENCY RESOLUTION

The analysis in this chapter is based on Monte Carlo simulations that analyse frequency response matrix estimates in the frequency range from 0.05 Hz to 5 Hz with a constant frequency resolution of 0.01 Hz. This frequency range spans two decades and includes the phygoid, short period, Dutch roll and roll modes. The frequency resolution of 0.01 Hz is intentionally below the guideline (see Table 3-1) for the Phygoid and the Dutch roll, to show the bias effect on FRM estimates.

The fast LPM is used to estimate the frequency response functions from all three inputs (roll-, pitch- and yaw-command) to the respective rotational rates measurements p_S, q_S, r_S. The estimation is based on two periods of a random phase multisine signal.

4.1.2 LPM USER CHOICES

The FRM is estimated with the LPM algorithm. The estimation is based on 2 full periods, the polynomial order is 2, the full FRM with 3 inputs and 3 outputs is estimated and the covariance matrix estimate has 10 degrees of freedom.

Table 4-1: LPM User choices for MIMO estimation.

Parameter	Value
Polynomial order R	2
Number of full periods	2
Parameter m[47]	2

[47] See section 2.5.2 for details on m.

4.1.3 Flight Conditions and Aircraft Configuration

The initial flight conditions are the same as in chapter 3. The flight starts in trimmed level flight at 610 m altitude and at 24 m/sec speed.

For the analysis of the estimation bias in section 4.2, no additional noise sources (turbulence, sensor noise) are contained in the simulation, as they would disturb the estimation result.

The analysis of the covariance estimates is based on simulation with light turbulence and a generic tactical grade IMU.

4.2 Bias Estimate and Estimation Bias

As shown in section 2.5.4.6 the LPM algorithm requires a minimum frequency resolution Δf to be accurate. According to the design rules, a frequency resolution Δf of 0.01 Hz ensures an accurate estimation of short period dynamics, while the estimation of phygoid- and Dutch roll dynamics should be estimated with a finer frequency resolution. To study the effect of the coarse frequency resolution on the FRF estimates, the estimation results are compared to analytically linearized dynamics.

4.2.1 Estimation Bias

Figure 4-1 shows the nominal frequency response functions $G_{q_K\eta_c}$ and $G_{r_K\zeta_c}$ as magenta dashed lines; the relevant eigenmodes are highlighted. The estimates of the primary pitch and yaw responses, $\hat{G}_{q_K\eta_c}$ and $\hat{G}_{r_K\zeta_c}$, are shown as blue solid lines. The estimate is averaged over 50 repeated simulations with different random phase excitation signals, so that excitation specific deviations from trim speed are compensated.

The respective estimation errors $|\varepsilon(\hat{G})|$, $\angle\varepsilon(\hat{G})$ are shown as orange crosses. Magnitudes are shown in dB, phases in degree. The estimates are based on simulations under clean conditions (no turbulence, no sensor noise), as otherwise the effect may be covered by noise.

It can be seen that the LPM estimate follows the nominal dynamics of the short period and Dutch roll. In the vicinity of the respective eigenfrequencies (at 0.33 and 0.48 Hz), the estimation magnitude errors $\varepsilon(|\hat{G}_{q_K\eta_c}|)$ and $\varepsilon(|\hat{G}_{r_K\zeta_c}|)$ are within ± 1 dB (± 10 deg) and hence in the same order as the error in other frequency ranges, i.e. especially at higher frequencies. The precise values at the eigenfrequencies are listed in Table 4-2.

A different result is found for the Phygoid and the zero $\eta_{r_K\zeta_c}$: Due to the too coarse frequency resolution, the polynomials cannot follow the FRF in the vicinity of the eigenfrequencies. This results in estimation errors due to the polynomial approximation. The amplitude estimation errors in the vicinity of the frequencies of the Phygoid and the zero $\eta_{r_K\zeta_c}$ (0.050 and 0.082 Hz) exhibit larger magnitude errors in the order of ± 10 to ± 15 dB. The respective phase errors $\varepsilon(\angle\hat{G}_{q_K\eta_c})$ and $\varepsilon(\angle\hat{G}_{r_K\zeta_c})$ range from -18 deg to $+71$ deg, cmp. Table 4-4.

When compared to the MUAD bounds (see Figure 4-2), it is seen that the error is within the bounds around the Dutch roll mode and outside around the Phygoid.

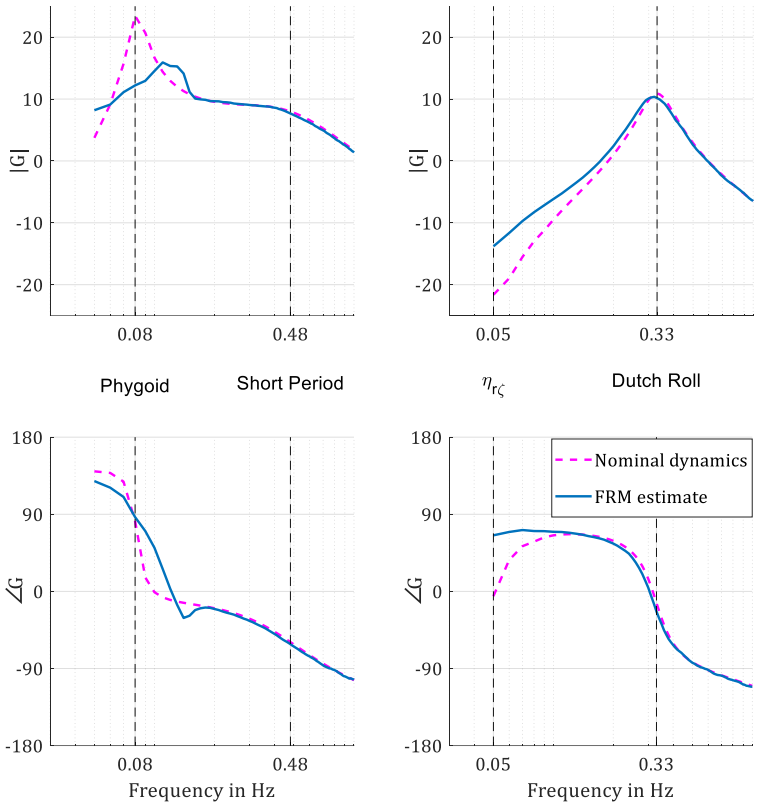

Figure 4-1: Effect of coarse frequency resolution on LPM estimate.

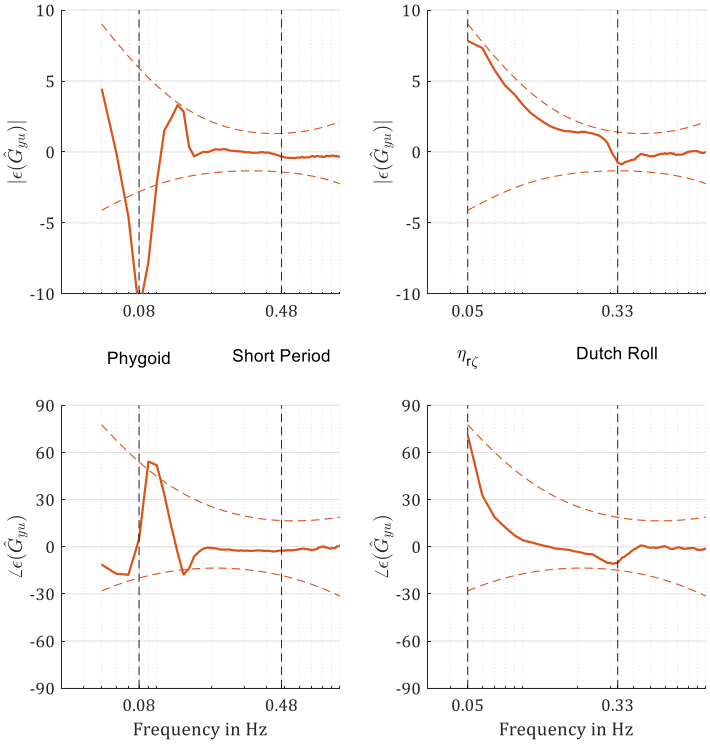

Figure 4-2: Magnitude and phase interpolation error compared to MUAD bounds (dashed).

Table 4-2: Magnitude and phase estimation bias at the eigenmodes.

	Phygoid	Short period	$\eta_{r\zeta}$	Dutch roll
Magnitude error in dB	-11.2	-0.32	7.8	-0.74
Phase error in angle	4.85	-2.5	71.1	-10.1

Table 4-3: Mean magnitude estimation errors.

	Pitch response	Yaw response
Mean magnitude error in dB	-0.13 dB	-0.026 dB

Table 4-4: Estimation error range.

Largest errors	Pitch response	Yaw response
upper magnitude error	4.5 dB	7.8 dB
lower magnitude error	-11.2 dB	-0.8 dB
upper phase error	54.1 deg	71.1 deg
lower phase error	-17.8 deg	-10.9 deg

4.2.2 Border Effect

As the Phygoid eigenfrequency of 0.082 Hz and the frequency of the transfer function zero $\eta_{r\zeta}$ (at 0.050 Hz) are close to the low frequency bound of the frequency range of interest, the estimation errors due to polynomial approximation are further amplified by the border effect (cmp. section 2.4.3.2). Due to the LPM approximation the first 10 frequencies (0.05 to 0.15 Hz) are correlated and hence exhibit increased estimation errors.

From equation (2.133) an estimate of the approximation error due to coarse frequency resolution is given by

$$\varepsilon_{pa}\left(\left|\hat{G}\right|\right) \approx 0.857\left(\frac{B}{2\zeta_0\omega_0}\right)^{R+2}, \tag{4.1}$$

where R is the polynomial order, ζ_0 the damping and ω_0 the eigenfrequency of the respective mode and B the frequency range of the local polynomial estimate, where $B = \Delta f \cdot n_E$, where $\Delta f = 0.01\ Hz$ is the frequency resolution and $n_E = 10$ the number of DFT lines in the least squares estimate.

The resulting error estimates with the amplification due to the border effect are listed in Table 4-5 for the phygoid and $\eta_{r_K\zeta_c}$-estimates. They are compared to the observed amplification, i.e. the actual magnitude errors (Table 4-2) divided by the mean magnitude errors, averaged over all frequencies (Table 4-3).

$$\text{Observed Amplification} = \frac{\text{magnitude error at eigenmode}}{\text{mean magnitude error, averaged over all frequencies}}$$

It is seen that the error estimates (41 dB and 53 dB) are slightly conservative, but close to the observed amplification factors (38 dB and 49 dB).

Table 4-5: Estimated and actual relative errors due to local approximation.

Mode	Estimated amplification $\boldsymbol{\varepsilon_{pa}}(\lvert\widehat{\boldsymbol{G}}\rvert)$	Observed amplification
Phygoid	41 dB	38 dB
$\eta_{r_K\zeta_c}$	53 dB	49 dB

4.2.3 Interpolation Bias Estimate

The interpolation bias estimate introduced in section 2.5.4 is computed for the phygoid (at 0.08 Hz) and the Dutch roll mode (at 0.33 Hz). The bias estimates are respectively

$$\hat{b}_{PH} = 13.8 \text{ dB} \tag{4.2}$$

and

$$\hat{b}_{DR} = 5.4 \text{ dB}. \tag{4.3}$$

When compared to the magnitude bias observed at the eigenmodes of -11 dB (phygoid) and 0.74 dB (Dutch roll) respectively, cmp. (Table 4-2), it is seen that the estimates are very conservative. This emphasizes, that the estimates should be interpreted as worst-case approximations.

4.3 Variance Estimates

The LPM algorithm estimates the FRM and the (co-)variance for each experiment. While the FRM estimate and its errors have been discussed in preceding section, the focus is now on the covariance estimates.

(Pintelon & Schoukens, 2012, pp. 236–237) state that the covariance estimate $\hat{C}_{vec\hat{G}}$ is asymptotically ($N \to \infty$) complex Wishart distributed, where N is the number of observed samples. The actual distribution of $\hat{C}_{vec\hat{G}}$ for finite N is generally not analytically known. Furthermore, systematic errors like the estimation bias due to frequency resolution (see section 2.5.4), border effect (see section 2.4.3.2), and correlation of adjacent frequencies, can cause deviations from the expected distribution. As a consequence, there is no "true" distribution of the covariance estimates that the estimates could be compared to.

Due to these difficulties, the covariance matrix estimates are not directly validated. However, the confidence levels, that are a direct function of the covariance estimates, are validated in chapter 5 with Monte Carlo simulations. The analysis here is limited to a more qualitative comparison of the covariance matrix estimates with sample variances computed from repeated simulations, that at least shows the effect of the border effect on variance.

4.3.1 Analysis Method

The LPM algorithm provides estimates of the FRM $\hat{G}$ and its sample covariance matrix of $\hat{C}_{vec\hat{G}}$, based on local polynomial fits over adjacent frequencies. The diagonal elements of $\hat{C}_{vec\hat{G}}$ are the variance of the respective entries in $\hat{G}$; the off-diagonal elements are the complex covariances. To assess the accuracy of the covariance estimates, an additional, independent way to compute the variance of $\hat{G}$ is required.

This is based on multiple, independent experiment. For each experiment, the LPM algorithm provides an estimate $\hat{G}_{LPM}^{[i]}$, where the index [i] indicates the i-th experiment. Hence for each element of $\hat{G}$ its variance can be estimated as

$$\hat{\sigma}^2_{\hat{G},MC} = var\left(\hat{G}_{LPM}^{[i]}\right) \tag{4.4}$$

where MC indicates the Monte Carlo-approach. The resulting values are compared to the respective diagonal elements of $\hat{C}_{vec\hat{G}}$.

This approach can be interpreted as a 2-dimensional problem: The FRM estimation is performed for multiple frequencies and for multiple experiments, i.e. the result can be described in a frequency-experiment plane. The LPM algorithm basically estimates variance along the frequency axis, while the Monte Carlo approach estimates variance along the experiment-axis. Neighboured samples along the frequency axis are correlated; samples along experiment axis are independent. It is noted that both approaches are based on the same set of estimates $\hat{G}$ and systematic errors in the $\hat{G}$ will affect both approaches.

The Gaussian approximation requires an input signal-to-noise ratio larger than 20 dB, cmp. section 2.6.2. To ensure this, the estimation is limited to a reduced set of 70 frequencies, cmp. section 3.2.5.3. A detailed discussion of the signal-to-noise ratio is found in section 5.2.

4.3.2 Validation of Covariance Estimates

Figure 4-3 shows a boxplot of the estimation results $\hat{\sigma}^2_{\hat{G},LPM}$ in blue colour; $\hat{\sigma}^2_{\hat{G},MC}$ is shown as orange line. For improved clarity, only a subset of the estimated frequencies is shown. As a consequence, the x-axis scale changes over frequency, as boxes are drawn equidistantly:

- At the low and high frequency borders, all full frequency resolution (0.01 Hz) is shown.
- In the intermediate range from 0.2 Hz to 4.85 Hz, only *every tenth frequency* is plotted for better clarity; the shown frequency resolution is 0.1 Hz.

The absolute values of $\hat{\sigma}^2_{\hat{G}}$ cover more than 5 orders of magnitude and are scaled to dB for better readability; so Figure 4-3 actually shows $dB\left(\hat{\sigma}^2_{\hat{G}}\right)$. From Figure 4-3 it is seen that the median of $\hat{\sigma}^2_{\hat{G},LPM}$ coincides well with $\hat{\sigma}^2_{\hat{G},MC}$ for all responses.

It is noted that in the pitch and yaw responses, the covariance is increased around the lightly damped poles (phygoid around 0.08 Hz, Dutch roll around 0.33 Hz). Due to the scale changes, this increase seems very sharp.

4.3.3 Border Effect

At the low and high frequencies, the increase of variance due to the border effect is clearly seen. In Figure 4-3 this increase is especially pronounced for the first and last five frequencies, but it actually affects the first and last 10 estimated frequencies, i.e. frequencies 1 (0.05 Hz) to 10 (0.15 Hz) and frequencies 491 to 500 (4.9 to 5.0 Hz) respectively.

The maximum effect occurs at the edges, where the average[48] increase of $\hat{\sigma}^2_{\hat{G}.MC}(0.05\text{ Hz})/\hat{\sigma}^2_{\hat{G},MC}(0.15\text{ Hz})$ [49] is a factor 7.2 (rounded to one digit) which is close to the approximate factor of 8 that is expected for estimates with $R = 2$, cmp. section 2.4.3.2.

At the high frequency border, the average increase is a factor of 3.3 and thus slightly smaller than the estimation that is thus conservative. The increase is consistently contained in the LPM-covariance estimates, and thus also in the confidence levels.

[48] The average is computed over all nine input/output pairs.
[49] These are the first (largest border effect) and 11th frequency (first frequency without border effect).

4.3.4 SUMMARY

The comparison of $\hat{\sigma}^2_{\hat{G},LPM}$ with $\hat{\sigma}^2_{\hat{G},MC}$ shows a close match. This emphasized the accuracy of the (co-)variance estimate provided by the LPM algorithm. As it is seen, the border effect increases variance as expected from theory.

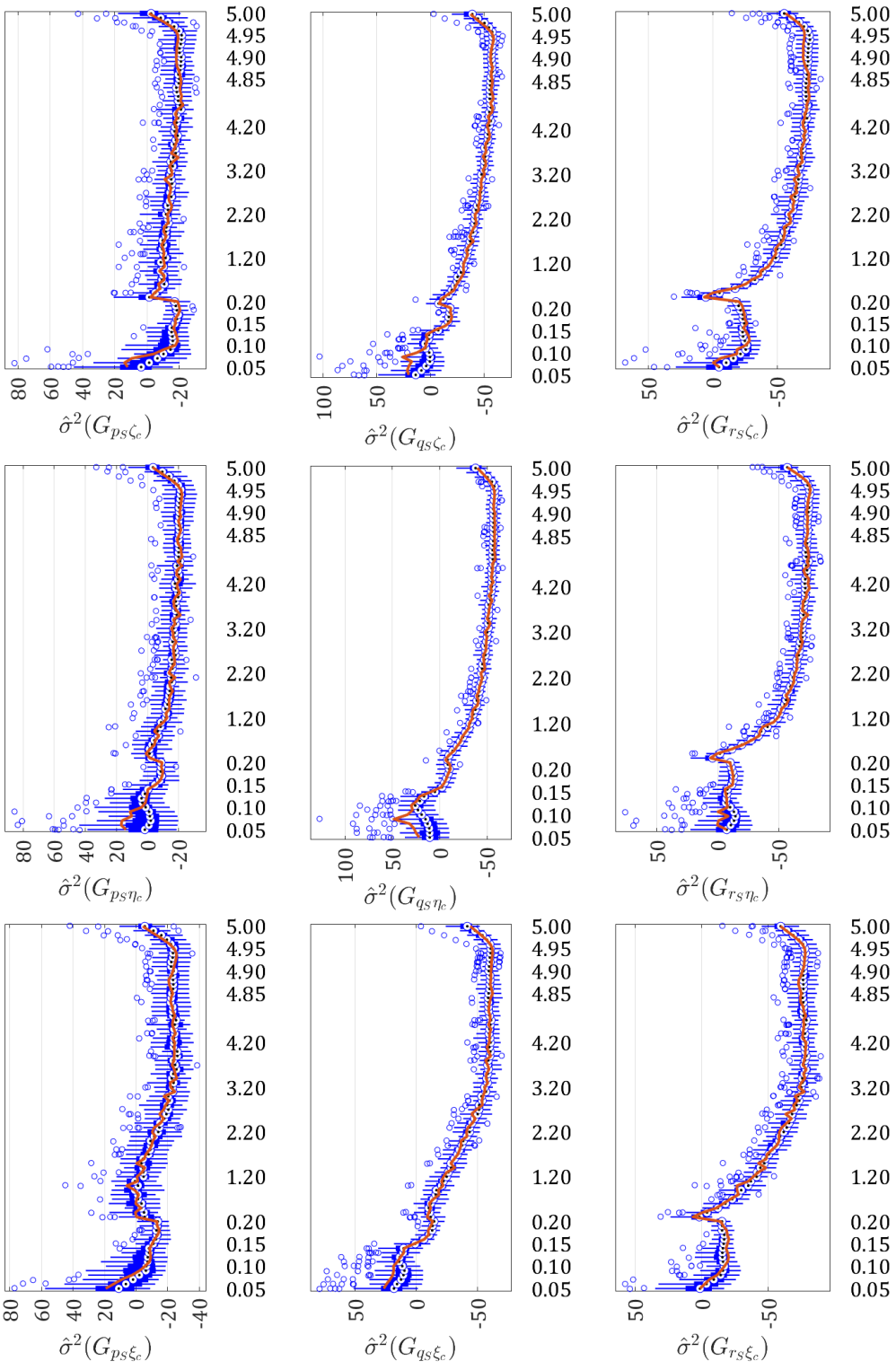

Figure 4-3: Comparison of $\hat{\sigma}^2_{\hat{G},LPM}$ (blue boxplot) and $\hat{\sigma}^2_{\hat{G},MC}$ (orange line)both in dB. In the range from 0.2 Hz to 4.85 Hz only every tenth excited frequency is plotted.

5 CONFIDENT ROBUST STABILITY

In the following chapter, the robust stability criteria for MIMO systems (sections 2.7, 2.8) are applied to the estimated plant to assess its stability. The criteria require frequency response matrices with full frequency resolution, i.e. for each frequency the entire FRM must be available. Before the development of the local polynomial methods, this could not be computed from a single experiment. The stability criteria provide measures of the largest uncertainty that can be tolerated by the controller. They are related to the estimates' confidence regions, giving the probability of the system to be not instable, cmp. section 2.8.

For the FCS stability, often only a part of the system frequency range is critical. For piloted aircraft, the slow eigenmodes (spiral mode, phygoid) are allowed to be "slightly" instable for some flight conditions (Department of Defense, 1997), where slightly means that the time to double is larger (i.e. it increases slower) than some threshold. The limits are such that the pilot can easily stabilize the dynamics[50]. For the faster modes, esp. the Dutch roll, short period, roll mode, this is not feasible, as a human pilot would easily be overstrained by the steady control task. Thus, handling quality criteria require the faster modes to be stable for all flight phases (Department of Defense, 1997).

In this chapter, the focus is on fast dynamics, with a focus on the short period and the Dutch roll modes and eventual higher frequency (elastic) modes. The oscillating rigid body mode eigenfrequencies typically range from 0.01 Hz (phygoid) over 0.1 Hz (Dutch roll) to about 1 Hz (short period). The slowest elastic modes have typical eigenfrequencies of some Hertz.

The controller bandwidth[51] often ranges up to several Hertz, so that provisions must be taken to avoid excitations of structural modes by the FCS. Typical measures are notch-filters, that exclude the eigenfrequencies, and roll-off filters, that limit the controller bandwidth. However, if the eigenmodes are not accurately known, the filter design may be inadequate, or modes may be entirely unknown. In such cases, it can be important to carefully conduct flight tests and verify if the flight control design matches the actual dynamic. In such situations, the combined estimation and stability analysis approach described in chapter 2 provides a valuable tool to assess the system stability.

The chapter starts with a description of the experiment setup (section 5.1) and an analysis of the simulation results - this includes the analysis of the signal-to-noise ratio of the input signal, its aircraft specific sensitivity and its estimation from flight data (section 5.2) and the validation of the extended confidence regions in section 5.3. After that, the confident robust stability analysis, that was introduced in section 2.8, is applied to the flight test data. The proposed stability test is based on a nominal model, the multiple input frequency response matrix and its sample covariance matrix; the two latter are provided by the fast LPM.

The confident stability measures are based on a three step approach:

- First, the stability of the estimated system is tested with respect to the nominal model.
- Second, the stability of the uncertain system (with a 1σ-uncertainty) is tested.
- The third step computes the confidence level that corresponds to the largest uncertainty (from step 2) that is robust stable.

[50] An overview over different pilot models, that include the concept of a limited pilot bandwidth is found in chapter 7 of Schuck (2013).
[51] The bandwidth of a controller is defined as the frequency, where the closed-loop response drops to 0.707 of ist zero frequency (DC) value Levine (1999, p. 161).

In the first step (section 5.4), it is shown, that the estimated FRM is stable. For this, the nominal model error between the estimate and the nominal model is interpreted as an uncertainty and the robust stability are applied to it. When the nominal model is stable and the robust stability criteria hold, it is ensured that the estimated FRM is stable, too. Here it is strictly required, that the nominal model *must* be stable. However, it *need not* be close to the true system (!), which however helps, as it reduces the nominal model error.

In the scenario introduced in the introduction, when flight control systems for legacy aircraft are designed, that are based on (nominal) models with uncertainties, this first step accounts for the structural and parametric model errors of the nominal model. As the estimated FRM is a non-parametric model of the true dynamics, it is not susceptible to structural and parametric model errors and naturally includes e.g. (not a priori known) elastic modes.

The second and third steps (section 5.5) deal with the estimation uncertainty, that is caused by measurement noise, but also the additional variance due to the nonlinear dynamics in the plant (like speed changes of the aircraft). Thus, the proposed stability test accounts for systematic effects and random effects: Systematic effects on the estimates are accounted for by nominal stability (first step). Random effects are accounted for by the robust stability (steps two and three).

The combined total confidence is studied in section 5.6; finally followed by the discussion of time varying dynamics and the application of confident stability for integrity monitoring (section 5.7).

5.1 Simulation Setup

5.1.1 Frequency Range and Frequency Resolution

The analysis in this chapter is based on Monte Carlo simulations that analyse frequency response matrix estimates in the frequency range from 0.29 Hz to 2.89 Hz. This frequency range spans about one decade and includes the Dutch roll, short period and roll mode. The fast LPM is used to estimate the frequency response functions from all three inputs (roll-, pitch- and yaw-command) to the respective rotational rates measurements p_S, q_S, r_S. The estimation is based on two periods of a random phase multisine signal.

The frequency resolution is adjusted piecewise as listed in Table 5-1, so that the recommended frequency resolution is achieved for all three modes, cmp. Figure 3-6. The resulting signal contains 73 excited frequencies.

Table 5-1: Piecewise adjusted frequency resolution.

Frequency range	Frequency resolution Δf
0.285 Hz to 0.38 Hz	0.005 Hz
0.38 Hz to 0.58 Hz	0.01 Hz
0.58 Hz to 2.89 Hz	0.7 Hz

5.1.2 LPM User Choices

The FRM is estimated with the fast LPM algorithm. The estimation is based on 2 full periods, the polynomial order is 2, the full FRM with 3 inputs and 3 outputs is estimated and the covariance matrix estimate has 10 degrees of freedom. A summary of the LPM settings is found in Table 5-2.

Table 5-2: LPM User choices for MIMO estimation.

Parameter	Value
Polynomial order R	2
Number of full periods	2
Parameter m	1

5.1.3 Flight Conditions and Aircraft Configuration

The simulation setup from chapter 3 are adjusted to achieve better input signal-to-noise ratios: the turbulence intensity is reduced to one third[52] and the controller gains are reduced to 0.1 (one fifth of their original value). The reference signal amplitude is increased by a factor of 5 to keep the excitation level constant; in combination, this increases the signal-to-noise ratio of the input signal. The approach of reducing controller gains for improved estimation of frequency response functions is similarly recommended in (Tischler & Remple, 2006, p. 95).

5.2 Signal-To-Noise Ratio

The estimation of circular confidence regions requires a Gaussian approximation of the probability distribution of $\hat{G}$. (Pintelon et al., 2003) show that the Gaussian approximation holds if the input signal-to-noise ratio is larger than 20 dB; the fast LPM does not require this limit, cmp. section 2.6.2. Nevertheless, the accuracy of the estimates depends on the signal-to-noise ratio. Hence it is generally advantageous to test the SNR in the input signal, as it informs about frequency regions that may be insufficiently excited.

As introduced in (Pintelon et al., 2003), the input SNR is defined as

$$SNR_U(k) = \frac{|U_0(k)|}{|V_U(k)|} \tag{5.1}$$

where U_0 are the DFT coefficients of the useful signal and V_U are the DFT coefficient of the noise contributions and the total input signal is $U(k) = U_0(k) + V_U(k)$. It is noted for systems operated in closed loop, the indirect LPM algorithm will treat any signal component in $u(t)$ that is not linearly related to the reference signal $r(t)$ as noise. (Pintelon & Schoukens, 2012, p. 241)

If the noise level $|V_U|$ is independent of $|U_0|$, the SNR_U can be easily increased by increasing $|U_0|$, i.e. by injecting more power to the system input, cmp. (Pintelon & Schoukens, 2012, p. 47). In case of aircraft applications there are operational limitations to the maximum excitation amplitude. Hence it is useful to analyse the signal-to-noise ratio of the system under closed loop conditions in more detail to identify factors that limit the achievable SNR_U.

[52] With light turbulences the required excitation to achieve $SNR(U) \geq 20$dB results in roll- and pitch attitude angles larger than 60 degrees. Such flying conditions are usually considered beyond the valid range of linear models.

5.2.1 Influence of Aircraft Dynamics on Input SNR

Under closed loop conditions, the input signal consists of the reference signal and the contributions due to the feedback loop. While the reference signal is known exactly, all other contributions may contain noise. Figure 5-1 shows a detailed block diagram of the closed loop system with turbulence and sensor noise separated. The control loop with the reference input r, controller K, aircraft dynamics G_1, output y and the unit feedback have been introduced already in Figure 2-29.

For the further study of the effect of turbulence and sensor noise on the signal-to-noise ratio of the input signal u, denoted as SNRu, the aircraft dynamics-block must be split in two parts. The first ones, denoted with G_1 contains the control allocation, actuator dynamics and control surface aerodynamics, i.e. it relates the controller commands u to the control forces $\vec{F}^G_{ctrl}$and control moments $\vec{M}^G_{ctrl}$. The second part denoted by G_2 contains the effect of all non-aerodynamic forces & moments (e.g. gravity), the equations of motion (EOM) and the entire sensor dynamics (gyro dynamics & deterministic gyro error models, see appendix A.5). Its input are the aerodynamic forces and its output the measured kinematic rotational rates $(\vec{\omega}^{IB}_K)_{IMU,0}$ without sensor noise; adding sensor noise v_{IMU} results in the control system output y, that is here physically the rotation rates $(\vec{\omega}^{IB}_K)_{IMU}$ as measured by the IMU. The turbulence is denoted as t and is filtered white noise with $t = G_3 v_{turb}$, where G_3 describes the Dryden turbulence model and v_{turb} is the driving white noise source. When the turbulence t hits the aircraft, the aerodynamic forces $\vec{F}^A_{turb}$ and moments $\vec{M}^A_{turb}$ act on the aircraft. Their relation on the turbulence t (i.e. the aircraft's turbulence sensitivity) is described by block G_4. Lists with all signals and transfer functions are found in Table 5-3 and Table 5-4.

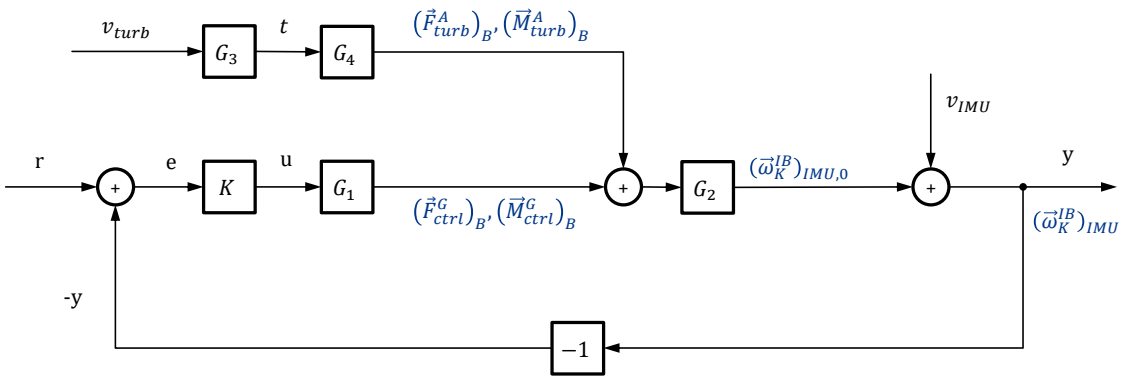

Figure 5-1: Block diagram with turbulence and sensor noise.

From the block diagram follows directly

$$G_{ur} = \frac{K}{G_1 G_2 K + 1} \tag{5.2}$$

$$G_{uv_{IMU}} = \frac{-K}{G_1 G_2 K + 1} \tag{5.3}$$

$$G_{uv_{turb}} = \frac{-G_2 G_3 G_4 K}{G_1 G_2 K + 1} \tag{5.4}$$

The useful input signal U_0, i.e. the contribution of u that is related to r, is given by

$$U_0 = G_{ur} \cdot r \tag{5.5}$$

The noise contribution is

$$V_U = G_{uv_{IMU}} v_{IMU} + G_{uv_{turb}} v_{turb} \tag{5.6}$$

With equations (5.5) and (5.6) the signal-to-noise ratio (5.1) becomes

$$SNR(U) = \frac{|U_0|}{|V_U|} = \frac{|G_{ur} r|}{\left|G_{uv_{IMU}} v_{IMU} + G_{uv_{turb}} v_{turb}\right|} \tag{5.7}$$

More detailed simulations with varied noise models show that the sensor noise contribution is usually smaller than the turbulence contribution[53]. It thus can be assumed that $G_{uv_{IMU}} v_{IMU} \ll G_{uv_{turb}} v_{turb}$ and equation (5.7) can be approximated as

$$SNR(U) = \frac{|U_0|}{|V_U|} \approx \frac{|G_{ur}|}{\left|G_{uv_{turb}}\right|} \cdot \frac{|r|}{|v_{turb}|} \tag{5.8}$$

Inserting equations (5.2) and (5.4) results in

$$\begin{aligned} SNR(U) &= \left| \left(\frac{-1}{G_2 G_4} \right) \cdot \frac{|r|}{G_3 v_{turb}} \right| \\ &= \left| \left(-S_{SNR_u} \right) \cdot \frac{|r|}{G_3 v_{turb}} \right| \end{aligned} \tag{5.9}$$

where $G_3 v_{turb}$ describes the turbulence and $S_{SNR_u} = \frac{1}{G_2 G_4}$ is an aircraft specific term that describes the aircraft insensitivity to turbulences[54]. As the turbulence insensitivity is proportional to the inverse of the aircraft dynamics G_2, it is expected that S_{SNR_u} is small at the lightly damped eigenfrequencies of the phygoid and Dutch roll modes.

If a detailed simulation model of the aircraft is available, the turbulence insensitivity S_{SNR_u} can be computed numerically and equation (5.9) can be used to estimate the achievable signal-to-noise ratio of flight tests or to derive limits for the maximum tolerated turbulence level. If no such model is available, it is difficult to determine G_2 and G_4 from experiments only.

Equation (5.9) gives further insight into the distribution of signal-to-noise ratio over frequency. As indicated in Figure 5-1, both turbulence forces and moments contribute to the input noise. For the FAT aircraft with its pure rate feedback controller, the effect of moments is larger than the effect of forces. Furthermore, each input channel is primarily affected by the corresponding rotational rate, i.e. roll command is primarily a function of roll turbulence and so on). Hence the further analysis is limited to these responses.

Figure 5-2 shows the primary elements of $|S_{SNRu}|$ for the FAT simulation model in dB. It is seen that the roll input has rather lower sensitivity over the entire FRoI (close to 0 dB) with an increase to 8 dB for high frequencies. The pitch and yaw sensitivity show larger values up to 38 dB with significant dips in the region of the eigenfrequencies (around 0.08 Hz and 0.33 Hz respectively; this is due to already mentioned the inverse proportional relation of the turbulence insensitivity to the rigid body dynamics. Hence it is expected that the $SNR(U)$ around the eigenfrequencies tends to be low.

[53] This result is intuitively clear, when one keeps in mind that the sensors measurements are used to control the aircraft motion due to turbulence; if aircraft motion in turbulence would be covered in sensor noise, this was not possible.

[54] The turbulence (in)sensitivity should not be confused with the sensitivity function $1/(1 + GC)$ of control loops.

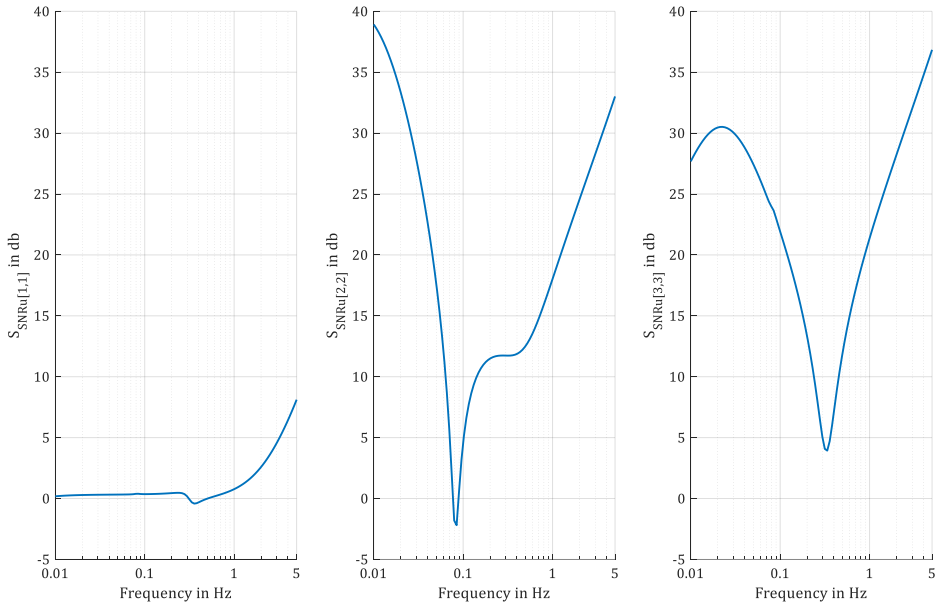

Figure 5-2: Sensitivity of FAT to turbulences.

This result can be used for excitation signal design: if the turbulence insensitivity is known, frequencies with low insensitivity can be excited with larger amplitudes. With this approach, the insensitivity can be (at least partially) compensated, resulting in favourable signal-to-noise ratios over the entire frequency range.

Table 5-3: List of signals in Figure 5-1.

Signal	Description
$\boldsymbol{r}$	Reference input signal
$\boldsymbol{e}$	Control error
$\boldsymbol{u}$	Controller command / plant input
$\boldsymbol{y}$	Signal output, here: $(\vec{\omega}_K^{IB})_{IMU}$
$\boldsymbol{t}$	turbulence that acts on aircraft
$\boldsymbol{v_{IMU}}$	IMU noise (here: white noise) (cmp. appendix A.5)
$\boldsymbol{v_{turb}}$	white noise
$\left(\vec{F}_{turb}^{A}\right)_B$	Forces due to turbulence
$\left(\vec{M}_{turb}^{A}\right)_B$	Moments due to turbulence
$\left(\vec{F}_{ctrl}^{G}\right)_B$	Forces due to control surface deflection
$\left(\vec{M}_{ctrl}^{G}\right)_B$	Moments due to control surface deflection
$\left(\vec{\omega}_K^{IB}\right)_{IMU,0}$	Rotational rate of body frame w.r.t inertial frame noted in IMU-frame without noise
$\left(\vec{\omega}_K^{IB}\right)_{IMU}$	Rotational rate of body frame w.r.t inertial frame in IMU-frame with IMU noise

Table 5-4: List of transfer function blocks in Figure 5-1.

Block	Input	Output	Description of content
$\boldsymbol{K}$		u	Controller
$\boldsymbol{G_1}$	u	$\left(\vec{F}_{ctrl}^{G}\right)_B, \left(\vec{M}_{ctrl}^{G}\right)_B$	Control allocation, actuator dynamics and control surface aerodynamics
$\boldsymbol{G_2}$	All forces & moments	$\left(\vec{\omega}_K^{IB}\right)_{IMU,0}$	Effect of non-aerodynamic forces & moments, equations of motion (EOM), gyro dynamics & deterministic gyro error model
$\boldsymbol{G_3}$	v_{turb}	t	Dryden turbulence model
$\boldsymbol{G_4}$	t	$\left(\vec{F}_{turb}^{A}\right)_B, \left(\vec{M}_{turb}^{A}\right)_B$	Aircraft dynamics due to turbulence

5.2.2 Estimation of Input SNR From LPM Estimates

The input signal-to-noise ratio can be estimated from the LPM estimates, as both, the input sample mean (from equation (2.111)) and its variance (from equation (2.112)), are estimated by the fast LPM algorithm for each element of the FRM estimate.

As the input sample mean contains noise, the signal-to-noise ratio estimate is computed as

$$SNR(U)_{LPM} = \frac{\left|\hat{U}\right| - \sqrt{\hat{C}_{Z,[i,i]}}}{\sqrt{\hat{C}_{Z,[i,i]}}} \tag{5.10}$$

where $\hat{U}$ is the estimated input signal without transient, and $\hat{C}_{Z,[i,i]}$ are the corresponding diagonal entries of the estimated covariance matrix.

Equation (5.10) can also be used to detect outliers, that should be removed to ensure convergence of the Gaussian approximation. Here, input values $\left|\hat{U}\right|$ that contain the origin within the $3\hat{\sigma}_{\hat{U}}$ (i.e. $\left|\hat{U}\right| < 3\hat{\sigma}_{\hat{U}}$) are considered as possible outliers and are discarded. In the simulation examples, no outliers have been observed thanks to the good signal-to-noise ratios, cmp section 5.2.3.

5.2.3 SNR in Multiple Input Experiments

Figure 5-3 shows a boxplot of the estimated input signal-to-noise ratio $SNR(U)$. The figure is based on 50 independent simulations and shows the SNR for roll (left), pitch (middle) and yaw command (right). The x-axis shows frequency in Hz in logarithmic scale. The frequency resolution is stepwise constant: In the range from 0.29 to 0.37 Hz, frequency resolution is 0.005 Hz; from 0.37 Hz to 0.58 Hz it is 0.01 Hz and from 0.58 to 2.89 Hz the frequency resolution is 0.07 Hz.

It is seen from the figure that the input signal-to-noise ratio is larger than 20 dB for nearly all frequencies. The median roll input signal-to-noise varies between 25 to 45 dB; the minimum value is 21.8 dB. Pitch input median SNR ranges from 29 dB up to 60 dB for high frequencies; the minimum value is 26 dB. The yaw input median SNR ranges from 21.9 dB to 70 dB; the minimum value is 18.5 dB. The result shows that the SNR of the roll and pitch inputs is larger than 20 dB for all frequencies and all repetitions. In 7 simulations, the yaw SNR is smaller than 20 dB for at least one frequency.

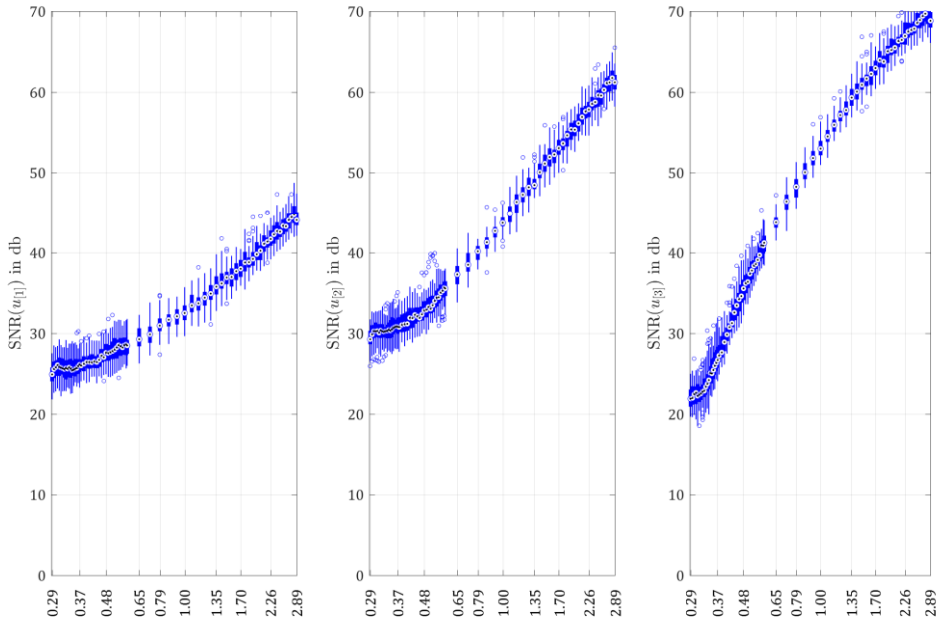

Figure 5-3: Estimated signal-to-noise ratio of input signal in dB.

Comparing the simulation results from Figure 5-3 to the turbulence insensitivity in Figure 5-2 clearly shows the conformity in shape of both curves. This underlines the effect of turbulence insensitivity on signal-to-noise ratios of the input signals, cmp. equation (5.9). Further it can be followed that the low signal-to-noise ratios in the pitch response in the vicinity of the phygoid eigenfrequency are aircraft specific and cannot be related to the estimation algorithm.

5.2.4 Summary

Based on an analytical derivation, it is shown that aircraft dynamics have a distinct influence on the input signal-to-noise ratio. The sensitivity of SNRu on disturbances can be easily computed from detailed simulation models, but not experimentally. Estimates of the SNRu can be computed directly from LPM results. For the FAT testbed, a modified simulation configuration is shown that results in favourable signal-to-noise ratios of more than 20 dB.

5.3 Analysis of Estimated Confidence Regions

To test the reliability of the estimated confidence regions, a series of 50 repeated experiments is conducted. For each experiment the true error is compared to the confidence radius based on the Gaussian approximation. This comparison allows to assess the reliability of the confidence regions under the given experimental conditions, i.e. under the influence of systematic errors due to frequency resolution, border effect, and correlation of adjacent frequencies. Therefore, the LPM estimates are compared to the error distribution of repeated simulation runs.

5.3.1 Extended Confidence Regions

The LPM algorithm provides covariance estimates $\hat{C}_{vec\hat{G}}$ for each element of the FRM estimate $\hat{G}$. As shown in section 2.6.5, confidence regions can be constructed from covariance estimates under the assumption of a Gaussian distribution. This results in circular confidence regions with radius

$$r_p(k) = \hat{\sigma}_{\hat{G}}(k)\sqrt{\mathbb{F}^{-1}(p, 2, 2M-2)} \tag{5.11}$$

cmp, equation (2.207), where $\hat{\sigma}_{\hat{G}}$ is the estimated standard deviation of the respective FRM entry. The observed errors are compared to the respective estimates; the focus is whether

$$\left|\hat{G} - G_0\right| < r_p \tag{5.12}$$

for any p-level. With equation (5.11) the inequality results in

$$\frac{\left|\hat{G} - G_0\right|^2}{\hat{\sigma}_{\hat{G}}^2(k)} < \mathbb{F}^{-1}(p, 2, 2M-2) \tag{5.13}$$

where M depends on the degrees of freedom of the covariance matrix. For experiments at hand M equals 11 and the right hand side of equation (5.13) becomes $\mathbb{F}^{-1}(p, 2, 20)$.

As seen from the experiments (cf. section 3.4), the LPM estimates from flight test experiments are biased. For the computation of confidence intervals, this systematic part need to be removed from the measured error $\hat{G} - G_0$. With the bias estimate from section 2.5.4, confidence regions that include the bias estimate, are found to be

$$\frac{\left|\left|\hat{G} - G_0\right| - \hat{b}\right|^2}{\hat{\sigma}_{\hat{G}}^2(k)} < \mathbb{F}^{-1}(p, 2, 2M-2) \tag{5.14}$$

To test the reliability of the confidence regions the cumulative distribution function (cdf) of $\left|\left|\hat{G} - G_0\right| - \hat{b}\right|^2 / \hat{\sigma}_{\hat{G}}^2(k)$ is computed for multiple independent experiments and compared to the analytical $\mathbb{F}(2, 2M-2)$-distribution.

5.3.2 Validation of Confidence Regions

The computation of circular confidence regions requires a Gaussian approximation of the probability distribution of $\hat{G}$. The approximation is valid for signal-to-noise ratios in the input signal of at least 20db; as in the preceding section to ensure a sufficient input signal-to-noise ratio, the FRM is estimated on a coarser frequency grid, see section 4.1. The experiment is repeated 50 times to study the effect of random disturbances.

As equation (5.11) should hold for all elements of the estimated FRM that are of interest, the analysis contains all frequencies of all responses. Hence a total of 32850 data points[55] are contained in the analysis. Table 5-5 lists some confidence levels (75%, 90%, 95% and 98%) with the respective number of expected and observed observations contained inside the confidence regions. As more data points are contained in the intervals than expected, the confidence levels are conservative.

Table 5-5: Confidence levels with expected and observed number of inliers.

Confidence Level	Expected number of contained estimates	Observed number of contained estimates	Contained estimates (in percent)
75%	24638	25813	78.6%
90%	29565	31856	97.0%
95%	31208	32727	99.6%
99%	32522	32850	100%

[55] Nine responses with 73 frequencies are estimated with 50 repetitions each.

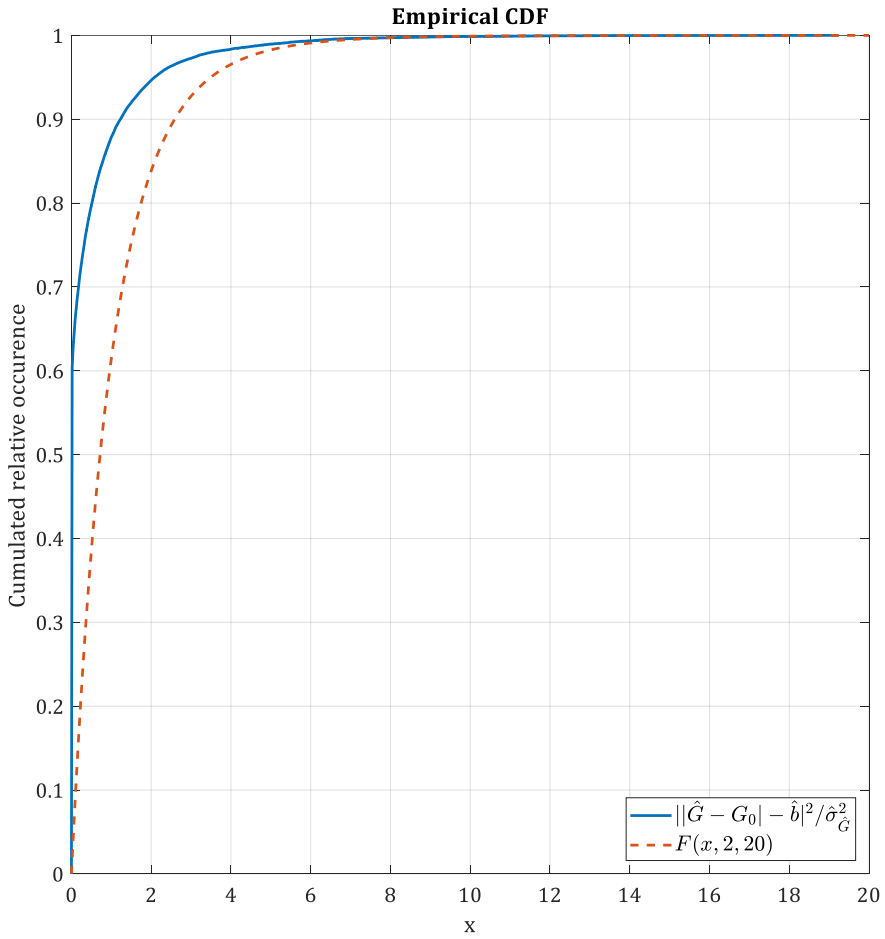

Figure 5-4: Empirical (blue) and analytical (orange, dashed) cumulative distribution function of $\left|\widehat{\boldsymbol{G}} - \boldsymbol{G_0} - \widehat{\boldsymbol{b}}\right|^2/\widehat{\boldsymbol{\sigma}}^2_{\widehat{\boldsymbol{G}}}$.

Figure 5-4 shows the cumulative distribution function of $\frac{\left|\left|\hat{G}-G_0\right|-\hat{b}\right|^2}{\hat{\sigma}^2_{\hat{G}}(k)}$ compared to the cdf of the expected $\mathbb{F}(2, 20)$-distribution. It is seen that the distributions differ clearly; the observed distribution function (blue) is larger than $\mathbb{F}(x, 2, 20)$ (orange) over the entire computed range. It follows that the observed errors are contained in the extended confidence regions and the extended confidence regions, including the bias estimate, are reliable.

5.3.3 Discussion

The experiments show that the observed errors $\frac{|\hat{G}-G_0|^2}{\hat{\sigma}^2_{\hat{G}}}$ are contained in the extended confidence regions. The extended confidence regions are conservative, as they contain more data points than expected.

Further analysis shows that the confidence regions r_p without the bias correction precisely describe the distribution of the sample errors, i.e. the errors $\left|\hat{G} - \mu_{\hat{G}}\right|$ w.r.t. the sample mean estimate $\mu_{\hat{G}}$ closely follow an $\mathbb{F}(2, 20)$ distribution. It follows that the differences between the observed and the expected distributions result from inaccurate bias estimates; the bias estimates introduced in section 2.5.4 are larger than the observed biases and are hence conservative.

5.4 Nominal Stability

To show nominal stability of the estimated system dynamics, the estimation error of $\hat{G}$ w.r.t to the nominal plant dynamics is assessed. The nominal plant G_n is designed to be stable. It is based on a pole-zero model of the linearized plant dynamics, see appendix A.3. The linearized model contains neutral poles on the unit circle; these are moved slightly inside the unit circle. The resulting dynamics are close to the linearized dynamics and stability is guaranteed as the system contains only poles inside the unit circle. The zeros remain unchanged as they have no influence on stability. The resulting positions of all poles are shown in appendix A.3.

The uncertainty model describes the estimation error as shown in section 2.8.1. The uncertainty weighting matrix W_{G_n} matches the estimation error w.r.t the nominal plant G_n as shown in equation (2.259). It is noted that the inverse $\left(I + K\hat{G}_{yu}\right)^{-1}$ existed in all experiments. However, as $\hat{G}_{yu}$ is a measured quantity, the existence of the inverse cannot be guaranteed.

Applying the robust stability criteria to the uncertainty model gives the results shown in Figure 5-5. The boxplot shows $H_{\infty,nom}$ in blue and ssv_{nom} in orange, both scaled in dB. Each box represents the result of 50 simulations. The critical boundary for both criteria at 0 dB is highlighted with a black dashed line; for any $H_{\infty,nom} < 0$ dB (or $ssv_{nom} < 0$), nominal stability is given. This is the case for all frequencies and for all repetitions.

In a wide part of the FRoI, $H_{\infty,nom}$ is smaller than -10 dB, decreasing for high frequencies to -17 dB. Around the Dutch roll eigenfrequency at 0.34 Hz, slightly larger values are observed. With structured singular values, a very similar result is achieved with about -5 dB smaller values for all frequencies.

These results show that all FRM estimates are stable w.r.t. the nominal model. This means that the estimated FRM $\hat{G}_{yu}$ without uncertainty, is stable.

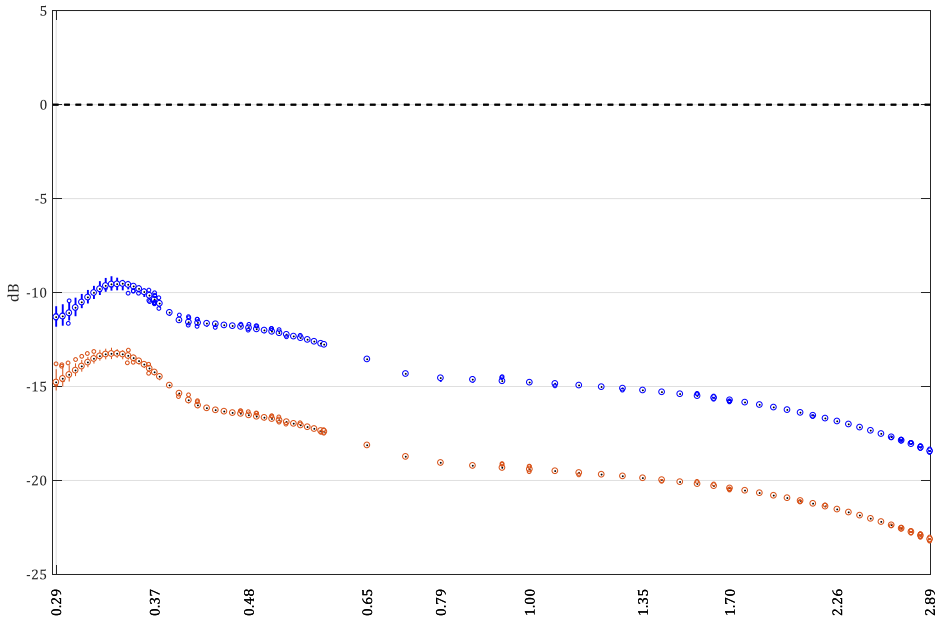

Figure 5-5: Nominal stability based on H_∞-criterion (blue, top) and structured singular values (orange, bottom).

5.5 Robust Stability

To test for robust stability, the uncertainty model (section 2.8.1) is computed from the extended confidence intervals (sections 2.6.5.2 and 5.3.1). Additionally, an maximum intergrid error of 3% of $|\hat{G}|$ is included; with a frequency resolution of 0.005 Hz, this accounts for the magnitude errors of any resonance peak with damping larger than 0.01. The robust stability criteria are applied and the corresponding confidence levels are computed frequency-wise (section 5.5.1). In section 5.5.2 the analysis is extended from single to multiple frequencies, i.e. to a frequency range.

5.5.1 Stability for Single Frequency

Based on the covariance estimates or confidence regions, robust stability of the system are assessed as shown in section 2.8.2. The system is robust stable w.r.t the respective uncertainty, if the H_∞-norm / the structured singular values ssv are smaller than 1 (or 0 dB).

Figure 5-6 shows H_∞ for the simulated data. The uncertainty is equal to one standard deviation. The stability bound at 0 dB is highlighted with a black dashed line. Simulations with $ssv < 0\ db$ are robust stable; otherwise no conclusion can be drawn.

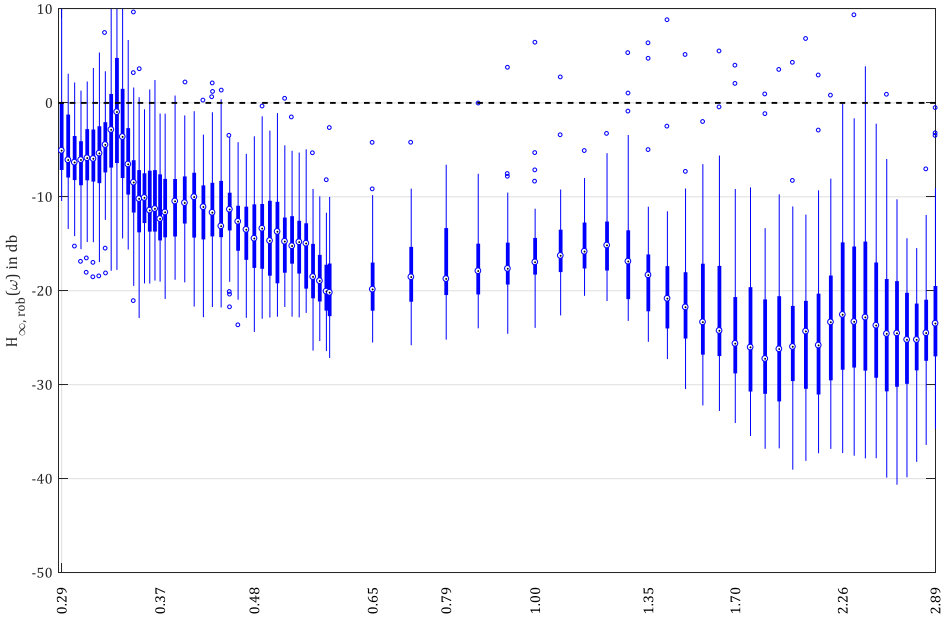

Figure 5-6: Robust stability with 1σ-uncertainty as function of frequency (H_∞-criterion).

It is seen from the figure, that over the entire frequency range of interest, outliers are observed that violate the stability criterion. In the low frequency range, from 0.29 to about 0.40 Hz, several spikes cross the critical line. In this regions, up to 25% of the simulation runs exceeded the 0 dB limit. Around 2.3 Hz some spikes touch the critical line.

Analogously, Figure 5-7 shows the structured singular values ssv for the identical uncertainty. It is seen from the figure, that the spikes cross the boundary only at 0.29 and 0.38 Hz, with few nonstable outliers, mostly at low frequencies. All other simulations are robust stable. Compared to the H_∞-values, the structured singular values are several dB smaller, indicating the conservatism of the H_∞-criterion.

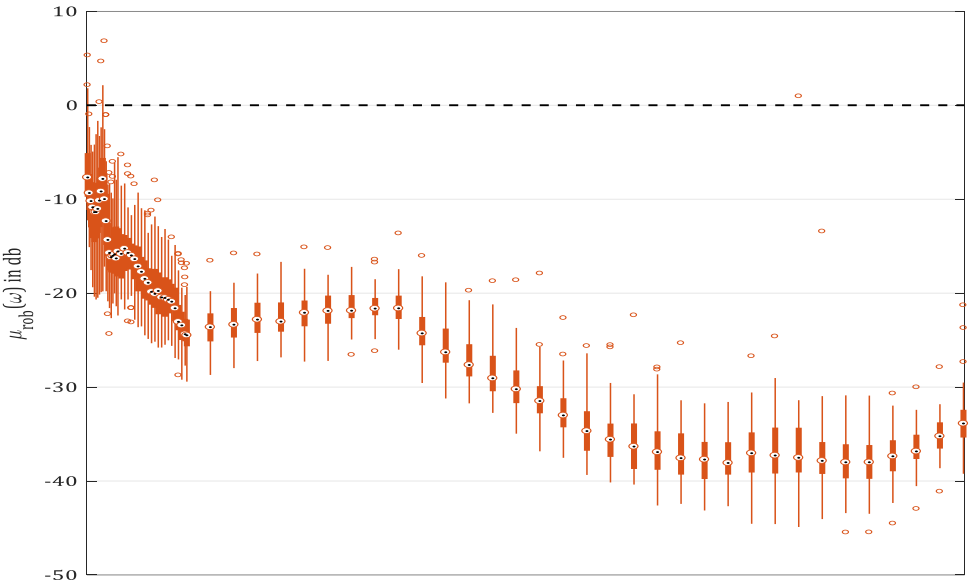

Figure 5-7: Robust stability with 1σ-uncertainty as function of frequency (ssv).

The corresponding confidence levels p_κ of the maximum tolerable uncertainties are computed as outlined in section 2.8.4: Values of p_κ close to 1 indicate, it is likely that robust stability is given; values close to 0 indicate that this is unlikely. If the maximum tolerable uncertainty $r_{p,\kappa}$ is smaller than the bias estimate $\hat{b}$, the confidence level p_κ is zero.

The results for the H_∞-criterion are shown in Figure 5-8. In the frequency range from 0.35 Hz to 2.89 Hz, the median of RS confidence levels from H_∞-criterion is close to 1; the results are generally concentrated around the median. Some outliers with $p > 0.6$ are observed. Few outliers with $p = 0$ occure; these are simulations where the bias estimate is larger than the maximum tolerated uncertainty.

In the frequency range from 0.29 to 0.35 Hz, the variations are larger. While upper 25% of the observed values are close to 1 for all frequencies, the 25% percentile is in the range from 0.6 to 0.8. For the estimates at 0.33, 0.335 and 0.34 Hz, in more than 25% of the simulations the bias too large and the confidence is thus zero.

Figure 5-9 shows the respective results for the ssv-criterion. Over the entire frequency range of interest, the minimum median value is 0.9903. The minimum 25%-percentile is 0.94. Some outliers are observed at low frequencies (0.29 Hz to 0.45 Hz). In only 10 simulations, the bias estimate is too large resulting in zero probability estimates.

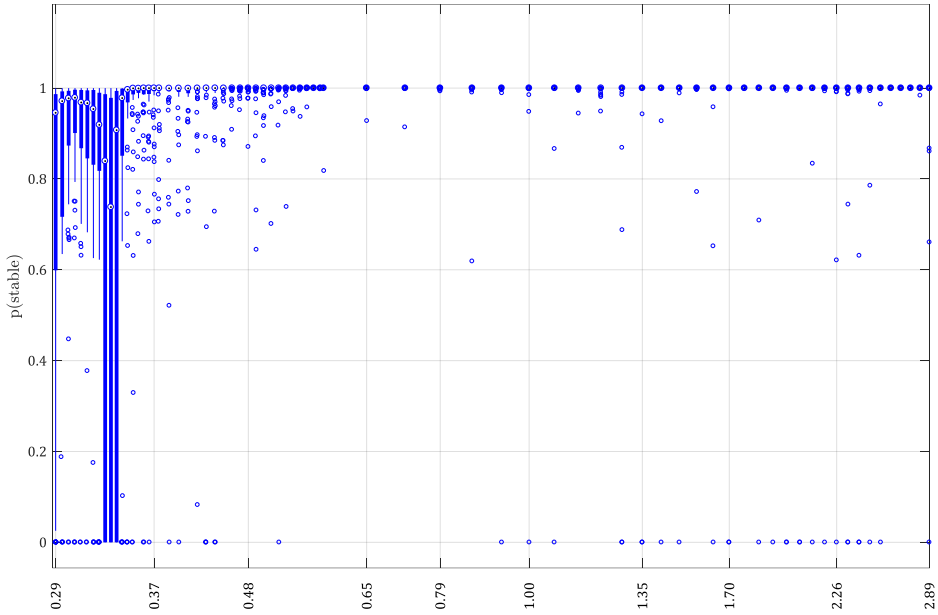

Figure 5-8: Confidence in robust stability from H_∞-criterion.

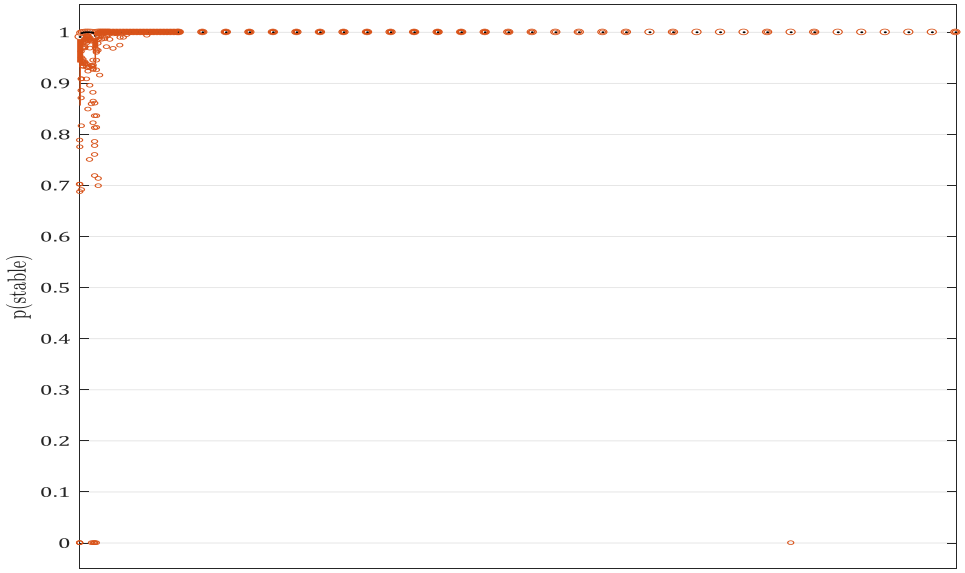

Figure 5-9: Confidence in robust stability from structured singular values.

5.5.2 Stability Over Frequency Range B

The foregoing analysis studies single frequencies only. Under the assumption of independence, the single frequency results can be combined as outlined in section 2.8.5.4, resulting in the confidence level $p(B) = \prod_{k=b_1}^{b_n} p_k(\omega_k)$, that the aircraft dynamics in the frequency range B are robust stable. Figure 5-10 shows a histogram of $p(B)$, computed with structured singular values, where B is the entire FRoI. In this example, for 26% of the simulations the confidence level $p(B)$ is larger than 99% and 60% have a confidence level larger than 90%. In 4 simulations $p(B)$ is zero due to large bias estimates.

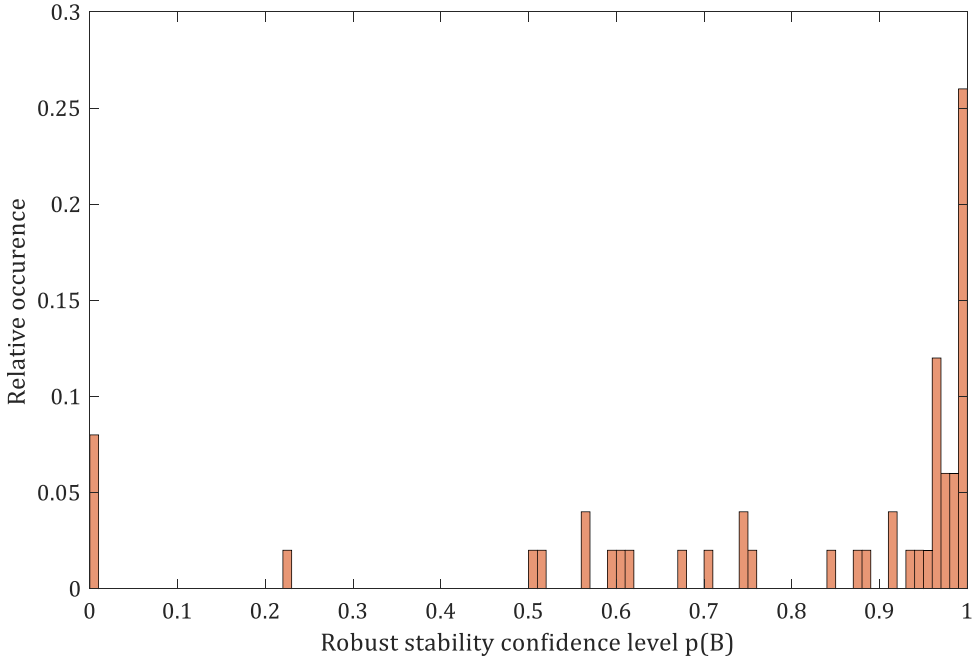

Figure 5-10: Occurrence of robust stability probability level $p(B)$ (from ssv).

It is noted that the approach, to extend the result of single frequencies to a frequency range, implies that the measured data is representative for the entire frequency range. Non-excited frequencies within the frequency range are not considered in this analysis, c.f. section 2.8.4.

5.5.3 Summary

From the results it is seen that both, the H_∞- and the structured singular value criteria can be used to compute confidence levels for robust stability. The results show the conservatism of the H_∞-criterion, as it results in lower confidence levels, compared to the structured singular value criterion; as the H_∞-criterion can be computed more efficiently, it is advantageous in online applications.

Assuming independency, the frequency-by-frequency confidence levels can be extended to a frequency range by computing their joint probability. The resulting confidence level holds for the entire range. It is noted that the individual p_{max} for single frequencies hold, irrespective of the correlation over frequency. The correlation is only relevant if statements are made over a frequency range, i.e. over multiple frequencies.

5.6 Total Confidence

To assess the confidence in stability of the entire system, nominal stability, robust stability and the signal-to-noise ratio of the input must be considered. For any estimate that does not fulfil nominal stability or the signal-to-noise ratio requirement, its confidence is set to zero. As shown in section 5.4 nominal stability is fulfilled for all simulations and all frequencies. The input SNR requirement is not fulfilled for seven estimates and their confidence levels are set to zero. The resulting total confidence levels are shown in Figure 5-11 and Figure 5-12 for the H_∞- and ssv-estimates.

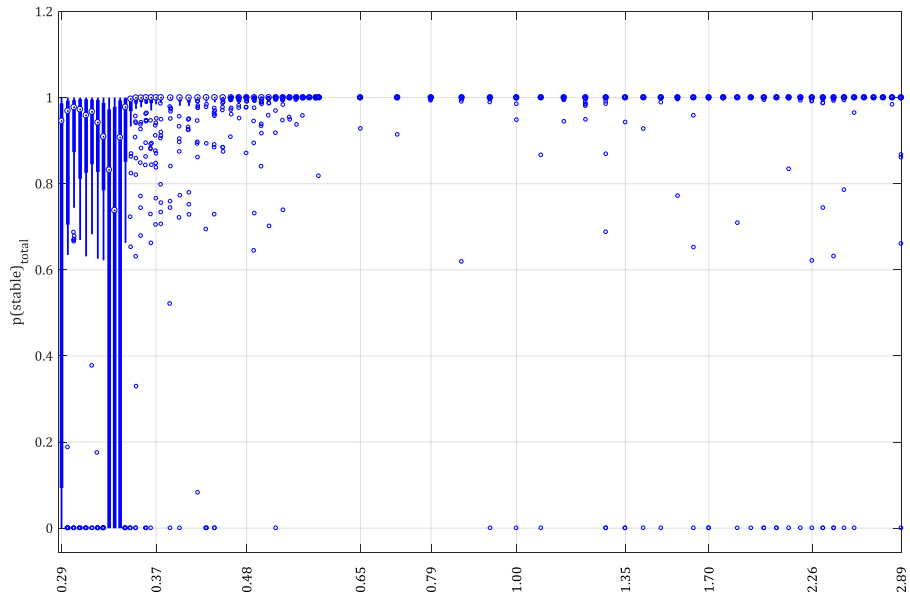

Figure 5-11: Total probability for stability based on H_∞-criterion

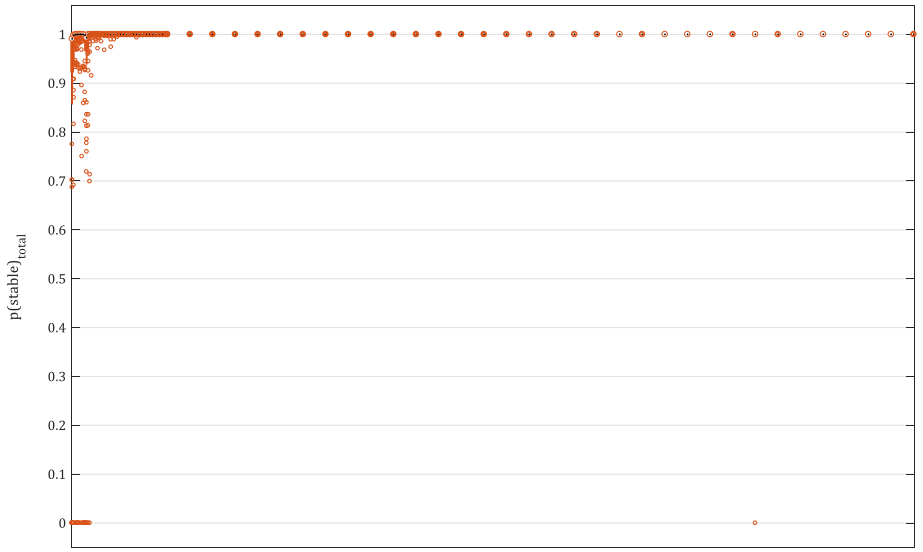

Figure 5-12: Total probability for stability based on ssv-criterion.

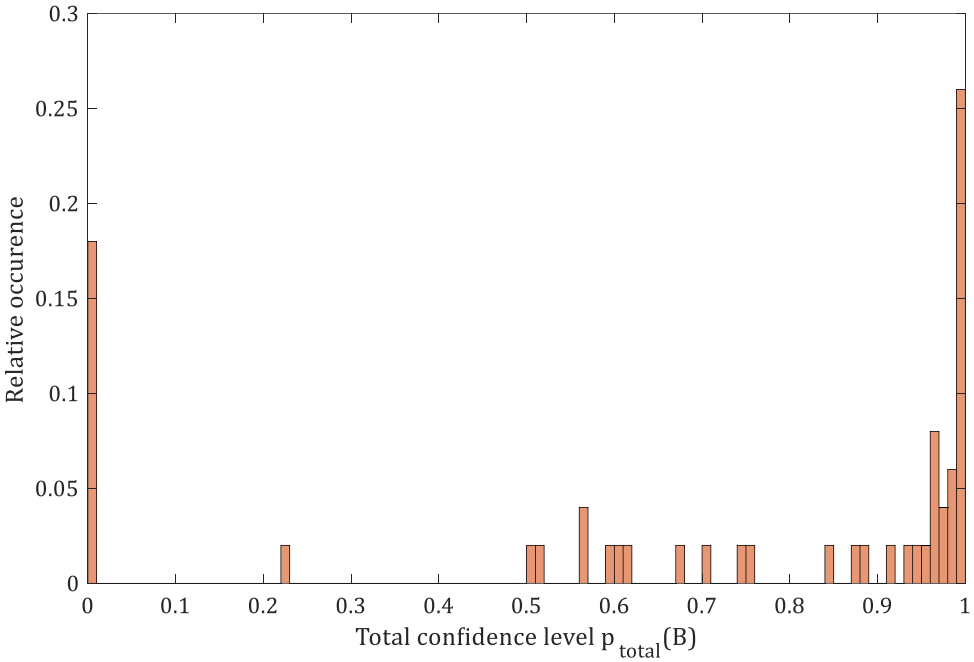

Figure 5-13: Occurrence of total confidence levels based on ssv-criterion.

This result shows that the presented algorithm can be used to assess robust stability of closed loop aircraft dynamics solely based on nonparametric measurements of the input-output dynamics. The algorithm does not require a parametric model and thus no assumptions on model structure or model order. The only assumptions made are linearity and smoothness of the FRM over frequency.

5.7 Integrity Monitoring

The total confidence level introduced in section 2.8.5.3 provides a measure of the probability that the closed loop aircraft dynamics are stable, based on a fixed set of measurements. So far, the focus of this thesis was on time invariant systems. In this final section, the effect of system variations on the estimation is discussed. The major motivation is to combine confident stability measure with a moving data window to monitor the system stability. This is an alternative approach to monitor the system stability of e.g. time varying systems or adaptive control systems. The identification of parameter varying systems is a topic of current research interests (Fujimori & Ljung, 2006; Morari, Thoma, & Tóth, 2010). Also adaptive control approaches, that are closely related to systems with varying dynamics, gained popularity, see e.g. (Christian D. Heise, Leitao, & Holzapfel, 2013).

The proposed confident stability measure takes a slightly different approach: Its intention is to provide a measure of the probability that the aircraft behaves as expected, where “as expected” is here equal to “being stable”. The “as expected” implicitly includes time invariance, as the estimation algorithms have been developed for time invariant systems.

As a consequence, variations in the system dynamics will result in some kind of estimation errors. In this section, the effect of dynamics changes on the total confident stability level are discussed; two cases are considered:

- A slow change of the plant dynamics
- A sudden change of the plant dynamics

For each case, the effect on the frequency response estimate $\hat{G}$ (affecting nominal stability) and the covariance estimate $\hat{C}_{\hat{G}}$(affecting robust stability) are discussed. It is noted, that time varying systems are non-linear. It is shown in (Pintelon & Schoukens, 2012), that the fast LPM provides a *best linear approximation* (BLA) when applied to non-linear systems.

To apply the confident stability measure for integrity monitoring, the estimation runs continuously, based on a fixed length moving data window. When the data window is shifted over time, the confident stability level can be computed as function of time[56]. The principle of a moving window is sketched in Figure 5-14: as the fixed length window moves with time, new data points are added at the right, while old data points are dropped at the left.

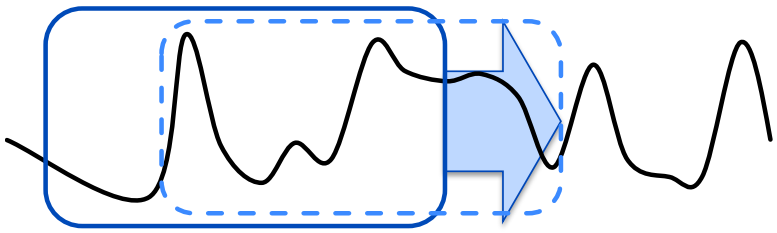

Figure 5-14: Principle of moving data window.

5.7.1 Slow Dynamics Change

With slow changes of the system dynamics, it is meant that the change of system dynamics during the experiment are (very) small and the dynamics art thus close to time invariant. Examples for slow dynamics changes are e.g. the weight loss of aircraft due to fuel burn. The measurements considered in this thesis extend over few minutes; the mass change of a typical aircraft over that period can usually be neglected.

When the system dynamics change is slow compared to the data window length, the system is approximately time invariant. The estimate $\hat{G}$ will then follow the dynamics change in the course of time. As a consequence, the primary effect is on $\hat{G}$ and eventually on nominal stability; the effect on covariance is minor. As a consequence, slow dynamics changes have little impact on p_{max}, as long as the overall stability of the system is not affected.

5.7.2 Sudden Dynamics Change

Here, sudden changes are assumed to take place instantaneous at time t_{change} or at least much faster than the highest observed frequency, so that the observed data can be split in sets measured before and after the change. Examples for sudden changes are structural damages due to explosions or weight changes due to dropping of internal or external loads. Obviously, an estimate solely based on data measured before t_{change} will estimate the unchanged dynamics. Analogously, an estimate solely based on data measured after t_{change} estimates the changed dynamics. In-between, the estimate blends from the original to the changed dynamics, resulting in increased variance estimates that account for the introduced uncertainty of the FRM estimate (similarly shown in (van der Maas, van der Maas, & Oomen, 2015)). For a fixed length data window, the blending takes one full window length. This principle is visualized in Figure 5-15, where the dynamics change at t_{change} is indicated by the dashed black line; the blue data window contains entirely data of the unchanged dynamics, the orange window data of the change dynamics. In between, the green window contains a mixture of both.

[56] The approach is basically the same used for the short time Fourier transform (STFT).

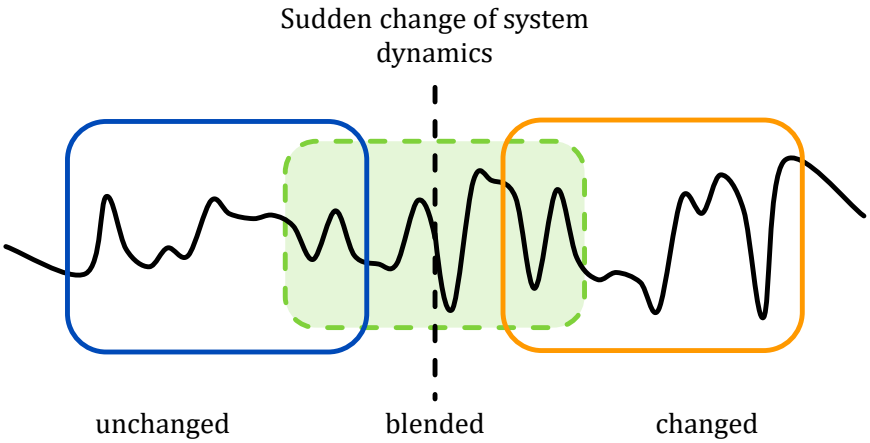

Figure 5-15: Principle of blending in case of a sudden dynamics change.

The blending and its effect on the confident stability level p_{max} are studied based on the FAT simulation model. To simulate the dynamics change, the control surface deflections are increased by a constant factor of 5. This change increases all frequency responses by about 14 dB. The resulting confident stability level p_{max}, including the Bonferroni correction, is shown in Figure 5-16. At $t = 0$ the dynamics change takes effect. During the initial phase the data window (which is 400 seconds wide) is gradually filled with flight data; the respective CSL is dashed to indicate that the data window is partly filled with initial zeros. At the very beginning, from -450 seconds to -430 seconds (dotted values), the data window is mainly filled with zeros. The resulting confidence level is close to one, but does not represent the aircraft dynamics.

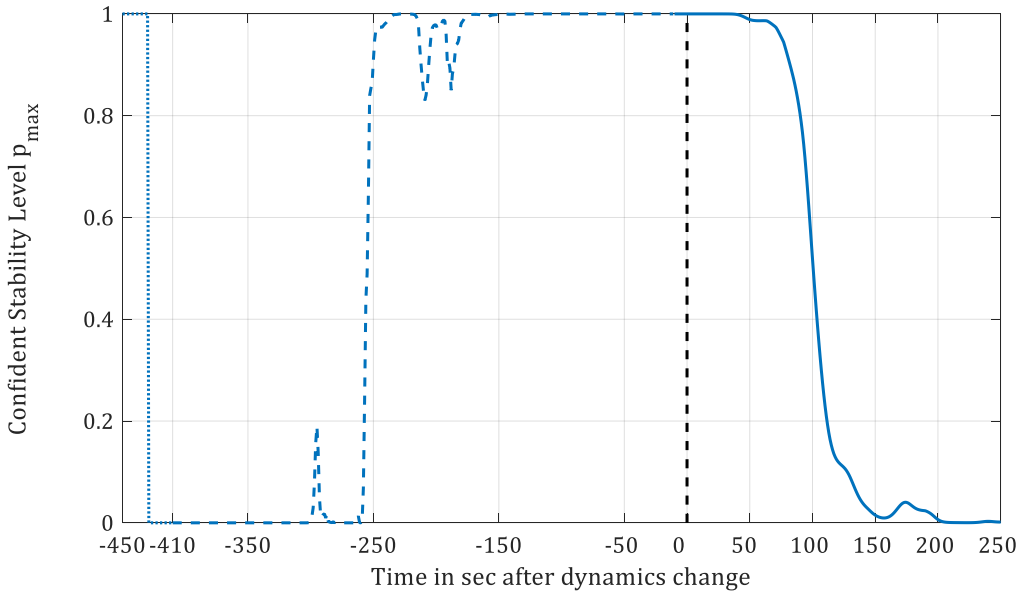

Figure 5-16: Confident stability level after a sudden dynamics change. The confident stability level drops after about 100 sec, i.e. after one half period of the lowest frequency.

After the dynamics change, the data window gradually contains "new" data; the blending results in an increase of the covariance and a drop of the confident stability level. The main drop of p_{max} is observed about 100 seconds after the dynamics change; this equals half a period of the lowest frequency or one fourth of the windowlength. Similar results have been observed for SISO systems (Merkl & Holzapfel, 2018).

5.7.3 Summary of Integrity Monitoring

As discussed above, the CSL is suited for stability monitoring of flight control systems. As a summary it can be stated that sudden changes in system dynamics can be monitored with the described algorithm *at the latest* one window length after the change. Simulation results indicate that the CSL indicates a dynamics change already after one fourth window length.

Slow changes are assumed to occur (much) slower than the lowest frequency of interest, so that the dynamics can be assumed to be time-invariant during the experiment. As these changes occur only gradually, the system dynamics are approximately time-invariant. The LPM algorithm can thus be applied straight forward and the estimate $\hat{G}$ reflects the current dynamics.

5.8 Performance

5.8.1 Computational Performance

The entire code was implemented in Matlab[57]. For online use, the code was adjusted to the reduced command set available in Simulink Coder. This limits the scope for parallelization, as Simulink is basically limited to single threaded execution. With the given implementation, the estimation of the frequency set of chapter 5 containing 73 excited frequencies runs at about 25 Hz, i.e. each estimation of the full frequency response matrix takes about 0.04 seconds. The μ-analysis takes significantly more time: it takes about 1 second for each epoch. The overall algorithm thus runs at about 1 Hz.

The computational performance of the integrity monitoring algorithm obviously depends on the number of analysed frequencies. Thus, a limitation to a smaller frequency range is the most direct way to improve it. From an algorithmic point of view, the monitoring algorithm includes three costly computational steps, namely

- the discrete Fourier transform,
- the solution of the least squares problem for the LPM estimate, and
- the μ-analysis.

In the following, possible improvements on the computational performance are shortly discussed.

Recursive Fast Fourier Transform

The discrete Fourier transform is implemented as a standard FFT with a moving window. In each computation step, the window is shifted by several samples and a new FFT is computed. As only few samples change between consecutive runs, recursive or cyclic FFT algorithms may provide better performance.

Online μ-Analysis

The costliest part of the monitoring algorithm is the computation of the structured singular values. As a general, less complex but also more conservative alternative, the H_∞-norm can be used. In the given algorithm, the computation of structured singular values is a separate task for each single frequency, so that the algorithm can be parallelized to increase computational performance.

[57] The computations were primarily done with Matlab R2016b. Only the simulations were conducted with R2013b for compatibility issues with legacy models.

5.8.2 Estimation Accuracy

The accuracy of the frequency response estimates have been discussed in detail in chapter 2. Here, the focus is on eventual improvements of the overall integrity monitoring algorithm, with focus on three aspects: The interpolation bias, intergrid dynamics and the effect of parameter variations on the variance of FRM estimates.

Intergrid Dynamics

The intergrid dynamics are accounted for with a worst-case assumption. This simple approach is conservative and provides a safe and simple way to account for the unknown dynamics between discrete frequencies. A more detailed (but also computationally more complex) approach is provided in (Vries & Hof, 1992).

Interpolation Error

As analysed in section 2.5.4, the interpolation error strongly depends on frequency resolution. To keep the bias small, a rather fine frequency resolution is required – and thus rather long experiments. Tighter bias estimates would give the experimenter some freedom to relax the frequency resolution requirement.

Violation of Time Invariance Assumption

The estimation of frequency responses as used in this thesis is generally based on the assumption, that the system is approximately linear time invariant (LTI). In section 3.4 it was seen that the true system dynamics however vary due to speed changes during the experiment. It was further seen, that this violation results in additional variance of the frequency response estimates. The exact effect is however not obvious. A more detailed understanding may be provided by linear parameter varying (LPV) models.

5.9 Summary of Confident Robust Stability

As discussed above, the CSL is suited for stability monitoring of flight control systems. It has several important advantages:

- The CSL is solely based on a dynamics model that is identified from flight test data. Thus it is ensured that the dynamics model resembles the true aircraft dynamics.
- The non-parametric approach avoids structural model errors. Unknown dynamic modes, like elastic structural modes, are naturally included in the model and in the stability analysis.
- The estimation provides an accurate model of the estimation uncertainty, that is used directly and without approximations in the robust stability analysis. Thus, no assumptions on the uncertainty model must be made.
- With a moving data window, the CSL can be computed online; this provides fast estimation results, allows to combine multiple tests (e.g. with different flap settings) in a single flight test and allows for online monitoring of system stability.
- With the fast local polynomial method, it can be applied to multiple input systems.

6 CONCLUSION

The focus of this thesis is on the estimation of frequency responses and the combination with robust control methods. Such combined approaches bring two difficulties: First, the estimation of frequency response matrices for multiple input systems required multiple experiments, which makes them unsuited for online applications. Second, the frequency response function gives information only for a discrete frequency grid; reasonable assumptions are necessary to assess the intergrid dynamics. For both aspects, improvements beyond the state of the art have been presented.

FREQUENCY RESPONSE ESTIMATION

In the preceding chapters, the local polynomial method was introduced and utilized to estimate frequency response matrices of the aircraft dynamics of the FAT testbed with full frequency resolution. The estimates are based only on a single experiment and include the first two periods of data. Compared to previous methods, this results in a reduction of the required measurement time or – equivalently – an improved accuracy, if the same experiment time is applied:

- For single input systems, previous methods required to discard the first two periods due to the non-steady state conditions. The local polynomial methods account for them explicitly, so that the first two periods can be included in the estimate. It is further shown, that the first two periods are sufficient for the accurate estimation, so that the reliable estimates can be computed solely from the data, that would be discarded with previous methods.
- For multiple input systems, the fast local polynomial method provides frequency response matrix estimates from one single experiment. As previous methods require one independent experiment for each input, the fast local polynomial method allows for a further reduction of experiment time.

The advantage for multiple input system comes at the cost that the frequency response is approximated with local polynomials, that can result in an additional interpolation error. In the literature, an estimate of the interpolation error is provided for lightly damped systems, that is, however, non-conservative for systems with larger damping. In chapter 2.5.4, an alternative bias estimate is derived, that is conservative also for systems with larger damping.

The LPM is applied to a representative aircraft example. The accuracy of both, single input and multiple input estimates are studied. The estimation results show that the transient term that accounts for non-zero initial and final conditions can efficiently be compensated.

The statistical properties of the estimates have been studied in detail. Confidence levels of the measurement uncertainty are computed based on Gaussian approximations of the probability density function. Their accuracy is validated with Monte Carlo experiments. The accuracy of frequency response estimates is significantly affected by the signal-to-noise ratio of the input signal(s). It is shown that the signal-to-noise ratio of the input signal can be calculated from the LPM estimates. It is further shown that the signal-to-noise ratio of the input signal has a characteristic sensibility to turbulence and sensor noise. The sensitivity function is aircraft specific and can be computed from a parametric aircraft dynamics model. It is shown, that the noise sensitivity can limit the practically achievable signal-to-noise ratio, especially in the frequency range of the lightly damped poles like the phygoid mode.

ROBUST STABILITY OF FREQUENCY RESPONSE ESTIMATE

The rareness of combinations of non-parametric methods like frequency response functions with robust control approaches is mainly due to the limitations of the estimation methods. With the improved estimation methods, this combination becomes more attractive. The transformation of simultaneous confidence regions in a structured uncertainty model that provides the fundament for the robust stability analysis is shown in sections 2.7 and 2.8, thereby linking the non-parametric estimation method to the robust stability framework.

The applied robust stability criteria require a nominal model that is known to be stable a priori; in this thesis, the nominal model is a simplified parametric LTI model with all stable poles. Beyond this, the algorithm is solely based on nonparametric estimates, i.e. on frequency response matrix estimates provided by the LPM estimation algorithm. Thus, no assumptions are required on the system structure or model order; given sufficient frequency resolution, the FRM estimate will follow any observed dynamics accurately. As the frequency responses provide information only for a discrete frequency grid, the intergrid dynamics need to be considered as additional uncertainty. The shown approach, based on worst-case assumptions of the intergrid dynamics, can be easily incorporated in the stability criterion.

The uncertainty model is based on covariance estimates, provided by the LPM algorithm. Starting from 1σ-uncertainty regions and bias estimates, the maximum tolerated uncertainty is computed with the H_∞-criterion and structured singular values. The maximum uncertainty is related to confidence levels of same size to assess the probability of the system to be robust stable. The confidence regions include for the interpolation bias, that is the primary systematic estimation error. The confidence levels are validated with Monte Carlo simulations.

As the objective of this thesis is a stability monitoring algorithm, the focus is on robust *stability*. The aspect of *control design*, based on frequency response estimates is not considered in this thesis, but it offers interesting options, e.g. for the tuning of control gains in case of uncertain dynamics.

INTEGRITY MEASURE

The one-frequency-at-a-time confidence levels are combined in a single measure that covers an entire frequency range: Under the assumption of independence, confidence levels for multiple frequencies have been combined to compute total probabilities of robust stability. The total probability combines the compliance with the requirements (SNRu, nominal stability) with the estimated confidence level. It can be computed online to provide a continuous integrity measure of the robust stability of the flight control system, that is based on estimated dynamics only. The flight control system and the flight dynamics are only assumed to be linear; no further assumptions are required.

The response of the stability monitoring to sudden changes in system dynamics has been illustrated with an example. It is shown that the stability monitoring accounts for system changes. This demonstrates the suitability of the proposed confident stability level as an integrity measure of flight control systems. Its sensitivity is shown exemplarily. An in-depth analysis of the sensitivity to system dynamic changes, based on the linear parameter varying (LPV) framework, may provide further insight in the relation of the confident stability level to system dynamics changes.

DIRECTIONS OF FUTURE WORK

The foregoing summary of the results indicates directions for future work. These can be roughly grouped in two categories:

- Improvements of the monitoring algorithm
- Practical applications and further testing

As already mentioned, the described monitoring algorithm leaves room for improvements. When it comes to estimation accuracy, the interpolation bias and its estimation are a primary source of conservatism. A more accurate estimation of the bias can reduce conservatism and thus improve monitoring accuracy. The Local Rational Method (LRM) (see section 2.5.9) offers further potential to reduce the interpolation bias, provided that its numerical difficulties can be avoided. The Linear Parameter Varying (LPV) framework offers potential to reduce the variance due to aircraft velocity changes.

The calculation speed is dominated by the computation of the H_∞-norm (or the structured singular value respectively). In the implementation used in this thesis, the calculations cannot be run in parallel. Since the H_∞ (or structured singular value) calculation step is performed independently for each frequency, it makes sense to parallelize this part of the algorithm, e.g. with the aid of FPGAs. In the example of chapter 5, the calculation could be accelerated by a factor of about 70 just by parallelization[58] - this would allow an almost real-time evaluation of the confident stability level.

From an application point of view, it must be mentioned that the analysis shown in this thesis is soley based on simulation data. As is the case for any simulation, the results should be validated with real flight data. In addition, further variations of the plant dynamics and the respective response of the confident stability level should be analysed to determine lower limits for the confident stability level that can be tolerated for safe flight operation.

As a summary, it can be said that the confident stability level is a promising measure of the system integrity of aircraft. Due to its non-parametric approach it can be easily applied in flight tests to monitor the stability, even if the true model order of the system is unknown. Its flexibility makes it also especially suited for the flight testing and stability monitoring of unconventional aircraft configurations – either manned or unmanned – including large multicopters and other VTOL-configurations, that are currently developed.

[58] This assumes that the computation time for a single frequency remains unchanged.

7 References

Analog Devices. (2007). *ADIS 16350: Tri-Axis Inertial Sensor*. Norwood. Retrieved from http://www.analog.com/media/en/technical-documentation/data-sheets/ADIS16350_16355.pdf

Anderson, T. W. (2003). *An introduction to multivariate statistical analysis* (3rd ed). *Wiley series in probability and statistics*. Hoboken, N.J.: Wiley-Interscience.

Åström, K.-J., & Bohlin, T. (1965). Numerical Identification of Linear Dynamic Systems from Normal Operating Records. *IFAC Proceedings Volumes*, *2*(2), 96–111. https://doi.org/10.1016/S1474-6670(17)69024-4

Bailey, R. E., & Markofski, A. R. (2001). *Real Experiences in the Frequency Domain* (Pilot-Induced Oscillation Research: Status at the End of the Century No. NASA/CP-2001-210389/VOL3). Retrieved from NASA website: https://ntrs.nasa.gov/archive/nasa/casi.ntrs.nasa.gov/20010037948.pdf

Baker, G. A., & Graves-Morris, P. R. (2010). *Padé approximants* (2. ed., digitaly print. version). *Encyclopedia of mathematics and its applications: Vol. 59*. Cambridge: Cambridge University Press.

Bendat, J. S., & Piersol, A. G. (2010). *Random data: Analysis and measurement procedures* (4. ed). Hoboken (N.J.): Wiley (Original work published 1971).

Billings, S. A. (2013). *Nonlinear System Identification*. Chichester, UK: John Wiley & Sons, Ltd.

Bombois, X., Gevers, M., Scorletti, G., & Anderson, B.D.O. (2001). Robustness analysis tools for an uncertainty set obtained by prediction error identification. *Automatica*, *37*(10), 1629–1636. https://doi.org/10.1016/S0005-1098(01)00104-2

Bombois, X., & Date, P. (2003). Connecting PE identification and robust control theory: The multiple-input single-output case. part I: uncertainty region validation. *IFAC Proceedings Volumes*, *36*(16), 21–26. https://doi.org/10.1016/S1474-6670(17)34732-8

Bonferroni, C. E. (1936). *Teoria statistica delle classi e calcolo delle probabilità*. *Pubblicazioni del R. Istituto superiore di scienze economiche e commerciali di Firenze*: Libreria internazionale Seeber. Retrieved from https://books.google.de/books?id=3CY-HQAACAAJ

Bonferroni, C. E. (1935). Il calcolo delle assicurazioni su gruppi di teste. In *Studi in Onore del Professore Salvatore Ortu Carboni* (pp. 13–60). Rom.

Borglund, D., & Nilsson, U. (2004). Robust Wing Flutter Suppression Considering Aerodynamic Uncertainty. *Journal of Aircraft*, *41*(2), 331–334. https://doi.org/10.2514/1.9328

Bottasso, C. L., Luraghi, F., & Maisano, G. (2009). Time-domain parameter estimation for first-principle rotorcraft models using recursive and batch procedures: Formulation and preliminary results. In Deutsche Gesellschaft für Luft- und Raumfahrt - Lilienthal-Oberth e.V. (DGLR) (Ed.), *35th European rotorcraft 2009: (ERF 2009) Hamburg, Germany 22-25 September 2009* (Vol. 2, pp. 607–619). Red Hook, N.Y.: Curran Associates, Inc. Retrieved from

http://citeseerx.ist.psu.edu/viewdoc/download?doi=10.1.1.659.7650&rep=rep1&type=pdf

Brigham, E. O. (1974). *The Fast Fourier Transform and Its Applications*. *Prentice-Hall signal processing series*. Englewood Cliffs, N.J: Prentice Hall.

Bureau International des Poids et Mesures. (2006). *The international system of units (SI)* (8.th ed.). Sèvres. Retrieved from https://www.bipm.org/utils/common/pdf/si_brochure_8_en.pdf

Christian D. Heise, Leitao, M., & Holzapfel, F. (2013). Performance and Robustness Metrics for Adaptive Flight Control - Available Approaches. In : *Guidance, Navigation, and Control and Co-located Conferences, AIAA Guidance, Navigation, and Control (GNC) Conference.* American Institute of Aeronautics and Astronautics. https://doi.org/10.2514/6.2013-5090

Clarke, R., Burken, J. J., Bosworth, J. T., & Bauer, J. E. (1994). *X-29 Flight Control System: Lessons Learned* (No. NASA TM-4598). Retrieved from NASA website: http://www.nasa.gov/centers/dryden/pdf/88335main_H-1995.pdf

Cooley, J. W., & Tukey, J. W. (1965). An algorithm for the machine calculation of complex Fourier series. *Mathematics of Computation*, *19*(90), 297. https://doi.org/10.1090/S0025-5718-1965-0178586-1

Department of Defense (1997, December 19). *Flying Qualities of Piloted Aircraft*. (MIL-HDBK-1797).

Doyle, J. (1983). Synthesis of robust controllers and filters. In *The 22nd IEEE Conference on Decision and Control* (pp. 109–114). https://doi.org/10.1109/CDC.1983.269806

Doyle, J. (1984). *Advances in Multivariable Control: Lecture Notes*. with contributions by Cheng-Chih Chu, Bruce Francis, Pamod Khargonekar, Gunter Stein. Minneapolis. Retrieved from ONR / Honeywell Workshop website: http://www.dtic.mil/dtic/tr/fulltext/u2/a225164.pdf

Dryden, H. L. (1943). A Review of the Statistical Theory of Turbulence. *Quaterly of Applied Mathematics*. (1), 7–42. Retrieved from http://www.jstor.org/stable/43633324

Dunn, O. J. (1961). Multiple Comparisons among Means. *Journal of the American Statistical Association*, *56*(293), 52–64. https://doi.org/10.1080/01621459.1961.10482090

Etkin, B., & Reid, L. D. (1996). *Dynamics of flight: Stability and control* (3rd ed.). Chichester: Wiley.

Federal Aviation Administration (FAA). (2014). *Aeronautical Information Manual: Official Guide to Basic Flight Information and ATC Procedures.*

Feng, X., Lin, C.-F., Yu, T.-J., & Whorton, M. (1998). Automatic closed-loop identification and robust control synthesis. In *Guidance, Navigation, and Control Conference and Exhibit* (pp. 765–771). Boston. https://doi.org/10.2514/6.1998-4234

Fisher, R. A. (1912). On an Absolute Criterion for Fitting Frequency Curves. *Messenger of Mathmatics*, *41*, 155–160.

Frigo, M., & Johnson, S. G. (2005). The Design and Implementation of FFTW3. *Proceedings of the IEEE*, *93*(2), 216–231.

Fujimori, A., & Ljung, L. (2006). Parameter Estimation of Polytopic Models for a Linear Parameter Varying Aircraft System. *TRANSACTIONS OF THE JAPAN SOCIETY FOR AERONAUTICAL AND SPACE SCIENCES*, *49*(165), 129–136. https://doi.org/10.2322/tjsass.49.129

Gauss, C. F. (1809). *Theoria motus corporum coelestium in sectionibus conicis solem ambientium*: sumtibus Frid. Perthes et I. H. Besser.

Gevers, M. (1996). Identification for control. *Annual Reviews in Control*, *20*, 95–106. https://doi.org/10.1016/S1367-5788(97)00008-4

Gevers, M., Mišković, L., Bonvin, D., & Karimi, A. (2006). Identification of multi-input systems: Variance analysis and input design issues. *Automatica*, *42*(4), 559–572. https://doi.org/10.1016/j.automatica.2005.12.017

Gevers, M., Hägg, P., Hjalmarsson, H., Pintelon, R., & Schoukens, J. (2012). The Transient Impulse Response Modeling Method and the Local Polynomial Method for Nonparametric System Identification. In *16th IFAC Symposium on System Identification* (pp. 55–60). https://doi.org/10.3182/20120711-3-BE-2027.00359

Gevers, M. (2014). System identification in a historical perspective. DISC Summer School on Data-Driven Modelling for Control. Retrieved from https://perso.uclouvain.be/michel.gevers/PublisMig/History-of-Sysid.pdf

Gevers, M., Pintelon, R., & Schoukens, J. (2011). The Local Polynomial Method for nonparametric system identification: Improvements and experimentation. *Proceedings of 50th IEEE Conference on Decision and Control and European Control Conference*, 4302–4307. https://doi.org/10.1109/CDC.2011.6160311

Giri, N. (1965). On the Complex Analogues of T^2- and R^2-Tests. *The Annals of Mathematical Statistics*, *36*(2), 664–670. https://doi.org/10.1214/aoms/1177700173

Girija, G., & Raol, J. (1996). Controller information based identification for unstable/augmented aircraft. In : *Aerospace Sciences Meetings, 34th Aerospace Sciences Meeting and Exhibit* (pp. 1–10). Retrieved from https://arc.aiaa.org/doi/pdf/10.2514/6.1996-900

Goodman, N. R. (1963). Statistical Analysis Based on a Certain Multivariate Complex Gaussian Distribution (An Introduction). *The Annals of Mathematical Statistics*, *34*(1), 152–177. https://doi.org/10.1214/aoms/1177704250

Goos, J. (2016). Modeling and identification of Linear Parmeter-Varying systems (Dissertation). Vrije Universiteit Brussel, Brüssel.

Gosset, W. S. (1908). The probable error of a mean. *Biometrika*, *6*(1), 1–25. https://doi.org/10.1093/biomet/6.1.1

Grauer, J., & Morelli, E. (2013). Method for Real-Time Frequency Response and Uncertainty Estimation. *Journal of Guidance, Control, and Dynamics*, *37*(1), 336–344. https://doi.org/10.2514/1.60795

Greenberg, H. (1951). *A survey of methods for determining stability parameters of an airplane from dynamic flight measurements* (No. NACA-TN-2340). Moffett Field, CA, United States. Retrieved from National Advisory Committee for Aeronautics (NACA) website: https://ntrs.nasa.gov/archive/nasa/casi.ntrs.nasa.gov/19930082979.pdf

Grewal, M. S., Weill, L. R., & Andrews, A. P. (2007). *Global Positioning Systems, Inertial Navigation, and Integration*. Hoboken, NJ, USA: John Wiley & Sons, Inc.

Groves, P. D. (2008). *Principles of GNSS, inertial, and multisensor integrated navigation systems*. *GNSS technology and applications series*. Boston: Artech House.

Hägg, P., & Hjalmarsson, H. (2012). Non-Parametric Frequency Function Estimation Using Transient Impulse Response Modelling. In *16th IFAC Symposium on System Identification* (pp. 43–48). https://doi.org/10.3182/20120711-3-BE-2027.00327

Hägg, P., Hjalmarsson, H., & Wahlberg, B. (2011). A least squares approach to direct frequency response estimation. *Transaction on 50th IEEE Conference on Decision and Control and European Control Conference*, 2160–2165. https://doi.org/10.1109/CDC.2011.6161098

Hägg, P., Wahlberg, B., & Sandberg, H. (2011). On Identification of Parallel Cascade Serial Systems. *IFAC Proceedings Volumes*, *44*(1), 9978–9983. https://doi.org/10.3182/20110828-6-IT-1002.02068

Hamel, P. G., & Kaletka, J. (1997). Advances in rotorcraft system identification. *Progress in Aerospace Sciences*, *33*(3-4), 259–284. https://doi.org/10.1016/S0376-0421(96)00005-X

Härdle, W. K., & Simar, L. (2015). *Applied Multivariate Statistical Analysis* (4.th ed.). Berlin, Heidelberg: Springer Berlin Heidelberg.

Harris, F. J. (1978). On the Use of Windows for Harmonic Analysis with the Discrete Fourier Transform. *Proceedings of the IEEE*, *66*(1), 51–83.

Ho, B. L., & Kalman, R. E. (1966). Effective construction of linear state-variable models form input/output functions. *Regelungstechnik*, *14*(12), 545–548.

Holzel, M., Lacy, S., & Babuska, V. (2009). Direct Optimal Controller Identification for Uncertain Systems using Frequency Response Function Data. In E. Walter (Ed.), *Proceedings of 15th IFAC Symposium on System Identification 2009: Saint-Malo, France, 6-8 July 2009* (Vol. 42, pp. 1056–1061). Red Hook, New York: Curran Associates. https://doi.org/10.3182/20090706-3-FR-2004.00175

Holzel, M. S., & Morelli, E. A. (2012). Real-Time Frequency Response Estimation from Flight Data. *Journal of Guidance, Control, and Dynamics*, *35*(5), 1406–1417. https://doi.org/10.2514/1.56782

Hotelling, H. (1931). The Generalization of Student's Ratio. *The Annals of Mathematical Statistics*, *2*(3), 360–378. https://doi.org/10.1214/aoms/1177732979

ICAO. (2006). *The Convention on International Civil Aviation* (No. 7300/9). Retrieved from https://www.icao.int/publications/Documents/7300_cons.pdf

IEEE (1997). *IEEE standard specification format guide and test procedure for single-axis interferometric fiber optic gyros*. (IEEE Standard, 952). New York, N.Y., USA: Institute of Electrical and Electronics Engineers.

IEEE (2004). *IEEE standard specification format guide and test procedure for coriolis vibratory gyros*. (IEEE Standard, 1431). Piscataway, NJ, USA: IEEE.

IEEE (2006). *IEEE standard specification format guide and test Procedure for Single-Axis Laser Gyros*. (IEEE Standard, 647). New York, N.Y., USA: Institute of Electrical and Electronics Engineers.

IEEE (2014). *IEEE Standard for Sensor Performance Parameter Definitions*. (IEEE Standard, 2700). Piscataway, NJ, USA: Institute of Electrical and Electronics Engineers.

Jammalamadaka, S. R., & SenGupta, A. (2001). *Topics in circular statistics*. *Series on multivariate analysis: Vol. 5*. Singapore, New Jersey, London: World Scientific.

Jategaonkar, R. V., & Plaetschke, E. (1985). Maximum Likelihood Estimation of Parameters in Nonlinear Flight Mechanics Systems. *IFAC Proceedings Volumes*, *18*(5), 663–668. https://doi.org/10.1016/S1474-6670(17)60636-0

Jategaonkar, R. V. (2006). *Flight Vehicle System Identification: A time domain methodology*. Reston, Va.: American Institute of Aeronautics and Astronautics.

Johnson, R. A., & Wichern, D. W. (2007). *Applied multivariate statistical analysis* (6.th ed.). Upper Saddle River, N.J.: Pearson Prentice Hall.

Jupp, P. E., & Mardia, K. V. (1989). A Unified View of the Theory of Directional Statistics, 1975-1988. *International Statistical Review / Revue Internationale de Statistique*, *57*(3), 261. https://doi.org/10.2307/1403799

Kiencke, U., & Jäkel, H. (2008). *Signale und Systeme* (4., korrigierte Aufl.). München: Oldenbourg.

Klein, V., & Morelli, E. A. (2006). *Aircraft System Identification: Theory and Practice*. *AIAA Education Series*. Reston, Va: American Institute of Aeronautics and Astronautics.

Levine, W. S. (1999). *The Control Handbook: (in two Volumes)*. Mumbai: Jaico Publishing House.

Lind, R., & Brenner, M. (1999). *Robust Aeroservoelastic Stability Analysis*. London: Springer London.

Ljung, L. (1976). On The Consistency of Prediction Error Identification Methods. *Mathematics in Science and Engineering*, *126*, 121–164. https://doi.org/10.1016/S0076-5392(08)60871-1

Ljung, L. (1996). Development of System Identification. *IFAC Proceedings Volumes*, *29*(1), 3026–3031. https://doi.org/10.1016/S1474-6670(17)58138-0

Ljung, L. (2009). *System identification: Theory for the user* (2nd ed.). Upper Saddle River, NJ: Prentice-Hall.

Maine, R. E., & Iliff, K. W. (1981). *The Theory and Practice of Estimating the Accuracy of Dynamic Flight-Determined Coefficients* (No. NASA-RP-1077). Retrieved from https://ntrs.nasa.gov/archive/nasa/casi.ntrs.nasa.gov/19810019327.pdf

Maine, R. E., & Iliff, K. W. (1985). *Identification of Dynamic Systems, Theory and Formulation* (No. NASA-RP-1138). Edwards, CA. Retrieved from NASA Dryden Flight Research Center website: https://www.nasa.gov/centers/dryden/pdf/88007main_H-1255.pdf

Martin, G. M. (2005). *Chirp Z-Transform Spectral Zoom Optimization with MATLAB* (No. SAND 2005-7084). Albuquerque. Retrieved from Sandia National Laboratories website: http://prod.sandia.gov/techlib/access-control.cgi/2005/057084.pdf

McKelvey, T., & Gúerin, G. (2012). Non-Parametric Frequency Response Estimation Using a Local Rational Model. In *16th IFAC Symposium on System Identification.* https://doi.org/10.3182/20120711-3-BE-2027.00299

McRuer, D. T. (1974). *Mathematical Models of Human Pilot Behavior* (No. AGARD-AG-1 88). Paris. Retrieved from Advisory Group for Aerospace Research and Development website: http://www.dtic.mil/dtic/tr/fulltext/u2/775905.pdf

Merkl, C., & Holzapfel, F. (2018). Application of nonparametric methods for integrity monitoring of flight control systems. In tbd (Ed.), *Proceedings of the 18th IFAC Symposium on System Identification SYSID 2018* (tbd, tbd). Retrieved from tbd

Mettler, B. (2003). *Identification Modeling and Characteristics of Miniature Rotorcraft*. Boston, MA: Springer US.

Milliken, W. F., Jr. (1947). Progress in Dynamic Stability and Control Research. *Journal of the Aeronautical Sciences*, *14*(9), 493–519. https://doi.org/10.2514/8.1434

Monteyne, G., Ugryumova, D., & Vandersteen, G. (2012). Extension of Local Polynomial Method for Periodic Excitations. In *16th IFAC Symposium on System Identification* (pp. 61–65). https://doi.org/10.3182/20120711-3-BE-2027.00015

Morari, M., Thoma, M., & Tóth, R. (2010). *Modeling and Identification of Linear Parameter-Varying Systems* (Vol. 403). Berlin, Heidelberg: Springer Berlin Heidelberg.

Morelli, E. (2003). *Multiple Input Design for Real-Time Parameter Estimation in the Frequency Domain* (Proceedings on 13th IFAC Conference on System Identification No. Paper REG-360). Retrieved from NASA Langley Research Center website: http://hdl.handle.net/2060/20030066907

Morelli, E. A. (1998). In-flight system identification. In : *Guidance, Navigation, and Control and Co-located Conferences, 23rd Atmospheric Flight Mechanics Conference.* American Institute of Aeronautics and Astronautics. https://doi.org/10.2514/6.1998-4261

Morelli, E. A. (2000). Real-Time Parameter Estimation in the Frequency Domain. *Journal of Guidance, Control, and Dynamics*, *23*(5), 812–818. https://doi.org/10.2514/2.4642

National Institute of Standards and Technology (NIST). (2018). e-Handbook of Statistical Methods: Engineering Statistics Handbook. Retrieved from http://www.itl.nist.gov/div898/handbook/

North Atlantic Treaty Organization. (1991). *Rotocraft system identification*. *North Atlantic Treaty Organization. AGARD. Lecture series: Vol. 178*. England: AGARD.

Northrop Grumman LITEF. (2013). *µIMU-I: Micro Inertial Measurement Unit*. Technical Data. Freiburg. Retrieved from http://www.northropgrumman.litef.com/fileadmin/downloads/Datenblaetter/Datenblatt_uIMU-I.pdf

Nyquist, H. (1932). Regeneration Theory. *Bell System Technical Journal*, *11*(1), 126–147. https://doi.org/10.1002/j.1538-7305.1932.tb02344.x

Oppenheim, Willsky, & Young. (1997). *Signals and Systems* (2. ed., internat. ed.). Upper Saddle River, NJ: Prentice-Hall.

Packard, A., & Doyle, J. (1993). The complex structured singular value. *Automatica*, *29*(1), 71–109. https://doi.org/10.1016/0005-1098(93)90175-S

Papoulis, A. (1962). *The Fourier integral and its applications*. New York: McGraw-Hill.

Papoulis, A., & Pillai, S. U. (2002). *Probability, random variables, and stochastic processes* (4th ed). Boston: McGraw-Hill.

Picinbono, B. (1993). *Random signals and systems*. *Prentice Hall signal processing series*. Englewood Cliffs, N.J.: Prentice Hall.

Pintelon, R., & Schoukens, J. (1997). Frequency-domain identification of linear time-invariant systems under nonstandard conditions. *IEEE Transactions on Instrumentation and Measurement*, *46*(1), 65–71. https://doi.org/10.1109/19.552159

Pintelon, R., & Schoukens, J. (2001). Measurement of frequency response functions using periodic excitations, corrupted by correlated input/output errors. *IEEE Transactions on Instrumentation and Measurement*, *50*(6), 1753–1760. https://doi.org/10.1109/19.982976

Pintelon, R., Schoukens, J., & Vandersteen, G. (1997). Frequency domain system identification using arbitrary signals. *IEEE Transactions on Automatic Control*, *42*(12), 1717–1720. https://doi.org/10.1109/9.650025

Pintelon, R., Schoukens, J., Vandersteen, G., & Barbé, K. (2010a). Estimation of nonparametric noise and FRF models for multivariable systems—Part I: Theory. *Mechanical Systems and Signal Processing*, *24*(3), 573–595. https://doi.org/10.1016/j.ymssp.2009.08.009

Pintelon, R., Schoukens, J., Vandersteen, G., & Barbé, K. (2010b). Estimation of nonparametric noise and FRF models for multivariable systems—Part II: Extensions, applications. *Mechanical Systems and Signal Processing*, *24*(3), 596–616. https://doi.org/10.1016/j.ymssp.2009.08.010

Pintelon, R., Guillaume, P., Rolain, Y., Schoukens, J., & van Hamme, H. (1994). Parametric identification of Transfer Functions in the Frequency Domain - A Survey. *IEEE Transactions on Automatic Control*, *39*(11), 2245–2260.

Pintelon, R., Rolain, Y., & van Moer, W. (2003). Probability density function for frequency response function measurements using periodic signals. *IEEE Transactions on Instrumentation and Measurement*, *52*(1), 61–68. https://doi.org/10.1109/TIM.2003.809097

Pintelon, R., & Schoukens, J. (2012). *System identification: A frequency domain approach* (2nd ed). Hoboken, N.J: John Wiley & Sons, Inc.

Postlethwaite, I., Edmunds, J. M., & MacFarlane, A. G. J. (1981). Principal gains and principal phases in the analysis of linear multivariable feedback systems. *IEEE Transactions on Automatic Control*, *26*(1), 32–46. https://doi.org/10.1109/TAC.1981.1102556

Qin, S. J. (2006). An overview of subspace identification. *Computers & Chemical Engineering*, *30*(10-12), 1502–1513. https://doi.org/10.1016/j.compchemeng.2006.05.045

Rabiner, L. R., Schafer, R. W., & Rader, C. M. (1969). The Chirp z-Transform Algorithm. *IEEE Transaction on Audio and Electroacoustics*, *17*(2), 86–92.

Råde, L., Westergren, B., & Vachenauer, P. (2000). *Springers mathematische Formeln: Taschenbuch für Ingenieure, Naturwissenschaftler, Informatiker, Wirtschaftswissenschaftler* (3., durchgesehene Auflage). *Studentlitteratur*. Berlin, Heidelberg, New York, Barcelona, Hongkong, London, Mailand, Paris, Singapur, Tokio: Springer.

Ragazzini, J. R., & Zadeh, L. A. (1952). The analysis of sampled-data systems. *Electrical Engineering*, *71*(12), 1102. https://doi.org/10.1109/EE.1952.6437836

Ross, S. M. (2000). *Introduction to probability and statistics for engineers and scientists* (2nd ed). San Diego, CA: Academic Press.

SAE International (2007-07). *Aerospace - Flight Control Systems - Design, Installation and Test of Piloted Military Aircraft, General Specification For*. (Aerospace Standard, AS94900).

Safonov, M. G. (1982). Stability margins of diagonally perturbed multivariable feedback systems. *IEE Proceedings, Part D*, *129*(6), 251–256. https://doi.org/10.1049/ip-d:19820054

Scheid, R. E., Bayard, D. S., Chaing, R. Y., & Mettler, E. (1995). Structured uncertainty identification and control synthesis. In *Guidance, Navigation, and Control Conference* (pp. 1629–1638). https://doi.org/10.2514/6.1995-3353

Schmidt, G. T. (2009). INS/GPS Technology Trends. *Low-Cost Navigation Sensors and Integration Technology*. Retrieved from https://www.sto.nato.int/publications/STO%20Educational%20Notes/RTO-EN-SET-116-2008/EN-SET-116(2008)-01.pdf

Schoukens, J., Vandersteen, G., Pintelon, R., Emedji, Z., & Rolain, Y. (2012). Study of the maximal interpolation errors of the local polynomial method for frequency response function measurements. In *International Instrumentation and Measurement Technology Conference Proceedings // IEEE International Instrumentation and Measurement Technology Conference (I2MTC), 2012: 13 - 16 May 2012, Congress Graz, Graz, Austria ; proceedings* (pp. 1395–1399). Piscataway, NJ, Piscataway, NJ: IEEE. https://doi.org/10.1109/I2MTC.2012.6229145

Schuck, F. (2013). Ein integriertes Auslegungskonzept zur Sicherstellung exzellenter Handling Qualities für Kleinflugzeuge (Dissertation). Technische Universität München, München. Retrieved from http://nbn-resolving.de/urn/resolver.pl?urn:nbn:de:bvb:91-diss-20141009-1175979-0-9

Shannon, C. E. (1949). Communication in the Presence of Noise. *Proceedings of the IRE*, *37*(1), 10–21. https://doi.org/10.1109/JRPROC.1949.232969

Sinha, N. K. (1972). Estimation of transfer function of continuous system from sampled data. *Proceedings of the Institution of Electrical Engineers*, *119*(5), 612. https://doi.org/10.1049/piee.1972.0130

Skogestad, S., & Postlethwaite, I. (2005). *Multivariable feedback control: Analysis and design* (2nd ed). Hoboken, NJ: John Wiley.

Smith, R. S., & Doyle, J. C. (1992). Model validation: a connection between robust control and identification. *IEEE Transactions on Automatic Control*, *37*(7), 942–952. https://doi.org/10.1109/9.148346

Stengel, R. F. (2004). *Flight dynamics*. Princeton, NJ: Princeton University Press.

Stevens, B. L., & Lewis, F. L. (2003). *Aircraft control and simulation* (2nd ed.). Hoboken, N.J.: Wiley.

Stoica, P., & Moses, R. (2005). *Spectral analysis of signals*. Upper Saddle River, NJ: Pearson Education.

Takaya, K., Ma, T.-n., Shimizu, K., Kitama, M., & Mikami, T. (1990). Application of Image Reconstruction by Means of Chirp z-Transform. *Proceedings of the IAPR Workshop on Machine Vision Applications*, 77–80. Retrieved from http://www.mva-org.jp/Proceedings/CommemorativeDVD/1990/papers/1990077.pdf

The Mathworks. (2009). Matlab - Help: frestimate. Retrieved from https://de.mathworks.com/help/slcontrol/ug/frestimate.html

The Mathworks. (2017a). Matlab Help: Fast Fourier Transform. Retrieved from https://de.mathworks.com/help/matlab/ref/fft.html

The Mathworks. (2017b). Matlab Help: Simulink - Quantizer. Retrieved from https://de.mathworks.com/help/simulink/slref/quantizer.html?searchHighlight=quantizer&s_tid=doc_srchtitle

The Mathworks. (2017c). Matlab Help: Simulink Control Design - Exact Linearization Algorithm. Retrieved from https://de.mathworks.com/help/slcontrol/ug/exact-linearization-algorithm.html

The Mathworks. (2018). Band-Limited White Noise: Introduce white noise into continuous system. Retrieved from https://de.mathworks.com/help/simulink/slref/bandlimitedwhitenoise.html

Tischler, M. B. (1987). *Frequency-response identification of XV-15 tilt-rotor aircraft dynamics* (No. NASA-TM-89428). Retrieved from NASA website: http://hdl.handle.net/2060/19870013257

Tischler, M. B., & Remple, R. K. (2006). *Aircraft and Rotorcraft System Identification*. Engineering Methods with Flight Test Examples (1st ed.). *AIAA Education Series*. Reston, VA: American Institute of Aeronautics and Astronautics.

Van den Hof, P. M.J., & Schrama, R. J.P. (1993). An indirect method for transfer function estimation from closed loop data. *Automatica*, *29*(6), 1523–1527. https://doi.org/10.1016/0005-1098(93)90015-L

Van der Maas, R., van der Maas, A., & Oomen, T. (2015). Accurate frequency response function identification of LPV systems: A 2D local parametric modeling approach. In *2015 54th IEEE Conference on Decision and Control (CDC): Date: 15-18 Dec. 2015* (pp. 1465–1470). [Piscataway, NJ], [Piscataway, NJ]: IEEE. https://doi.org/10.1109/CDC.2015.7402417

VectorNav Technologies. Inertial Sensor Market. Retrieved from http://www.vectornav.com/support/library/inertial-sensor-market

Vries, D. K. de, & Hof, P. M. J. Van den (1992). Quantification of model uncertainty from data: input design, interpolation, and connection with robust control design specifications. In : *Vol. 1992. Proceedings of the American control conference, Proceedings of the 1992 American Control Conference, the Westin Hotel, Chicago, Illinois, June 24-26, 1992: Papers and programme.* IEEE.

Wahlberg, B., Hjalmarsson, H., & Martensson, J. (2008). Variance analysis for identification of cascade systems. In I. Staff (Ed.), *2008 47th IEEE Conference on Decision and Control* (pp. 131–136). [Place of publication not identified]: IEEE. https://doi.org/10.1109/CDC.2008.4738617

Wahlberg, B., Hjalmarsson, H., & Mårtensson, J. (2008). On Identification of Cascade Systems. *IFAC Proceedings Volumes*, *41*(2), 5036–5040. https://doi.org/10.3182/20080706-5-KR-1001.00846

Welch, P. D. (1967). The Use of Fast Fourier Transform for the Estimation of Power Spectra: A Method Based on Time Averaging Over Short, Modified Periodograms. *IEEE Transaction on Audio and Electroacoustics*, *15*(2), 70–74.

Wise, K. (2003). X-45 Program Overview and Flight Test Status. In *Proceedings of 2nd AIAA "Unmanned Unlimited" Conference and Workshop & Exhibit.* https://doi.org/10.2514/6.2003-6645

Wishart, J. (1928). The Generalised Product Moment Distribution in Samples from a Normal Multivariate Population. *Biometrika*, *20A*(1-2), 32–52. https://doi.org/10.1093/biomet/20A.1-2.32

Wood, J. R., & Hodgkinson, J. (1980). *Definition of Acceptable Levels of Mismatch of Equivalent Systems of Augmented CTOL Aircraft* (No. AD-A145 619). Retrieved from McDonnel Aircraft Company website: http://www.dtic.mil/get-tr-doc/pdf?AD=ADA145619

Young, P. M., & Doyle, J. C. (1990). Computation of μ with real and complex uncertainties. In *Proceedings of the 29th IEEE Conference on Decision and Control* (pp. 1230–1235). Retrieved from http://www.cds.caltech.edu/~doyle/wiki/images/5/5f/CDC1990u.pdf

Young, P. M., Newlin, M. P., & Doyle, J. C. (1992). Practical computation of the mixed μ problem. In : *Vol. 1992. Proceedings of the American control conference, Proceedings of the 1992 American Control Conference, the Westin Hotel, Chicago, Illinois, June 24-26, 1992: Papers and programme* (pp. 2190–2194). IEEE. Retrieved from http://ieeexplore.ieee.org/stamp/stamp.jsp?tp=&arnumber=4792521

Zadeh, L. (1962). From Circuit Theory to System Theory. *Proceedings of the IRE*, *50*(5), 856–865. https://doi.org/10.1109/JRPROC.1962.288302

Zhou, K., Doyle, J. C., & Glover, K. (1996). *Robust and Optimal Control* (2nd ed.). Upper Saddle River, NJ: Prentice Hall.

Zipfel, P. H. (2007). *Modeling and Simulation of Aerospace Vehicle Dynamics* (2nd). Reston, Va.: American Institute of Aeronautics and Astronautics.

A FAT SIMULATION MODEL

A.1 FAT AIRCRAFT DYNAMICS

The simulation model of the FAT aircraft is a nonlinear, parametric model. Linearizing in the analysed trim point (see section 3.2.4) results in the eigenfrequencies and relative damping coefficients shown in Table A-1 (longitudinal modes) and Table A-2 (lateral modes).

The transfer dynamics from the three control inputs for roll (pitch-/yaw-command) to the resulting rotational rates are shown as bode diagram in Figure A-1. Note that the phase angles are wrapped to the range from -360° to 0° for a more compact view.

Table A-1: Frequencies and time constants of FAT for longitudinal motion.

Pole/Zero	Frequency	Time constant	Damping
Phygoid ω_{PH}	0.083 Hz	12.2 sec	0.077
$T_{\Theta 1}$	0.078 Hz	12.9 sec	-
Short period ω_{SP}	0.48 Hz	2.0 sec	0.67
$T_{\Theta 2}$	0.486 Hz	2.1 sec	-

Table A-2: Frequencies and time constants of FAT for lateral motion.

Pole/Zero	Frequency	Time constant	Relative Damping
Spiral mode T_S	<0.001 Hz	$>$ 1000 sec	1
Roll constant T_R	2.25 Hz	0.44 sec	1
Dutch roll ω_{DR}	0.33 Hz	3.0 sec	0.18
$\eta_{\psi\xi_c}$	0.32 Hz	3.0 sec	-
$\eta_{r_K\zeta_c}$	0.05 Hz	20 sec	0.199[59]

[59] Damping is used here analogously to conjugate complex pole pairs, although the term *damping* is not generally applied to conjugate complex zeros.

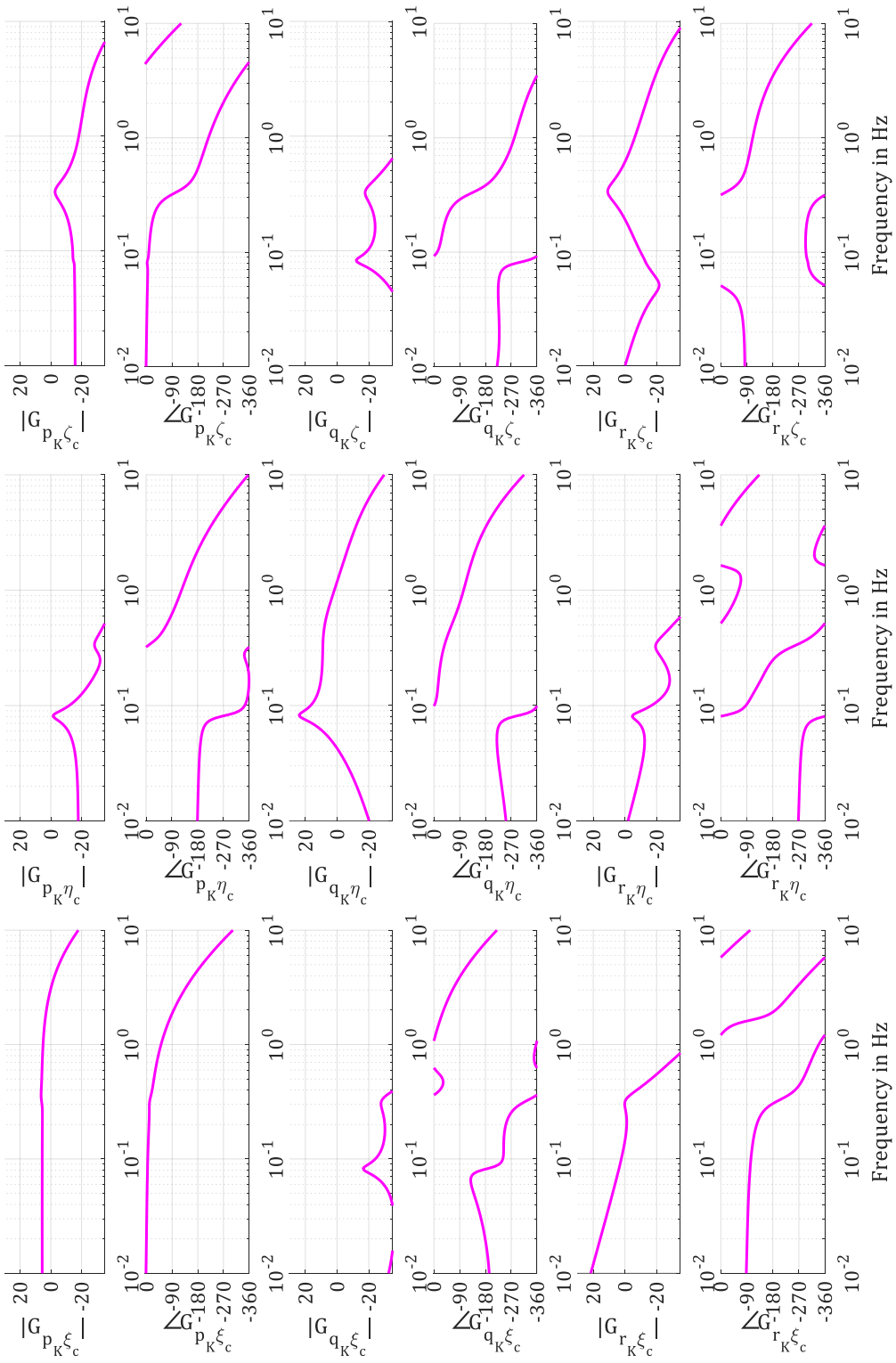

Figure A-1: Analytically linearized FRM G_0.

A.2 Actuator Dynamics

The FAT actuators are modelled as PT2-systems with parameters given in Table A-3. The maximum deflection of the control surfaces is limited, as well as the maximum angular rates and the maximum angular acceleration. Table A-4 lists the respective maximum values for each control surface. Note that the maximum angular accelerations are physically not feasible and are included only for completeness. The maximum accelerations would allow accelerating from maximum speed in positive direction to maximum speed in negative direction within less than $1e^{-5}$ sec.

Table A-3: PT2-Parameters of FAT actuator dynamics.

PT2-Parameter	Value
Gain	1
Eigenfrequency	40 rad/sec
Damping	0.9

Table A-4: FAT control surface performance limits.

Control Surface	Limit	Approximate Limit in deg
Aileron attitude	± 0.6981 rad	approx. ± 40 deg
Ruddervator attitude	± 0.6981 rad	approx. ± 40 deg
Aileron angular rates	± 1.0472 rad/sec	approx. ± 60 deg/sec
Ruddervator angular rates	± 1.047 rad/sec	approx. ± 60 deg/sec
Aileron angular acceleration	± 25000 rad/sec^2	more than $\pm 1.4e^6$ deg/sec^2
Ruddervator angular acceleration	± 25000 rad/sec^2	more than $\pm 1.4e^6$ deg/sec^2

A.3 Nominal Aircraft Dynamics

Based on the poles and zeros of the linearized system dynamics shown in appendix A.1 a nominal model is constructed. The poles of the nominal model are adjusted to be stable, i.e. they are moved inside the unit circle. To account for numeric uncertainty, any pole with a distance further away from the origin than $1 - 10^{-8}$ is moved on the circle around the origin with this radius. The resulting poles are shown in Table A-5. Poles with corresponding time constants larger than 10000 sec are not shown.

Table A-5: Poles of nominal FAT dynamics.

Pole[60]	Magnitude	Damping	Frequency	Time constant
0.99991516	0.99991516	1.000000	0.00 Hz	235.728 sec
0.99915172 +0.01023491j	0.99920414	0.077493	0.08 Hz	25.120 sec
0.99915172 -0.01023491j	0.99920414	0.077493	0.08 Hz	25.120 sec
0.99158273 +0.04031928j	0.99240212	0.184453	0.33 Hz	2.622 sec

[60] The position of poles is truncated after the eighth digit.

Pole[60]	Magnitude	Damping	Frequency	Time constant
0.99158273 -0.04031928j	0.99240212	0.184453	0.33 Hz	2.622 sec
0.95745316	0.95745316	1.000000	0.35 Hz	0.460 sec
0.95937241 +0.04359207j	0.96036227	0.665126	0.48 Hz	0.495 sec
0.95937241 -0.04359207j	0.96036227	0.665126	0.48 Hz	0.495 sec
0.75293386	0.75293386	1.000000	2.26 Hz	0.070 sec
0.45745640 +0.16631718j	0.48675226	0.900000	6.37 Hz	0.028 sec
0.45745640 -0.16631718j	0.48675226	0.900000	6.37 Hz	0.028 sec
0.45745640 +0.16631718j	0.48675226	0.900000	6.37 Hz	0.028 sec
0.45745640 -0.16631718j	0.48675226	0.900000	6.37 Hz	0.028 sec
0.32389493	0.32389493	1.000000	8.97 Hz	0.018 sec

A.4 Turbulence Model

To study the effect of turbulence on the estimation results, different turbulence levels are added to the clean configuration. Turbulences are simulated with the widely used Dryden turbulence model (Dryden, 1943) that is included in (Department of Defense, 1997). The Dryden model defines turbulence as function of altitude. For the simulation at hand the turbulence model for altitudes larger than 2000 feet is relevant. It assumes isotropic turbulences, i.e. the turbulence has the same scale lengths and intensities in all directions of space.

The Dryden model describes turbulence as filtered white noise. The standard deviation is defined as a function of altitude and the desired intensity level[61] (light, moderate, severe). At 2000 ft the respective standard deviation for all wind components are defined as

- light: $\sigma_{turb} = 5.1$ ft/sec
- moderate: $\sigma_{turb} = 9.9$ ft/sec
- severe: $\sigma_{turb} = 14.5$ ft/sec

(source: Department of Defense, 1997, p. 673). In chapters 3 and 4, the simulations contain light turbulence. For the robust stability analysis in chapter 5, a fourth intensity level with very light turbulence ($\sigma_{turb} = 1.7$ ft/sec) is introduced. The respective standard deviations in imperial and approximate metrical units are listed in Table A-6.

Table A-6: Turbulence levels and standard deviation at 2000ft.

Turbulence level	$\boldsymbol{\sigma_{turb}}$ at 2000ft (imperial units)	$\boldsymbol{\sigma_{turb}}$ at 2000 ft (metrical units, approximated)
very light	1.7 ft/sec	0.5 m/sec
Light	5.1 ft/sec	1.5 m/sec
Moderate	9.9 ft/sec	3.0 m/sec
Severe	14.5 ft/sec	4.4 m/sec

[61] The turbulence intensity levels correspond to typical behaviour of the aircraft; further details can be found e.g. in Federal Aviation Administration [FAA] (2014), table 7-1-10

A.5 Sensor Model

A.5.1 IMU Sensor Grades

The studied FCS configuration is a rate controller. Thus only rigid body rotational rates are fed back to the controller. Rotational rates can be directly measured by inertial measurement units (IMUs). Hence the only sensors considered in this thesis are IMUs.

Different IMU types cover a wide performance range. For better overview, IMUs are categorized in grades. Each grade corresponds to a rough performance range that is typically required for the respective application. Common grades are

- strategic grade,
- navigation grade,
- tactical grade,
- industrial grade,
- consumer grade.

Strategic grade is most demanding, containing the most accurate sensors (e.g. used for navigation of submarines). Consumer grade IMUs are least demanding and are used e.g. in electronic devices like smartphones. Figure A-2shows a rough mapping of IMU grades to gyro bias instability (Schmidt, 2009; VectorNav Technologies). Note that IMU grades are not formally defined and different authors use varying performance ranges (Grewal, Weill, & Andrews, 2007, p. 320; Groves, 2008, p. 98).

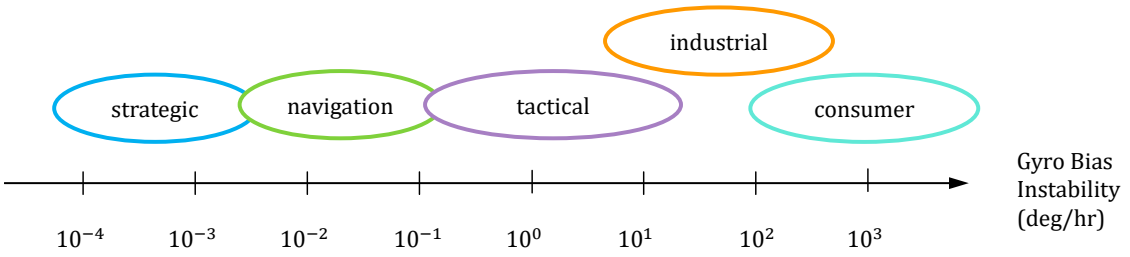

Figure A-2: Gyro Bias Instability of different IMU grades.

In this section, the effect of IMU performance on the FRM estimation is studied. The analysis is based on tactical and industrial grade IMU models based on specifications of two typical sensors. The section begins with the description of the sensor models, followed by the presentation of the simulation results and a final discussion.

A.5.2 Generic Tactical Grade IMU

The IMU model is based on the µIMU, manufactured by Northrop Grumman LITEF (Northrop Grumman LITEF, 2013). The µIMU is a typical tactical grade sensor, cmp. Table A-7 and Figure A-2.

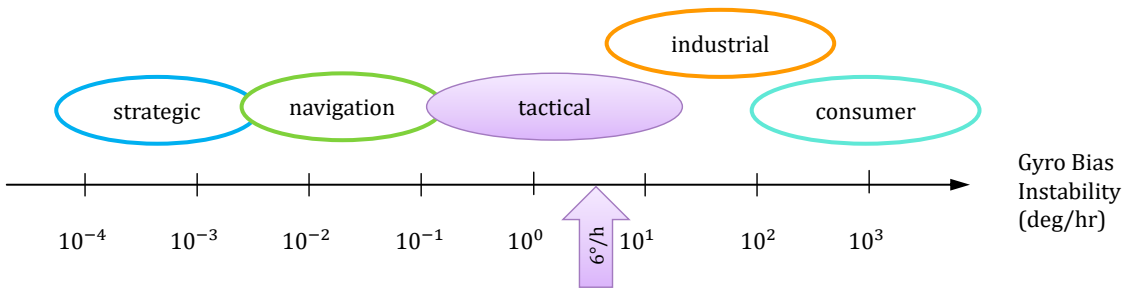

Figure A-3: IMU grade of sensor model.

Gyroscope sensor models have a common model structure that is described in (IEEE, 1997). It consists of a deterministic model part (including e.g. scale factor errors, bias, misalignment), an error model (containing environmental effects and perturbation) and a stochastic part. It is seen that the same general model structure can be used to model different gyroscope designs like fibre optical gyros (IEEE, 1997), ring laser gyros (IEEE, 2006), Coriolis vibratory gyros (IEEE, 2004) and micro electromechanical systems (MEMS) (IEEE, 2014).

The µIMU contain MEMS rate sensors. The sensor model used in this thesis focusses on deterministic and stochastic errors. The dynamic model contains scale factor errors, bias, misalignment and sensor dynamics. The stochastic model contains rate white noise and quantization noise. Environmental effects are not considered. It is assumed that temperature effects and other environmental influences are carefully compensated by the manufacturer and hence can be neglected. It is noted that MEMS are generally sensitive to temperature changes. However, modelling the thermodynamics at the sensor location is beyond the scope of this thesis.

A.5.3 Deterministic Sensor Error Model

A.5.3.1 Measurement Errors

The major deterministic sensor error contributions of gyroscopes are bias, scale factor errors and misalignment. They account for constant and linear measurement errors that are due to manufacturing tolerances and imperfect measurement principles. Together with the general noise term n_{gyro} the sensor error of a gyroscope can be modelled as

$$(\vec{\omega}_K^{IB})_S = \begin{bmatrix} b_x \\ b_y \\ b_z \end{bmatrix} + \underbrace{\begin{bmatrix} M_{xx} & 0 & 0 \\ 0 & M_{yy} & 0 \\ 0 & 0 & M_{zz} \end{bmatrix}}_{M_{sf}} \cdot (\vec{\omega}_K^{IB})_{B,0} + \underbrace{\begin{bmatrix} 0 & M_{xy} & M_{xz} \\ M_{yx} & 0 & M_{yz} \\ M_{zx} & M_{zy} & 0 \end{bmatrix}}_{M_{ma}} \cdot (\vec{\omega}_K^{IB})_{B,0} + v_{gyro} \tag{A.1}$$

where $(\vec{\omega}_K^{IB})_S$ is the measured, erroneous rotational rate of the IMU-frame w.r.t. the inertial frame, $[b_x, \quad b_y, \quad b_z]^T$ the bias vector, the matrix M_{sf} describes the scale-factor error, M_{ma} the sensor misalignment, i.e. the orientation of the IMU-frame w.r.t. the aircraft body frame, $(\vec{\omega}_K^{IB})_{B,0}$ is the true kinematic rotational rate of the body-fixed frame w.r.t. the inertial frame and v_{gyro} describes the sensor noise.

The components of $(\vec{\omega}_K^{IB})_S$ are denoted with p_S, q_S, q_S respectively, i.e.

$$(\vec{\omega}_K^{IB})_S = \begin{bmatrix} p_S \\ q_S \\ r_S \end{bmatrix} \tag{A.2}$$

The actual values for the deterministic sensor error model for the IMU are found in Table A-7. The values are based on the datasheets of the reference IMU.

Table A-7: Deterministic sensor error model parameters of IMU sensor models.

Parameter	Symbol	Tactical grade IMU
Bias	b_x, b_y, b_z	6 deg/h
Scale factor error	M_{xx}, M_{yy}, M_{zz}	150 ppm
Misalignment	M_{ma}	$\pm$0.01 deg

A.5.3.2 SENSOR DYNAMICS

The dynamics of gyroscopes can be relevant for some sensor types like spinning wheel gyros (IEEE, 1997). This is not the case for the MEMS modelled in this thesis. Even the industrial grade sensor has a 3db-bandwidth of 350 Hz, which is more than the simulation bandwidth. Hence sensor dynamics need not be considered in the simulation.

A.5.4 STOCHASTIC SENSOR ERROR MODEL

(IEEE, 1997) distinguishes a variety of different noise contributions. Each contribution has a specific dependence on frequency and hence dominates a certain frequency range of interest. The experiments in this thesis cover a frequency range from 0.05 to 200 Hz, with a special focus on the two decades from 0.05 to 5 Hz. It is seen later in this section that the dominating sensor noise contributions in this frequency range are rate white noise (also called angle random walk, ARW[62]) and quantization noise. Hence the gyro error model includes only

- rate white noise (ARW)
- quantization noise.

The respective noise levels and the quantization intervals are given in Table A-8. It is assumed that the entire measurement range ω_{max} is linearly mapped to the quantized output and the resulting. For a signal resolution with n_{bits} the resulting quantization interval $\Delta\omega$ is given by

$$\Delta\omega = 2\omega_{max}/2^{n_{bits}} \tag{A.3}$$

The quantization is included in the sensor model with Simulink's quantizer block (The Mathworks, 2017b).

Table A-8: Noise parameters of IMU sensor models.

Parameter	Tactical grade
Measurement range	$\pm$300 deg/sec
Quantization Resolution (interval)	32 bit[63] ($2.43 \cdot 10^{-9}$ deg/sec)
Rate white noise (ARW)	0.07 deg/$\sqrt{\text{h}}$
Bias Instability	6 deg/h

The resulting asymptotic PSDs for the tactical grade IMU model is shown in Figure A-4 as blue solid line. For comparison, a generic industrial grade IMU, based on the ADIS 16350 inertial sensor, manufactured by Analog Devices (Analog Devices, 2007) is shown as orange line. The ADIS 16350 has a lower accuracy than the µIMU and the PSD has thus larger values.

Dashed lines indicate the asymptotic PSD of the rate white noise and bias instability. The frequency where bias instability and rate white noise equally contribute to the noise are indicated with circles. Note that quantization noise does not contribute to the asymptotic PSD and hence does not show up in Figure A-4.

[62] In IMUs the rate measurements are integrated to compute the attitude angles. This makes rate white noise appear in angle measurements as random walk and lead to the name *angle random walk*.
[63] Typical value, not based on Northrop Grumman LITEF (2013)

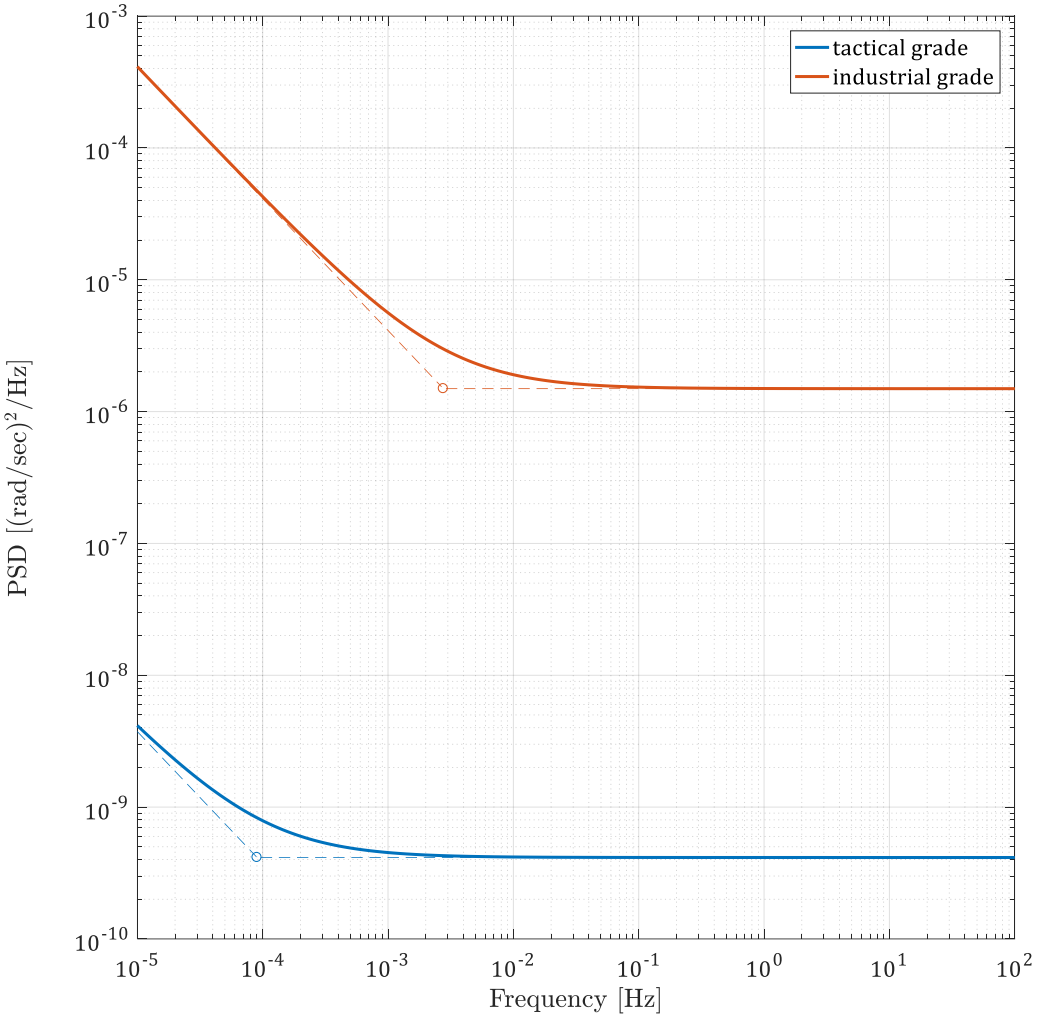

Figure A-4: Asymptotic PSD of IMU models (tactical grade: bottom, industrial grade: top).

A.6 Turn Coordination

To analyse the effect of the turn coordination on FRF estimates, the same simulation as in the baseline configuration is conducted, but *without* the turn coordinator. The FRF results from this second case are compared to the baseline configuration and the analytically linearized model. For simpler naming, the baseline configuration (*with* turn coordinator) is denoted as configuration 1. The configuration *without* turn coordinator is denoted as case 2.

The turn coordination commands an additional yaw command that is a function of roll angle ϕ, which is computed from integration of kinematic roll rate p_K. The additional yaw command results primarily in a yaw rate. The resulting linearized closed loop dynamics with and without turn coordination are shown in Figure A-6 (phase angles are wrapped to the range from -360° to 0° for a more compact view). The linearization is conducted in straight level flight. Hence the small angle approximation (3.3) can be applied. It is noted that the nonlinearity in (3.2) has no effect on the linearized dynamics, as the dynamics are linearized for $\Phi = 0$. It is seen that the turn coordinator causes differences in the FRM in $G_{q_K p_c}$ and $G_{r_K p_c}$. As the magnitude of $G_{q_K p_c}$ is very low compared to the other FRM elements, it has generally little effect on the overall response. Hence the additional dynamics due to

turn coordination affect primarily $G_{r_K p_c}$. Figure A-5 show the difference in dynamics due to the turn coordinator in $G_{r_K p_c}$. The major difference is found in the region from 1 to 10 Hz.

In this section the effect of the additional dynamics of the turn coordinator controller on the open loop estimate $\hat{G}_{yu}$ are analysed. The focus is on the yaw rate response due to roll command, i.e. on $\hat{G}_{r_K \xi_c}$.

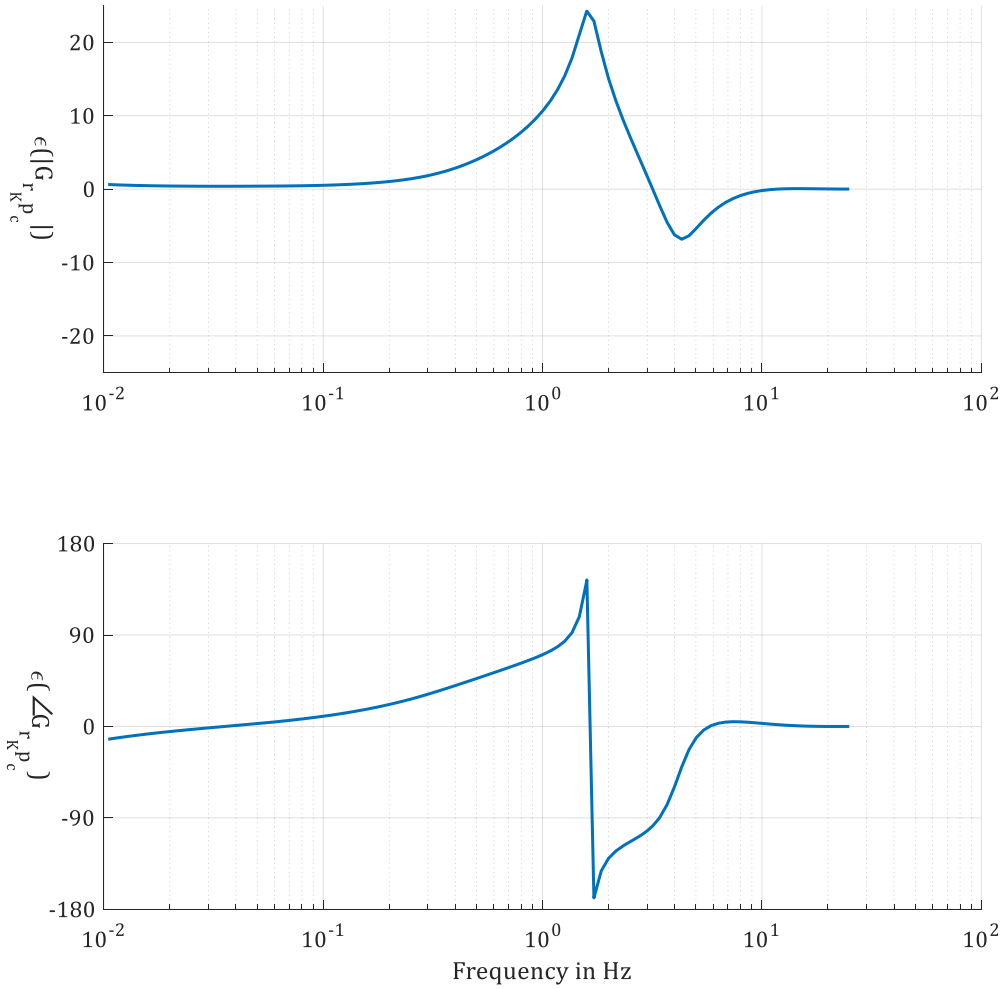

Figure A-5: Additional dynamics in $G_{r_K p_c}$ due to turn coordinator.

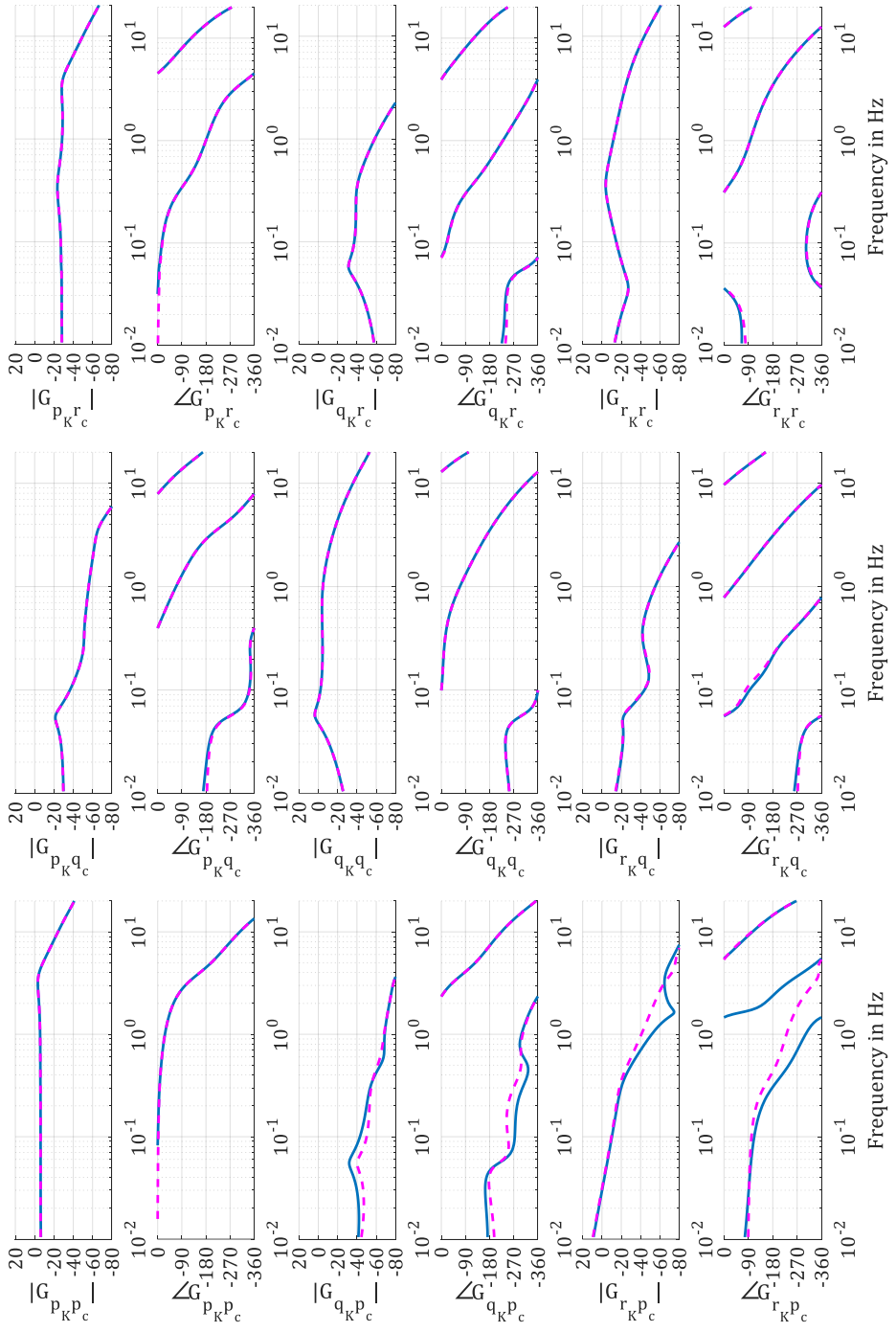

Figure A-6: Comparison of closed loop dynamics with and without turn coordinator. The dynamics with turn coordinator are shown as dashed magenta line, the dynamics without turn coordinator are shown as solid blue line.

A.7 Estimation of Nonparametric Noise Model

A nonparametric noise model consisting of the output noise pdf can be estimated from flight tests with fixed controls. The sample (co-)variances $\hat{\sigma}_U^2, \hat{\sigma}_Y^2, \hat{\sigma}_{YU}^2$ of V_U, V_Y, V_{YU} respectively are estimated from multiple observations of U and Y while keeping the controls fixed, i.e. with $U_0 = Y_0 = 0$. So the observed input and output signals contain only noise.

$$U = V_U \tag{A.4}$$

$$Y = V_Y \tag{A.5}$$

Similar to Bartlett's approach, the entire datasets are split in M separate segments $U^{[l]}, Y^{[l]}$ with $l = 1, \dots, M$. Each segment is treated as an independent observation of the noise process. The sample (co-) variances are estimated from the signals' DFT's with equations (2.44) to (2.46).

To result in accurate estimates, M should be large enough. Bendat and Piersol recommend the number of averages M to be

$$M_X = \frac{2}{CV(X)^2} \tag{A.6}$$

where $CV(X)$ is the coefficient of variation, also called normalized random error (Bendat & Piersol, 1971/2010, pp. 251, 285) with

$$CV(X) = \frac{std(\hat{X})}{X_0} \tag{A.7}$$

and X is the signal under consideration. The acceptable normalized error is chosen by the experimenter.

Hence for a given frequency resolution Δf and a given number of averages M the total observation length T_{total} is

$$T_{total} = M \cdot \frac{1}{\Delta f} \tag{A.8}$$

The total observation length may be in the order of multiple minutes, depending on required accuracy and frequency resolution. Flying with fixed controls for multiple minutes may be not feasible for real flight tests. Nevertheless, it worked well in simulations of straight level flight under light turbulence.

A.8 Confidence Regions for Noise DFTs

Each element of $V_U^{[l]}(k)$, $V_Y^{[l]}(k)$ is circular complex normally distributed with variance $\sigma_U(k), \sigma_Y(k)$ respectively.

$$V_U(k) \in \mathbb{N}^c\left(0, \sigma_U^2(k)\right) \tag{A.9}$$

$$V_Y(k) \in \mathbb{N}^c\left(0, \sigma_Y^2(k)\right) \tag{A.10}$$

Hence confidence regions for the expected amplitudes can be constructed from variance estimates. The computation is similar to the one for FRM-estimates shown in section 2.6.5. Hence with sample variance $\hat{\sigma}_U$ estimated from M independent observations circular confidence intervals with radius r_p can be constructed for V_U and V_Y. These include observed noise amplitudes with probability p:

$$r_{p,U}(k) = \hat{\sigma}_U(k)\sqrt{\mathbb{F}^{-1}(p, 1, M-1)} \tag{A.11}$$

$$r_{p,Y}(k) = \hat{\sigma}_Y(k)\sqrt{\mathbb{F}^{-1}(p, 1, M-1)} \tag{A.12}$$

As the confidence intervals are circular, the respective confidence radii correspond to the maximum expected amplitude of the input and output noise respectively, i.e. the absolute value of the expected amplitude is smaller than $r_{p,U}$ with probability p.

$$prob\left(|V_U(k)| \leq r_{p,U}(k)\right) = p \tag{A.13}$$

For MIMO systems simultaneous confidence regions need to be computed, cmp. section 2.6.5. Analogously to the SISO case circular confidence regions are constructed. For a system with n_{in} input- and n_{out} output signals the respective confidence regions for the i-th input and output channel are respectively

$$r_{p,U,[i]}(k) = \sqrt{\frac{n_{in}}{M-n_{in}}\mathbb{F}^{-1}(p, n_{in}, M-n_{in})\hat{C}_{vec(V_u),[i,i]}(k)} \tag{A.14}$$

and

$$r_{p,Y,[i]}(k) = \sqrt{\frac{n_{out}}{M-n_{out}}\mathbb{F}^{-1}(p, n_{out}, M-n_{out})\hat{C}_{vec(V_y),[i,i]}(k)} \tag{A.15}$$

B MATHS

B.1 DISCRETE TIME BAND LIMITED WHITE NOISE

White noise is a theoretical concept of a continuous time random process with constant power spectral density for all frequencies. In reality, no such process can exist, as it would contain infinite energy. Nevertheless, the effect of white noise on discrete time systems can be simulated within a limited bandwidth B by discrete time random number sequences; such sequences are sometimes denoted as band limited white noise (The Mathworks, 2018). To conserve the flat power spectral density within the bandwidth, the variance of the random number generator is scaled with the sample time, i.e. with $T_s = \frac{1}{B}$. To simulate white noise with variance σ^2 the random number series are independent realizations of a Gaussian distribution with

$$e[n] \in \mathbb{N}\left(0, \frac{\sigma^2}{T_s}\right), \tag{B. 1}$$

The DFT coefficients $E(k) = \mathrm{DFT}(e[n])$ are circular complex normally distributed with

$$E(k) \in \mathbb{N}^c\left(0, \frac{\sigma^2}{T_s}\right), \qquad \forall\, k \in \mathbb{Z}^+ \tag{B.2}$$

As proven in (Pintelon & Schoukens, 2012, p. 601) the DFT of filtered iid noise

$$v[n] = H(z^{-1})e[n], \tag{B.3}$$

with stable $H(z^{-1})$ and $e[n]$ with existing moments of any order, is asymptotically (for $N \to \infty$) independent, circular complex normally distributed. It follows that the DFT coefficients $V(k) = \mathrm{DFT}(v[n])$ are circular complex normally distributed with

$$V(k) \in \mathbb{N}^c\left(0, \sigma_k^2\right), \qquad \forall\, k \in \mathbb{Z}^+ \tag{B.4}$$

where $\sigma_k^2 = \frac{\sigma^2}{T_s} \cdot \left|H\left(z_k^{-1}\right)\right|^2$.

B.2 COMPLEX RANDOM VARIABLES

The following introduction of the relevant statistical distributions is based on (Pintelon & Schoukens, 2012, pp. 568–569). The focus is on complex random variables and their mathematical description.

B.2.1 COMPLEX RANDOM VARIABLES

B.2.1.1 GENERAL COMPLEX RANDOM VARIABLES

Complex numbers are defined by their real and imaginary parts. As an example, a complex number z is given by its real part x and its imaginary part y by

$$z = x + jy \tag{B.5}$$

This concept is directly extended to random variables: A complex random variable z can be constructed from two real random variables x and y. The random variable z is fully described by the multivariate distribution function of x and y (Picinbono, 1993, pp. 53–54). From (B.5) follows that complex random variables can be described either as complex random variables (here: z) or in terms of their real and imaginary parts, i.e. by a random vector (here: $[\mathrm{Re}(z), \quad \mathrm{Im}(z)]^T$). A third description, given in terms of magnitude and phase

of z, is not used in this thesis. For a detailed discussion of all three representations and their respective properties, the reader is referred to (Picinbono, 1993). Analogously to real random variables, the mean of a complex random variable is defined as its expected value (Picinbono, 1993, p. 53).

$$\begin{aligned} \mu_z &= \mathbb{E}\{z\} \\ &= \mathbb{E}\{x\} + j\mathbb{E}\{y\} \end{aligned} \tag{B.6}$$

Following the definition given in (Picinbono, 1993, p. 53), the variance of a complex random variable z is given by $\sigma_z^2 = \mathbb{E}\{|z - \mu_z|^2\}$, where $\mu_z = \mathbb{E}\{z\}$. For a complex random variable with zero mean, the variance is thus given by

$$\begin{aligned} \sigma_z^2 &= \mathbb{E}\{|z|^2\} = \mathbb{E}\{z\bar{z}\} \\ &= \mathbb{E}\{|x + jy|^2\} \\ &= \mathbb{E}\left\{\left(\sqrt{x^2 + y^2}\right)^2\right\} \\ &= \mathbb{E}\{x^2\} + \mathbb{E}\{y^2\} \\ &= \sigma_x^2 + \sigma_y^2 \end{aligned} \tag{B.7}$$

where $\sigma_x^2, \sigma_y^2, \sigma_z^2$ denotes the variance of x, y, z respectively (Picinbono, 1993, pp. 53–54).

Variance does not contain information about the correlation of the real and imaginary part. As a consequence, an additional quantity is required to fully describe the second order moments. It is called *pseudo-variance* or *relation* (matrix) and is defined as

$$\mathrm{R}_z = \mathbb{E}\{zz^T\} \tag{B.8}$$

Alternatively, the second order moment of z can be described by the variance and covariance of its real and imaginary parts. In this notation, the second order moment of the random variable is a real valued covariance matrix Γ_z [64], defined as

$$\Gamma_z = \begin{bmatrix} \mathrm{var}(x) & \mathrm{cov}(x,y) \\ \mathrm{cov}(y,x) & \mathrm{var}(y) \end{bmatrix} \tag{B.9}$$

It is seen that equation (B.10) has the form of a real bivariate random vector. The following derivation of circular distributed random variables and their properties is based on the real valued covariance matrix, as it is more descriptive; in the main part of this thesis only complex valued covariance matrices are used.

B.2.1.2 Circular Random Variables

When the real and imaginary parts are independent, identically distributed (iid), the covariance Γ_z becomes a diagonal matrix with $\mathrm{var}(x) = \mathrm{var}(y)$. In this case, the complex random variable is said to be *circular* distributed (Picinbono, 1993, p. 120). Its real valued covariance matrix has the shape

$$\Gamma_z = \frac{1}{2}\begin{bmatrix} \sigma_x^2 & 0 \\ 0 & \sigma_x^2 \end{bmatrix} \tag{B.10}$$

In (Picinbono, 1993, pp. 136–138) it is further shown that this condition is identical to

$$\mathbb{E}\{(z - \mathbb{E}\{z\})(z - \mathbb{E}\{z\})^T\} = 0 \tag{B.11}$$

[64] The nomenclature for real valued and complex valued covariance matrices differs in the cited literature. The thesis at hand follows the convention used in Pintelon and Schoukens (2012) and uses $C(Z)$ or C_Z for the *complex* valued covariance matrix; the *real* valued covariance matrix is denoted with Γ_Z. The nomenclature in Picinbono (1993) is, however, the other way round.

$$\text{or} \qquad \begin{aligned} Cov\big(Re(z)\big) &= Cov\big(Im(z)\big) \\ Cov\big(Re(z), Im(z)\big) &= -Cov\big(Im(z), Re(z)\big) \end{aligned} \tag{B.12}$$

Thus, the pseudo-variance of a circular complex random variable is zero. Figure B-7 shows scatter plots of the real and imaginary part of complex random variables[65] with the respective 95%-confidence regions. In the left plot, the real and imaginary part are correlated; its confidence region is an ellipsoid. The right plot shows a circular distribution; its confidence region is circular shaped.

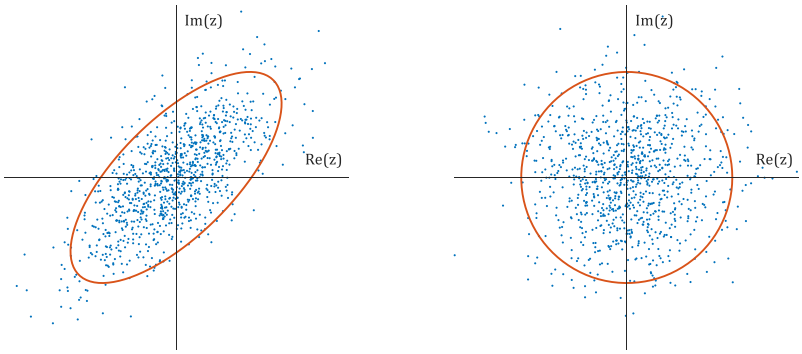

Figure B-7: Scatter plot of complex RV with correlated real and imaginary parts (left) and circular complex RV (right).

B.2.2 Complex Random Vectors

As for real random variables, also complex random variables can be easily extended to random vectors by stacking them together in a vector. Combining n complex random variables results either in a vector of n complex random variables (complex representation) or in a vector with $2n$ real random variables (real & imaginary parts).

B.2.2.1 Complex Valued Covariance Matrix

For two complex random variables $u = x + jy$ and $v = s + jt$ the covariance is defined as

$$C_{uv} = \mathbb{E}\big\{(u - \mathbb{E}\{u\})\overline{(v - \mathbb{E}\{v\})}\big\} \tag{B.13}$$

where $\overline{v - \mathbb{E}\{v\}}$ is the complex conjugate of $v - \mathbb{E}\{v\}$ (Picinbono, 1993, p. 54). For zero-mean random variables and in matrix notation with $Z = [u, v]^T$ the definition results in

$$\begin{aligned} C_X &= \mathbb{E}\{Z\bar{Z}^T\} \\ &= \mathbb{E}\{ZZ^H\} \end{aligned} \tag{B.14}$$

where $\bar{Z}$ is the complex conjugate of Z and Z^H the Hermitian matrix, i.e. the complex conjugate transpose. The pseudo-covariance or relation matrix R_Z and is defined as

$$R_Z = \mathbb{E}\{(Z - \mathbb{E}\{Z\})(Z - \mathbb{E}\{Z\})^T\} \tag{B.15}$$

For zero mean random variables R_X results in

$$R_Z = \mathbb{E}\{ZZ^T\} \tag{B.16}$$

Both, the covariance and the relation matrix are generally complex valued and of dimension $n \times n$.

[65] The random variables in this example are circular complex normally distributed, see section B.2.5.1.

B.2.2.2 REAL VALUED COVARIANCE MATRIX

When expressed by its real and imaginary parts, the second order moment of a complex random vector Z can be described by the (co-)variance of real and imaginary parts of u and v, i.e. by $\Gamma_u, \Gamma_v, \Gamma_{uv}$ and Γ_{vu}. This results in the real valued covariance matrix

$$\Gamma_Z = \begin{bmatrix} \Gamma_u & \Gamma_{uv} \\ \Gamma_{vu} & \Gamma_v \end{bmatrix} \tag{B.17}$$

(Picinbono, 1993, 118). The complex covariance matrix C_Z can be constructed from $\Gamma_u, \Gamma_v, \Gamma_{uv}$ and Γ_{vu} by

$$C_Z = \Gamma_u + \Gamma_v + j(-\Gamma_{uv} + \Gamma_{vu}) \tag{B.18}$$

The computation of Γ_z and its submatrices from C_Z is slightly more involved and is described in (Picinbono, 1993, pp. 118–119).

When described by its real and imaginary parts, the real covariance matrix is of dimension $2n \times 2n$ and includes the information of the complex covariance and complex relation matrix.

B.2.2.3 CIRCULAR COMPLEX RANDOM VECTORS

Analogously to a single random variable, also a complex random vector is called *circular*, if its relation matrix R is zero. It further follows that for a circular complex random vector, its real and imaginary parts have the same covariance, i.e.

$$Cov\big(Re(Z)\big) = Cov\big(Im(Z)\big) \tag{B.19}$$

and further

$$Cov\big(Re(Z), Im(Z)\big) = -Cov\big(Im(Z), Re(Z)\big)^T \tag{B.20}$$

To analyse the shape of the real valued covariance matrix of circular complex random variables, it is more convenient, to order the real parts of all vector elements first, followed by the imaginary parts, i.e. $\tilde{Z} = [\mathrm{Re}(Z), \quad \mathrm{Im}(Z)]^T$ which is written shorter as $\tilde{Z} = [\tilde{u}, \quad \tilde{v}]^T$. It follows from equations (B.9), (B.17), (B.19) and (B.20) that $\Gamma_{\tilde{Z}}$ conistists of four blocks $\Gamma_{\tilde{u}}$, $\Gamma_{\tilde{v}}$, $\Gamma_{\tilde{u}\tilde{v}}$, $\Gamma_{\tilde{u}\tilde{v}}$, where

$$\Gamma_{\tilde{u}} = \Gamma_{\tilde{v}} \tag{B.21}$$

and

$$\Gamma_{\tilde{u}\tilde{v}} = -\Gamma_{\tilde{u}\tilde{v}} \tag{B.22}$$

It follows that $\Gamma_{\tilde{Z}}$ has the shape

$$\begin{aligned} \Gamma_{\tilde{Z}} &= \begin{bmatrix} \Gamma_{\tilde{u}} & \Gamma_{\tilde{u}\tilde{v}} \\ \Gamma_{\tilde{v}\tilde{u}} & \Gamma_{\tilde{u}} \end{bmatrix} \\ &= \begin{bmatrix} & & & 0 & & \Gamma_{\tilde{u}\tilde{v},[k,l]} \\ & \Gamma_{\tilde{u}} & & & \ddots & \\ & & & \Gamma_{\tilde{u}\tilde{v},[l,k]} & & 0 \\ 0 & & \Gamma_{\tilde{v}\tilde{u},[k,l]} & & & \\ & \ddots & & & \Gamma_{\tilde{u}} & \\ \Gamma_{\tilde{v}\tilde{u},[l,k]} & & 0 & & & \end{bmatrix} \end{aligned} \tag{B.23}$$

where the blocks $\Gamma_{\tilde{u}\tilde{v}}$ and $\Gamma_{\tilde{v}\tilde{u}}$ have zero diagonal elements and non-zero elements $\Gamma_{\tilde{v}\tilde{u},[k,l]}$ for $k \neq l$. This implies that each element of a circular complex random vector is itself a circular complex random variable, cmp. equation (B.10).

However, a vector with circular complex distributed elements need *not* be circular, as circularity of each individual element does not ensure that (B.22) is fulfilled.

B.2.2.4 CIRCULAR COMPLEX NORMALLY DISTRIBUTED RANDOM VECTORS

As introduced before, the pseudo-variance R_Z is zero for circular complex distributed random variables. From this follows that circular complex *normally* distributed random vectors are fully described by their mean and covariance (Picinbono, 1993, pp. 118–119).

The frequency response estimates in this thesis are approximately zero-mean circular normally distributed. Their probability functions are fully described by the covariance matrix C and the pseudo-variance R need not be considered.

B.2.3 CIRCULAR CORRELATION COEFFICIENT

The correlation of two circular distributed random variables can be measure with different coefficients; an overview is found in (Jupp & Mardia, 1989). A circular variant of Pearson's correlation coefficient was proposed in (Jammalamadaka & SenGupta, 2001); it is denoted by ρ_{xy}^c and is defined as

$$\rho_{xy}^c = \frac{\mathbb{E}\{\sin(x - \mathbb{E}(x))\sin(y - \mathbb{E}\{y\})\}}{\sqrt{var(\sin(x - \mathbb{E}(x))) \cdot var(\sin(y - \mathbb{E}(y)))}} \tag{B.24}$$

where x and y are two circular random variables. The value of $|\rho_{xy}^c|$ is bounded in the range from 0 to 1, where a value of 0 indicates that the two RVs are uncorrelated. The circular correlation coefficient can be used to test for the uncorrelatedness of the phase arguments of optimized multisine signals.

B.2.4 REAL DISTRIBUTION FUNCTIONS

B.2.4.1 NOMENCLATURE FOR DISTRIBUTION FUNCTIONS

The nomenclature of probability distribution function follows the conventions:

- Distribution functions are denoted with double stroke letters (e.g. $\mathbb{m}$ or $\mathbb{N}$)
- Probability density functions (pdfs) are generally denoted with lowercase letters.
- Cumulative distribution functions (cdfs) are generally denoted with uppercase letters.

It is noted that the use of lowercase / uppercase is also used to differentiate signals and their Fourier transforms. Thus the meaning of lowercase / uppercase letters is either clear from the context or is explicitly stated in case of ambiguities.

B.2.4.2 REAL NORMAL DISTRIBUTION

A real random *variable* a is said to be *normally* distributed, i.e. $a \in \mathbb{N}(\mu, \sigma^2)$ with mean μ and variance σ^2, if its probability density function $p_a(x, \mu, \sigma^2)$ is

$$p_a(x, \mu, \sigma^2) = \frac{1}{\sqrt{2\pi} \cdot \sigma} e^{\frac{-(x-\mu)^2}{2\sigma^2}}, \qquad -\infty < x < \infty \tag{B.25}$$

The probability density function of a normally distributed variable with mean μ and variance σ^2 at some value x is denoted with $\mathbb{m}(x, \mu, \sigma^2)$. Analogously the cumulative distribution function is denoted with capital letters $\mathbb{N}(x, \mu, \sigma^2)$, cmp. (Ross, 2000, p. 160).

A real normally distributed random *vector* $b \in \mathbb{R}^n$ with mean μ_b and covariance matrix C_b is denoted as

$$b \in \mathbb{N}^n(\mu_b, C_b) \tag{B.26}$$

where μ_b is a real valued $n \times 1$ vector and C_b a real valued $n \times n$ matrix.

B.2.4.3 CHI SQUARED DISTRIBUTION

A real random variable c that is the sum of n independent identically distributed (iid) squared normal random variables $a_k \in \mathbb{N}(0,1),\ k = 1, \dots, n$ is said to be χ^2-distributed with n degrees of freedom (dofs).

$$c = a_1^2 + a_2^2 + \cdots + a_n^2 \tag{B.27}$$

This is denoted as

$$c \in \chi^2(n) \tag{B.28}$$

The pdf $p_c(x, n)$ of a χ^2-*distributed random variable* with n degrees of freedom is given by

$$p_c(x, n) = \frac{\frac{1}{2} e^{\frac{-x}{2}} \left(\frac{x}{2}\right)^{\left(\frac{n}{2}\right)-1}}{\Gamma\left(\frac{n}{2}\right)}, \qquad x > 0 \tag{B.29}$$

where $\Gamma(\alpha)$ is the gamma function $\Gamma(\alpha) = \int_0^\infty x^{\alpha-1} e^{-x} dx$. (Ross, 2000, pp. 173–179)

B.2.4.4 WISHART DISTRIBUTED RANDOM MATRIX

Let $d \in \mathbb{R}^{n \times n}$ be a matrix-valued random variable that is the sum of the product of p independent identically normally distributed random vectors $b_k \in \mathbb{N}^n(0, C_b),\ k = 1, \dots p$.

$$d = \sum_{k=1}^{p} b_k b_k^T \tag{B.30}$$

d is said to be Wishart distributed with n degrees of freedom and associated parameter matrix C_b (Wishart, 1928).

$$d \in \mathbb{W}^n(p, C_b) \tag{B.31}$$

The Wishart distribution is the multivariate generalization of the χ^2-distribution and hence

$$\mathbb{W}^1(n, 1) = \chi^2(n) \tag{B.32}$$

B.2.4.5 STUDENT T-DISTRIBUTED RANDOM VARIABLE

Let b and c be two independent random variables, where b is standard normally distributed, i.e. $b \in \mathbb{N}(0,1)$, and c is χ^2-distributed with n degrees of freedom i.e. $c \in \chi^2(n)$. Then the quotient

$$\mathfrak{e} = \frac{b}{\sqrt{\frac{c}{n}}} \tag{B.33}$$

is said to be t-distributed with n degrees of freedom (Gosset, 1908) and it is written shortly

$$\mathfrak{e} \in \mathbb{t}(n) \tag{B.34}$$

The t-distribution is often named *student t-distribution* after W. Gosset's pen name 'student'. Note that the student t- distribution is denoted with lower case $\mathbb{t}$. The distinction of its cdf and pdf follows from the context.

B.2.4.6 F- DISTRIBUTED RANDOM VARIABLE

The ratio g of two independent χ^2-distributed random variables $c_1 \in \chi^2(n_1)$ and $c_2 \in \chi^2(n_2)$ with n_1 and n_2 dofs, respectively, is *F-distributed* with n_1 and n_2 dofs. (Ross, 2000, 182-183)

$$g = \frac{c_1/n_1}{c_2/n_2} = \frac{n_2\, c_1}{n_1\, c_2} \tag{B.35}$$

This is denoted as

$$g \in \mathbb{F}(n_1, n_2) \tag{B.36}$$

The pdf p_g of an F-distributed random variable is denoted as $p_g \in \mathbb{f}(x, n_1, n_2)$, its cdf P_g as $P_g \in \mathbb{F}(x, n_1, n_2)$.

B.2.5 COMPLEX DISTRIBUTION FUNCTIONS

As introduced before in appendices B.2.1 and B.2.2, complex random variables can be derived from real valued random variables. Analogously, complex distribution functions are derived from real ones. In this section, the relevant complex distribution functions are introduced.

B.2.5.1 CIRCULAR COMPLEX NORMAL DISTRIBUTION

A random vector $x \in \mathbb{C}^n$ is called *circular complex normally* distributed, if its real and imaginary parts are jointly normally distributed (Picinbono, 1993, p. 118). Its probability function is uniquely determined by its mean μ_x and covariance matrix C_x and is given by

$$p_x(x) = p_{x_{re}}(x_{re}) = \frac{1}{\pi^n \det(C_x)} e^{\left[-(x-\mu_x)^H\, C_x^{-1}\, (x-\mu_x)\right]} \tag{B.37}$$

where $x_{re} = \mathrm{Re}(x)$ denotes the real part of x. A circular complex normally distributed random vector $x \in \mathbb{C}^n$ with mean μ_x and covariance matrix C_x is denoted as $x \in \mathbb{N}^{c,n}(\mu_x, C_x)$, where the superscript c indicates the circular distribution and the superscript n indicates the dimension of x.

B.2.5.2 COMPLEX WISHART DISTRIBUTION

The complex random matrix $y \in \mathbb{C}^{p\times p}$ that is the sum of n random variables $x_k \in \mathbb{N}^{c,p}(0, C_x)$, with $k = 1, \dots, n$ as shown in equation (B.38) is *complex Wishart* distributed with n degrees of freedom and associated parameter matrix C_x and is denoted as $y \in \mathbb{W}^{c,p}(n, C_x)$. (Pintelon & Schoukens, 2012, p. 569)

$$y = \sum_{k=1}^{n} x_k x_k^H \tag{B.38}$$

The probability density function y(x) is given in (Goodman, 1963, p. 162; Pintelon & Schoukens, 2012, p. 569) for $n \geq p$ and $y \geq 0$ as

$$f_y(y) = \frac{(\det(y))^{n-p}\; e^{-tr(C_x^{-1}y)}}{\pi^{\frac{p(p-1)}{2}} (\det(C_x))^n \prod_{k=1}^{n}(n-k)!} \tag{B.39}$$

B.3 Derivation of Gaussian Approximation With Taylor Series Expansion

The Gaussian approximation of probability density functions of FRF estimates can be derived from a Taylor expansion. In comparison to the derivation in (Pintelon et al., 2003), this approach is shorter, but less informative, as the true pdf's are not computed.

Starting from equation (2.162), the right hand side is slightly rewritten,

$$\begin{aligned}\hat{G} &= \frac{Y_0 + V_Y}{U_0 + V_U} \\ &= \frac{Y_0}{U_0} \cdot \frac{1 + V_Y/Y_0}{1 + V_U/U_0} \\ &= G_0 \cdot \frac{1 + V_Y/Y_0}{1 + V_U/U_0}\end{aligned} \tag{B.40}$$

Where V_U, V_Y are circular complex normally distributed, i.e. $V_U, V_Y \in \mathbb{N}^c\left(0, C_{U/Y}\right)$. For further analysis the denominator $\frac{1}{1+V_U/U_0}$ in (B.40) is expanded as a Taylor series, leading to

$$\hat{G} = G_0 \cdot \left(1 + \frac{V_Y}{Y_0}\right) \cdot \left(1 - \frac{V_U}{U_0} + \left(\frac{V_U}{U_0}\right)^2\right) + h.o.t \tag{B.41}$$

where h.o.t. denotes higher order terms. If only first order terms of the Taylor series are considered, equation (B.41) reduces to

$$\hat{G} \approx G_0 \cdot \left(1 + \frac{V_Y}{Y_0} - \frac{V_U}{U_0}\right) = G_0 + V_G \tag{B.42}$$

where $V_G = \frac{V_Y}{Y_0} - \frac{V_U}{U_0}$. As V_Y and V_U are circular complex normally distributed, so are V_G and $\hat{G}$. (Pintelon & Schoukens, 2012, p. 47)

C Details on Derivations and Computations

C.1 Derivation of Transient Terms

Detailed derivation of equation (2.64):

$$\begin{aligned} T_1(z) &= \sum_{q=0}^{n_b} b_q z^{-q} \cdot U_1(z) - \sum_{p=0}^{n_a} a_p z^{-p} \cdot Y_1(z) \\ &= \sum_{q=0}^{n_b} b_q z^{-q} \cdot \sum_{n=-q}^{-1} y[n] z^{-n} - \sum_{p=0}^{n_a} a_p z^{-p} \cdot \sum_{n=-p}^{-1} u[n] z^{-n} \\ &= \sum_{q=0}^{n_b} b_q z^{-q} \cdot \sum_{n=1}^{q} y[-n] z^{n} - \sum_{p=0}^{n_a} a_p z^{-p} \cdot \sum_{n=1}^{p} u[-n] z^{n} \\ &= \sum_{q=0}^{n_b} \sum_{n=1}^{q} b_q z^{-q}\, y[-n] z^{n} - \sum_{p=0}^{n_a} \sum_{n=1}^{p} a_p z^{-p}\, u[-n] z^{n} \\ &= \sum_{q=0}^{n_b} \sum_{n=1}^{q} b_q\, y[-n] z^{n-q} - \sum_{p=0}^{n_a} \sum_{n=1}^{p} a_p\, u[-n] z^{n-p} \end{aligned} \tag{C.1}$$

Similarly, T_2 in equation (2.74)is given by

$$\begin{aligned} T_2(z) &= \sum_{q=0}^{n_b} b_q z^{-q} \cdot U_2(z) - \sum_{p=0}^{n_a} a_p z^{-p} \cdot Y_2(z) \\ &= \sum_{q=0}^{n_b} b_q z^{-q} \cdot \sum_{n=1}^{q} u[N-n] z^{n} - \sum_{p=0}^{n_a} a_p z^{-p} \cdot \sum_{n=1}^{q} y[N-n] z^{n} \\ &= \sum_{q=0}^{n_b} \sum_{n=1}^{q} b_q\, u[N-n] z^{n-q} - \sum_{p=0}^{n_a} \sum_{n=1}^{p} a_p\, y[N-n] z^{n-p} \end{aligned} \tag{C.2}$$

C.2 Computation of α_{R+2}

The constant factor in the bias estimate can be easily computed numerically: For lightly damped ($\zeta < 0.25$) PT2-system, the frequency response is computed in a small frequency range B_{lpm} around the response peak at ω_N. The values given in 2.5.4.2 are computed with $B_{rel} = 0.02$. In this range, a large number of supporting points (here 10001) is computed; this range is approximated with a polynomial of order R.

The interpolation bias is the remaining error at ω_N; α_{R+2} can then be computed directly from equation (2.133) (solved for α_{R+2}):

$$\alpha_{R+2} = b(\omega_0) \left(\frac{B_{lpm}}{B_{3dB}}\right)^{-R-2} |G_{max}|^{-1} \tag{C.3}$$

In the given example, numerical accuracy limits the computation for $R > 6$.

C.3 Estimation of 3-dB Frequency Range

The estimation of the 3 dB frequency range is based on local polynomial approximations of the estimated FRF. The approach follows (Schoukens et al., 2012) and applies the same ansatz to MIMO dynamics. However, the MIMO system is treated as a collection of independent SISO systems. Note that this approach is similar, but slightly different from the LPM algorithm, especially as each input/output pair is approximated independently.

The MIMO response $\hat{G}$ is split in separate SISO

$$G_n = \widetilde{K}_n \widetilde{\Theta} \tag{C.4}$$

For R=2:

$$G_n = \begin{bmatrix} \hat{G}_{[i,j]}(k - n_E) \\ \hat{G}_{[i,j]}(k - n_E + 1) \\ \vdots \\ \hat{G}_{[i,j]}(k) \\ \vdots \\ \hat{G}_{[i,j]}(k + n_E - 1) \\ \hat{G}_{[i,j]}(k + n_E) \end{bmatrix} \tag{C.5}$$

With dimension $(2n_E + 1 \times 1)$

$$\widetilde{K}_n = \begin{bmatrix} (-n)^0 & (-n)^1 & (-n)^2 \\ (-n+1)^0 & (-n+1)^1 & (-n+1)^2 \\ \vdots & \vdots & \vdots \\ 1 & 0^1 & (0)^2 \\ \vdots & \vdots & \vdots \\ (n-1)^0 & (n-1)^1 & (n-1)^2 \\ (n)^0 & (n)^1 & (n)^2 \end{bmatrix} \tag{C.6}$$

Of dimension $(2n_E + 1 \times R + 1)$

$$\widetilde{\Theta} = \begin{bmatrix} g_0 \\ g_1 \\ g_2 \end{bmatrix} \tag{C.7}$$

Of dimension $(R + 1 \times 1)$, where g_0, g_1, g_2 are the polynomial coefficients.

The polynomial

$$g_0 + g_1 r + g_2 r^2 \approx G_{[i,j]}(k + r) \tag{C.8}$$

Approximates the response from the j-th input to the i-th output. The 3 dB-frequency range corresponds approximately to a reduction of magnitude to about $1/\sqrt{2}$ of the reference value. This results in a quadratic equation

$$g_0 + g_1 r + g_2 r^2 \approx \frac{1}{\sqrt{2}}\, g_0, \tag{C.9}$$

or

$$\left(1 - \frac{1}{\sqrt{2}}\right) g_0 + g_1 r + g_2 r^2 = 0 \tag{C.10}$$

that can be solved with the quadratic formula:

$$r_{3dB\pm} = \frac{-g_1 \pm \sqrt{g_1^2 - 4\left(1 - \frac{1}{\sqrt{2}}\right) g_0 g_2}}{2g_2}, \tag{C.11}$$

where r_{3db+} and r_{3db-} denote the two separate solution respectively. If the linear term g_1 is neglected, the right hand side reduces to

$$r_{3dB\pm} = \frac{\pm\sqrt{\left(-4+\frac{4}{\sqrt{2}}\right)g_0 g_2}}{2g_2} = \pm\sqrt{\left(-1+\frac{1}{\sqrt{2}}\right)\frac{g_0}{g_2}} \tag{C.12}$$

and the 3db-frequency range results in

$$B_{3dB} = \Delta f \cdot |r_{3db+} - r_{3dB-}| \tag{C.13}$$

or respectively

$$B_{3dB} = 2 \cdot \Delta f \cdot \sqrt{\left(-1+\frac{1}{\sqrt{2}}\right)\frac{g_0}{g_2}} \tag{C.14}$$

Close to a pole, g_2 (the FRF curvature) will be negative, g_0 is always positive; hence (C.11) and (C.12) will have real solutions. A rough estimate is provided as $B_{3dB} \approx \Delta f \cdot \sqrt{\frac{-g_0}{g_2}}$, where $\sqrt{1-\frac{1}{\sqrt{2}}} \approx 0.5$ is assumed. To estimate the bias in the vicinity of zeros, the algorithm can be applied analogously.

C.4 Derivation of N_{11} for Additive Uncertainty

The derivation of the N_{11} from the general control configuration starts from equations (2.214) and (2.215), repeated here for convenience.

$$\begin{bmatrix} z \\ y \\ e \end{bmatrix} = P \begin{bmatrix} w \\ v \\ u \end{bmatrix} = \begin{bmatrix} P_{11} & P_{12} & P_{13} \\ P_{21} & P_{22} & P_{23} \\ P_{31} & P_{32} & P_{33} \end{bmatrix} \begin{bmatrix} w \\ v \\ u \end{bmatrix} \tag{C.15}$$

$$u = Ke \tag{C.16}$$

From equation (C.15) one finds $e = P_{31}w + P_{32}v + P_{33}u$; inserting in (C.16) results in

$$u\,(I - KP_{33}) = KP_{31}w + KP_{32}v \tag{C.17}$$

From equation (C.15) it is further found $z = P_{11}w + P_{12}v + P_{13}u$; replacing u with equation (C.17) leads to

$$\begin{aligned} z = &[P_{11} + P_{13}\,(I - KP_{33})^{-1}\,KP_{31}] \cdot w + \\ &+ [P_{12} + P_{13}\,(I - KP_{33})^{-1}\,KP_{32}] \cdot v, \end{aligned} \tag{C.18}$$

obviously resulting in (2.221) and (2.222).